ABSTRACT

Development of Ion Mobility Mass Spectrometry Deconvolution Strategies for Use in Data-Independent Acquisition Proteomics

Michael Edmund Pettit, Ph.D.

Mentor: Touradj Solouki, Ph.D.

Modern mass spectrometers are among the most sensitive and suitable analytical tools for high-throughput protein characterization. However, limitations in ion mobility (IM) and mass spectrometry (MS) resolving powers can limit the success of MS-based proteomics approaches. This work highlights the development of IM-MS deconvolution techniques and their utilization with commercial data processing software to improve results from IM-enhanced data-independent acquisition ($HDMS^E$) proteomics strategies.

Chemometric deconvolution and post-IM/collision-induced dissociation (post-IM/CID) MS were used to extract "pure component" IM profiles and construct CID mass spectra of IM-MS unresolved species. Collision-energy resolved and broadband IM-MS deconvolution strategies were developed and used for successful characterization of simulated complex mixtures and biological samples, respectively. As described in Chapter Two, utilizing *m/z*-isolation in a novel collision-energy resolved approach, a multicomponent IM unresolved peak was deconvoluted to construct fully resolved individual IM peaks.

A broadband data acquisition approach (*i.e.*, without the use of *m/z*-isolation) for improved IM-MS deconvolution is presented in Chapter Three where it is demonstrated that broadband IM-MS deconvolution provides time-saving and sensitivity advantages over the scan mode approach. Elimination of the ion isolation step also expands the applicability of IM-MS deconvolution to $HDMS^E$ acquisition. Ultra-performance liquid chromatography (UPLC) was used with $HDMS^E$ for high-throughput bottom-up proteomics analysis of rat brain tissue. The combined use of broadband IM-MS deconvolution and commercial $HDMS^E$ data processing software allowed more efficient precursor and product ion detections and improved proteins' sequence coverages.

The use of data-dependent acquisition (DDA) and $HDMS^E$ for high-throughput MS-based investigations of rat brain tissue is presented in Chapter Four. Infrared laser ablation microsampling was used to extract spatially localized rat brain samples for subsequent bottom-up proteomics analysis using both DDA and $HDMS^E$ strategies. The use of $HDMS^E$ acquisition for bottom-up proteomics of laser ablated rat brain samples provided greater numbers of peptides and proteins detected than DDA. Finally, in Chapter Five, potential future research directions are presented and discussed.

Development of Ion Mobility Mass Spectrometry Deconvolution Strategies for Use in Data-Independent Acquisition Proteomics

by

Michael Edmund Pettit, B.S.

A Dissertation

Approved by the Department of Chemistry and Biochemistry

_____

Patrick J. Farmer, Ph.D., Chairperson

Submitted to the Graduate Faculty of
Baylor University in Partial Fulfillment of the
Requirements for the Degree
of

Doctor of Philosophy

Approved by the Dissertation Committee

_____

Touradj Solouki, Ph.D., Chairperson

_____

C. Kevin Chambliss, Ph.D.

_____

Sung-Joon Kim, Ph.D.

_____

Elyssia S. Gallagher, Ph.D.

_____

Christopher Kearney, Ph.D.

Accepted by the Graduate School

May 2018

_____

J. Larry Lyon, Ph.D., Dean

Page bearing signatures is kept on file in the Graduate School.

Copyright © 2018 by Michael Edmund Pettit

All rights reserved

TABLE OF CONTENTS

LIST OF FIGURES ix

LIST OF SCHEMES xvi

LIST OF TABLES xvii

LIST OF ABBREVIATIONS xviii

AMINO ACID ABBREVIATIONS xx

ACKNOWLEDGMENTS xxi

DEDICATION xxiii

CHAPTER ONE 1

Introduction 1

1.1 Introduction to Mass Spectrometry 1

1.2 Mass Spectrometers and Allied Techniques 2

1.2.1 Ionization Sources 2

1.2.1.1 Electrospray Ionization 3

1.2.2 Mass Analyzers and Detectors 6

1.2.2.1 Quadrupole Mass Analyzer 8

1.2.2.2 Time-of-Flight (TOF) Mass Analyzer 9

1.2.3 Common Techniques for Online Analyte Separation Prior to MS Analysis 15

1.2.3.1 Traveling Wave Ion Mobility Spectrometry 17

1.2.3.2 Ion Mobility Deconvolution Strategies 21

1.2.4 Gas-Phase Ion Fragmentation Techniques in Mass Spectrometry 22

1.2.4.1 Fragment Ion Nomenclature for Peptides and Glycans 23

1.3 Mass Spectrometry Based Proteomics 26

1.3.1 Data Collection Strategies in High-throughput Bottom-up Proteomics 27

1.4 Justification of the Combined use of IM-MS Deconvolution and $HDMS^E$ 28

1.5 Author Contributions 30

CHAPTER TWO 31
Collision-energy Resolved Ion Mobility Characterization of Isomeric Mixtures 31
2.1 Abstract 31
2.2 Introduction 32
2.3 Experimental 36
2.3.1 Sample Preparation 36
2.3.2 Instrumentation 36
2.3.3 Data Analysis 38
2.3.4 Collision-energy Optimization to Enhance IM Resolving Power 38
2.3.5 Spectral Matching 39
2.4 Results and Discussion 40
2.4.1 Collision-energy Resolved Deconvolution of a Ternary Mixture of Trisaccharide Isomers 41
2.4.2 Collision-energy Resolved Deconvolution of a Quaternary Mixture of Hexapeptide Isomers 47
2.5 Conclusion 54

CHAPTER THREE 58
Broadband Ion Mobility Deconvolution for Rapid Analysis of Complex Mixtures 58
3.1 Abstract 58
3.2 Introduction 59
3.3 Experimental 64
3.3.1 Preparation of Simulated Complex Mixtures 64
3.4 Instrumentation 65
3.4.1 Direct Infusion IM-MS Data Acquisition 65
3.4.2 UPLC-HDMS^E of Rat Brain Tissue Samples 66
3.5 Data Analysis 67
3.6 Results and Discussion 70
3.6.1 Broadband IM-MS Deconvolution of Binary Isomer Mixtures 71
3.6.2 Broadband IM-MS Deconvolution of a Complex Mixture 79
3.6.3 Comparison of Broadband and m/z-isolated Approaches 85
3.6.4 Broadband Deconvolution of UPLC-HDMS^E Proteomics Data 88
3.7 Conclusions 91
3.8 Acknowledgments 93

CHAPTER FOUR 94
Infrared Laser Ablation Sampling Coupled with Data Independent High Resolution UPLC-IM-MS/MS for Tissue Analysis 94
4.1 Abstract 94
4.2 Introduction 94
4.3 Materials and Methods 97
4.3.1 Chemicals, Supplies, and Solvents 97
4.3.2 Tissue Samples 98
4.3.3 Laser Ablation Sample Transfer 98
4.3.4 Microscopy Imaging 99
4.3.5 Filter Aided Sample Processing 99
4.3.6 UPLC-MS/MS 100
4.3.7 Data Analysis 102
4.4 Results 103
4.4.1 DDA and $HDMS^E$ of Brain Tissue Extracts Collected via LAST 103
4.5 Discussion 109
4.6 Conclusions 112
4.7 Acknowledgments 113

CHAPTER FIVE 114
Overview of Dissertation and Future Directions 114
5.1 Dissertation Overview 114
5.2 Future Directions 116

APPENDIX A 120
Supplementary Information for Chapter Two: Collision-energy Resolved Ion Mobility Characterization of Isomeric Mixtures 120

APPENDIX B 123
Supplementary Information for Chapter Three: Broadband Ion Mobility Deconvolution for Rapid Analysis of Complex Mixtures 123
B.1 Differences in Pre-IM/CID between $[MGRYGF + 2H]^{2+}$ and $[FRMYGG + 2H]^{2+}$ 123
B.2 Preparation of Biological Samples 127
B.3 $HDMS^E$ Data Acquisition 129
B.4 $HDMS^E$ Data Processing 130

B.5 Improper Application of AIMD to Single Component IM Peaks 131
B.6 Successful IM-MS Deconvolution of Components that have a 10x Concentration Difference 132
B.7 Background Species from Broadband Deconvolution of the Simulated Complex Mixture 133
B.8 Comparison of Broadband and m/z-isolated Approaches 135
B.9 Comparison of UPLC Retention Times using 60 min. and 15 min. Separation 139

APPENDIX C 142
Supplementary Information for Chapter Four: Infrared Laser Ablation Sampling Coupled with Data Independent High Resolution UPLC-IM-MS/MS for Tissue Analysis 142
C.1 Microscopy Images of Rat Brain Tissue Sections Before and After LAST 142
C.2 Example of Duty Cycle Limitations in DDA Separation 143
C.3 Correlation between UPLC Separation and UPLC Congestion 143
C.4 Complete List of Proteins Identified in this Study 146

BIBLIOGRAPHY 184

LIST OF FIGURES

Figure 1.1. Schematic drawing of an ESI source operating in positive-ion mode. Please note that components are not drawn to scale. This representation was recreated based on the work of Konermann *et al*. (reference number 42). 5

Figure 1.2. Pictorial representation of three proposed ionization mechanisms in ESI. The ion ejection model (left), charge residue model (middle), and chain ejection model (right) have been proposed for the ionization of low molecular weight (MW) analytes, globular proteins, and disordered polymers, respectively. This representation was recreated based on the work of Konermann *et al*. (reference number 42). 6

Figure 1.3. Experimental design of a quadrupole mass analyzer. Red components correspond to electrical connections for DC and RF voltages. The Cartesian projection is provided for visualization of the *xz* and *yz* planes. This representation was recreated based on the work of Skoog *et al.* (reference number 61). 8

Figure 1.4. Representation of a TOF mass analyzer (a) before and (b) after ion acceleration *via* application of high voltage to the pusher electrode. This representation is based on the work of Watson *et al.* (reference number 62).....10

Figure 1.5. Representation of a reflectron as utilized in TOF MS. This representation is based on the work of Watson *et al.* (reference number 62). 14

Figure 1.6. Representation of a traveling wave ion guide (TWIG). (a) Alternating RF voltages are applied to adjacent ring electrodes to radially confine ions. (b) Ions are propelled through the TWIG using a repeating pattern of DC voltages that are superimposed on the confining RF electric fields. This representation is based on the work of Giles *et al.* (reference number 81). 19

Figure 1.7. Representation of the Synapt G2-S HDMS used to collect all data presented in this dissertation. This representation is based on the work of Giles *et al.* (reference number 98). 21

Figure 1.8. Roepstorff nomenclature system for protein and peptide product ions. Red circles indicate the positions of all alpha carbons in the amino acid sequence. 24

Figure 1.9. Domon and Costello nomenclature system for (a) glycan fragmentation including the (b) numbering system used for cross ring cleavages. 25

Figure 2.1. (a) Three dimensional plot of arrival time, collision-energy, and ion intensity from collision-energy resolved IM-MS deconvolution of a ternary mixture of lithiated-raffinose (red profiles), -isomaltotriose (blue profiles), and -cellotriose (green profiles). IM profiles shown in color and gray denote successful and unsuccessful deconvolution, respectively. (b) IM profiles (shown in color) for [raffinose + Li]$^+$, [isomaltotriose + Li]$^+$, and [cellotriose + Li]$^+$ from optimal IM-MS deconvolution at a collision-energy sweet-spot of 45 V. Black IM profiles denote pure samples measured under identical conditions. Deconvoluted arrival times are shown at the 95% confidence interval (n = 3). 42

Figure 2.2. Optimal IM-MS deconvolution of a ternary mixture of [raffinose + Li]$^+$, [isomaltotriose + Li]$^+$, and [cellotriose + Li]$^+$ at 45 V collision-energy. (a) Ternary mixture's IM profiles before (black profile) and after (colored profiles) deconvolution. (b) Deconvoluted CID spectra match (c) corresponding CID mass spectra from pure sugar isomer samples. 48

Figure 2.3. (a) Three dimensional plot of arrival time, collision-energy, and ion intensity from collision-energy resolved IM-MS deconvolution of a quaternary mixture of MGRYGF (orange profiles), MFRYGG (pink profiles), MFGRYG (dark cyan profiles), and FRMYGG (purple profiles). IM profiles shown in color and gray denote successful and unsuccessful deconvolution, respectively. (b) IM profiles (shown in color) for [MGRYGF + 2H]$^{2+}$, [MFRYGG + 2H]$^{2+}$, [MFGRYG + 2H]$^{2+}$, and [FRMYGG + 2H]$^{2+}$ from optimal IM-MS deconvolution at a 26 V collision-energy. Black IM profiles denote pure samples measured under identical conditions. Deconvoluted arrival times are shown at the 95% confidence interval (n = 5) 50

Figure 2.4. Optimal IM-MS deconvolution of a quaternary mixture of MGRYGF, MFRYGG, MFGRYG, and FRMYGG at 26 V collision-energy. (a) Quaternary mixture's IM profiles before (black profile) and after deconvolution (colored profiles). (b) Deconvoluted CID mass spectra match (c) corresponding CID mass spectra from pure peptide isomer samples. 52

Figure 3.1. Unresolved broadband mobiligram and mass spectra of the binary hexapeptide isomer mixture (containing MGRYGF and FRMYGG) using a data acquisition time of 1 minute. (a) Total ion mobiligram from AT of 0 ms to 13.8 ms measured using a 4 V collision-energy and (b) a representative mass spectrum generated using MS data corresponding to IM AT region 2.08 ms to 3.18 ms in Fig. 3.1a. (c) Total ion mobiligram from AT of 0 ms to 13.8 ms measured using a 26 V CE and (d) a representative mass spectrum generated using MS data corresponding to IM AT region 2.08 ms to 3.18 ms in Fig. 3.1c (please refer to text (and previous report[134]) for details on observed IM shifts between low- and high-collision-energy experiments). Yellow rectangles in (a) and (c) denote data-notching windows from IM AT 2.08 ms to 3.18 ms. The asterisk with red dashed line in (d) shows the precursor ion [M_P + 2H]$^{2+}$ region at *m/z* 365 and indicates a complete signal reduction for [M_P + 2H]$^{2+}$due to post-IM/CID. 73

Figure 3.2. Broadband deconvolution of $[M_P + 2H]^{2+}$ using a 26 V collision-energy and a data acquisition time of 1 minute. (a) Deconvoluted IM profiles for the two peptide isomers and corresponding post-IM/CID mass spectra for (b) [MGRYGF + 2H]$^{2+}$ (orange) and (c) [FRMYGG + 2H]$^{2+}$ (purple). (d) Pure SIM profiles and pure CID mass spectra for (e) [MGRYGF + 2H]$^{2+}$ and (f) [FRMYGG + 2H]$^{2+}$ were individually measured using a 26 V collision-energy. Black asterisk above the MS peak at *m/z* 166 in (c) denotes an example of partially misassigned MS peak intensity by AIMD. 74

Figure 3.3. Unresolved broadband mobiligram and mass spectra of binary trisaccharide isomer mixture (containing [D-(+)-raffinose + Li]$^+$ and [D-(+)-isomaltotriose + Li]$^+$) using a data acquisition time of 1 minute. (a) Total ion mobiligram from AT 0 ms to 13.8 ms measured using a 4 V collision-energy and (b) a representative mass spectrum generated using MS data corresponding to IM AT region 3.74 ms to 5.12 ms in Fig. 3.3a. (c) Total ion mobiligram from AT of 0 ms to 13.8 ms measured using a 45 V collision-energy and (d) a representative high collision-energy CID mass spectrum generated using MS data corresponding to IM AT region 3.74 ms to 5.12 ms in Fig. 3.3c. Yellow rectangles (a) and (c) denote data-notching windows from IM AT of 3.74 ms to 5.12 ms. 77

Figure 3.4. Broadband deconvolution of $[M_T + Li]^+$ using a 45 V collision-energy and a data acquisition time of 1 minute. (a) Deconvoluted IM profiles for the two trisaccharide isomers and their corresponding post-IM/CID mass spectra for (b) [D-(+)-raffinose + Li]$^+$ (blue) and (c) [D-(+)-isomaltotriose + Li]$^+$ (red). (d) Pure SIM profiles and pure CID mass spectra for (e) [D-(+)-raffinose + Li]$^+$ and (f) [D-(+)-isomaltotriose + Li]$^+$ were individually measured using a 45 V collision-energy. 78

Figure 3.5. Unresolved broadband mobiligram and mass spectra of the simulated complex mixture collected using a 35 V collision-energy and a data acquisition time of 1 minute. (a) Total ion mobiligram from AT of 0 to 13.8 ms. Yellow rectangles in (a) denote data-notching windows from IM ATs of 2.08 ms to 3.18 ms (left) and 3.74 ms to 5.12 ms (right). Representative post-IM/CID mass spectra at 35 V for (b) ions with IM ATs ranging from 2.08 ms to 3.18 ms and (c) ions with IM ATs ranging from 3.74 ms to 5.12 ms).....80

Figure 3.6. Broadband deconvolution of $[M_P + 2H]^{2+}$ from the simulated complex mixture using a 35 V collision-energy and a data acquisition time of 1 minute. (a) Deconvoluted IM profiles for the two peptide isomers and corresponding post-IM/CID mass spectra for (b) [MGRYGF + 2H]$^{2+}$ (orange solid trace) and (c) [FRMYGG + 2H]$^{2+}$ (purple solid trace). (d) Pure SIM profiles and pure CID mass spectra for (e) [MGRYGF + 2H]$^{2+}$ and (f) [FRMYGG + 2H]$^{2+}$ were individually measured using a 35 V collision-energy. In (a), gray IM traces correspond to background species 1 to 9 that were also present in the deconvoluted IM AT region 2.08 ms to 3.18 ms. 84

Figure 3.7. Broadband deconvolution of $[M_T + Li]^+$ from the simulated complex mixture using a 35 V collision-energy and a data acquisition time of 1 minute. (a) Deconvoluted IM profiles for the two trisaccharide isomers and corresponding post-IM/CID mass spectra for (b) [D-(+)-raffinose + Li]$^+$ (blue solid trace) and (c) [D-(+)-isomaltotriose + Li]$^+$ (red solid trace). (d) Pure SIM profiles and pure CID mass spectra for (e) [D-(+)-raffinose + Li]$^+$ and (f) [D-(+)-isomaltotriose + Li]$^+$ were individually measured using a 35 V collision-energy. In (a), gray IM traces correspond to background species 1 to 10 that were also present in the deconvoluted IM AT region 3.74 ms to 5.12 ms.....86

Figure 3.8. Broadband deconvolution of peptides from UPLC-HDMS^E proteomics analysis of a rat brain tissue digest. The broadband mobiligram of the proteolytic digest in (a) was generated by extracting IM data that corresponded to the convolved UPLC retention time region 10.5 min. to 11.5 min. in the 15-minute UPLC-HDMS^E dataset. The yellow rectangle in (a) spans the IM AT region 2.69 ms to 3.80 ms; this IM AT region was deconvoluted using AIMD. The convoluted XMS in (b) was generated by integrating the highlighted IM AT region of interest shown in (a). (c) Deconvoluted IM profiles of the isobaric peptides $[LIETYFSK]^{2+}$ and $[VLSIGDGIAR]^{2+}$ have IM ATs (3.17 ms and 3.24 ms, respectively) that match the results from PLGS analysis (3.167 ms and 3.241 ms, respectively). Deconvoluted post-IM/CID MS data for $[LIETYFSK]^{2+}$ and $[VLSIGDGIAR]^{2+}$ are shown in (d) and (e), respectively.....90

Figure 4.1. Microscopy image of rat brain whole tissue section 1 (S1) after tissue extraction *via* LAST. Rat brain tissue was collected from four spatially localized quadrants of the brain. Sampling quadrants 1 through 4 are indicated by Q1, Q2, Q3, and Q4.....104

Figure 4.2. Representative UPLC-DDA and UPLC-HDMS^E data from analyses of Q1S3. Base peak chromatograms (BPCs) corresponding to peptide elution from (a) DDA and (b) HDMS^E data acquisition modes. For peaks at 11.4, 29.6, 42.1, and 52.2 minutes, precursor ion mass spectra are in (c)-(f) for DDA (left) and HDMS^E (right). Precursor ion mass spectra of (c) $[AGFAGDDAPR]^{2+}$ at *m/z* 488.72, (d) $[LLIEMEQR]^{2+}$ at *m/z* 516.29, (e) $[AILVDLEPGTMDSVR]^{2+}$ at *m/z* 808.40, and (f) $[LICCDILDVLDK]^{2+}$ at *m/z* 738.85. The base peak in each mass spectra is designated with (*) and corresponds to the named precursor peptide ion. 105

Figure 4.3. Representation of the number of (a) peptides and (b) proteins identified by DDA (empty white bars) and HDMS^E (solid black bars) as a function of separation time. Separation times of 15, 30, 60, 120, and 150 minutes were used.....110

Figure A.1. Suboptimal IM-MS deconvolution at a 20 V collision-energy. (a) IM distribution for the quaternary mixture of hexapeptide isomers shown before (black profile) and after (colored profiles) deconvolution. While deconvoluted arrival times match corresponding pure samples when individually measured under similar conditions, deconvoluted CID mass spectra (b) for $[MGRYGF + 2H]^{2+}$, $[MFGRYG + 2H]^{2+}$, and $[FRMYGG + 2H]^{2+}$ have negative intensity values that are greater than 15% of the respective base peak intensities. According to the criteria described in the experimental section of the main text, deconvolution results for $[MGRYGF + 2H]^{2+}$, $[MFGRYG + 2H]^{2+}$, and $[FRMYGG + 2H]^{2+}$ were classified as unsuccessful. 122

Figure B.1. Representative low collision-energy IM profiles and mass spectra for pure solutions of either MGRYGF peptide (top, data represented in orange) or FRMYGG peptide (bottom, data represented in purple). The yellow rectangles in (a) and (c) are used to highlight the IM AT region from 2.08 ms to 3.18 ms that contains the doubly-charged precursor ion (*i.e.*, $[M + 2H]^{2+}$). The MS data corresponding to highlighted IM regions in (a) and (c) were averaged to generate the extracted mass spectra (XMS) displayed in (b) and (d), respectively. Labels are provided in (a-d) to indicate identities of peptide-related fragment ions. Parentheses are used in (b) and (d) to include *m/z*-values of unidentified ions. 126

Figure B.2. Six IM profiles generated by improper application of AIMD to a single component solution of isomaltotriose (a). As expected, AIMD successfully generated IM (red trace in (a)) and post-IM/CID (b) data for $[isomaltotriose + Li]^{+}$. The remaining five black IM traces in (a) correspond to "non-real" (*i.e.*, noise) components. The non-real mass spectrum shown in (c) corresponds to the highest intensity noise component (arrow labeled with "c" in (a)). 132

Figure B.3. Broadband deconvolution was performed on IM-MS data of a solution containing 10 μM $[raffinose + Li]^{+}$ and 1 μM $[isomaltotriose + Li]^{+}$. (a) Deconvoluted IM profiles for the two isomers and corresponding post-IM/CID mass spectra for (b) $[raffinose + Li]^{+}$ (blue) and (c) $[isomaltotriose + Li]^{+}$ (red) 133

Figure B.4. Representative mass spectra of background species present in the IM AT region 2.08 ms to 3.18 ms for the simulated complex mixture. Deconvoluted mass spectra of background species (a) 5, (b) 7, and (c) 9. Raw XMS corresponding to single IM AT data points of (d) 2.770 ms, (e) 2.978 ms, and (f) 3.185 ms. Data displayed in Figure B.4 were collected using a 35 V collision-energy. Please refer to Figure 3.6a (main text) for deconvoluted IM profiles of background species 1 to 9.....136

Figure B.5. Representative mass spectra of background species present in the IM AT region 3.74 ms to 5.12 ms for the simulated complex mixture. Deconvoluted mass spectra of background species (a) 2, (b) 3, and (c) 9. Raw XMS corresponding to single IM AT data points of (d) 3.878 ms, (e) 4.016 ms, and (f) 5.055 ms. Data displayed in Figure B.5 were collected using a 35 V collision-energy. The red asterisks at *m/z* 273 and 393 in (b) signify negative relative intensity values that were > 15% of the base peak intensity. Please refer to Figure 3.7a (main text) for deconvoluted IM profiles of background species 1 to 10. 137

Figure B.6. Sensitivity comparison of AIMD results obtained *via m/z*-isolated and broadband data acquisition. A 340 nM solution of MGRYGF and FRMYGG isomers was used to collect convoluted IM-MS data *via* (a) *m/z*-isolation of $[M_P + 2H]^{2+}$ at *m/z* 365 and (d) broadband data acquisition; the black IM profiles and inset mass spectra in (a) and (d) represent convoluted IM-MS data prior to deconvolution using AIMD. Results from deconvolution of (a) and (d) from the 340 nM solution *via* AIMD are represented in (b) and (e) respectively. The 340 nM solution was diluted to 34 nM (column 3), and AIMD results from this solution are shown in (c) and (f) for *m/z*-isolated and broadband data acquisitions, respectively. A black "X" is used to indicate "unacceptable results" in (c). 139

Figure B.7. Representative UPLC chromatograms corresponding to small chromatographic windows from $HDMS^E$ analysis of a rat brain whole tissue digest using a (a) 60 minute and (b) 15 minute UPLC separation time. The peptides $[VLSIGDGIAR]^{2+}$ (blue) and $[LIETYFSK]^{2+}$ (red) are identified by PLGS using a 60 minute separation. Using a 15-minute separation, $[VLSIGDGIAR]^{2+}$ is UPLC unresolved and not identified by PLGS. The black circle in (b) indicates the unresolved elution of peptide VLSIGDGIAR. 141

Figure C.1. Microscopy images of (a) section 2 and (b) section 3 of rat brain tissue taken before (left) and after performing LAST (right). Sections 2 and 3 are abbreviated as S2 and S3, respectively, and the four laser ablation sampling quadrants are labeled as Q1, Q2, Q3, and Q4. Sections 1 (main text), 2, and 3 were consecutive tissue sections from the same specimen.....142

Figure C.2. Representative mass spectrum from *m/z* 350 to 700 corresponding to ions with UPLC retention times between 19.9 and 20.8 minutes from DDA analysis of Q2. Labeled arrows pointing to *m/z* values at 362.20, 622.36, 678.33, and 682.83 indicate that these peptide precursor ions were present in the DDA dataset but not selected for MS/MS because of duty cycle limitations.....144

Figure C.3. Representative base peak chromatograms from HDMS^E analysis of a whole rat brain tissue digest sample using UPLC separation times of (a) 150 (b) 120 (c) 90 (d) 60 (e) 30 (f) 15 minutes. Solvent gradient compositions from the start to end of all six measured separation times were kept identical at 5% to 45% acetonitrile. The gray dashed lines in (a-f) represent the 30 minute intervals used for washing the UPLC column. The red dashed lines in (b-f) represent the time saved by using shortened separation times (as compared to (a))....145

LIST OF SCHEMES

Scheme 2.1. Molecular structures for the trisaccharide isomers used in this study.....35

LIST OF TABLES

Table 1.1. Approximate values of performance characteristics of common mass analyzers. 7

Table 3.1. Ion mobility arrival times (IM ATs) and spectral matching factors (*R*-values) from broadband IM-MS deconvolution of the simulated complex mixture. Data were collected using a 35 V transfer collision-energy and are compared at 1 minute and 2 second data acquisition times. Uncertainty values were calculated as 95% confidence intervals (n = 3). Ion mobility arrival times were compared using Student's *t*-test at the 95% confidence interval ($n_1 = n_2 = 3$) and no statistical differences were observed..... 87

Table 4.1. Summary of proteins identified by DDA and $HDMS^E$ analyses of the 12 laser ablation sampling positions. For each LAST position (Column 1), the number of proteins identified by DDA (Column 2) and $HDMS^E$ (Column 3) are reported. Column 4 reports the number of proteins that were identified only by DDA. Results from DDA and $HDMS^E$ were combined, and the total number of proteins identified is provided in Column 5 with duplicate identification removed.....108

Table A.1. Experimental parameters used in this study.....120

Table A.2. Calculated *R* Values for **(a)** $[M_T + Li]^+$ and **(b)** $[M_P + 2H]^{2+}$ at each measured collision-energy. *R* values greater than 0.75 qualified as an acceptable match when comparing an isomer's deconvoluted mass spectrum to its pure counterpart 121

Table B.1. Experimental parameters used in this study. Please note that the gas pressures (*) reported in Table S1 are direct instrument readouts and have not been corrected for geometry or chemical sensitivity factors. Factory-set default settings were used for all parameters related to ion transmission. 123

Table C.1. Proteins identified by combined use of DDA and $HDMS^E$ from rat brain tissues (listed in alphabetical order).....146

LIST OF ABBREVIATIONS

Abbreviation	*Description*
AIMD	Automated Ion Mobility Deconvolution
AMRT	Accurate Mass Retention Time
AT	Arrival Time
CCS	Collision Cross Section
CEM	Chain Ejection Model
CI	Chemical Ionization
CID	Collision-induced Dissociation
CRM	Charged Residue Model
Da	Dalton
DC	Direct Current
DDA	Data-dependent Acquisition
DIA	Data-independent Acquisition
DTIMS	Drift Tube Ion Mobility Spectrometry
ECD	Electron Capture Dissociation
EI	Electron Ionization
EMT	Electron Multiplier Tube
ESI	Electrospray Ionization
ETD	Electron Transfer Dissociation
eV	Electronvolt
FAIMS	High-field Asymmetric Ion Mobility Spectrometry
GC	Gas Chromatography
GLC	Gas-liquid Chromatrography
GSC	Gas-solid Chromatography
HDX	Hydrogen-deuterium Exchange
He	Helium
HPLC	High-performance Liquid Chromatography
IEM	Ion Ejection Model
IM	Ion Mobility
IMS	Ion Mobility Spectrometry
IR	Infrared
IRMPD	Infrared Multiphoton Dissociation
LAST	Laser Ablation Sample Transfer
LC	Liquid Chromatography
LD	Laser Desorption
M	*m/z* of the ion of interest (in MRP calculation)
M	Molarity
MALDI	Matrix Assisted Laser Desorption Ionization
MRP	Mass Resolving Power

Abbreviation	*Description*
MS	Mass Spectrometry
MW	Molecular Weight
N_2	Nitrogen
OCT	Optimal Cutting Temperature
PLGS	ProteinLynx Global Server
RF	Radio-frequency
ROI	Region of Interest
SID	Surface-induced Dissociation
SIMPLISMA	SIMPLe-to-use Interactive Self-modeling Mixture Analysis
SORI-CID	Sustained Off-resonance Irradiation CID
SRIG	Stacked Ring Ion Guide
SWATH	Sequential Window Acquisition of all Theoretical Spectra
TIMS	Trapped Ion Mobility Spectrometry
TOF	Time-of-Flight
TWIG	Traveling Wave Ion Guide
TWIMS	Traveling Wave Ion Mobility Spectrometry
UPLC	Ultra-Performance Liquid Chromatography
UV	Ultraviolet
V	Voltage
$\Delta M_{50\%}$	MS peak width at half-height (in MRP calculation)

AMINO ACID ABBREVIATIONS

One Letter Abbreviation	*Three Letter Abbreviation*	*Amino Acid*
A	Ala	Alanine
C	Cys	Cysteine
D	Asp	Aspartic Acid
E	Glu	Glutamic Acid
F	Phe	Phenylalanine
G	Gly	Glycine
H	His	Histidine
I	Ile	Isoleucine
K	Lys	Lysine
L	Leu	Leucine
M	Met	Methionine
N	Asn	Asparagine
P	Pro	Proline
Q	Gln	Glutamine
R	Arg	Arginine
S	Ser	Serine
T	Thr	Threonine
V	Val	Valine
W	Trp	Tryptophan
Y	Tyr	Tyrosine

ACKNOWLEDGMENTS

I would like to express my sincerest gratitude to my advisor, Dr. Touradj Solouki, for his kindness, leadership, and patience throughout my years at Baylor. He provided me an opportunity to work in a state-of-the-art research environment with outstanding colleagues and distinguished collaborators. Through his support, I have been able share my research in peer-reviewed journals and international conferences and interact with leaders in the field of mass spectrometry. He consistently pushed me to tackle increasingly difficult analytical challenges, and he never failed to encourage me in times when I fell short. He has greatly influenced my development as a scientist, co-worker, and overall person, and I am truly happy to consider him a friend.

My thanks are also extended to my committee members, Dr. C. Kevin Chambliss, Dr. Sung-Joon Kim, Dr. Elyssia S. Gallagher, and Dr. Christopher Kearney. Each committee member has had tremendous influence on my personal and professional growth. I greatly appreciate their accessibility and willingness to offer helpful suggestions through valuable discussions.

Additional thanks must be given to the faculty, staff, and graduate students of the Department of Chemistry and Biochemistry at Baylor University. In particular, I would like to acknowledge the outstanding members of Dr. Solouki's research group with whom I have had the pleasure of working beside: Matthew Brantley, Ian Anthony, Luke Richardson, Amy Schnelle, Raul Villacob, Brett Harper, Behrooz Zekavat, and, of course,

the undergraduates. They have each helped shape my graduate experience into a great memory that I will forever cherish.

I gratefully acknowledge all collaborators who have facilitated my research in a variety of disciplines and applications. I would like to especially thank Dr. Kermit K. Murray and Dr. Fabrizio Donnarumma at Louisiana State University for their dynamic contributions to my research. I have sincerely enjoyed our synergistic efforts, and the experiences gained through this collaboration have absolutely impacted my career trajectory in a positive manner.

I genuinely thank the close friends I've gained while at Baylor, Ricardo Francis, Thomas Dunnam, Zachry Theis, Casey Maguire, Graham Carlson, and Jacob Ford, and my lifelong friends, Chris Jeffries, Joey Delaney, Justin Trimble, and Ernie Barber—I couldn't have made it through without them.

I am perpetually thankful to my parents and siblings for their transformative influence on my success and continued faith in me. Lastly, loving thankfulness is given to my fiancé, Micaela Dougherty, for her undying support, encouragement, patience, and love throughout some of the most challenging years of my life.

DEDICATION

To my future wife, Micaela, for her endless love.

To my parents, Brian and Catherine, for their immeasurable support.

CHAPTER ONE

Introduction

1.1 Introduction to Mass Spectrometry

Mass spectrometry (MS) is a class of gas-phase analytical techniques which allows measurement of the mass-to-charge ratio (*m/z*) of ionized molecules and atoms. MS provides high rates of data acquisition, sensitivity, selectivity, and specificity.[1] Because chemical elements have discrete masses and isotopic distributions, the measured *m/z* of gas-phase ions can be used to identify and quantify[2,3] analytes such as metals,[4-6] lipids,[7,8] glycans,[9,10] and proteins.[11-13] MS allows determination of molecular structure(s) and function(s)[14,15] and has impacted a wide variety of scientific fields including, but not limited to, analysis of petroleum fractions,[16] molecular imaging of tissues,[17] detection of disease biomarkers,[18] and biopharmaceutical drug development efforts.[19,20]

Despite the widespread impacts of MS analysis across many facets of science, successful sample characterization using MS is traditionally limited by the mass resolving power (MRP) of the instrument being utilized. MRP can be calculated using the formula $M/\Delta M_{50\%}$, where M is the *m/z* of the ion of interest and $\Delta M_{50\%}$ is the corresponding ion's MS peak width at half-height; MS instruments with higher MRPs yield greater separation between two MS peaks (further details provided in Section 1.2.2.2).[21] The focus of the research presented in this dissertation is to (i) develop strategies which circumvent MRP limitations of high-performance MS instruments for improved identification of isobaric and isomeric gas-phase ions and (ii) apply these developed strategies to high-throughput

MS-based proteomics experiments. This chapter provides an introduction to MS techniques, concepts, and terminologies relevant to the research and ideas presented in Chapters Two through Five.

1.2 Mass Spectrometers and Allied Techniques

Although diverse classes of high-performance MS instruments and advanced MS techniques are continuously being developed to address increasingly difficult analytical challenges, all mass spectrometers operate in the high (~10^{-7} Torr) or ultrahigh (~10^{-10} Torr) vacuum pressure regimes and include three key components: (i) an ionization source, (ii) a mass analyzer, and (iii) a detector. Various types of these three key components are summarized in the following sections, including detailed descriptions of those utilized in the research presented in this dissertation.

1.2.1 Ionization Sources

Ionization is the first step of MS analysis whereby neutral analyte molecules are converted to positively (cations) or negatively (anions) charged gas-phase ions. Ionization occurs in the ionization source of the mass spectrometer, and the mechanisms of ionization can be broadly classified as either "hard" or "soft" processes. Hard ionization (*e.g.*, electron ionization (EI)[22] and laser desorption (LD)[23]) refers to the formation of gas-phase ions accompanied by extensive fragmentation of the molecule of interest.[24] For example, EI is the most commonly utilized technique for ionization of volatile compounds. In EI, electrons are typically accelerated to an energy of 70 electronvolt (eV) toward neutral gas-phase molecules. Interaction with the accelerated electrons causes removal of one or more electrons from the gas-phase neutral molecules resulting in formation of radical molecular

ions (designated as $M^{\cdot+}$). The electron kinetic energy of 70 eV is greater than the energies required for ionization of molecules, therefore, the resulting radical molecular ions usually have sufficient internal energy after the ionization event to break into product ion fragments.[25] Although radical molecular ions may not be observed in cases of extensive fragmentation, diagnostic product ions can be used to identify analytes of interest.

Soft ionization (*e.g.*, chemical ionization (CI),[26] electrospray ionization (ESI),[13,27,28] and matrix assisted laser desorption ionization (MALDI)[12,29,30]) refers to the formation of gas-phase ions without extensive fragmentation.[31] Recent Nobel Prize winning techniques (*viz*., ESI and MALDI) have changed the field of MS-based proteomics because they allow ionization, and hence MS analysis, of large, non-volatile molecules such as proteins. During ESI and MALDI, positively or negatively charged ions can be formed by the addition or subtraction of protons, respectively. ESI typically yields singly- and/or multiply-charged ions,[32] and MALDI most commonly forms singly-charged ions.[33] For MALDI, analytes are embedded in a solid matrix, such as alpha-cyano-4-hydroxycinnamic acid or 2,5-dihydroxybenzoic acid, and gas-phase ions are formed by exposure to a (typically) pulsed laser.[34] In ESI, liquid-phase analytes are converted to gas-phase ions.[35] Because all MS data presented in this dissertation were collected using positive-ion mode ESI, a detailed description of ESI is presented in the following section.

1.2.1.1 Electrospray Ionization. Positive-ion mode ESI is an ambient ionization technique which yields protonated molecules (designated as $[M + nH]^{n+}$ where "n" is the number of protons). ESI is attractive for MS-based proteomics because it is (i) applicable to molecular weights ranging from daltons (Da) to ~100 megadaltons (MDa)[32,36] and analyte concentrations ranging from <0.1 micromolar (μM) to ~10 millimolar (mM), (ii)

capable of ionizing proteins without denaturation,[35] and (iii) easily coupled to liquid chromatography (LC, described in Section 1.2.3) for online separation of peptides and proteins.[37] It is widely accepted that ion generation in ESI includes three major steps: (i) production of charged droplets at the capillary tip, (ii) size reduction of the charged droplets by solvent evaporation and Coulombic fission, and (iii) formation of gas-phase ions.[35]

As depicted in Figure 1.1, ions are formed in ESI by applying a voltage to liquid-phase analyte molecules as they are passed through a glass or metal capillary tip. The voltage difference established between the inlet of the mass spectrometer and the capillary tip is typically in the range of ~1 kilovolt (kV) to ~5 kV. When high-voltage is applied, an electric field penetrates the analyte containing solution resulting in polarization of the (typically acidified) solvent. Negative ions move away from the liquid-phase meniscus, and positive ions move downfield near the surface of the meniscus. The enrichment of positive charges near the meniscus causes formation of a downfield pointing cone called a Taylor cone.[38,39] When the applied electric field is sufficiently high, a fine, positively charged jet emerges from the tip of the Taylor cone, and charge repulsion in the jet yields small charged droplets. As they are drawn downfield through the air, solvent evaporates from the charged droplets until they reach the Rayleigh limit.[40] At the Rayleigh limit, the electrostatic repulsion between the charges exceeds the surface tension at the droplet surface resulting in Coulombic fission of the charged droplet. Coulombic fission causes the original droplet to explode into even smaller droplets called progeny droplets. The process of solvent evaporation and Coulombic fission leads to repeated droplet explosions that ultimately releases gas-phase ions. Depending on the size or type of molecule being ionized, different mechanisms for ion release during ESI have been proposed (Figure 1.2).

Low molecular weight molecules follow the ion evaporation model (IEM),[41] the charged residue model (CRM) applies to large globular species,[42] and the chain ejection model (CEM) has been proposed for disordered polymeric chains.[42] In the IEM, it is proposed that smaller analytes, such as pharmaceutical molecules, retain charge as they "evaporate" from the charged surface of the solvent droplet. In the CRM, it is proposed that the droplets' surface charges are deposited on globular species, such as folded proteins, by repeated

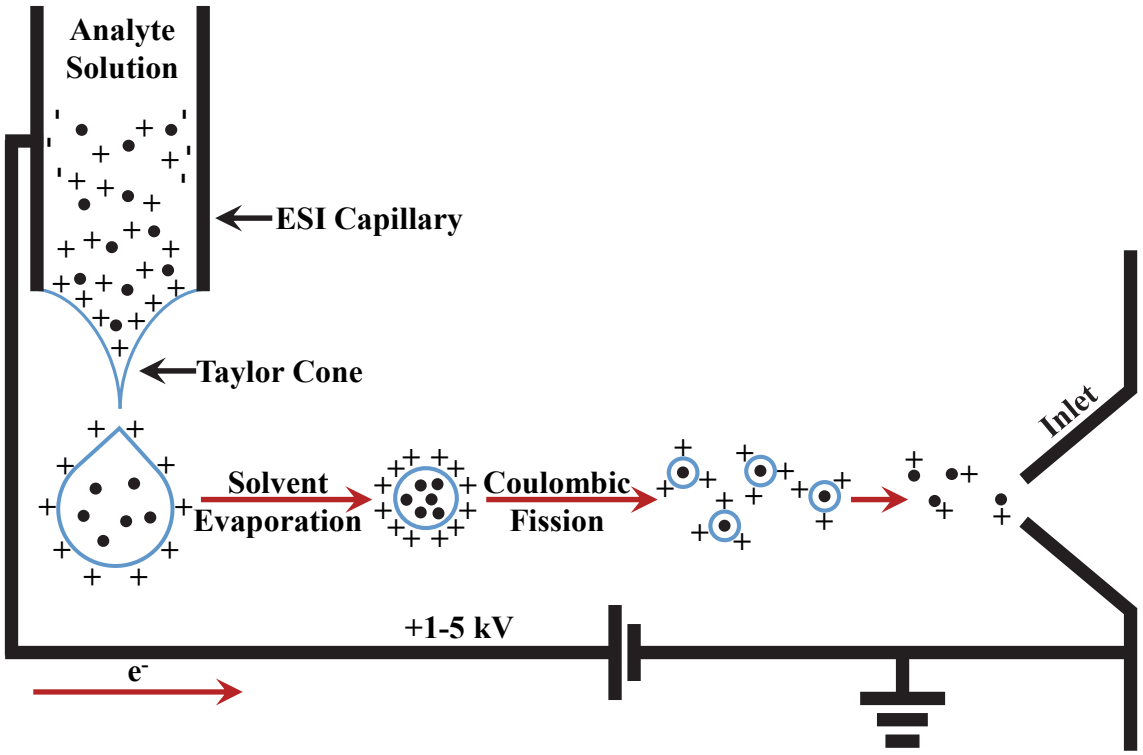

Figure 1.1. Schematic drawing of an ESI source operating in positive-ion mode. Please note that components are not drawn to scale. This representation was recreated based on the work of Konermann *et al*. (reference number 42).

solvent evaporations and Coulombic fissions. In the CEM, it is presumed that a portion of a polymeric chain escapes the droplet. As the analyte chain is pulled out of the droplet by charge repulsion, it picks up additional charges until it is eventually ejected from the solvent droplet. The CEM has been used to explain the observation of unfolded protein

ions. Once the analytes of interest are converted to gas-phase ions, they can be directed to a mass analyzer and detector for *m/z* differentiation and detection, respectively.

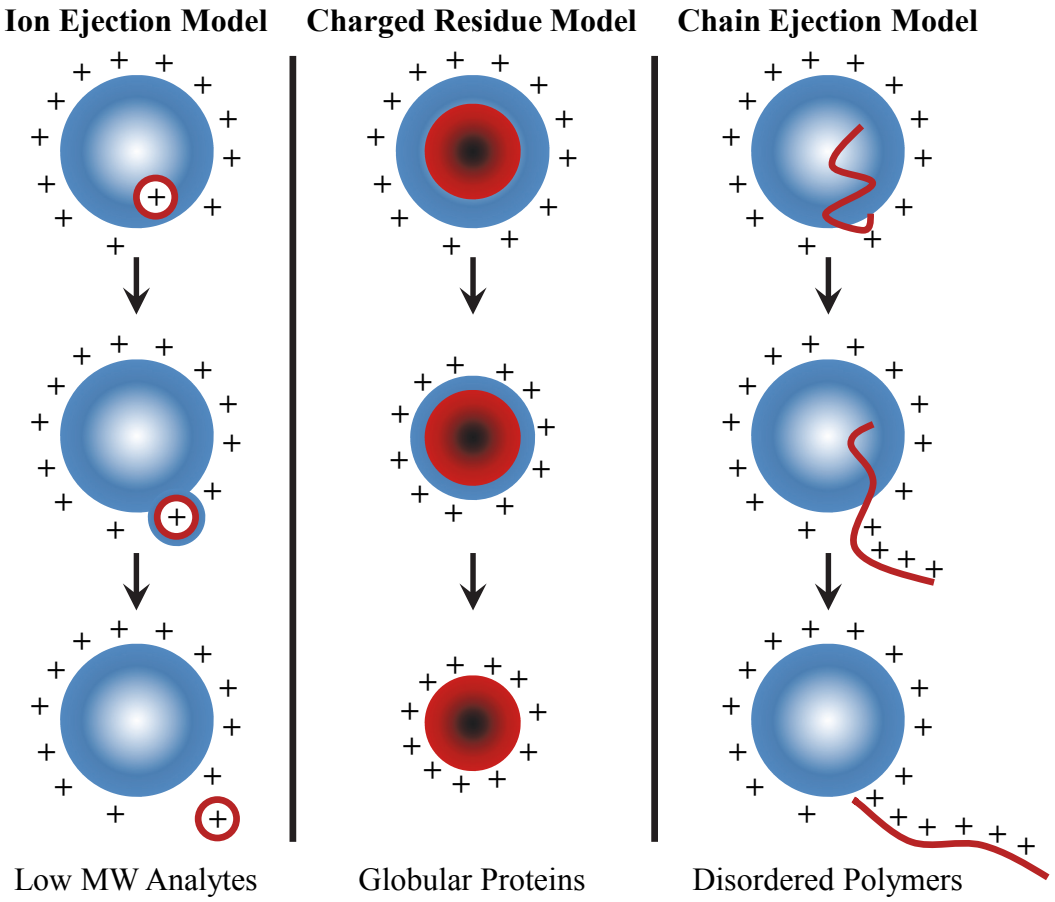

Figure 1.2. Pictorial representation of three proposed ionization mechanisms in ESI. The ion ejection model (left), charge residue model (middle), and chain ejection model (right) have been proposed for the ionization of low molecular weight (MW) analytes, globular proteins, and disordered polymers, respectively. This representation was recreated based on the work of Konermann *et al*. (reference number 42).

1.2.2 Mass Analyzers and Detectors

The mass analyzer component of the mass spectrometer differentiates ions by relating the charge of an ion to its trajectory in the presence of an electric and/or magnetic field. The third key component of the mass spectrometer, the detector, records either the charge induced or the current produced when an ion interacts with a conductive surface

(*e.g.*, an electrode); the recorded signals are subsequently utilized to generate a mass spectrum. Mass spectrometers can be categorized as "spatial" or "temporal" depending on the physical location of the mass analyzer relative to the detector. In spatially resolved mass spectrometers, the mass analyzer and detector are physically separated in space. Examples of mass analyzers used in spatial mass spectrometers include quadrupole devices,[43] time-of-flight (TOF) assemblies,[44] and magnetic and electrostatic sectors.[45,46] In temporally resolved mass spectrometers, mass analysis and ion detection are accomplished in the same physical space but as different events separated in time. For example, in Fourier-transform ion cyclotron resonance (FT-ICR)[47,48] and Orbitrap[49] mass spectrometers, ions are trapped, excited, and detected in the same cell (though different electrodes might be utilized for the two events). Although each type of mass analyzer has its own operating principles, merits, and limitations,[50] the proficiency of a mass analyzer can be described using specific performance characteristics such as MRP, mass accuracy, mass range, sensitivity, and scan rate.[51] Detailed descriptions of quadrupole and TOF mass analyzers, as well as a brief description of electron multiplier tube (EMT) detectors, are provided in the following two sections.

Table 1.1 Approximate values of performance characteristics of common mass analyzers.

Mass Analyzer	Quadrupole[52,53]	TOF[52,53]	Sector[52,53]	FT-ICR[53-55]	Orbitrap[56,57]
Mass Resolving Power	10^3	10^4	10^3-10^5	$>10^6$	10^5
Mass Measurement Accuracy (ppm)	50-100	2-50	1-5	<1	<5
Mass Range Upper Limit (*m/z*)	4,000	unlimited	20,000	10,000	20,000
Sensitivity (grams)	10^{-15}	10^{-12}	10^{-12}	10^{-15}	10^{-12}

1.2.2.1 Quadrupole Mass Analyzer. A quadrupole mass analyzer is composed of four parallel, usually, cylindrical electrodes. Diagonally opposite electrode pairs are connected electrically and to radio-frequency (RF) and direct current (DC) power sources as shown in Figure 1.3. Variable RF voltages (with "DC rides") are applied to pairs of diagonally opposite electrodes.

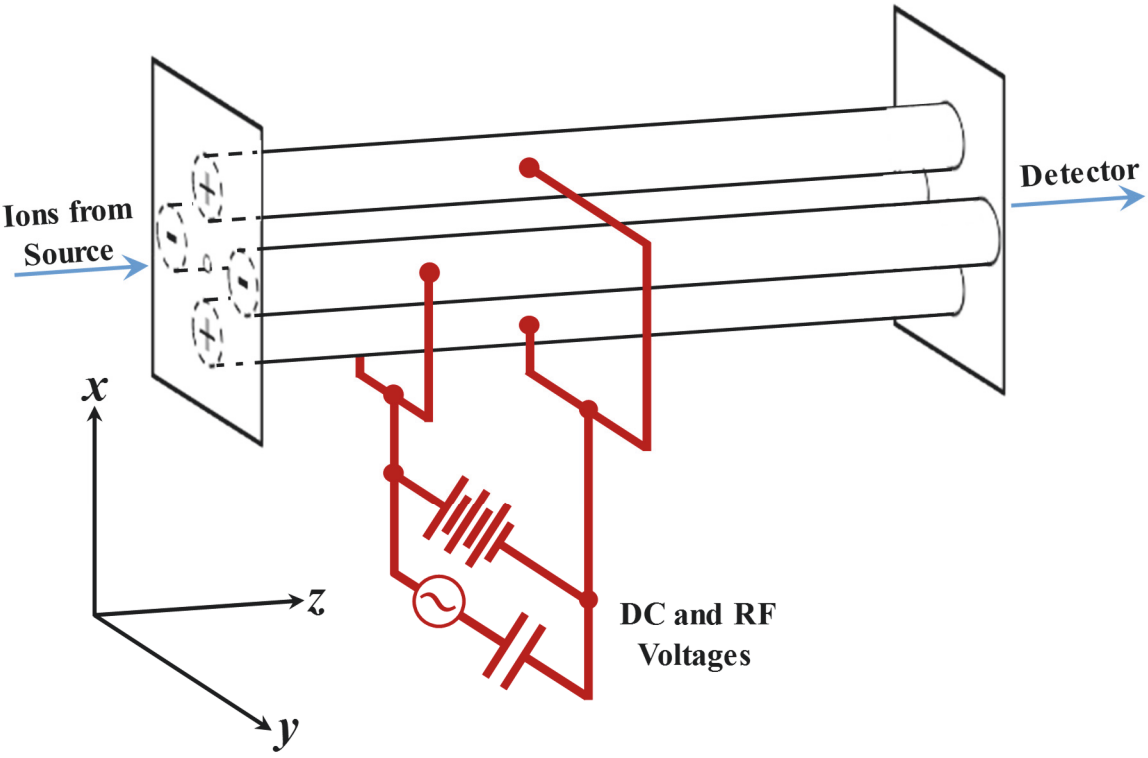

Figure 1.3. Experimental design of a quadrupole mass analyzer with DC and RF electrical connections to four rods of the quadrupole assembly. The Cartesian projection is provided for visualization of the *xz* and *yz* planes. This representation was recreated based on the work of Skoog *et al.* (reference number 61).

In other words, one pair of electrodes is connected to a positive DC voltage (*xz* plane in Figure 1.3), and the other pair is connected to a negative DC voltage of equal amplitude (*yz* plane in Figure 1.3). Ions are accelerated into the central space that constitutes the quadrupole electric field and along the longitudinal axis (*z*-axis) toward the detector. As

ions are accelerated along the *z*-axis, the amplitudes of the RF and DC voltages are simultaneously ramped at a fixed ratio. For a given set of RF and DC voltage values, only ions of a specific *m/z* value (or range of values) successfully traverse along the *z*-axis; all other ions collide with the electrodes and are neutralized.[58-62]

1.2.2.2 Time-of-Flight (TOF) Mass Analyzer. The TOF mass analyzer was first hypothesized by W. E. Stephens in 1946.[63] Stephens and M. M. Wolff published data collected on the first TOF mass analyzer in 1953,[64] and the first design of a commercially available TOF was published by W.C. Wiley and I. H. McLaren in 1955.[65] In principle, TOF mass analyzers (Figure 1.4) allow differentiation of gas-phase ions based on their velocities after their initial acceleration and subsequent travel in a field-free vacuum tube (i.e., TOF drift tube). Ions with different m/z values that are accelerated in the same electric field will have different velocities. Consequently, m/z values can be calculated by measuring ions' flight times through a field-free drift tube.[44]

The TOF measurement begins at the TOF start time (time zero) where all ions are simultaneously accelerated. The TOF start time can be an ionization event such as a (pulsed) laser desorption event,[66] but time zero can also be recorded using a time regulated pusher electrode (often a pulsed "source acceleration voltage"). Typically, ions are accelerated into the TOF drift tube by applying a single, high-voltage pulse (ranging from ~10 kV to ~20 kV or beyond) to a pusher electrode, and all ions that experience the same pulse event are considered to have the same TOF start time. A field-free region is established in the TOF drift tube by applying the same voltage used for ion acceleration to two grid electrodes that are positioned at the beginning and end of the drift tube. Ion acceleration converts each ion's electric potential energy (E_p, Equation 1.1) to kinetic

energy (E_k, Equation 1.2) according to Equation 1.3 where z is the integer value of an ion's charge, e is the elementary charge in Coulombs, V is the applied voltage in volts, m is the ion's mass in kilograms (kg), and v is the ion's velocity in meters second^{-1}:

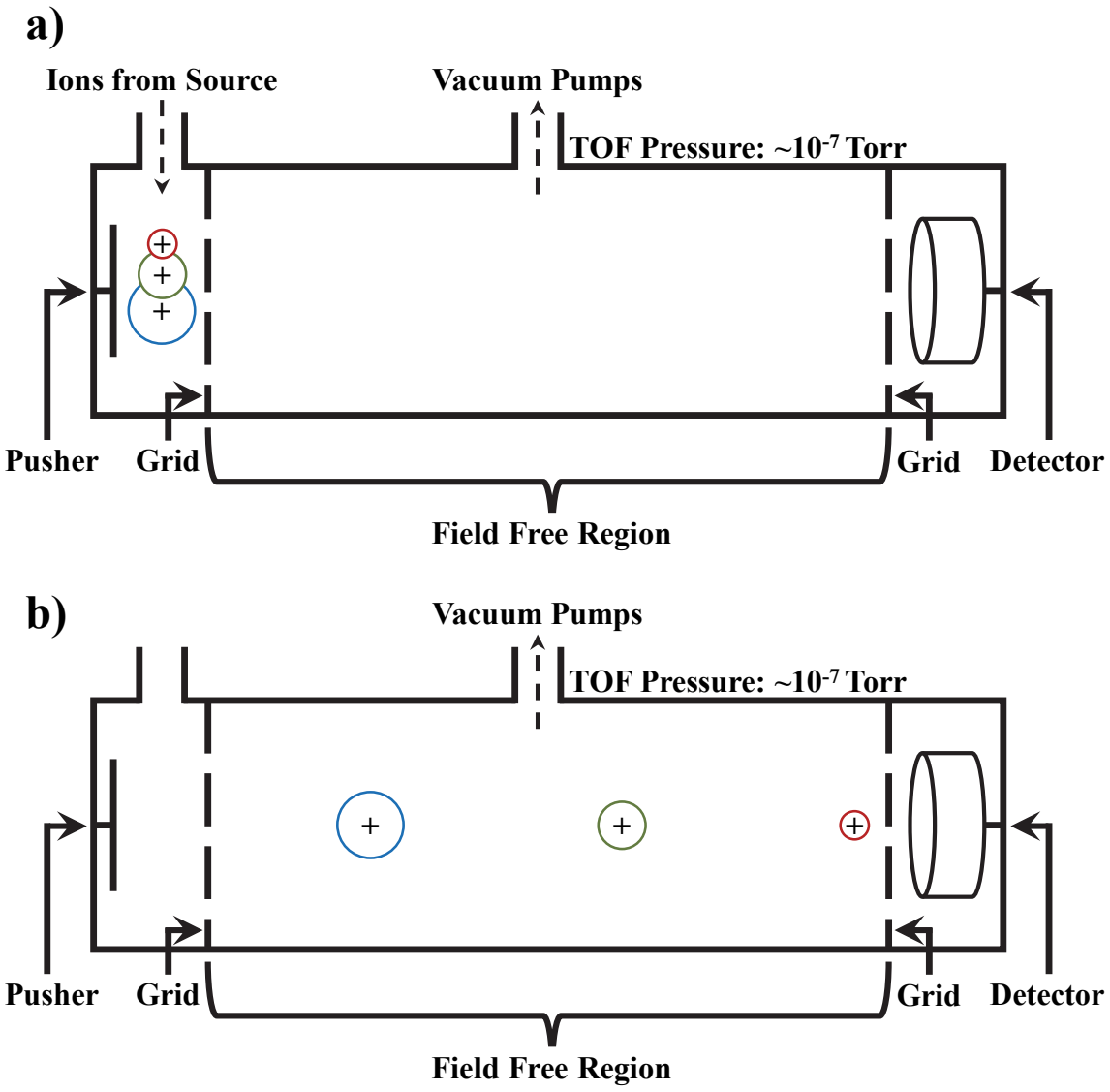

Figure 1.4. Representation of a TOF mass analyzer (a) before and (b) after ion acceleration *via* application of high voltage to the pusher electrode. This representation is based on the work of Watson *et al.* (reference number 62).

$$E_p = zeV \quad \text{Equation 1.1}$$

$$E_k = \frac{mv^2}{2} \quad \text{Equation 1.2}$$

$$zeV = \frac{mv^2}{2} \quad \text{Equation 1.3}$$

Velocity is defined using Equation 1.4 where *d* is the distance of the ion flight path (*i.e.*, length of the TOF drift tube) in meters and *t* is time (*i.e.*, time of flight) in seconds:

$$v = \frac{d}{t} \quad \text{Equation 1.4}$$

Substituting Equation 1.4 into Equation 1.3 allows derivation of an expression for an ion's expected TOF (variable *t* in Equation 1.5):

$$t = \sqrt{\frac{md^2}{2zeV}} \quad \text{Equation 1.5}$$

Equation 1.5 can be rearranged to solve for *m/z* (Equation 1.6). For a given experiment, the acceleration voltage and length of the drift tube (variables *V* and *d* in Equation 1.6, respectively) are set to known values. Therefore, an ion's measured TOF can be converted to its corresponding *m/z* using Equation 1.6.

$$m/z = \frac{2eVt^2}{d^2} \quad \text{Equation 1.6}$$

A critical assumption when using Equation 1.6 is that all ions of identical *m/z* will have identical flight times. In reality, ions of the same *m/z* will likely have a range of flight times due to small uncontrolled variations in their placements relative to the pusher electrode. If the pusher electrode is thought of as a source charge, then the electric force experienced by gas-phase ions (as obtained from Coulomb's Law) is indirectly proportional to the square of their distances from the pusher electrode. In other words, ions will have higher kinetic energies (than other ions of the same *m/z*) if they are closer to the pusher electrode during application of the high-voltage pulse. Because of this, a

distribution of kinetic energies often exists for all ions of a particular *m/z* that are measured using TOF MS. According to Equation 1.1 through Equation 1.6, if ions of the same *m/z* are imparted a distribution of kinetic energies, they will have a distribution of flight times and thus be calculated as a distribution of *m/z* values.

Flight time distributions for ions of a single *m/z* value influence mass resolving power (MRP) in TOF MS. To understand this, an expression for MRP (*i.e.*, $M/\Delta M$) can be derived. As noted in Section 1.1, M is the *m/z* of the ion of interest and ΔM is the corresponding ion's MS peak width. Therefore, Equation 1.6 can be used to derive an expression for $M/\Delta M_{50\%}$ in TOF MS as follows:

$$m/z = M = \frac{2eVt^2}{d^2} \qquad \text{Equation 1.7}$$

$$f'(M)\, dM = f'\left(\frac{2eVt^2}{d^2}\right) dt \qquad \text{Equation 1.8}$$

$$dM = \frac{2eV}{d^2} \cdot 2t\, dt \qquad \text{Equation 1.9}$$

The relationship M/dM takes the form of Equation 1.10.

$$M/dM = t/(2\, dt) \qquad \text{Equation 1.10}$$

In Equation 1.10, dt represents the range of measured flight times (*i.e.*, flight time distribution) for the ion of interest and can be rewritten as Δt. Similarly, dm in Equation 1.10 represents the MS peak width of the ion of interest and can be rewritten as ΔM. For calculating MRP, flight time distributions, and hence MS peak widths, are often obtained by measuring the full-width at half maximum (FWHM, represented using subscript "50%") of the Gaussian-like MS signal. Therefore, Δt and ΔM are commonly written as $\Delta t_{50\%}$ and $\Delta M_{50\%}$, respectively, and MRP in TOF MS (MRP_{TOF}) can be written as:

$$MRP_{TOF} = M/\Delta M_{50\%} = t/2\Delta t_{50\%} \qquad \text{Equation 1.11}$$

As mentioned in Section 1.1, MS instruments with higher MRPs yield greater separation between MS peaks.[21] In other words, high MRP instruments provide narrow MS peak widths (*viz.*, low values for $\Delta M_{50\%}$). Based on Equation 1.11, the MRP_{TOF} can be increased by minimizing flight time distributions (*viz.*, low values for $\Delta t_{50\%}$) for ions of a particular *m/z*. A second way of increasing MRP in TOF MS is by lengthening the ion flight path distance. Reflectrons are commonly utilized in TOF MS to improve MRP by (i) minimizing the flight time distributions for ions of a particular *m/z* and (ii) increasing the overall distance of the ion flight path.[67] A reflectron is an ion mirror, in the form of an electric field, that opposes and is of greater magnitude than the electric field at the TOF pusher electrode.[62]

The operating principles of a reflectron are represented conceptually in Figure 1.5.[62] After ions of a particular *m/z* enter a reflectron, they are decelerated by an opposing electric field until their kinetic energy reaches zero. At this point, they are reaccelerated in the opposite direction towards the detector. Compared to ions with lower initial kinetic energies, ions with higher initial kinetic energies will experience (i) longer flight paths because they penetrate the reflectron more deeply and (ii) higher velocities after reacceleration because they are exposed to a longer segment of the opposing electric field.[62] By increasing ions' flight paths by an amount that is proportional to their initial kinetic energies, reflectrons focus ions of the same *m/z* and synchronize their arrival at the detector, resulting in improved MRPs in TOF MS. Ions' detection at the detector correspond to their TOF "stop" times. The most common type of detector used in TOF mass spectrometers is some variation of the electron multiplier tube (EMT).[68]

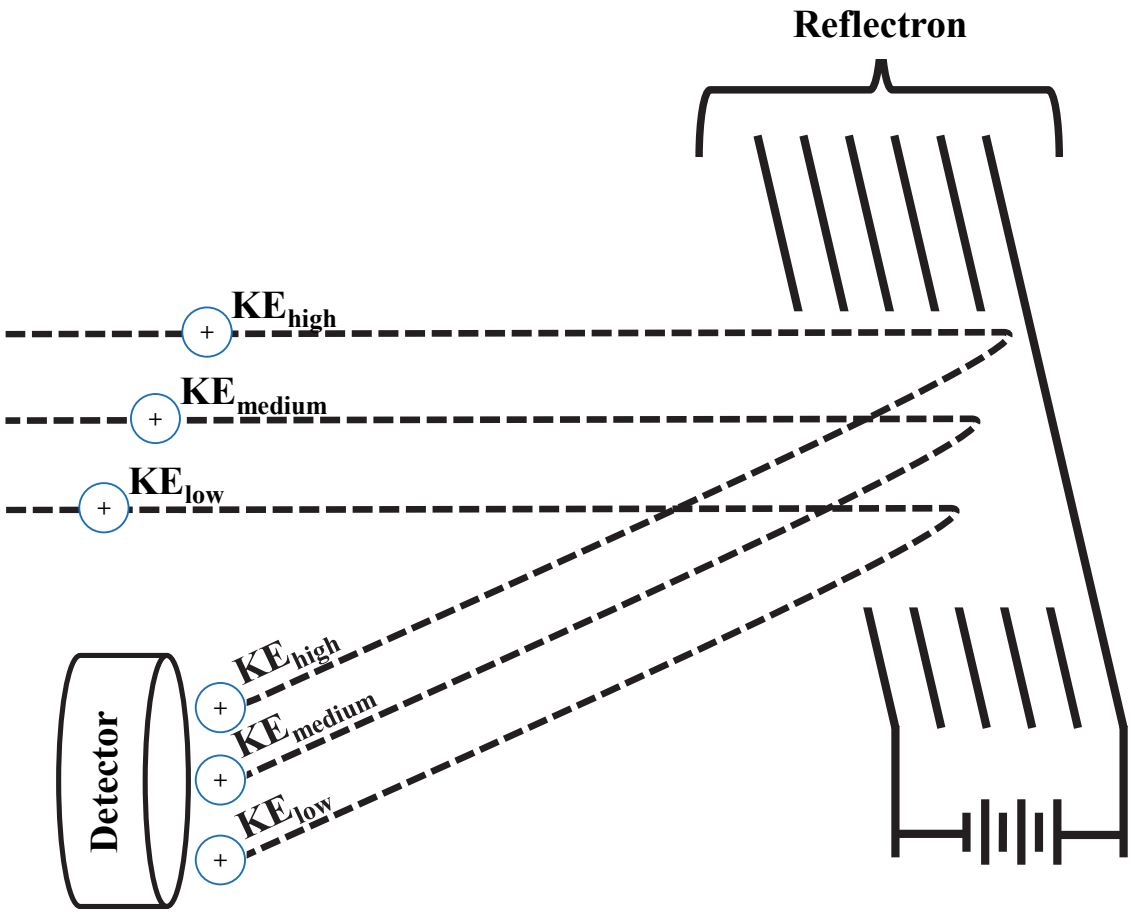

Figure 1.5. Representation of a reflectron as utilized in TOF MS. This representation is based on the work of Watson *et al.* (reference number 62).

In EMTs, ion impact at the cathode results in emission of secondary electrons that are subsequently accelerated towards a series of dynodes. Each time an accelerated secondary electron collides with a dynode, a greater number of secondary electrons are emitted and accelerated toward the next dynode. This "acceleration and impact" process of electron amplification repeats until secondary electrons strike the EMT anode where the current can be measured and recorded as the TOF "stop" time.

1.2.3 Common Techniques for Online Analyte Separation Prior to MS Analysis

Interpretation of data from MS analysis of complex samples can be challenging due to the presence of isomeric and isobaric ions. Isomers can be defined as molecules with the same elemental composition but different spatial arrangements; isomeric ions have identical exact masses. Isobars correspond to molecular species with the same nominal mass but different exact masses. High-resolution MS instruments, such as FT-ICR[47,48] and Orbitrap,[49] are frequently used to differentiate isobaric ions present in complex samples. Moreover, specialized MS analysis techniques, such as hydrogen-deuterium exchange (HDX)[69] or other ion-molecule reactions,[70] can be used to distinguish isomers and/or isobars. However, discerning the identities of isomeric and isobaric ions is difficult to address by MS alone. Hence, MS analysis of complex mixtures containing isomeric and isobaric species often requires some form of analyte separation prior to MS analysis.

Column chromatography methods allow separation of sample components based on differences in their migration velocities through a column.[71] For example, gas chromatography (GC) and liquid chromatography (LC) are commonly used for online separation of volatile and non-volatile samples, respectively. In GC or LC separation, samples are carried by a mobile phase through a column that contains a stationary phase; sample components separate from one another based on their relative affinities for the stationary phase. In GC, for example, samples are vaporized and carried by a gaseous mobile phase (generally an inert gas) through the column where samples partition into the stationary phase. Consequently, GC methods allow separation of gas-phase molecules based on their relative vapor pressures and stationary phase affinities.[72] Stationary phases

in GC are commonly made of liquid (*i.e.*, gas-liquid chromatography or GLC)[73] or solid (*i.e.*, gas-solid chromatography or GSC)[74] material.

Modern applications of LC, such as high-performance LC (HPLC) and ultra-performance LC (UPLC), utilize pressures as high as 20,000 psi (*e.g.*, as used in UPLC) to drive a liquid mobile phase through a column containing a stationary phase. The various types of LC (*e.g.*, partition chromatography,[75] adsorption chromatography,[76] ion-exchange chromatography,[77] size-exclusion chromatography,[78] *etc*.) can be classified by their stationary phases, and hence, separation mechanisms. Partition chromatography, for example, is the most widely utilized type of UPLC and can be further divided into normal-phase and reversed-phase separations based on the relative polarities of the mobile and stationary phases. By employing relatively nonpolar mobile phases (such as hexane) and highly polar stationary phases (such as triethylene glycol) for normal-phase separations, the least polar component is eluted first from the column. On the other hand, the most polar component is eluted first in reversed-phase separations by using relatively polar mobile phases (such as a mixture of water and acetonitrile) and a nonpolar stationary phase (commonly composed of hydrocarbons). All LC separations presented in this dissertation were performed using reversed-phase UPLC.

Ion mobility spectrometry (IMS or IM)[79-83] can be utilized prior to MS analysis for separation of gas-phase ions based on their mobilities in a gaseous medium (*i.e.*, buffer gas). The mobility of an ion under low electric fields can be obtained using the Mason-Schamp equation[84] (Equation 1.12) where K is mobility of an ion (expressed in $cm^2\ V^{-1}\ s^{-1}$), μ is the reduced mass of the diffusing ions and buffer gas molecules, k_B is the Boltzmann constant, T is the gas temperature in Kelvin, z is the number of elemental charges (on the

ion), e is the elemental charge, N is the number density of the drift gas, and Ω is the collision cross section (CCS) of the diffusing ions.

$$K = \frac{3}{16}\left(\frac{2\pi}{\mu k_B T}\right)^{\frac{1}{2}}\frac{ze}{N\Omega} \qquad \text{Equation 1.12}$$

The millisecond timescale of IM separation (compared to minutes for GC and UPLC[85] separations) and vacuum compatibility of IM devices are suitable for coupling IM with MS (IM-MS) for high-throughput analysis[86] of complex mixtures. Moreover, ion flight times are typically in the range of tens of microseconds in TOF MS; therefore, a single detector can be used to measure ions' IM drift times and *m/z* values in IM-MS. Because IM is considered a "charge-to-size" separation technique,[84] it can be used to differentiate chemical isomers[87] and separate product fragment ions.[69] Furthermore, IM can provide insight into atomic arrangements and molecular structures and conformations[88] that can be used as molecular fingerprinting tools.[89,90] Although a variety of IM instruments have been developed (*e.g.*, drift tube IMS (DTIMS),[91] high-field asymmetric IMS (FAIMS),[92] trapped IMS (TIMS),[93,94] traveling wave IMS (TWIMS),[81] *etc.*), all utilize electric fields to accelerate gas-phase ions through a buffer gas, where ions are slowed down due to collisions with molecules of the buffer gas. Because all IM data presented in this dissertation were collected using TWIMS prior to MS detection, the following section provides further details on TWIMS.

1.2.3.1 Traveling Wave Ion Mobility Spectrometry. The seminal TWIMS instrument, developed in 2004 by Giles et al.,[81] was based on an RF-only stacked ring ion guide (SRIG)[95,96] and coupled to a TOF mass analyzer.[97] The IM drift cell in TWIMS is a chamber that houses a series of ring electrodes, filled with an (typically) inert buffer gas

such as nitrogen. Ions are radially confined by applying alternating RF voltages to adjacent rings (Figure 1.6a), and ions are propelled through the drift cell using a repeating pattern of DC voltages that is superimposed on the confining RF electric fields (Figure 1.6b). Moving the DC voltages across adjacent ring electrodes generates a non-uniform, moving electric field in the form of a half-sinusoidal traveling wave pulse;[81,98,99] a SRIG that is operated in this way is commonly referred to as a traveling wave ion guide (TWIG). As ions traverse the IM drift cell, they collide with molecules of the buffer gas resulting in temporal dispersion[100] based on their CCS differences.[101,102] It is well documented that the direct relationship between an ion's mobility and its CCS, as provided in Equation 1.12, is not valid in TWIMS due to the use of a time varying electric field (viz., traveling wave pulse).[84,102-106] However, it remains true in TWIMS that ions' mobilities are proportional to their CCSs, and ions with smaller CCSs have fewer collisions with molecules of the buffer gas and exit the IM drift cell earlier (i.e., corresponding to shorter IM arrival times (ATs)) than ions with larger CCSs.

The first commercially available TWIM-MS instrument, the Synapt G1 High Definition Mass Spectrometer (HDMS), was released by Waters Corporation in 2006. The reported IM resolving power (*i.e.,* $CCS/\Delta CCS_{50\%}$) for the Synapt G1 HDMS is ~11,[98] which is sufficient for performing routine CCS measurements on a range of ionic species at physiologically relevant concentrations. In 2009, Waters released an improved, second generation TWIM-MS instrument, the Synapt G2 HDMS, followed by the subsequent release of improved versions such as the Synapt G2-S HDMS and Synapt G2-Si HDMS. All data presented in this dissertation were collected using a Synapt G2-S HDMS system.

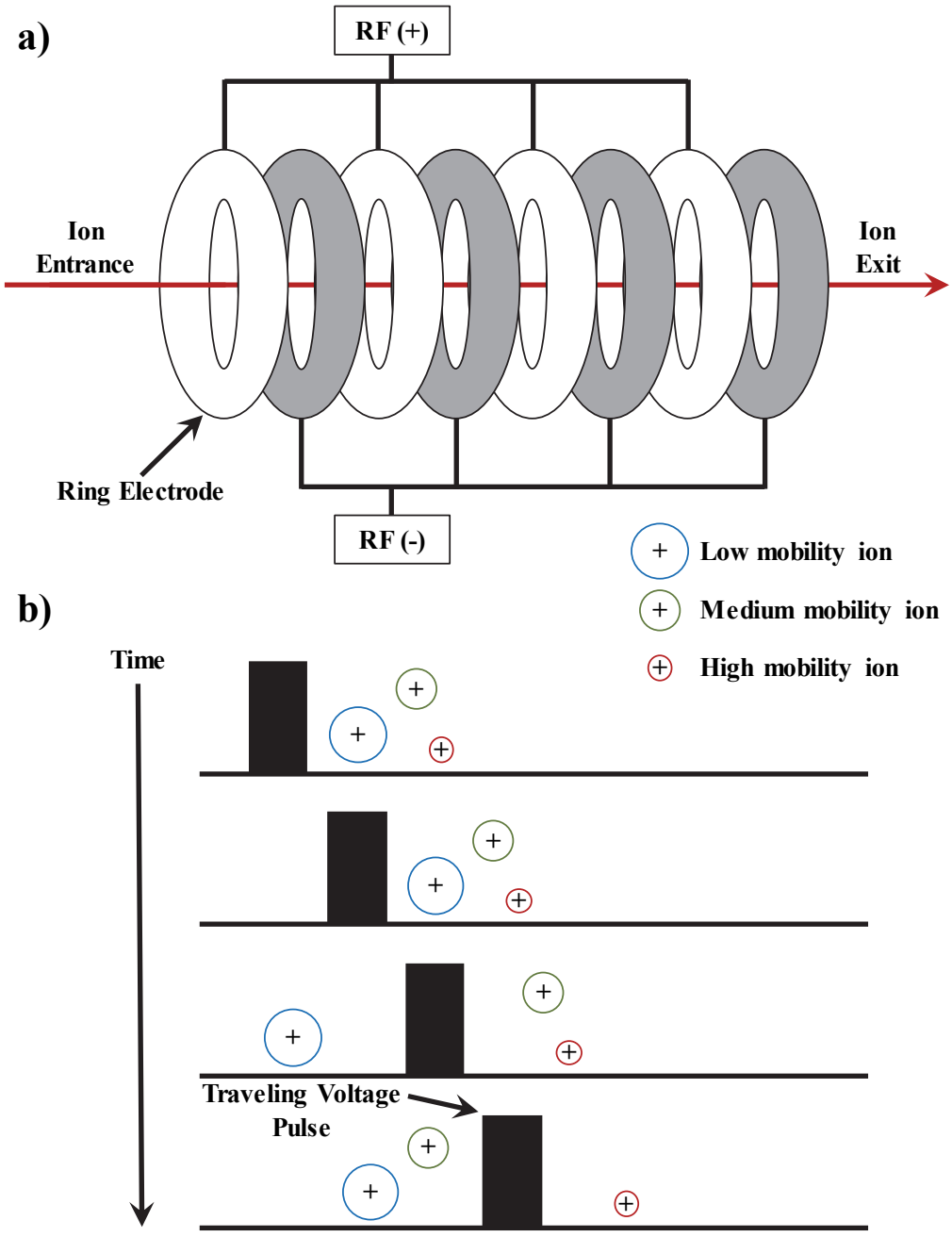

Figure 1.6. Representation of a traveling wave ion guide (TWIG). (a) Alternating RF voltages are applied to adjacent ring electrodes to radially confine ions. (b) Ions are propelled through the TWIG using a repeating pattern of DC voltages that are superimposed on the confining RF electric fields. This representation is based on the work of Giles *et al.* (reference number 81).

The five main components of the Synapt G2-S HDMS (Figure 1.7) system include: (i) an ionization source that can be switched between a variety of ionization types such as ESI, MALDI, corona discharge,[107,108] *etc.*, (ii) a StepWave TWIG for improved ion transmission from the source to the mass analyzer, (iii) a quadrupole mass filter, (iv) a TriWave region comprised of three successive TWIGs that are used as a trap cell for ion accumulation, an IM drift cell (a helium curtain is placed directly before the IM drift cell for collisional cooling), and a transfer cell for transmitting ions to (v) the orthogonal acceleration TOF mass analyzer.

The technical improvements to the first generation Synapt HDMS instrument have been well documented.[81,82,98] The notable increase in IM resolving power from ~11 for the G1 to ~45 for the G2, G2-S, and G2-Si is primarily due to the use of increased IM operating pressures (*i.e.*, ~0.5 mbar N_2 for G1 *vs* ~3.0 mbar N_2 for G2).[98] Compared to the G1, a higher outflow of N_2 gas in the IM drift cell of G2 instruments requires higher electric fields to drive ions into and through the IM drift cell. The use of higher fields for ion injection into the IM drift cell can increase the collision-energy[25] between ions of interest and gaseous N_2 molecules and result in unwanted ion losses by way of ion scattering and/or fragmentation. Additionally, high ion injection energies may cause substantial ion heating[109,110] that can induce unwanted structural changes and alter IM drift time distributions for ions of interest.[111-113] To facilitate the use of higher IM operating pressures (of N_2) in the second generation Synapt HDMS instruments, a helium curtain (*i.e.*, He cell) was placed between the trap cell and IM cell. In a TWIG, ion mobilities are significantly higher in He than N_2.[114] Therefore, maintaining a higher He pressure (in the He cell) than N_2 pressure (in the IM drift cell) helps reduce ion scattering and/or fragmentation by

allowing ion injection to occur in a medium of gaseous He. Furthermore, the He cell can minimize unwanted artifacts associated with ion heating because ions are collisionally cooled when injected into high pressures of He.[109]

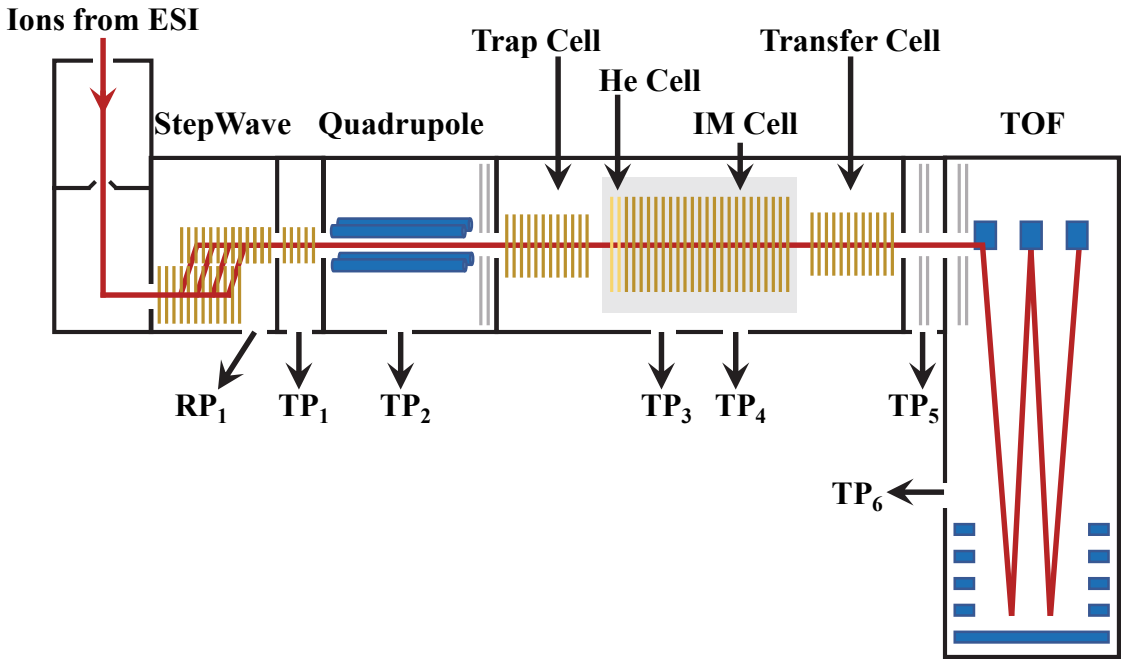

Figure 1.7. Representation of the Synapt G2-S HDMS used to collect all data presented in this dissertation. This representation is based on the work of Giles *et al.* (reference number 98).

1.2.3.2 Ion Mobility Deconvolution Strategies. Despite the development of improved IM-MS instruments and experimental strategies,[115-118] including enhanced chromatographic separation technologies,[119-121] successful IM characterization of complex mixtures is (traditionally) hardware limited by the instrument's IM resolving power (defined as $AT/\Delta AT_{50\%}$ or $CCS/\Delta CCS_{50\%}$).[99,122,123] Several groups have utilized post-IM fragmentation of partially IM separated molecules to determine the presence and identities of IM-MS unresolved ions.[124-128] For example, IM convolution has been addressed by correlating extracted fragment ion drift time distributions of species-specific fragment ions

with extracted ion drift time distributions of precursor ions.[127] Likewise, the observed change in AT distributions of precursor and product ions at varying post-IM fragmentation energies can be used to ascertain the number of IM unresolved components contained within a mixture.[126] Although these experimental strategies have allowed improved structural characterization of partially IM separated ions, they cannot be used to extract "pure component" IM profiles or associated fragment ion spectra from partially resolved IM profiles of co-eluting analytes.

In 2012, Zekavat and Solouki introduced a chemometric data analysis technique that could be used to extract the pure component IM profiles and corresponding mass spectra of unresolved ions from post-IM fragmentation data.[129] Their approach for IM-MS deconvolution, which is based on SIMPLe-to-use Interactive Self-modeling Mixture Analysis (SIMPLISMA),[130] was automated in 2014 by developing the Automated Ion Mobility Deconvolution (AIMD) software.[131] AIMD has since been used to investigate several IM unresolved systems.[87,132-134] Both Chapters 2 and 3 of this dissertation present IM profiles and associated mass spectra that were generated using AIMD.

1.2.4 Gas-Phase Ion Fragmentation Techniques in Mass Spectrometry

Ion fragmentation is used in tandem mass spectrometry (MS/MS) for characterizing a wide variety of molecules including lipids,[135] carbohydrates,[136] and proteins.[137,138] Ion fragmentation techniques can be classified as either ergodic or non-ergodic ion activation methods. When a precursor ion's internal energy is increased by ergodic ion activation methods (*e.g.*, collision-induced dissociation (CID),[139-141] sustained off-resonance irradiation collision-induced dissociation (SORI-CID),[142] infrared multiphoton dissociation (IRMPD),[143] *etc*.), the increased internal energy of the precursor ion is

randomly distributed in its rovibrational and electronic modes until the accumulated energy surpasses the appearance energies of specific fragment ions (product ions).[25,144] The fragmentation pathways that are accessed using ergodic activation methods depend on bond dissociation energies and the amount of energy deposited, and weaker bonds are preferentially cleaved.[145] Among ergodic ion activation methods, CID is the most commonly used activation method in mass spectrometry.[141] All fragment ions presented in this dissertation were generated using CID. In non-ergodic methods, such as surface-induced dissociation (SID),[146,147] electron capture dissociation (ECD),[148] and electron transfer dissociation (ETD),[149,150] fragmentation is independent of the bond dissociation energies.[145] Typically, the fragmentation pattern produced by ergodic ion activation of a precursor ion can be replicated by any ergodic fragmentation method that imparts the same amount of internal energy to the precursor ion of interest.[151] On the other hand, fragmentation patterns obtained using a specific non-ergodic fragmentation technique are difficult to reproduce by other means.[151]

1.2.4.1 Fragment Ion Nomenclature for Peptides and Glycans. Systematic naming schemes have been adopted for the various types of product ions because various types of product ions can be generated depending on the specific types of precursor ions being fragmented and the fragmentation methods being used. For example, the nomenclature introduced by Roepstorff and Fohlman (Figure 1.8) has been widely accepted for describing product ions generated from the fragmentation of protein and peptide precursor ions.[152] The types of product ions formed from dissociation of protein and peptide ions are named based on the cleavage site along the polypeptide chain and which terminus retains the charge after fragmentation. Cleaving the bond between the alpha carbon and the

carbonyl carbon (i.e., Cα-C bond) yields "a_n" type product ions if the charge is retained on the N-terminus and "x_n" type product ions if the charge is retained on the C-terminus.

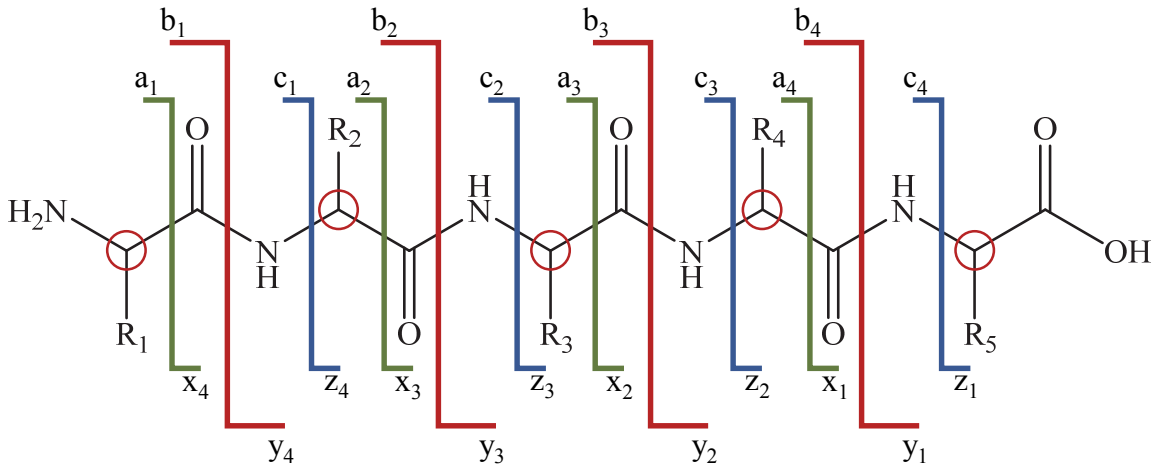

Figure 1.8. Roepstorff nomenclature system for protein and peptide product ions. Red circles indicate the positions of all alpha carbons in the amino acid sequence.

Amide bond cleavage (*i.e.*, C-N bond) yields "b_n" or "y_n" type product ions if the charge is retained on the N- or C-terminus, respectively. Similarly, dissociation of the bond between the amine nitrogen and the alpha carbon (N-Cα) yields "c_n" (charge on N-terminus) or "z_n" (charge on C-terminus) type ions. Different fragmentation techniques preferentially generate different types of fragments. For example, the predominant product ions formed *via* ECD and ETD are c_n, x_n, and z_n type ions,[148-150] and CID predominantly yields a_n, b_n, and y_n type ions.[141] A similar nomenclature was introduced by Domon and Costello for product ions from glycan dissociation (Figure 1.9a).[153] Labels "A_n", "B_n", and "C_n" designate fragments containing a terminal (non-reducing end) sugar unit, whereas "X_n", "Y_n" and "Z_n" designate fragments containing the reducing sugar unit. Notation for cross-ring cleavages is shown in Figure 1.9b. For both the peptide and glycan naming schemes, subscripts indicate the position relative to the termini.

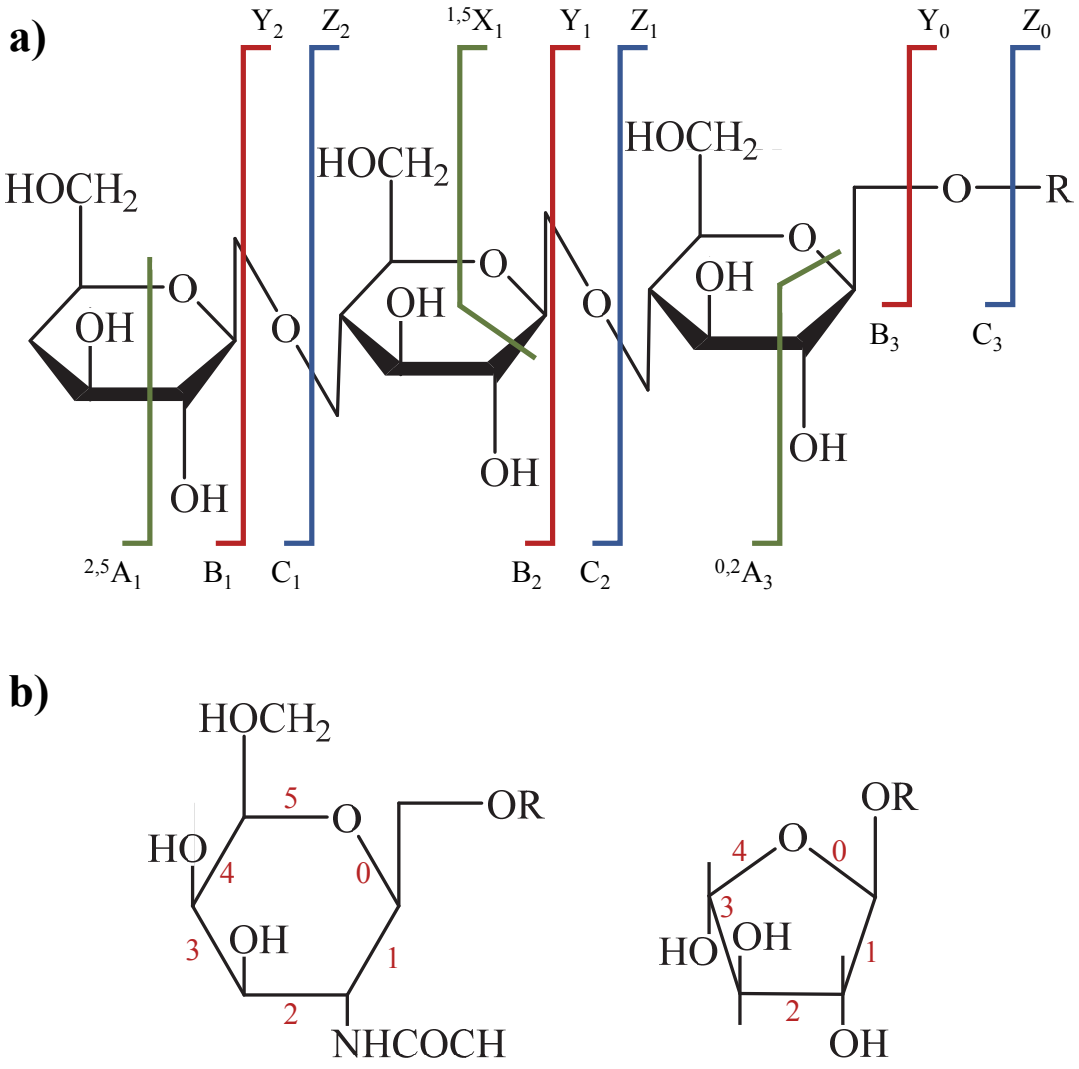

Figure 1.9. Domon and Costello nomenclature system for (a) glycan fragmentation including the (b) numbering system used for cross ring cleavages.

1.3 Mass Spectrometry Based Proteomics

Proteomics is an umbrella term for any technique (or combination of techniques) that allows qualitative or quantitative profiling of proteins. The use of proteomics has facilitated countless investigations ranging from fundamental studies of structure-function relationships for better understanding of basic human physiology[154] to the discovery of novel pharmaceuticals[155] and even biomarker discovery for early detection of diseases such as cancer[156] and Alzheimer's.[157] A variety of analytical methods, including gel electrophoresis,[158] binding affinity assays,[159] tissue imaging techniques,[160] and MS-based approaches,[3] have been developed for analyzing proteins from tissues, cells, and body fluids.[161,162] The widespread use of MS-based proteomics evolved from the development of Nobel Prize winning ionization techniques such as MALDI[11,30] and ESI[13,28] that allow ionization of large, intact proteins for subsequent mass spectrometry analysis.

MS-based protein characterizations are typically performed using either top-down[163-178] or bottom-up[138,179-185] approaches. By investigating intact proteins, top-down approaches can yield in-depth primary structure information, including site-specific mutations and post-translational modifications.[179] In bottom-up approaches, intact proteins are subjected to chemical or enzymatic proteolysis prior to LC separation and subsequent MS analysis.[183] High-throughput applications of MS-based proteomics more commonly utilize a bottom-up approach because peptides from proteolytic digests are typically easier to solubilize for LC separation and more readily analyzed with MS than intact large proteins.[186] Gas-phase ion fragmentations[139-141,148-151,187] (described in Section 1.2.4) are employed in bottom-up approaches to generate product ions that are subsequently correlated to their corresponding precursor peptide ions. The resulting list of precursor-

product ion assignments are searched through protein databases (*e.g.*, UniProt Knowledgebase[188]) to identify tryptic peptide and subsequently infer the presence of proteins.[189-192]

1.3.1 Data Collection Strategies in High-throughput Bottom-up Proteomics

Generating precursor-product ion assignments for high-throughput MS-based proteomics is typically achieved using an either data-dependent acquisition (DDA) or data-independent acquisition (DIA) strategy. DDA is a well-established approach for collecting MS/MS data in bottom-up MS-based proteomics, and a variety of data processing and databank searching algorithms have been developed that support analysis of DDA-type datasets (*e.g.*, Mascot,[190] SEQUEST,[189] ProteinLynx Global Server,[193] *etc.*). In DDA approaches, MS/MS data are collected in serial by utilizing sequential ion isolation and fragmentation of ions of interest. Data collection using DDA approaches begins with an MS survey mode (*i.e.*, precursor ion scan) for measuring precursor ions. When signal intensity (or signal-to-noise ratio) in the precursor ion scan reaches a user-defined threshold, the mass spectrometer is triggered to record a "snapshot" of the precursor ion scan and collect MS/MS data (*i.e.*, product ion scan). Precursor ions are preferentially selected for MS/MS based on their signal intensities, and higher intensity ions are isolated and fragmented before lower intensity ions. Because precursor ions are isolated and their product ions are exclusively monitored in DDA approaches, generating precursor-product ion assignments for subsequent use in databank searches is a relatively straightforward task. However, the constant switching between MS and MS/MS modes during DDA is an inefficient use of instrumental duty cycle.[194-196]

Recently developed DIA approaches utilize instrumental duty cycles more efficiently than DDA approaches by applying broadband ion fragmentation to all ions within large *m/z* ranges.[197-205] Similar to DDA approaches, DIA approaches measure an entire *m/z* range of interest for collection of precursor ion data. In contrast to DDA approaches, DIA approaches do not require isolation of specific *m/z* values prior to gas-phase fragmentation. Instead, all detectable ions (within either sequentially scanned smaller windows[197,198,200-202,205] or the full *m/z* range[199,203,204]) are fragmented simultaneously. The use of alternating low and high collision-energies in DIA for parallel collection of precursor and product ion scans is markedly faster than scanning through individual precursor ions as is done in DDA. In addition, elimination of the ion isolation step in DIA yields higher sensitivity by avoiding unnecessary ion losses.[206] However, because ion isolation is not performed, correlating product ions to their corresponding precursor ions is significantly more difficult in DIA than DDA. Ion mobility[79,82,83] enhanced DIA (*i.e.*, HDMS^E) was developed for improved precursor-product ion correlation. In HDMS^E, IM drift time and accurate mass and retention time (AMRT) alignment are used to facilitate assignment of precursor and product ions from the three-dimensional data.[207-210] All high-throughput bottom-up proteomics data presented in this dissertation were collected using HDMS^E acquisition.

1.4 Justification of the Combined use of IM-MS Deconvolution and HDMS^E

The objective of the research presented in this dissertation was to enhance peak capacity for improved analysis of complex biological samples. Specific aims of this dissertation were to (i) develop experimental strategies for improved IM-MS deconvolution of unresolved species, (ii) establish that IM-MS deconvolution can be

utilized to improve results from IM-enhanced data-independent acquisition approaches such as HDMS^E, and (iii) demonstrate that integrating IM-MS deconvolution with HDMS^E provides an opportunity to increase numbers of proteins identified in high-throughput MS-based bottom-up proteomics experiments in reduced analysis times. In Chapter Two, an experimental strategy for improved IM-MS deconvolution is presented which utilizes a range of collision-energies to deconvolute single IM peaks that corresponded to three and four component mixtures. Specifically, it is shown that measuring IM-MS unresolved species using the collision-energy resolved approach allows for identification of specific collision-energies most suitable for successful IM-MS deconvolution of all unresolved components. The results in Chapter Two demonstrate that IM-MS deconvolution of highly complex samples is more successful when a range of collision-energies is used. In Chapter Three, a broadband data collection approach is used for IM-MS deconvolution. Results in Chapter Three show that broadband IM-MS deconvolution has throughput and sensitivity advantages over the collision-energy resolved approach. Additionally, Chapter Three reports the first use of IM-MS deconvolution with HDMS^E acquisition for improved results from high-throughput bottom-up proteomics analysis. In Chapter Four, DDA and HDMS^E approaches for bottom-up proteomics analysis of rat brain tissue digests are investigated. It is shown that HDMS^E can identify substantially greater numbers of peptides and proteins than DDA. Additionally, it is shown that the use of shorter UPLC separation times can result in increased UPLC congestion and decreased numbers of peptides and proteins identified by both DDA and HDMS^E.

1.5 Author Contributions

One-hundred percent of the data reported in Chapters Two and Three, including data reported in Appendices A and B, were collected by Michael E. Pettit. Approximately ninety-five percent of the data reported in Chapter Four and Appendix C were collected by Michael E. Pettit, and the remaining five percent correspond to microscopy images that were obtained by Fabrizio Donnarumma. Approximately seventy percent of the text in Chapter Two was written by Michael E. Pettit, and the remaining thirty percent was written by equal contributions from Brett Harper, Matthew R. Brantley, and Touradj Solouki. All samples used to generate data reported in Chapter Two, including Appendix A, were purchased by Touradj Solouki and prepared by Michael E. Pettit. Approximately eighty percent of the text in Chapter Three was written by Michael E. Pettit, and the remaining twenty percent was written by equal contributions from Matthew R. Brantley, Fabrizio Donnarumma, Kermit K. Murray, and Touradj Solouki. The samples used for direct infusion IM-MS experiments reported in Chapter Three, including Appendix B, were purchased by Touradj Solouki and prepared by Michael E. Pettit. Approximately seventy percent of the text in Chapter Four was written by Michael E. Pettit, twenty percent was written by Fabrizio Donnarumma, and the remaining ten percent was written by equal contributions from Kermit K. Murray and Touradj Solouki. The rat brain samples used to generate data reported in Chapters Three and Four, including Appendices B and C, were obtained by Kermit K. Murray and Fabrizio Donnarumma from the Louisiana State University School of Veterinary Medicine Division of Laboratory Animal Medicine; these samples were prepared by Fabrizio Donnarumma using materials purchased by Kermit K. Murray.

CHAPTER TWO

Collision-energy Resolved Ion Mobility Characterization of Isomeric Mixtures

This chapter is published as: Pettit, M. E., Harper, B., Brantley, M. R., Solouki, T., Collision-energy Resolved Ion Mobility Characterization of Isomeric Mixtures. *Analyst*. **2015**, *140*, 6886-6896.

2.1 Abstract

Existing instrumental resolving power limitations in ion mobility spectrometry (IMS) often restrict adequate characterization of unresolved or co-eluting chemical isomers. Recently, we introduced a novel chemometric deconvolution approach that utilized post-IM collision-induced dissociation (CID) mass spectrometry (MS) data to extract "pure" IM profiles and construct CID mass spectra of individual components from a mixture containing two IM-overlapped components [*J. Am. Soc. Mass Spectrom.* **2012,** 23, (11), 1873-1884]. In this manuscript we extend the capabilities of IM-MS deconvolution methodology and demonstrate the utility of energy resolved IM deconvolution for successful characterization of ternary and quaternary isomer mixtures with overlapping IM profiles. Furthermore, we show that the success of IM-MS deconvolution is a collision-energy dependent process where different isomers can be identified at various ion fragmentation collision-energies. Details on how to identify a single collision-energy or suitable collision-energy ranges for successful characterization of isomer mixtures are discussed. To confirm the validity of the proposed approach, deconvoluted IM and MS spectra from IM overlapped analyte mixtures are compared to IM and MS data from individually run mixture components. Criteria for "successful"

deconvolution of overlapping IM profiles and extraction of their corresponding pure mass spectra are discussed.

2.2 Introduction

Mass spectrometry (MS) analysis of complex sample mixtures often necessitates exploitation of sample separation techniques prior to MS detection. For example, high performance liquid chromatography (HPLC)[120] and gas chromatography (GC)[73] are commonly used in tandem with MS for separation of nonvolatile and volatile samples, respectively. Similar to HPLC or GC separation of neutral species, gas-phase ions can also be separated prior to MS analysis using ion mobility spectrometry (IMS).[79,81-83] IMS offers unique advantages over HPLC and GC such as: orders of magnitude shorter timescale for mixture separation (*e.g.,* milliseconds for IMS versus minutes for HPLC and conventional GC)[85] and the ability to separate product fragment ions.[133] Furthermore, IMS provides the ability to differentiate chemical isomers based on their collision cross section (CCS) differences.[101,102] Differences in collision cross sections (CCSs) can also provide insight into atomic arrangements, and molecular structure(s) and conformation(s)[88] that can be used as molecular fingerprinting tools for sample identification and/or characterization.[89, 90] Moreover, the millisecond timescale of IM separation and vacuum compatibility of IM devices are suitable for coupling IM with MS for high-throughput analysis[86] of complex mixtures.

The introduction of commercially available IM-MS instrumentation has promoted molecular structure based investigations in a variety of MS fields including, but not limited to, proteomics,[211] glycomics and glycoproteomics,[212] petroleomics,[213] and lipidomics.[214] Successful sample characterization using IM-MS is traditionally limited by the

instrument's IM resolving power (peak arrival time (AT)/$AT_{50\%}$ or CCS/$CCS_{50\%}$).[99,122,123] Several recent advances have improved IM resolving powers, including the development of custom-built IMS and IM-MS devices,[115,116,118,215-217] hardware modifications to commercially available instruments,[98,218] and the use of alternative IM buffer gasses/gas modifiers.[117,219-222] Although these valuable developments have generated impressive results, it may be challenging to implement them in shared instruments, such as in core facilities, or for the everyday user. Also, IM based characterization of complex mixtures using instruments that have limited IM resolving powers may be challenging.[98,117,129,131,133,220-223] Hence, it is desirable to complement instrument development efforts by designing improved methods for IM-MS data acquisition and interpretation that are independent of the IMS and/or IM-MS instrumental hardware.

To probe for the presence of unresolved molecules in IM-MS systems, several groups have utilized post-IM fragmentation of partially IM separated molecules to correlate fragment ions' mass spectra with precursor ions.[124-128] For example, Clemmer *et al.* addressed IM resolving power limitations by correlating extracted fragment ion drift time distributions of species-specific fragment ions with extracted ion drift time distributions of precursor ions.[127] Their findings indicated that, for each precursor ion contained within an unresolved IM distribution, only a single diagnostic fragment ion was needed to extract representative IM distributions from the complex mixture's unresolved IM distribution.[127] Although these recent improvements in IM resolving power capabilities have enhanced structural characterization of partially IM separated ions, the abovementioned approaches cannot be used to extract "pure" collision-induced dissociation (CID) mass spectra from partially resolved IM profiles of co-eluting analytes.

In 2012, we introduced a chemometric data analysis technique, based on the SIMPLe-to-use Interactive Self-modeling Mixture Analysis (SIMPLISMA) approach,[130] that could be used to extract the pure IM profiles *and* CID mass spectra of unresolved ions from post-IM/CID data.[129] Subsequently, we developed an "Automated IM-MS Deconvolution" (AIMD) data analysis software to improve the speed of post-IM/CID MS deconvolution.[131] In addition to improving the speed of IM deconvolution, the new preprocessing algorithm integrated into the AIMD software package also eliminated potential errors that were introduced in the original data resampling approach.[129,131]

All of our previously reported post-IM/CID MS deconvolution results have been from experiments conducted at single collision-energies.[129,131,133,223,224] However, ion fragmentation pathways in CID are collision energy dependent and recent studies have confirmed that IM-MS characterization of isomers can also be an energy dependent process.[126,225,226] For example, Hanozin *et al.* demonstrated that capistruin (a lasso-folded peptide) could be conformationally isomerized in an energy-dependent manner by varying collisional-activation energies prior to IM separation.[226] Collisional-isomerization of gas-phase capistruin ions investigated by Hanozin *et al*.[226] could be related to previously reported solution-phase isomerization of capistruin[227] and hence thorough IM analyses of some biologically relevant structures may necessitate energy-resolved approaches. Likewise, in 2014, Pagel and coworkers proposed an energy-resolved approach to improve IM resolving capabilities.[126] By monitoring the change in AT distributions of precursor and product ions at varying post-IM collision-energies, it was demonstrated that the number of trisaccharide isomers contained within a complex mixture (and their individual IM arrival times) could be determined.[126] Their results indicated that energy-resolved IMS analysis of

co-eluting isomers was most successful if individual mixture components exhibited differences in gas-phase stabilities.[126]

In this manuscript, we demonstrate the utility of a collision-energy resolved approach for deconvolution of overlapping IM profiles for isomeric mixtures. To show that successful IM-MS deconvolution of unresolved post-IM/CID MS data is a collision-energy dependent process, we performed IM-MS deconvolution on two *m/z*-isolated isomer mixtures (*i.e.*, a ternary mixture of trisaccharide-Li adduct isomers (sugar structures shown in Scheme 2.1) and a quaternary mixture of hexapeptide isomers) as a function of increasing post-IM collision-energy. Our results suggest that identification of the most suitable CID energy ranges or "sweet-spots" is required for optimal IM-MS deconvolution. At these appropriate CID energy ranges, post-IM CID mass spectra and chemometric analyses can be used to deconvolute the IM profiles of an isomeric mixture and construct IM and CID mass spectra for all individual components (*i.e.*, isomers) of the mixture. Detailed discussions on successful comparisons between deconvoluted and pure mass spectra for ternary and quaternary isomer mixtures are presented.

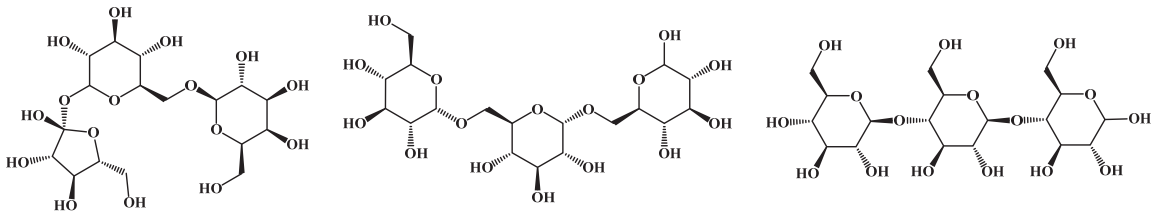

D-(+)-raffinose **D-(+)-isomaltotriose** **D-(+)-cellotriose**

Scheme 2.1. Molecular structures for the trisaccharide isomers used in this study.

2.3 Experimental

2.3.1 Sample Preparation

D-(+)-cellotriose, D-(+)-raffinose, D-(+)-isomaltotriose, and lithium chloride (LiCl) were purchased from Sigma-Aldrich (St. Louis, MO, USA). Hexapeptides (MGRYGF, MFRYGG, MFGRYG, and FRMYGG) were synthesized by Peptide 2.0, Inc. (Chantilly, VA, USA). Optima grade methanol and acetic acid were purchased from Fisher-Scientific (Waltham, MA, USA). Water (with a resistivity of 18.2 MΩ·cm at 25 °C and an overall ionic concentration of <0.1 ppb) was purified in-house using a Direct-Q 3 UV water purification system (EMD Millipore Corporation, Billerica, MA, USA). All samples and chemical solvents were used "as is" and without further purification.

Micromolar range concentrations of each trisaccharide and hexapeptide solutions were prepared in a spray solvent containing methanol: water: acetic acid (at respective volume % of ~49.95: ~49.95: ~0.01). Trisaccharide samples were spiked with an excess (~10: 1) of LiCl to generate trisaccharide-Li adducts. Final sample mixtures contained equimolar (~1.0 x 10^{-6} M) concentrations of each of the three lithiated trisaccharide (*i.e.,* D-(+)-cellotriose, D-(+)-raffinose, and D-(+)-isomaltotriose) or four hexapeptide (*i.e.,* MGRYGF, MFRYGG, MFGRYG, and FRMYGG) isomers.

2.3.2 Instrumentation

All experiments were performed using a Synapt G2-S HDMS system (Waters Corporation, Manchester, England, UK) operated in positive-ion mode electrospray ionization[69] (ESI). For the ternary mixture of isomeric trisaccharide-Li adduct ions, the Synapt time-of-flight (TOF) mass spectrometer was operated in resolution mode for

increased discrimination between potential isobaric species. Mass spectra for the mixture of isomeric hexapeptide ions were acquired in sensitivity mode using a 0.450 ms IMS wave delay for enhanced detection of low abundance fragment ions. Argon (Ar) was used as the buffer and collision gas in the trap and transfer cells, helium (He) gas was used for collisional cooling prior to IM, and nitrogen (N_2) was used as the IM drift gas. Detailed experimental parameters and instrument operating conditions are listed in Table A.1. Please note that the gas pressures reported in Table A.1 are direct instrument readouts and have not been corrected for geometry[224,228] or chemical sensitivity[229] factors. Sample flow rates were set to 0.5 μL/min using a Standard Infusion 11 Plus Syringe Pump (Harvard Apparatus, Holliston, MA, USA). Singly-charged trisaccharide-Li adduct ions (at *m/z* 511 and designated as $[M_T + Li]^+$) and doubly-charged hexapeptide ions (at *m/z* 365 and designated as $[M_P + 2H]^{2+}$) were *m/z*-isolated prior to IM in the quadrupole assembly. After traversing the IM device, $[M_T + Li]^+$ or $[M_P + 2H]^{2+}$ species were fragmented *via* CID (*i.e.,* post-IM/CID) in the transfer cell and as a function of collision-energy (*i.e.*, electric potential difference applied between the exit of the IM cell and entrance of transfer cell). Collision-energy resolved post-IM/CID MS data were obtained by increasing the collision-energy from 20 V to 80 V in 5 V increments for the ternary mixture of trisaccharide isomers ($[M_T + Li]^+$) and 20 V to 28 V in steps of 2 V for the quaternary mixture of hexapeptide isomers ($[M_P + 2H]^{2+}$). The selection of appropriate collision-energy ranges will be discussed in the results and discussion section. The total ion accumulation times per IM scan were 13.8 and 10.8 ms for the ternary and quaternary mixtures, respectively.

2.3.3 Data Analysis

Raw IM-MS data were analyzed using MassLynx software (version 4.1) (Waters Corporation, Manchester, England, UK). Reported IM-MS data were the average of a 5 minute acquisition time for the ternary trisaccharide isomer mixture (Figures 2.1 and 2.2) and a 45 minute acquisition time for the quaternary hexapeptide isomer mixture (Figures 2.3 and 2.4) which provided signal-to-noise ratios >3 for all reported ions in the deconvoluted mass spectra. An acquisition time of 5 minutes was adequate for all pure samples used for validation sets. Data preprocessing and AIMD analysis for IM-MS deconvolution were carried out as previously described.[131] AIMD offset values were optimized to minimize negative IM and *m/z* values.[129]

2.3.4 Collision-energy Optimization to Enhance IM Resolving Power

For all experiments, AIMD was set to the known number of mixture components (*i.e.*, "3" components for the trisaccharide mixture and "4" components for the hexapeptide mixture). For mixtures of unknown composition, the number of IM unresolved species can be ascertained using chemical rank determination techniques.[129,131,223] Based on the criteria for IM deconvolution described later in this section, deconvoluted IM profiles and corresponding mass spectra were individually classified as "successful" or "unsuccessful" results. IM-MS deconvolution of an individual mixture component was classified as "successful" if the following criteria were met: (1) deconvoluted data had no or negligible negative values (*i.e.*, less than 15% of the corresponding base peak intensity; see supporting information Figure A.1),[129] (2) the deconvoluted IM AT was within a ±1 IM scan range (*viz.*, 1 IM scan corresponded to 0.069 ms for the trisaccharide mixture and 0.054 ms for the hexapeptide mixture) of the corresponding pure sample's IM AT when individually

measured under similar conditions, and (3) deconvoluted CID mass spectrum "matched" the corresponding pure sample (used for validation sets) obtained under similar conditions. The degree of correlation between a deconvoluted mass spectrum and its pure counterpart was quantified using a spectral matching factor "*R*" (*R* values greater than 0.75 qualified as "matching" mass spectra or "successful" reconstruction of the mass spectrum for that specific IM profile) as described in the following section. Results from IM-MS deconvolution were considered "unsuccessful" when the deconvoluted data failed to meet any one of the abovementioned three criteria. At a given collision-energy, IM-MS deconvolution of an isomer mixture was classified as "optimal" when the previously mentioned three criteria were met for all mixture components. In the following sections, collision-energies corresponding to "optimal" IM deconvolutions are referred to as collision-energy "sweet-spots".

2.3.5 Spectral Matching

At a single collision-energy, the degree of correlation between an individual isomer's deconvoluted post-IM/CID mass spectrum and its corresponding pure sample's post-IM/CID mass spectrum was quantified using Equation 2.1:

$$R = 1 - \frac{\sum_{m=1}^{n} |x_m - x_{m'}|}{\sum_{m=1}^{n} (x_m + x_{m'})} \qquad \text{Equation 2.1}$$

The integer value *n* represents the total number (*i.e.*, considering fragment ions in both the deconvoluted and pure mass spectra) of fragment ion *m/z* values, *m,* with relative intensities (RI) above 10% of the base peak's relative intensity. For a given value of *m*, x_m and x_m' correspond to ion intensities from the deconvoluted and pure mass spectra, respectively. In other words, [$x_1, x_2, \ldots, x_n$] represent the intensity of each peak above 10% RI in the deconvoluted mass spectrum, and [$x_1', x_2', \ldots, x_n'$] represent the intensity of each

peak above 10% RI in the pure mass spectrum. As expected, regarding the presence or absence of "matching" peaks or *m/z* values in both reconstructed (from the deconvolution process) and pure (experimentally acquired using a single isomer) mass spectra, there were discrepancies in cases where matches were not ideal. In the case of a peak being present in one spectrum but absent in its corresponding "matching" mass spectrum (*e.g.,* present in the "pure" mass spectrum but absent in the deconvoluted mass spectrum or vice versa), the absent peak's ion intensity was assigned a value of zero, as discussed in an earlier publication.[131] Possible values of R were in the range of 0 to 1, where $R = 1$ indicates a perfect match between the deconvoluted spectrum and the corresponding pure mass spectrum; $R = 0$ signified no correlation. In this report, an R value of greater than 0.75 is designated as an acceptable match between the deconvoluted and pure mass spectra. Table A.2 displays calculated R values for all successfully deconvoluted isomers at each measured collision-energy.

2.4 Results and Discussion

By performing post-IM/CID MS analysis and deconvoluting overlapping IM profiles at varying collision-energies (*i.e.*, 20-80 V for the trisaccharide mixture and 20-28 V for the hexapeptide mixture), we show that the level of success for IM-MS characterization of isomeric mixtures depends on the CID energy employed for ion fragmentation. Additionally, we describe how to identify appropriate collision-energy ranges to differentiate all sample components (*i.e.,* collision-energies which generate significant detectable differences in CID mass spectra for all components). In the following section, we first show results from collision-energy resolved IM-MS deconvolution of a ternary mixture of IM unresolved trisaccharide-Li adduct isomers (*i.e.*, D-(+)-cellotriose,

D-(+)-raffinose, and D-(+)-isomaltotriose). Next, we extend our approach to a quaternary mixture of IM overlapped hexapeptide isomers (*i.e.*, MGRYGF, MFRYGG, MFGRYG, and FRMYGG). We validate our IM-MS deconvolution approach for each mixture by comparing deconvolution results to post-IM/CID MS data of isomerically pure samples (*i.e.*, single components run under similar experimental conditions and used as validation sets).

2.4.1 Collision-energy Resolved Deconvolution of a Ternary Mixture of Trisaccharide Isomers

As an initial proof of concept for the identification of collision-energy sweet-spots *via* collision-energy resolved IM-MS deconvolution, a ternary mixture of lithiated trisaccharide isomers ($[M_T + Li]^+$ at *m/z* 511) was subjected to post-IM/CID at varying collision-energies from 20 V to 80 V, in steps of 5 V. Based on multiple experiments and analysis of unpublished data collected during previously reported IM-MS deconvolution projects[129,131,133,223,224] it can be affirmed that unsuccessful deconvolution at: (1) low collision-energies (*e.g.,* $\leq$ ~20 V for singly-charged ions) result from insufficient fragmentation pattern differences between various isomers and (2) high collision-energies (*e.g.,* $\geq$ ~80 V for singly-charged ions) result from excessive ion fragmentations that yield MS patterns for different isomers that are too similar for deconvolution purposes. Because it was desirable to monitor the utility of our approach across a broad range of collision-energies, a wide range of collision-energies (*i.e.,* 20-80 V) was chosen for the ternary isomer mixture prior to collision-energy resolved analysis. Results from IM-MS deconvolution of post-IM/CID MS data were obtained for each collision-energy and classified as either "optimal" or "suboptimal" (according to the three step criteria described

earlier in the experimental section). Figure 2.1a shows a composite three dimensional plot of IM ATs, collision-energy voltages, and normalized ion intensities for the ternary isomer mixture ($[M_T + Li]^+$). Three different colors of red (for raffinose), blue (for isomaltotriose), and green (for cellotriose) are used to show deconvoluted IM peaks for each sugar isomer, respectively; also, this coloring scheme is utilized to denote the maximum number of isomers that can be successfully deconvoluted at each collision-energy voltage. For each collision-energy voltage, unsuccessfully deconvoluted IM profiles were summed and displayed as a single, unresolved profile (Figure 2.1a, gray profiles).

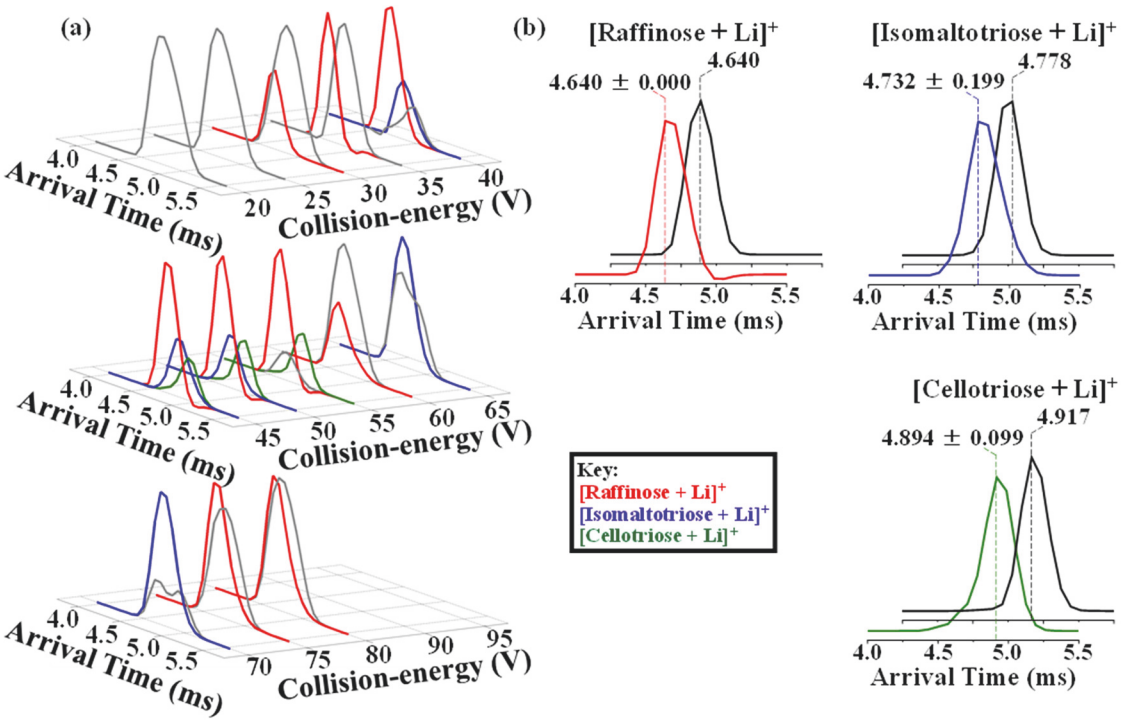

Figure 2.1. (a) Three dimensional plot of arrival time, collision-energy, and ion intensity from collision-energy resolved IM-MS deconvolution of a ternary mixture of lithiated-raffinose (red profiles), -isomaltotriose (blue profiles), and -cellotriose (green profiles). IM profiles shown in color and gray denote successful and unsuccessful deconvolution, respectively. (b) IM profiles (shown in color) for $[raffinose + Li]^+$, $[isomaltotriose + Li]^+$, and $[cellotriose + Li]^+$ from optimal IM-MS deconvolution at a collision-energy sweet-spot of 45 V. Black IM profiles denote pure samples measured under identical conditions. Deconvoluted arrival times are shown at the 95% confidence interval (n = 3).

Notably, 45 V and 50 V were the only tested collision-energies where IM-MS deconvolution of all three $[M_T + Li]^+$ components was successful; these energies represent collision-energy "sweet-spots" (Figure 2.1a, three-colored profiles) for the analysis of this ternary sugar isomer mixture.

At the lowest tested collision-energies (*i.e.,* 20 V and 25 V, Figure 2.1a), presumably, there are no characteristic fragmentation pattern differences between trisaccharide isomers (*e.g.,* where only minor losses of small neutrals such as H_2O are available reaction or fragmentation channels); hence the resulting CID mass spectra are indistinguishable from one another and thus IM-MS deconvolution of $[M_T + Li]^+$ is suboptimal at these low CID fragmentation energies.

Within the 25 V to 80 V collision-energy range (with exception to previously identified sweet-spots), $[M_T + Li]^+$ can be suboptimally deconvoluted such that only one (*i.e.*, 30-35 V and 60-80 V, Figure 2.1a) or two (*i.e.*, 40 V and 55 V, Figure 2.1a) mixture components can be appropriately identified. For example, IM-MS deconvolution of $[M_T + Li]^+$ at 30 V, 35 V, 60 V, 75 V, and 80 V collision-energies allows for successful extraction of [raffinose + Li]$^+$ mass spectrum from the mixture's unresolved post-IM/CID MS data (Figure 2.1a, red profiles). However, [isomaltotriose + Li]$^+$ and [cellotriose + Li]$^+$ could not be successfully deconvoluted at these energies (*i.e.*, 30 V, 35 V, 60 V, 75 V, and 80 V), suggesting that only [raffinose + Li]$^+$ has a significant detectable difference in its CID mass spectrum when compared to the mass spectra of the two other isomers in the mixture. Likewise, IM-MS deconvolution at 65 V and 70 V collision-energies allows the successful extraction of [isomaltotriose + Li]$^+$ profile from $[M_T + Li]^+$ (Figure 2.1a, blue profiles) but it does not allow for successful deconvolution of [raffinose + Li]$^+$ and [cellotriose + Li]$^+$.

Similarly, it may be concluded that a significant detectable CID pattern difference is generated from [isomaltotriose + Li]$^+$ at these collision-energies (*i.e.*, 65 V and 70 V) while the CID mass spectra for [raffinose + Li]$^+$ and [cellotriose + Li]$^+$ are indistinguishable.

IM-MS deconvolution at suboptimal collision-energies of 40 V and 55 V (Figure 2.1a) allows for extraction of appropriate ATs and corresponding CID mass spectra for only two of the three ternary mixture isomers. For example, [raffinose + Li]$^+$ and [isomaltotriose + Li]$^+$ are successfully deconvoluted from [M_T + Li]$^+$ at a collision-energy of 40 V, however, the deconvoluted CID mass spectra that *should* correspond to [cellotriose + Li]$^+$ (*i.e.*, AT from deconvolution matches AT of pure sample when measured under similar experimental conditions) erroneously contains negative intensity values. Negative values in the deconvoluted CID mass spectra indicate inappropriate deconvolution and signify the presence of fragment ions that are common between mixture components;[129,131] hence, it is concluded that deconvolution of [cellotriose + Li]$^+$ is unsuccessful at a collision-energy of 40 V and is shown as a gray IM profile in Figure 2.1a. Furthermore, IM-MS deconvolution of [M_T + Li]$^+$ at 55 V allows for successful separation of [raffinose + Li]$^+$ and [cellotriose + Li]$^+$ profiles. However, the deconvoluted CID mass spectra that *should* correspond to [isomaltotriose + Li]$^+$ similarly contains negative values and is also shown as a gray IM profile in Figure 2.1a.

Although, as discussed above, individual mixture components can be successfully deconvoluted at several suboptimal collision-energies, optimal IM-MS deconvolution for data presented here occurs only at identified collision-energy sweet-spots where all mixture components can be successfully deconvoluted. However, it is probable that collision-energy sweet-spots would not be present for all complex mixtures. In other words, complex

mixtures whose individual components fail to generate sufficiently different CID patterns at a single collision-energy value would likely not have a collision-energy sweet-spot. In the case of complex mixtures that are suboptimally deconvoluted at all measured collision-energies, IM-MS data for individual isomers can still be successfully deconvoluted using the following proposed collision-energy resolved approach that utilizes a combination of two or more CID collision energies. For instance, collision-energy resolved IM-MS deconvolution of $[M_T + Li]^+$ allows for successful deconvolution of IM-MS data for [raffinose + Li]$^+$ at a suboptimal collision-energy of 30 V, [isomaltotriose + Li]$^+$ at a suboptimal collision-energy of 65 V, and [raffinose + Li]$^+$ and [cellotriose + Li]$^+$ at a suboptimal collision-energy of 55 V. Similar to the approach demonstrated by Pagel and coworkers,[126] isomer-specific information (*i.e.*, IM profiles, CID mass spectra, and precursor/fragment ion dissociation energy thresholds) may be obtained for complex mixtures irrespective of the presence or absence of an identifiable single or multiple collision-energy sweet-spot(s).

Figure 2.1b compares the normalized IM profiles of each isomeric trisaccharide-Li adduct at the 45 V collision-energy sweet-spot (Figure 2.1b, colored IM profiles) to the normalized IM profiles of the individually run isomers (Figure 2.1b, offset black IM profiles). IM ATs for each of the deconvoluted isomers at the 45 V collision-energy are within ±0.069 ms (*viz.*, 1 IM scan equals 0.069 ms) of the ATs for the isomerically pure samples (Figure 2.1b) suggesting that IM-MS deconvolution of the ternary mixture of isomeric trisaccharide-Li adducts is optimal when utilizing the experimental conditions shown in Table A.1. Figure 2.2a shows the IM profiles of the ternary mixture of trisaccharide isomers at the 45 V post-IM/CID collision-energy before (black IM profile)

and after (colored IM profiles) IM-MS deconvolution. The IM profile of the overlapped trisaccharide ion isomers (Figure 2.2a, black IM profile) resembles a "Gaussian-like" distribution with tailing at the longer AT shoulder. An initial (incorrect) interpretation of these results may suggest that the black IM profile in Figure 2.2a belongs to a single component or conformer. IM-MS deconvolution of the post-IM/CID MS data, however, correctly identifies the IM profiles for all three components (Figure 2.2a, colored IM profiles). Although all three trisaccharides were mixed in equimolar concentrations, differences in IM peak heights were observed for the three isomers. The observed differences in IM peak heights for the three equimolar isomers are likely due to a combination of competing proton affinities for each isomer during the ionization process[126] and potential fragment ion losses prior to the detection event (*e.g.,* from metastable ion decay in the field-free region of the TOF mass analyzer[230] or charge-transfer reactions); this apparent "detector response"-like phenomena is an effect that we have previously reported on.[131]

By mapping differences in relative ion intensities of post-IM/CID fragment ions (including presence or absence of isomer specific fragments) across the unresolved IM profile, optimal IM-MS deconvolution at identified collision-energy sweet-spots (*i.e.*, 45 V and 50 V for $[M_T + Li]^+$) allows for pure IM profiles (*i.e.*, Figures 2.1 and 2.2a) and associated CID mass spectra (Figure 2.2b) to be constructed for each mixture component. Deconvolution of $[M_T + Li]^+$ at 45 V yields reconstructed CID mass spectra (Figure 2.2b) that match (*i.e.*, $R > 0.75$ for each MS pair) experimentally acquired CID mass spectra of counterpart pure isomers (Figure 2.2c). Similar to the energy-resolved approach proposed by Pagel and coworkers,[126] collision-energy resolved IM-MS deconvolution does not

explicitly require a diagnostic fragment ion to be associated with each unresolved mixture component (such as in the method utilized by Clemmer *et al.*[127]), but rather depends on the presence of detectable changes in relative ion intensities between fragment ions as a function of IM scan number. In other words, optimal IM-MS deconvolution using the proposed collision-energy resolved approach could be accomplished even in the absence of diagnostic fragment ions. For example, subjecting [raffinose + Li]$^+$ to post-IM/CID MS at 45 V (Figure 2.2b) primarily generates three fragment ions which are common to all ternary mixture components: $[Z_1 - H]^+$ at *m/z* 169, $[C_1 + H]^+$ at *m/z* 187, and $[C_2 + H]^+$ at *m/z* 349 (fragment ion assignments and labeling are based on the nomenclature of Domon and Costello[153]). However, the relative fragment ion intensities for each isomeric trisaccharide-Li adduct are sufficiently different to allow successful deconvolution of overlapped IM profiles.

Our findings demonstrate that IM-MS deconvolution of a ternary mixture of isomeric trisaccharide-Li adducts is an energy dependent process that requires IM-MS deconvolution of unresolved post-IM/CID MS data at various collision-energies. In the next section, application of collision-energy resolved analysis for optimal IM-MS deconvolution of a quaternary mixture of hexapeptide isomers is presented.

2.4.2 Collision-energy Resolved Deconvolution of a Quaternary Mixture of Hexapeptide Isomers

To further demonstrate the utility of our approach, a quaternary mixture of isomeric hexapeptides ($[M_P + 2H]^{2+}$ at *m/z* 365) was subjected to post-IM/CID at increasing collision-energies and analyzed using IM-MS deconvolution.

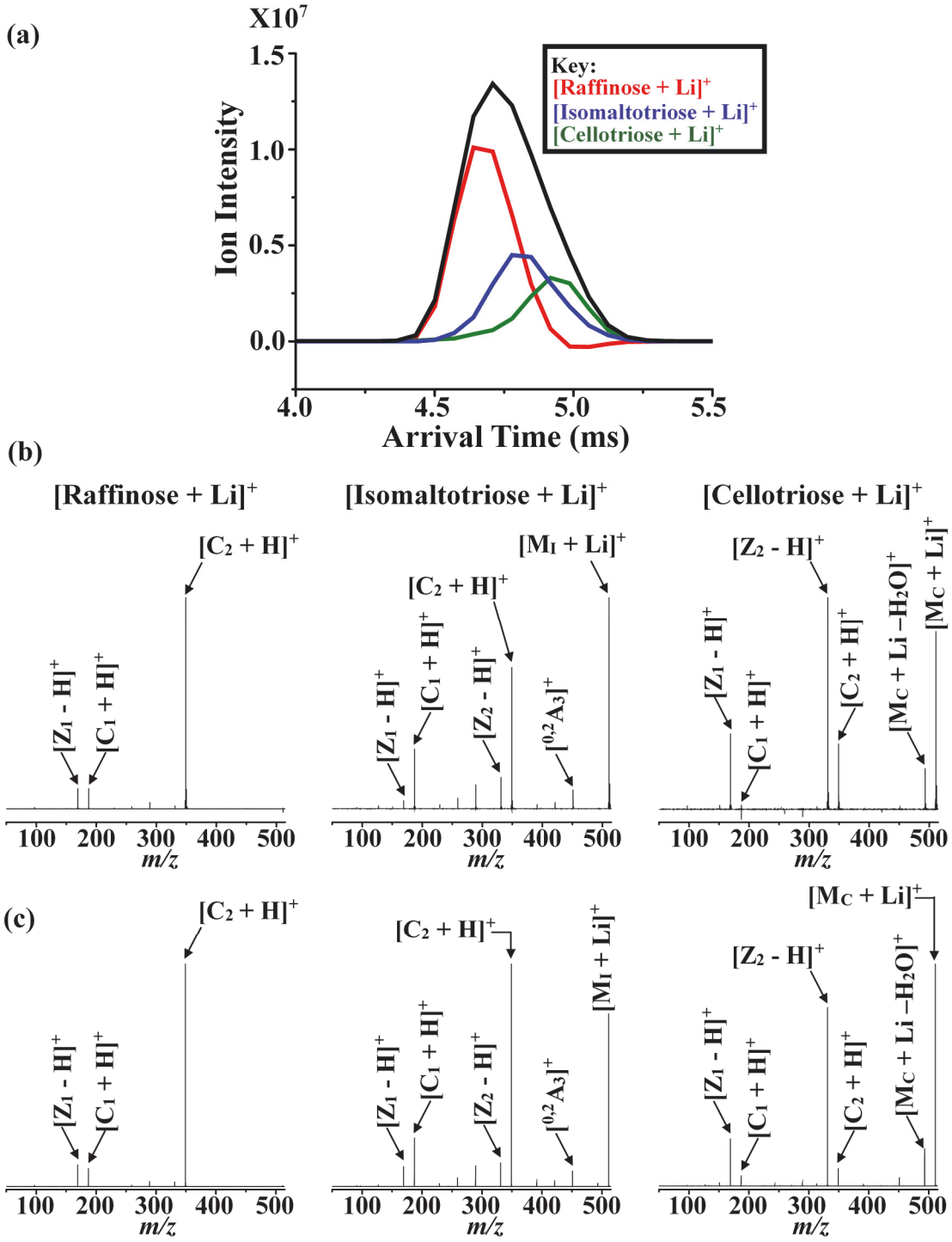

Figure 2.2. Optimal IM-MS deconvolution of a ternary mixture of [raffinose + Li]$^+$, [isomaltotriose + Li]$^+$, and [cellotriose + Li]$^+$ at 45 V collision-energy. (a) Ternary mixture's IM profiles before (black profile) and after (colored profiles) deconvolution. (b) Deconvoluted CID spectra match (c) corresponding CID mass spectra from pure sugar isomer samples

In the previous section we showed that: (1) low collision-energies generated insufficient fragmentation for optimal deconvolution and (2) high collision-energies generated excessive fragmentation that, similarly, could not be utilized to distinguish between all isomers. Prior to collision-energy resolved analysis, an appropriate collision-energy range was selected for the peptide isomer mixture by changing the post-IM collision-energy and subsequently observing the degree of fragmentation in the MS tune window. Visual optimization suggested that $[M_P + 2H]^{2+}$ generated extensive (but not excessive) fragmentation when using collision-energies between ~20 V and ~28 V. Therefore, the quaternary isomer mixture was measured across a narrow range (*i.e.*, 20-28 V) of collision-energies (as compared to the ternary sugar isomer mixture).

Analogous to the ternary mixture, IM-MS deconvolution of post-IM/CID MS data at each collision-energy was classified as "optimal" or "suboptimal", and a single collision-energy sweet-spot of 26 V was identified for the quaternary mixture (Figure 2.3a, four colored profiles). Four different colors of orange (for MGRYGF), pink (for MFRYGG), dark cyan (for MFGRYG), and purple (for FRMYGG) are used to show deconvoluted IM peaks for each hexapeptide isomer, respectively. Similar to Figure 2.1a, the coloring scheme in Figure 2.3a also denotes the maximum number of isomers that can be successfully deconvoluted at each collision-energy voltage. Individual IM profiles that were unsuccessfully deconvoluted were summed and shown as a single, unresolved IM profile (Figure 2.3a, gray profiles). Similar to the ternary mixture, $[M_P + 2H]^{2+}$ could be partially deconvoluted at several suboptimal collision-energies (*i.e.*, 20-24 V and 28 V, Figure 2.3a). For example, IM-MS deconvolution of $[M_P + 2H]^{2+}$ at collision-energies of

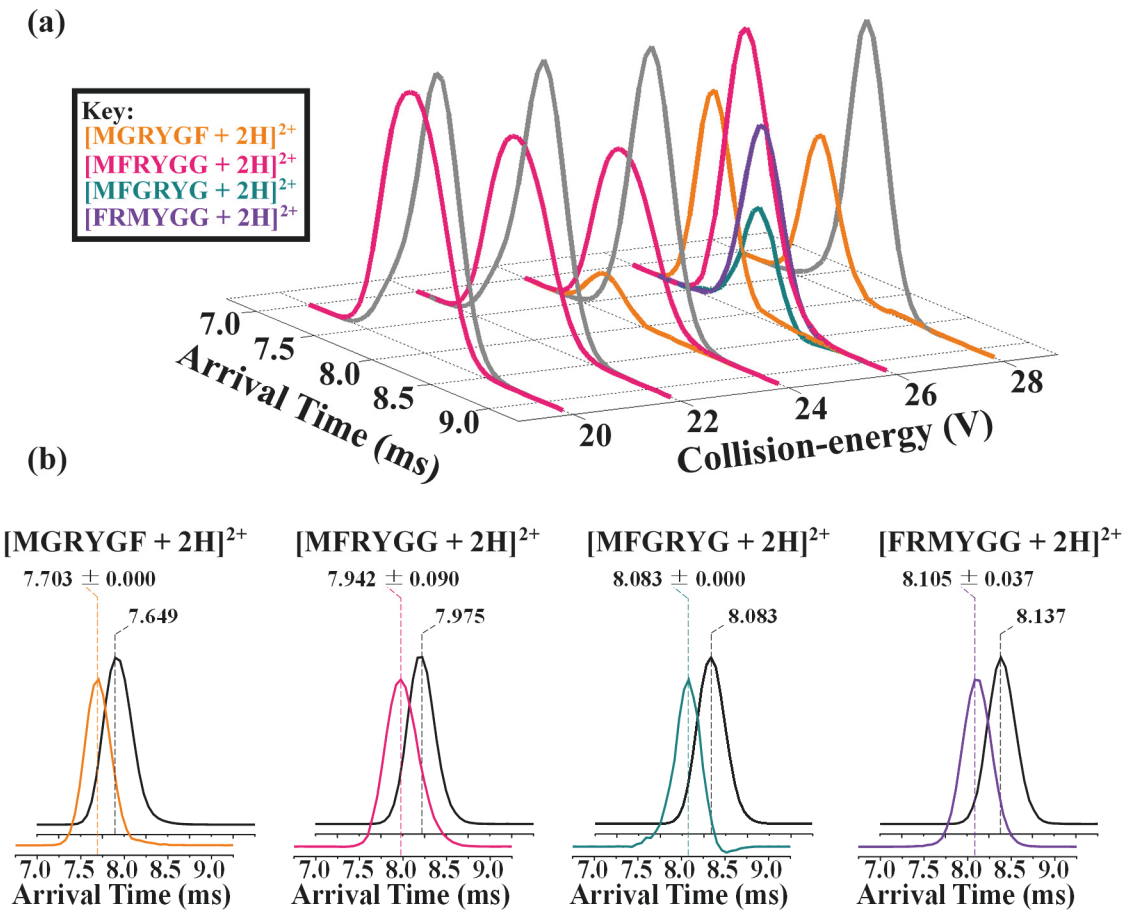

Figure 2.3. (a) Three dimensional plot of arrival time, collision-energy, and ion intensity from collision-energy resolved IM-MS deconvolution of a quaternary mixture of MGRYGF (orange profiles), MFRYGG (pink profiles), MFGRYG (dark cyan profiles), and FRMYGG (purple profiles). IM profiles shown in color and gray denote successful and unsuccessful deconvolution, respectively. (b) IM profiles (shown in color) for $[MGRYGF + 2H]^{2+}$, $[MFRYGG + 2H]^{2+}$, $[MFGRYG + 2H]^{2+}$, and $[FRMYGG + 2H]^{2+}$ from optimal IM-MS deconvolution at a 26 V collision-energy. Black IM profiles denote pure samples measured under identical conditions. Deconvoluted arrival times are shown at the 95% confidence interval (n = 5).

20 V and 22 V allows for extraction of the appropriate AT and correlating CID mass spectrum for only $[MFRYGG + 2H]^{2+}$ while the other three hexapeptide isomers (*i.e.*, $[MGRYGF + 2H]^{2+}$, $[MFGRYG + 2H]^{2+}$ and $[FRMYGG + 2H]^{2+}$) show an overlapped (gray) IM profile. However, at collision-energies of 24 V and 28 V, IM-MS deconvolution of $[M_P + 2H]^{2+}$ successfully separates $[MGRYGF + 2H]^{2+}$ and $[MFRYGG + 2H]^{2+}$ from

the remaining two components. Collision-energies above and below the 26 V collision-energy sweet-spot did not generate sufficient post-IM/CID MS fragmentation for optimal IM-MS deconvolution of $[M_P + 2H]^{2+}$. Specifically, a lack of sufficient fragmentation pattern differences (*i.e.,* unique fragment ions and/or significant difference in fragment ion intensities) between hexapeptide isomers at collision-energies outside of the sweet-spot resulted in suboptimal deconvolution.

In Figure 2.3b, the normalized IM profiles of each hexapeptide isomer at the 26 V collision-energy sweet-spot (Figure 2.3b, colored IM profiles) are compared to the normalized IM profiles of the individually run isomers (Figure 2.3b, offset black IM profiles). For each hexapeptide isomer in $[M_P + 2H]^{2+}$, extracted IM ATs from IM-MS deconvolution at a 26 V collision-energy are within ±0.054 ms (*viz.*, 1 IM scan equals 0.054 ms when using an IMS wave delay of 0.450 ms) of the ATs for the isomerically pure samples (Figure 2.3b, offset black IM profiles) suggesting that IM-MS deconvolution of the quaternary mixture of hexapeptide isomers is optimal under these experimental conditions.

Figure 2.4a shows the IM profiles for the quaternary hexapeptide mixture at the 26 V collision-energy before (black IM profile) and after (colored IM profiles) deconvolution. Similar to the trisaccharide mixture, prior to deconvolution, the four hexapeptide isomers were unresolved and exhibited a Gaussian-like distribution with a slight shoulder at the early AT side of the IM profile (Figure 2.4a, black IM profile). After deconvolution, we were able to construct individual IM profiles for $[MGRYGF + 2H]^{2+}$, $[MFRYGG + 2H]^{2+}$, $[MFGRYG + 2H]^{2+}$, and $[FRMYGG + 2H]^{2+}$ (Figure 2.4a, colored IM profiles). Moreover, IM-MS deconvolution of $[M_P + 2H]^{2+}$ at 26 V generated CID mass spectra for

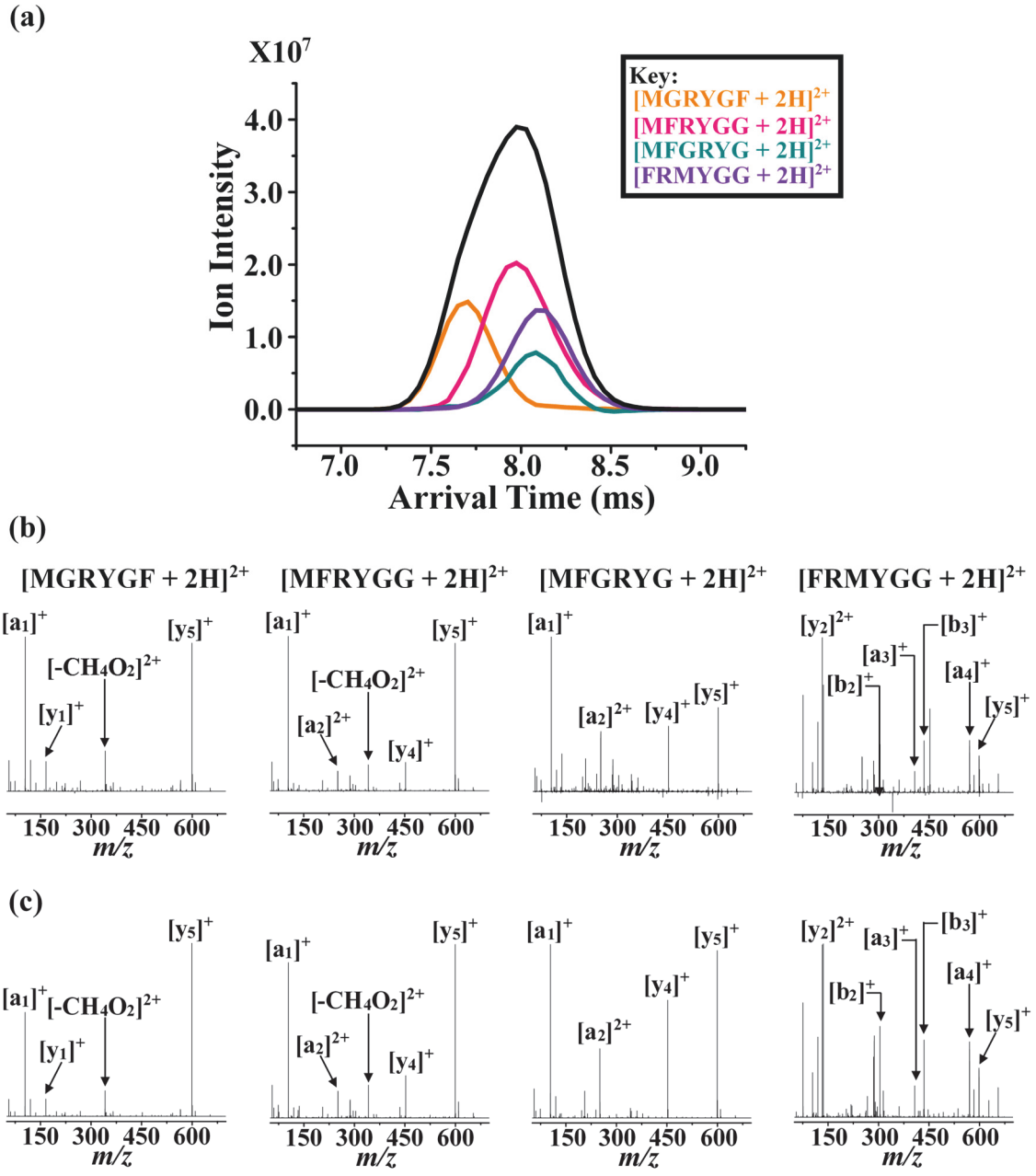

Figure 2.4. Optimal IM-MS deconvolution of a quaternary mixture of MGRYGF, MFRYGG, MFGRYG, and FRMYGG at 26 V collision-energy. (a) Quaternary mixture's IM profiles before (black profile) and after deconvolution (colored profiles). (b) Deconvoluted CID mass spectra match (c) corresponding CID mass spectra from pure peptide isomer samples.

$[MGRYGF + 2H]^{2+}$, $[MFRYGG + 2H]^{2+}$, $[MFGRYG + 2H]^{2+}$, and $[FRMYGG + 2H]^{2+}$ (Figure 2.4b) which matched (*i.e.*, $R > 0.75$ for each MS pair) those of isomerically pure samples (Figure 2.4c). The collision-energy sweet-spots observed for the $[M_T + Li]^+$ mixture (*i.e.*, 45 V and 50 V, Figure 2.1a) are higher than the collision-energy sweet-spot of 26 V observed for the $[M_P + 2H]^{2+}$ mixture (Figure 2.3a). Differences in collision-energy sweet-spots are likely due to several factors. First, the trisaccharide isomers and hexapeptide isomers have different masses, molecular compositions, and bond types (*e.g.,* glycosidic bonds in saccharides versus amide bonds in the peptides), which influence the bond-dissociation energies of each molecular class.[231-233] Further, the *m/z*-isolated trisaccharide isomers were singly-charged, whereas the *m/z*-isolated hexapeptide isomers were doubly-charged. The electric potential energy (U) "felt" by a point charge placed between two electrodes is equal to the magnitude of the point charge (q) times the applied electric potential difference (V) divided by the distance (d) between the two electrodes:

$$U = \frac{qV}{d} \qquad \text{Equation 2.2}$$

According to Equation 2.2, at any particular collision-energy (*i.e.*, applied electric potential difference between the IM cell exit and entrance to the transfer cell), doubly-charged hexapeptide isomers should "experience" approximately twice the force as the singly-charged trisaccharide isomers (assuming, for the moment, that the only difference between the two species is their charge states). Our experimental data indicates that the collision-energy sweet-spot for the trisaccharide mixture (*i.e.,* 45 V and 50 V for singly-charged components) is a factor of ~1.7 to ~1.9 times that of the hexapeptide mixture (*i.e.,* 26 V for doubly-charged species); as expected, these numbers suggest that the major factor affecting sweet-spot collision-energies is the precursor ions' charge state. However,

differences between the experimental (*i.e.,* ~1.7x to ~1.9x) and theoretical (*i.e.,* 2x) collision-energies (for singly-charged compared to doubly-charges species), implies that factors beyond charge-states must also be considered when determining the specific collision-energy(ies) required for optimal deconvolution. Although these simple assumptions and calculations offer some explanation for the apparent differences in collision-energy sweet-spots between $[M_T + Li]^+$ and $[M_P + 2H]^{2+}$, additional experimental and theoretical investigations (*e.g.,* kinetic investigations of fragment ion formation/depletion) are necessary to fully characterize the source(s) of these differences, but are outside the scope of the current manuscript. For the present work, however, it is important to note that the collision-energy sweet-spot(s) for optimal deconvolution of isomeric mixtures is/are not constant, but rather species-specific.

2.5 Conclusion

In our previous communications, chemometric deconvolution of post-IM/CID MS data was limited to the analysis of binary sample mixtures (*i.e.*, containing two components) at single collision-energies.[129,131,133,223,224] Here, we extend those results to include IM-MS deconvolution of three and four component mixtures at multiple collision-energies. By systematically deconvoluting IM unresolved post-IM/CID MS data at multiple collision-energies, we demonstrated that IM-MS deconvolution of IM overlapping mixtures is a collision-energy dependent process. Moreover, we were able to identify collision-energy sweet-spots for both sugar and hexapeptide mixtures that yielded successfully deconvoluted IM profiles for IM overlapped species. Estimations based on the experimental IM resolving power for the two most overlapped isomers analyzed (*i.e.,* MFGRYG and FRMYGG in Figures 2.3 and 2.4) suggest that the IM resolving power of

the Synapt G2-S would have to be increased by roughly six and a half times to successfully IM resolve these two isomers at their respective peak half-heights. Although some newer IM instruments may be capable of surpassing this IM resolving power range, the post-acquisition data analysis approach presented in this paper could still be utilized to overcome IM-resolving power limitations on newer instruments. In other words, energy-resolved IM deconvolution can be used to deconvolute partially resolved IM peaks in any IM-MS capable of post-IM fragmentation, regardless of the inherent instrumental IM resolving power limitations.

According to the criteria established herein, IM-MS deconvolution of two mixtures was suboptimal (*i.e.*, at least one isomer could not be successfully deconvoluted) at collision-energies above and below the identified sweet-spots. Below the collision-energy sweet-spot(s), suboptimal deconvolution is likely due to an insufficient abundance of unique CID fragment ions. Conversely, suboptimal deconvolution above the collision-energy sweet-spot(s) are likely caused by insufficient CID differences resulting from a high abundance of fragment ions that are common to all isomers within the mixture. Additionally, it was demonstrated that isomer-specific information can be obtained by systematically varying the applied collision-energy and deconvoluting post-IM/CID MS data, even in the absence of collision-energy sweet-spots. Results from analysis of IM-unresolved sugar (Figures 2.1 and 2.2) and peptide (Figures 2.3 and 2.4) isomers suggest that IM-MS deconvolution of isomers and conformers in unknown mixtures should be examined at different ion fragmentation energies to improve the probability of successful sample characterization.

A limitation of the current technique is the use of long acquisition times (*i.e.,* 5 to 45 minutes) to collect sufficient ion intensities when differentiating between similarly fragmenting molecules. The time for data acquisition must increase as the number of unresolved components increases because the total relative ion abundance is a linear combination of all possible overlapping isomers at a given *m/z* value. The original mass spectral data are apportioned between all mixture components during the deconvolution process resulting in decreased signal-to-noise ratios for each deconvoluted *m/z* value. In other words, because AIMD assigns each component's relative contribution at each *m/z* data point across the IM profile, the original convoluted CID mass spectrum is not equivalently distributed to all sample components. Therefore, although one component in a mixture may require short acquisition times for successful deconvolution, it may take substantially longer acquisition times to resolve other components that exhibit high degrees of similarities between their respective product ion mass spectra. To date, and without modifying the experimental conditions or post-acquisition deconvolution methods, we have successfully deconvoluted the two most closely eluting isomers (*i.e.*, MFGRYG and FRMYGG in Figures 2.3 and 2.4) using a 1-minute acquisition time. Future work will focus on shortening the time necessary for data acquisition thereby making IM deconvolution process compatible with HPLC elution (and shorter) time scales.

Even though deconvolution was accomplished for equimolar analyte ratios, it is worth noting that the extent of CID fragmentation is primarily dominated by the total number of collisions in the collision cell (*i.e.*, total pressure in the trap cell) and the amount of applied kinetic energy (*i.e.*, collision-energy) "felt" by individual gas phase ions and hence the identified suitable collision energies should not change as a function of analyte

concentrations. Within the MS/MS TOF detection limits of ~ 0.1 mM[234] to sub-femtomoles,[235] changes in trap cell pressure and collision-energy deposition caused by variations in sample concentrations are negligible when considering the operating pressures and collision-energies used in this study (*i.e.*, 1.75 x 10^{-5} bar of argon and 20 to 80 V, respectively). Because deconvolution requires detection of fragmentation differences, it is improbable that a change in isomer concentration would alter the identified sweet-spot collision energy. The dynamic range of our approach, as it relates to concentration differences between sample components, has not yet been totally characterized. To confirm our predictions, additional experiments were performed by varying isomaltotriose concentrations between 50 μM to 10 nM (when keeping the other two trisaccharides at micromolar range concentrations) and equivalent deconvolution results were obtained. However, these experiments were limited and the dynamic range will be fully investigated in a forthcoming manuscript.

CHAPTER THREE

Broadband Ion Mobility Deconvolution for Rapid Analysis of Complex Mixtures

This chapter is accepted for publication in *Analyst* as: Pettit, M. E., Brantley, M. R., Donnarumma, F., Murray, K. K., Solouki, T., Broadband Ion Mobility Deconvolution for Rapid Analysis of Complex Mixtures.

3.1 Abstract

High resolving power ion mobility (IM) allows for accurate characterization of complex mixtures in high-throughput IM mass spectrometry (IM-MS) experiments. We previously demonstrated that pure component IM-MS data can be extracted from IM unresolved post-IM/collision-induced dissociation (CID) MS data using an Automated Ion Mobility Deconvolution (AIMD) software [*J. Am. Soc. Mass Spectrom.,* **2014,** 25, 1810-1819]. In our previous reports, we utilized a quadrupole ion filter for *m/z*-isolation of IM unresolved monoisotopic species prior to post-IM/CID MS. Here, we utilize a broadband IM-MS deconvolution strategy to remove the *m/z*-isolation requirement for successful deconvolution of IM unresolved peaks. Broadband data collection has throughput and multiplexing advantages; hence, elimination of the ion isolation step reduces experimental run times and thus expands the applicability of AIMD to high-throughput bottom-up proteomics. We demonstrate broadband IM-MS deconvolution of two separate and unrelated pairs of IM unresolved isomers (*viz.*, a pair of isomeric hexapeptides and a pair of isomeric trisaccharides) in a simulated complex mixture. Moreover, we show that broadband IM-MS deconvolution improves high-throughput bottom-up characterization of a proteolytic digest of rat brain tissue. To our knowledge, this manuscript is the first to

report successful deconvolution of pure component IM and MS data from an IM-assisted data-independent analysis (DIA) or HDMS^E dataset.

3.2 Introduction

Mass spectrometry (MS) is utilized in a wide variety of omics fields (*e.g.*, lipidomics,[236] petroleomics,[237] proteomics,[238] metabolomics,[239] and glycomics[240]) to study complex sample mixtures. Frequently, to distinguish between isobaric species present in complex samples and improve data quality, high-resolution MS instruments such as Fourier transform ion cyclotron resonance (FT-ICR) MS and Orbitrap MS are used.[241] Although specialized MS analysis techniques, for example, ion-molecule reactions,[69] can be used to distinguish isomers, differentiating them is difficult to address by MS alone. Hence, high-throughput MS analysis of complex mixtures containing isomeric and isobaric species often requires some form of analyte-separation prior to MS analysis.

High performance liquid chromatography (HPLC)[121] and gas chromatography (GC)[119] can be readily interfaced with mass spectrometers for multidimensional analyses; however, these chromatographic techniques are occasionally insufficient to resolve isobaric or isomeric species and thus tandem use of additional separation systems is an attractive alternative. For example, ion mobility (IM) has seen recent growth for complex sample separations[85,87,89,90,116,117,124-128,131,133,213,215,216,219,220,223,226,242,243] and has been combined with other chromatographic techniques for multidimensional separations such as LC-IM-MS[243,244] and GC-IM-MS.[242] In IM experiments, ions are separated based on their collisional cross sections (CCSs) as they move through an (typically) inert gas environment.[100,245]

Despite the recent improvements in MS instrumentation[118,241] and separation technologies,[119-121] co-elution continues to impede adequate characterization of complex mixtures in areas such as petroleomics[246] and biological sample analyses.[247-249] Previously, methods such as energy-resolved IM-MS[126] and species-specific fragment identification[127] have been used to address IM convolution issues. In 2012, we utilized a chemometric data analysis technique that allows extraction of pure component IM profiles and their associated collision-induced dissociation (CID) mass spectra from convoluted post-IM/CID MS data.[129] In 2014, we automated the IM-MS deconvolution approach by developing the Automated Ion Mobility Deconvolution (AIMD) software[131] and subsequently used AIMD to investigate several IM unresolved systems.[87,132-134,250] Although the acronym "AIMD" is also utilized to mean "ab initio molecular dynamics",[251] here it strictly refers to "Automated Ion Mobility Deconvolution". To date, pure component IM-MS deconvolution techniques have not been applied to MS-based proteomic workflows.

MS-based proteomic workflows are typically classified as either top-down[164,175,178] analysis of intact proteins or bottom-up[179,180,186] characterization of proteolytic digests. Top-down approaches can yield in-depth primary structure information, including site-specific mutations and post-translational modifications[179] that are often lost during chemical and enzymatic proteolysis.[183] However, because peptides from proteolytic digests are typically easier to solubilize for LC separation and more readily analyzed with MS than intact large proteins, bottom-up approaches are more commonly utilized in high-throughput MS-based proteomics.[186]

Bottom-up proteomic workflows typically utilize HPLC for peptide separation prior to introduction into a mass spectrometer. Gas-phase ion fragmentations, using CID[139-141] or other ion activation methods,[187] such as electron capture dissociation (ECD)[148] or electron transfer dissociation (ETD),[150] are employed to generate product ions that are subsequently correlated to their corresponding precursor ions. The resulting list of precursor-product ion assignments can be searched manually or automatically queried[189-192] through protein databases to identify amino acid sequences for elucidation of protein primary structures.

Peptide fragmentations and subsequent precursor-product ion assignments are typically achieved using an either data-dependent acquisition (DDA) or data-independent acquisition (DIA) strategy. DDA methods[252] utilize sequential ion isolation for fragmenting specific ions of interest. In contrast, DIA methods[196,199,204,206] do not require sequential isolations of single ionic species and can be implemented by alternating the CID activation energies between low and high energy regimes for all ions. The former produces minimal ion fragmentation for generation of precursor ion data whereas the latter yields increased ion fragmentation for generation of product ion data. Precursor-product ion assignments are more difficult to generate in DIA compared to DDA and require time alignment[200,207,253] by accurate mass retention time (AMRT) correlations[194] or by ion mobility drift-time alignments[209] as is done in HDMS^E data processing. However, DIA offers multiplexing (similar to Fellgett's advantage[254]) and throughput (similar to Jacquinot's advantage[255]) benefits for high-throughput proteomics. Alternating the energy regime in a DIA approach for simultaneous fragmentation of all ions is markedly faster than scanning through individual precursor ions as is done in DDA. In addition, elimination

of the ion isolation step in DIA yields higher sensitivity by avoiding unnecessary ion losses and improving efficient use of instrumental duty cycle.[206]

The benefits in throughput and sensitivity for DIA[206,256] are often outweighed by the difficulty of establishing reliable precursor-product ion assignments using AMRT or drift-time alignment. Specifically, IM co-elution limits accurate assignment of drift times in complex mixtures.[87,126,127,129,131,133,223,224] Although custom methods and instrument modifications have resulted in increased IM resolving powers[98,115-118,215-217,219-222] (defined as peak arrival time (AT)/$\Delta AT_{50\%}$ or CCS/$\Delta CCS_{50\%}$),[99,122,123] these improvements have not been widely applied to proteomic workflows. For example, several groups have proposed experimental strategies to probe for the presence of unresolved species in IM-MS.[124-128] Chemometric data processing has also been applied for untargeted precursor-product ion assignment; however, this approach does not allow IM-MS deconvolution.[125] These strategies do not allow for extraction of pure component IM profiles and/or MS data from co-eluting species,[124-128] and thus have not been used to enhance precursor-product ion assignment in current proteomic workflows.

We previously demonstrated that deconvolution of IM unresolved post-IM/CID MS data using AIMD allowed for rapid generation of both pure component IM profiles and CID mass spectra of co-eluting components.[131] These deconvoluted IM profiles and associated CID mass spectra can potentially be used to establish precursor-product ion assignments from unresolved IM-MS data in IM-enhanced DIA (*e.g.*, $HDMS^E$) bottom-up proteomics experiments. However, to date, all reported AIMD results have used an *m/z*-isolation step prior to post-IM/CID analysis; this single *m/z*-isolation step precludes the use of AIMD in MS-based proteomics. Our IM-MS deconvolution workflows are not

compatible with IM-enhanced DDA (*e.g.*, HD-DDA) approaches that utilize pre-IM/CID.[257] On the other hand, HDMS^E approaches employ broadband post-IM/CID.[209] Consequently, broadband IM-MS deconvolution is distinct from previous IM deconvolution approaches as it provides an exclusive avenue for combining AIMD with MS-based bottom-up proteomics.

In this manuscript, we report results from a modified AIMD approach that avoids *m/z*-isolation and yields broadband ion fragmentation. Moreover, we demonstrate the suitability of this new and rapid broadband approach for improved HDMS^E data processing capabilities. Prior to this report, precursor ions that were unresolved in the LC and IM dimensions could not be correlated to their respective product ions using currently available HDMS^E data processing algorithms. Here, we report the use of broadband IM-MS deconvolution for generating precursor-product ion correlations from UPLC-IM-MS unresolved HDMS^E data.

In direct infusion IM-MS, HDMS^E can be emulated with separate low and high collision-energy experiments. As examples of broadband ion fragmentation and IM peak deconvolution, we show extracted pure component IM profiles and mass spectra for two IM unresolved binary isomer mixtures: a hexapeptide mixture containing MGRYGF and FRMYGG peptide isomers and a trisaccharide mixture containing D-(+)-raffinose and D-(+)-isomaltotriose trisaccharide isomers. To confirm the validity of AIMD analyses in broadband mode, we compare deconvolution results to validation sets comprising IM-MS data of corresponding single component solutions. Additionally, we evaluate the efficacy of broadband IM-MS deconvolution in the presence of high-intensity background ions by deconvoluting IM-MS data of a simulated complex mixture that contains both

abovementioned binary isomer mixtures and polypropylene glycol species. Furthermore, we apply broadband IM-MS deconvolution to HDMS^E analysis of a proteolytic digest of rat brain tissue.

3.3 Experimental

3.3.1 Preparation of Simulated Complex Mixtures

Hexapeptide isomers, MGRYGF and FRMYGG, were synthesized by Peptide 2.0, Inc. (Chantilly, VA, USA). D-(+)-raffinose, D-(+)-isomaltotriose, and lithium chloride (LiCl) were purchased from Sigma-Aldrich (St. Louis, MO, USA). A mixture of polypropylene glycol (PPG) 425 and PPG 1000 was purchased from Agilent Technologies (Santa Clara, CA, USA). Optima grade methanol and acetic acid were purchased from Fisher-Scientific (Waltham, MA, USA). Water, with an overall ionic concentration of < 0.1 ppb and a resistivity of ~18.2 MΩ·cm at 25 °C, was purified in-house using a Direct-Q 3 UV water purification system (EMD Millipore Corporation, Billerica, MA, USA). All commercial samples and chemical solvents were used as received and without further purification.

All analytes used in sample solutions were initially prepared as stock solutions in a methanol:water solvent (1:1, v/v) with 0.1% acetic acid. Analyte concentrations for single component samples (*i.e.*, pure isomer solutions used as validation sets) were optimized such that comparable ion counts were measured for all monitored precursor ions. Pure MGRYGF and pure FRMYGG hexapeptide isomers were individually prepared as ~1.7 μM solutions; pure D-(+)-raffinose and pure D-(+)-isomaltotriose trisaccharide isomers were each prepared as ~3.3 μM solutions and spiked with 15:1 excess LiCl to ensure the

formation of Li-adducts. The binary hexapeptide mixture contained ~1.7 μM each of MGRYGF and FRMYGG isomers (~3.4 μM total peptide concentration), and the binary trisaccharide mixture contained ~3.3 μM each of D-(+)-raffinose and D-(+)-isomaltotriose isomers (~6.6 μM total trisaccharide concentration) with an excess (~15:1 per isomer) of LiCl. The simulated complex sample solution contained ~1.7 μM MGRYGF, ~1.7 μM FRMYGG, ~3.3 μM D-(+)-raffinose, ~3.3 μM D-(+)-isomaltotriose, ~0.2 mM LiCl and ~0.3 μM PPG. It was experimentally determined (data not shown) that the formation of Li-adducts in the complex mixture required increasing the LiCl to trisaccharide isomer ratio from ~15:1 (as used for the pure trisaccharide solutions) to ~60:1 per isomer, presumably due to the formation of PPG and peptide Li-adducts.

3.4 Instrumentation

3.4.1 Direct Infusion IM-MS Data Acquisition

All experiments were performed in positive-ion mode electrospray ionization[258] (ESI+) using a Synapt G2-S HDMS system (Waters, Milford, MA, USA) set to resolution mode (*i.e.*, V mode). Argon (Ar) was used in the trap and transfer cells as buffer and collision gases, respectively. Helium (He) gas was used for collisional cooling prior to IM, and nitrogen (N_2) was used as the IM drift gas. "Generic" ESI conditions and default instrument parameters were used for all experiments (*viz.*, Table B.1; reported pressures are direct measurement readouts without correcting for geometry[229] or sensitivity[228] factors) except the transfer collision-energies (*i.e.*, electric potential differences applied between the exit of the IM cell and entrance of the transfer cell) used during the post-IM CID experiments. Sample introduction was performed *via* direct infusion using a Standard

Infusion 11 Plus Syringe Pump (Harvard Apparatus, Holliston, MA, USA) at a sample flow rate of 0.5 μL/min. The pre-IM quadrupole was operated in transmission mode (rf-only, *i.e.*, no *m/z*-isolation in the quadrupole assembly prior to IM). Broadband data were collected for all detected ions in the *m/z* range of 50-1500. After IM separation, ions were fragmented *via* CID in the transfer cell (*i.e.*, post-IM/CID). The Synapt G2-S is configured such that HDMS^E data collection only operates in conjunction with LC separation and is not compatible with direct infusion sample introduction. Thus, HDMS^E was emulated for direct infusion IM-MS experiments by acquiring separate datasets using low (*i.e.*, minimal post-IM/CID) and high transfer collision-energy (*i.e.*, increased post-IM/CID) experiments. Previously optimized[87] transfer collision-energies of 26 V and 45 V were used to induce post-IM/CID for the binary hexapeptide mixture and binary trisaccharide mixture, respectively. Data for high-energy post-IM/CID of the simulated complex sample solution were acquired at a 35 V transfer collision-energy. The total ion accumulation time for all experiments was 13.8 ms (corresponding to a maximum IM drift time of 13.8 ms). Data acquisition times for direct infusion IM-MS experiments were 1 minute (Figures 3.1-3.7 and Table 3.1) or 2 seconds (Table 3.1). All direct infusion IM-MS experiments reported here were performed in triplicate to confirm reproducibility of broadband deconvolution using AIMD.

3.4.2 UPLC-HDMS^E of Rat Brain Tissue Samples

UPLC-HDMS^E data acquisition was used to collect, in parallel, broadband UPLC-IM-MS and UPLC-IM-MS/MS data of a rat brain tissue digest. Experimental details for biological sample preparation,[259] UPLC-HDMS^E data acquisition, data processing, and data searching against a UniprotKB/Swiss-Prot database[260] are provided in the

Supplementary Information. Briefly, a rat brain tissue digest was measured using both (i) 60-min. and (ii) 15-min. UPLC gradients of 5 to ~45% mobile phase B (acetonitrile with 0.1% formic acid).

3.5 Data Analysis

Raw IM-MS data were analyzed using MassLynx (Ver. 4.1; Waters). Unresolved high collision-energy IM-MS data (used for deconvolution) were the average of a 1 min. acquisition time (or 2 s for comparisons presented in Table 3.1) which provided signal-to-noise ratios > 3 for all reported ions in the AIMD deconvoluted spectra; 30 s acquisition times were adequate for generating validation datasets for all pure component samples. Data preprocessing and AIMD analysis for IM-MS data deconvolutions were performed as previously described[131] with the exception of data-notching for isolation of individual IM AT regions. The data-notching windows were centered on the mobiligraphic apexes (from low collision-energy experiments) and set to 200% of the IM peak widths at base to accommodate for the expected IM shifts[125,134] between low and high collision-energy post-IM/CID experiments; peak widths were approximated from low collision-energy experiments as four times the standard deviation (4σ) of the Gaussian-like IM drift distribution of interest. Analysis of a notched dataset improved the efficiency of AIMD by reducing data sizes of both the *m/z* and mobility axes, thus reducing data matrix build times.[131] For each IM deconvolution using AIMD, the number of components (*i.e.*, presumed convoluted peaks) and offset values[131] were manually optimized to minimize negative values in the deconvoluted data[129] and to maximize the degree of spectral matching[87] between the deconvoluted and pure post-IM/CID mass spectra. Although the numbers of convolved components were manually optimized for the deconvolutions

reported herein, the Malinowski's factor indicator function[261] (previously integrated with AIMD[131]) can be used for assigning the number of possible chemical "components" of post-IM/CID MS data matrices; the maximum number of possible components is limited to the number of IM bins input to AIMD. As previously described, the spectral matching *R*-values can range from 0 for no correlation between the pure and deconvoluted mass spectra to 1 for perfect match between the pure and deconvoluted mass spectra.[87]

Deconvolution of the isomers' IM profiles and their corresponding post-IM/CID mass spectra was classified as successful if: (1) deconvoluted data had no negative values more than 15% of the corresponding base peak intensity, (2) the deconvoluted IM AT peak maximum was within 1 IM bin (69 μs) of the corresponding pure sample's IM AT peak maximum when individually measured under identical experimental settings, and (3) *R*-values for deconvoluted isomers were 0.70 or higher. For the simulated complex mixture, experimental *R*-values and IM ATs (IM peak maxima) for each deconvoluted isomer are reported in Table 3.1. Please note that AIMD successfully regenerates the IM profile and post-IM/CID spectrum of single component IM peaks that are solved to a single component. As expected, AIMD yields non-real IM profiles and mass spectra when single component IM peaks are deconvoluted to two or more components (see Figure B.2).

In post-IM/CID, the precursor ion is fragmented after traversing the IM cell, thus the high collision-energy IM profile of a precursor ion cannot be directly extracted. However, drift time alignment between precursor-product ion pairs can be performed in post-IM/CID experiments. Therefore, the selected IM (SIM) profile of a fragmented precursor ion species can be indirectly extracted from post-IM/CID experiments by summing the IM data of corresponding post-IM/CID product ions. For example, accurate

SIM profiles for each pure isomer were generated by summing the IM data of the 10 most abundant product ions (rather than using a single ion) from the corresponding pure post-IM/CID MS data.

Please note that AIMD does not utilize curve fitting algorithms to generate peak shapes of deconvoluted IM profiles.[131] As previously described,[132] the 69 μs sampling interval used for collecting IM data is insufficient for accurately assigning IM ATs (*i.e.*, peak centroids). Therefore, cubic spline interpolation was used on AIMD output (deconvoluted IM profiles) and raw data (pure SIM profiles) for more accurate comparisons of deconvoluted and pure IM ATs.

The 60-minute and 15-minute UPLC-HDMS^E datasets were processed and searched using ProteinLynx Global Server (PLGS Ver. 2.5.2; Waters). Because pure stock solutions of rat brain tissue digests do not exist for use as validation sets, the 60-minute UPLC-HDMS^E run was used to generate a well resolved three-dimensional dataset. IM-MS unresolved ions were found by cross-referencing PLGS results from the 60-minute UPLC-HDMS^E validation dataset with the 15-minute UPLC-HDMS^E dataset. We hypothesized that peptides detected by PLGS from the 60-minute dataset, but absent from the 15-minute dataset, could correspond to precursor ions that were IM-MS unresolved. Our experimental findings confirmed our hypothesis, and we were able to identify and deconvolute IM profiles and post-IM/CID mass spectra for two IM-MS unresolved peptides present in the 15-minute UPLC-HDMS^E run. Deconvolution of IM-MS unresolved species in the 15-minute dataset was validated using results from PLGS processing of the 60-minute dataset. Please note that database searching of IM-MS deconvoluted data, using our current proteomics data processing workflow, would not be

impacted or hindered by the presence of negative values in AIMD output. The Apex3D algorithm employed by PLGS for precursor and product ion detections (during HDMS^E data processing) imposes minimum intensity thresholds of >1 count. Therefore, only positive values are considered by Apex3D when determining the LC, IM, and MS peak properties of ions. In cases where negative values could adversely impact proteomics data processing and databank searching, non-negativity constraints could be utilized.[262]

3.6 Results and Discussion

To demonstrate the advantages of broadband IM-MS deconvolution, we performed three sets of experiments. Firstly, we performed broadband IM-MS deconvolutions at optimized collision-energies[87] for two separate binary mixtures of IM unresolved compounds: (i) MGRYGF and FRMYGG hexapeptide isomers and (ii) D-(+)-raffinose and D-(+)-isomaltotriose trisaccharide isomers. Secondly, we performed broadband IM-MS deconvolution for a simulated complex mixture containing the abovementioned peptide and sugar isomer mixtures in the presence of high-intensity background PPG species. In two separate experiments, IM-MS deconvolutions of this simulated complex mixture (containing hexapeptide and trisaccharide isomers as well as the PPG background ions) were performed using data acquisition times of (a) 1 minute and (b) 2 seconds. Isomerically pure post-IM/CID MS data (*i.e.*, single component data) of each species were used to validate all direct infusion broadband IM-MS deconvolution results presented herein. Thirdly, we utilized IM-MS broadband deconvolution to demonstrate its advantage for analyzing high-throughput bottom-up HDMS^E proteomics data from a rat brain tissue sample.

3.6.1 Broadband IM-MS Deconvolution of Binary Isomer Mixtures

As an initial demonstration of broadband IM-MS deconvolution, low and high collision-energy IM-MS data were collected for a binary hexapeptide isomer mixture. The low collision-energy datasets contained IM-MS information for the intact precursor ions. The high collision-energy datasets contained product ion information and were used for IM-MS deconvolution. Broadband IM-MS deconvolution was validated by comparing each isomer's deconvoluted IM-MS data to its isomerically pure IM-MS data according to the three criteria outlined in the Data Analysis section.

At a low collision-energy of 4 V, both pure $[MGRYGF + 2H]^{2+}$ and pure $[FRMYGG + 2H]^{2+}$ had an IM AT of 2.56 ms (Figure B.1a). Based on alkali metal adduct formation under identical experimental settings, it was apparent that FRMYGG had more intense sodium and potassium adduct peaks than MGRYGF. Additionally, ion fragmentation was observed for the hexapeptide isomers despite using only a 4 V transfer collision-energy. Namely, the $[y_5]^+$ fragment of MGRYGF and the $[b_2]^+$, $[b_3]^+$, $[b_4]^+$, and $[b_5]^+$ fragments of FRMYGG were unintentionally generated prior to the IM cell *via* in-source CID and/or other pre-IM/CID and metastable decay events.[230] Thus, in addition to having a mobiligraphic apex at 2.56 ms, the mobiligrams of pure $[MGRYGF + 2H]^{2+}$ (Figure B.1a) and pure $[FRMYGG + 2H]^{2+}$ (Figure B.1c) showed several other IM peaks (at later ATs) corresponding to singly-charged fragment ions from pre-IM dissociation events. For both hexapeptide isomers, detailed discussions of unintentional adduct formation and pre-IM dissociation fragments, including their IM ATs and fragment identities, are provided in the Supplementary Information.

Figure 3.1 shows the convoluted broadband IM-MS data of the binary hexapeptide mixture (*i.e.*, containing isomers MGRYGF and FRMYGG) prior to broadband deconvolution. Representative low and high collision-energy mobiligrams of the binary hexapeptide mixture are shown in Figures 3.1a and 3.1c. The highlighted regions in Figures 3.1a and 3.1c denote the data-notching windows from IM AT of 2.08 ms to 3.18 ms and correspond to the regions of interest containing IM unresolved hexapeptide isomers. The extracted mass spectrum (XMS) corresponding to the highlighted IM region in Figure 3.1a (or Figure 3.1c) is shown in Figure 3.1b (or Figure 3.1d).

The mobiligraphic apex at 2.56 ms in Figure 3.1a corresponds to the precursor ion species at *m/z* 365 in Figure 3.1b. Additional IM peak features shown in Figure 3.1a, for example the IM peaks at 3.05 ms, 3.88 ms, 4.50 ms, 4.85 ms, 5.47 ms, 6.23 ms, and 6.86 ms, are the result of in-source fragmentation and other pre-IM/CID and metastable decay from either of the two isomeric hexapeptides (further discussions on fragment ion identities are available in Supplementary Information).

In Figure 3.1b, the base peak at *m/z* 365 corresponds to a combination of the doubly-charged hexapeptide precursor ions $[MGRYGF + 2H]^{2+}$ and $[FRMYGG + 2H]^{2+}$. Because the success of AIMD depends on the presence of detectable differences in post-IM/CID mass spectra as a function of IM bin number,[87] low collision-energy IM-MS data (*e.g.*, as for the binary hexapeptide mixture) is not always suitable for IM peak deconvolution. However, as discussed below, high collision-energy IM-MS experiments can provide additional fragment ions for IM peak deconvolution.

Because ion fragmentation from post-IM/CID occurs after the ions pass through the IM drift tube, the high collision-energy mobiligram of the binary hexapeptide mixture at 26 V in Figure 3.1c has a similar shape to the low collision-energy mobiligram at 4 V in

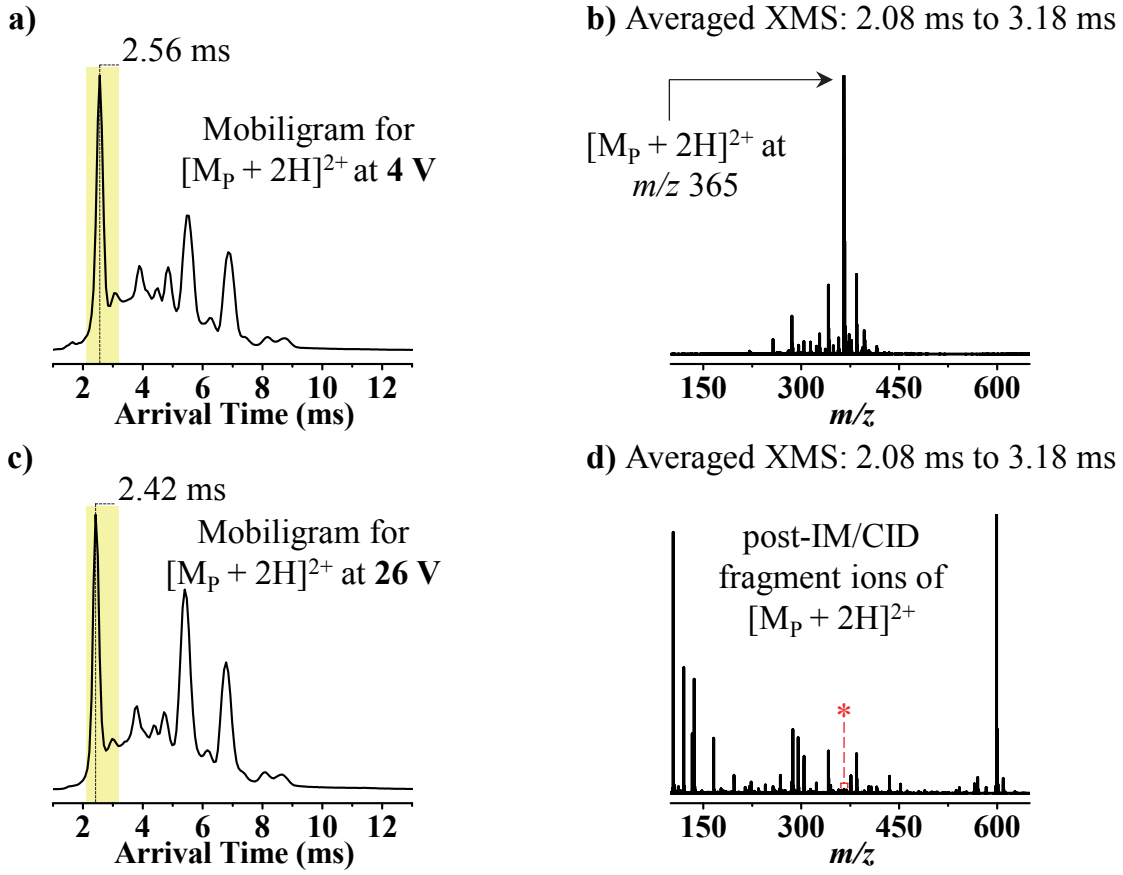

Figure 3.1. Unresolved broadband mobiligram and mass spectra of the binary hexapeptide isomer mixture (containing MGRYGF and FRMYGG) using a data acquisition time of 1 minute. (a) Total ion mobiligram from AT of 0 ms to 13.8 ms measured using a 4 V collision-energy and (b) a representative mass spectrum generated using MS data corresponding to IM AT region 2.08 ms to 3.18 ms in Fig. 3.1a. (c) Total ion mobiligram from AT of 0 ms to 13.8 ms measured using a 26 V CE and (d) a representative mass spectrum generated using MS data corresponding to IM AT region 2.08 ms to 3.18 ms in Fig. 3.1c (please refer to text (and previous report[134]) for details on observed IM shifts between low- and high-collision-energy experiments). Yellow rectangles in (a) and (c) denote data-notching windows from IM AT 2.08 ms to 3.18 ms. The asterisk with red dashed line in (d) shows the precursor ion $[M_P + 2H]^{2+}$ region at *m/z* 365 and indicates a complete signal reduction for $[M_P + 2H]^{2+}$due to post-IM/CID.

Figure 3.1a. However, as expected, there is a small IM shift of ~0.14 ms in Figure 3.1d to earlier ATs due to higher ion acceleration used for post-IM/CID.[125,134]

The unresolved IM peaks and mass spectrum in Figures 3.1c and 3.1d were deconvoluted using AIMD, and the resulting IM profiles and mass spectra are shown in Figures 3.2a and 3.2b-c, respectively. Deconvoluted mobiligrams in Figure 3.2a correspond to $[MGRYGF + 2H]^{2+}$ (orange) and $[FRMYGG + 2H]^{2+}$ (purple) and have IM ATs of 2.40 ms and 2.49 ms, respectively. For comparison, isomerically pure IM profiles

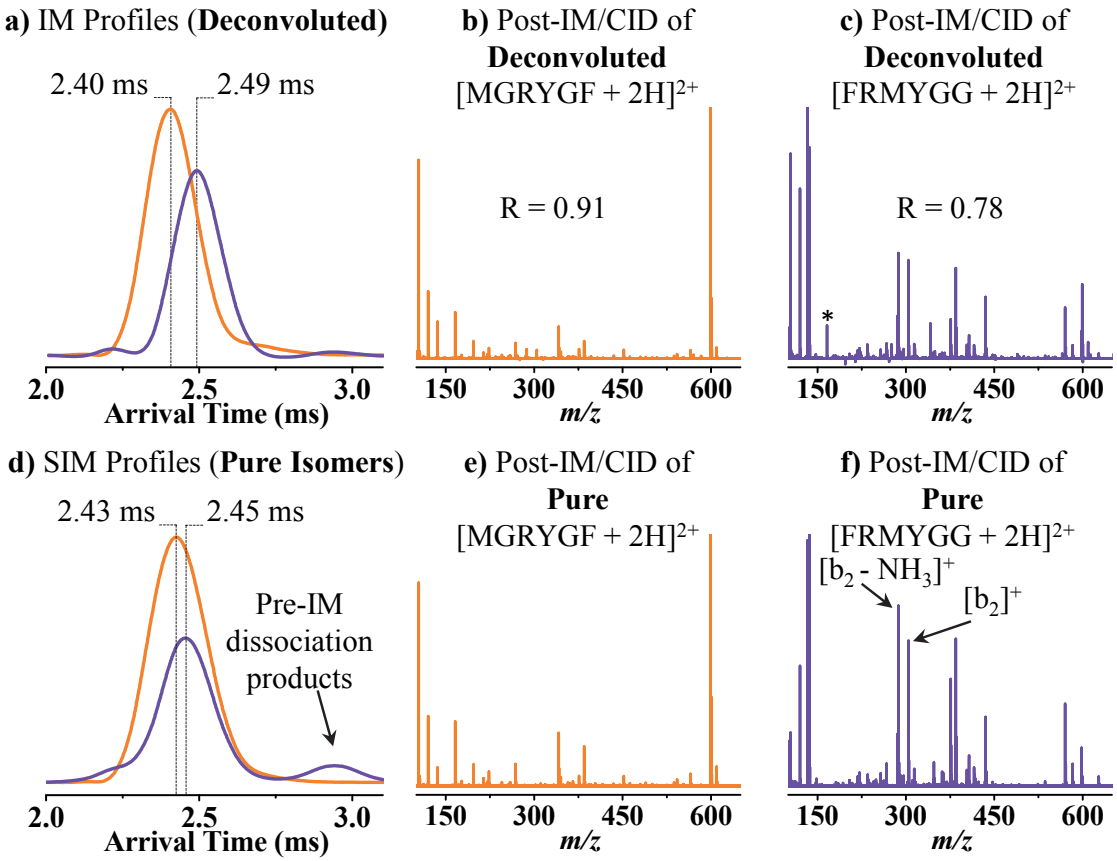

Figure 3.2. Broadband deconvolution of $[M_P + 2H]^{2+}$ using a 26 V collision-energy and a data acquisition time of 1 minute. (a) Deconvoluted IM profiles for the two peptide isomers and corresponding post-IM/CID mass spectra for (b) $[MGRYGF + 2H]^{2+}$ (orange) and (c) $[FRMYGG + 2H]^{2+}$ (purple). (d) Pure SIM profiles and pure CID mass spectra for (e) $[MGRYGF + 2H]^{2+}$ and (f) $[FRMYGG + 2H]^{2+}$ were individually measured using a 26 V collision-energy. Black asterisk above the MS peak at *m/z* 166 in (c) denotes an example of partially misassigned MS peak intensity by AIMD.

were individually measured using the same 26 V collision-energy and their SIM profiles are shown in Figure 3.2d (with IM ATs of 2.43 ms for $[MGRYGF + 2H]^{2+}$ and 2.45 ms for $[FRMYGG + 2H]^{2+}$). The low intensity peak at ~2.91 ms in Figure 3.2d is due to pre-IM dissociation products of $[FRMYGG + 2H]^{2+}$ (*viz.*, $[b_2 - NH_3]^+$ and $[b_2]^+$ fragments labelled in Figure 3.2f) and should not be misinterpreted as an additional isomer (see Figure B.1). Centroids of deconvoluted mobiligrams in Figure 3.2a match their isomerically pure counterparts (pure mobiligrams' centroids) in Figure 3.2d within 1 IM bin.

The pure hexapeptide isomer solutions contained ~1.7 μM of MGRYGF or FRMYGG, and the binary hexapeptide mixture contained ~1.7 μM of each peptide. The IM peak ratio of $[FMRYGG + 2H]^{2+}$ to $[MGRYGF + 2H]^{2+}$ in Figure 3.2a was 0.75 ± 0.46 whereas the corresponding ratio in Figure 3.2d was 0.55 ± 0.23 (value reported as 95% confidence interval for n = 3). This small peak ratio variation is statistically insignificant at the 95% confidence level (for $n_1 = n_2 = 3$, using Student's *t*-test, Case 2).

The deconvoluted post-IM/CID mass spectra of the isomeric peptides (Figures 3.2b and 3.2c) were quantitatively compared with the individual post-IM/CID mass spectra (Figures 3.2e and 3.2f) using mass spectral matching by calculating *R*-values, where $R = 1$ represents a perfect match and $R = 0$ indicates no spectral correlation.[87] The deconvoluted mass spectra matched the corresponding individual component mass spectra with *R*-values of 0.91 and 0.78 for MGRYGF and FRMYGG, respectively. *R*-values are calculated using deviations in relative intensities of peaks that are present in deconvoluted and/or pure mass spectra; misassigned peaks can lower the calculated *R*-values.[87] For instance, erroneous assignment of higher relative intensity to *m/z* 166 by AIMD,[131] denoted by a black asterisk

in deconvoluted mass spectrum of $[FRMYGG +2H]^{2+}$ in Figure 3.2c, contributes to the calculated *R*-value of 0.78.

Similar to the binary mixture of peptide isomers, broadband IM-MS deconvolution was used to extract IM profiles and mass spectra from a binary trisaccharide isomer mixture (*i.e.*, containing [D-(+)-raffinose + Li]$^+$ and [D-(+)-isomaltotriose + Li]$^+$). When separately measured at a 4 V collision-energy, the trisaccharide ions had distinct IM ATs of 4.43 ms and 4.57 ms, respectively (data not shown). However, when mixed, these ions yielded a single, convoluted IM peak. For example, Figure 3.3 shows the convoluted IM profiles (3.3a and 3.3c) and mass spectra (3.3b and 3.3d) of the trisaccharide mixture. The highlighted regions in Figures 3.3a and 3.3c denote the data-notching windows from IM AT of 3.74 ms to 5.12 ms; this region of interest contained the IM unresolved peak for the trisaccharide isomers.

The convoluted broadband mobiligram of the binary trisaccharide isomer mixture in Figure 3.3a has a mobiligraphic apex at an IM AT of 4.50 ms corresponding to the trisaccharide isomer precursor ion species at *m/z* 511 in Figure 3.3b. The XMS in Figure 3.3b was constructed by summing mass spectra of ions with mobility times between 3.74 ms to 5.12 ms in Figure 3.3a.

The apex of the mobiligram shown in Figure 3.3c is at 4.29 ms and corresponds to the $[M_T + Li]^+$ precursor ions. As expected, a ~0.21 ms shift to a shorter AT was observed for $[M_T + Li]^+$ after increasing the transfer collision-energy from 4 V (Figure 3.3a) to 45 V (Figure 3.3c).[125,134] The high collision-energy XMS for the binary trisaccharide isomer mixture in Figure 3d was constructed by summing mass spectra of ions with mobility times between 3.74 ms to 5.12 ms in Figure 3.3c; this average mass spectrum contains post-

IM/CID fragment ions generated from [D-(+)-raffinose + Li]$^+$ and/or [D-(+)-isomaltotriose + Li]$^+$.

The unresolved IM peak at AT = 4.29 ms (Figure 3.3c) and mass spectrum (Figure 3.3d) were deconvoluted using AIMD, and the deconvoluted IM profiles and mass spectra are shown in Figures 3.4a and 3.4b-c, respectively. The IM AT region 3.74 ms to 5.12 ms

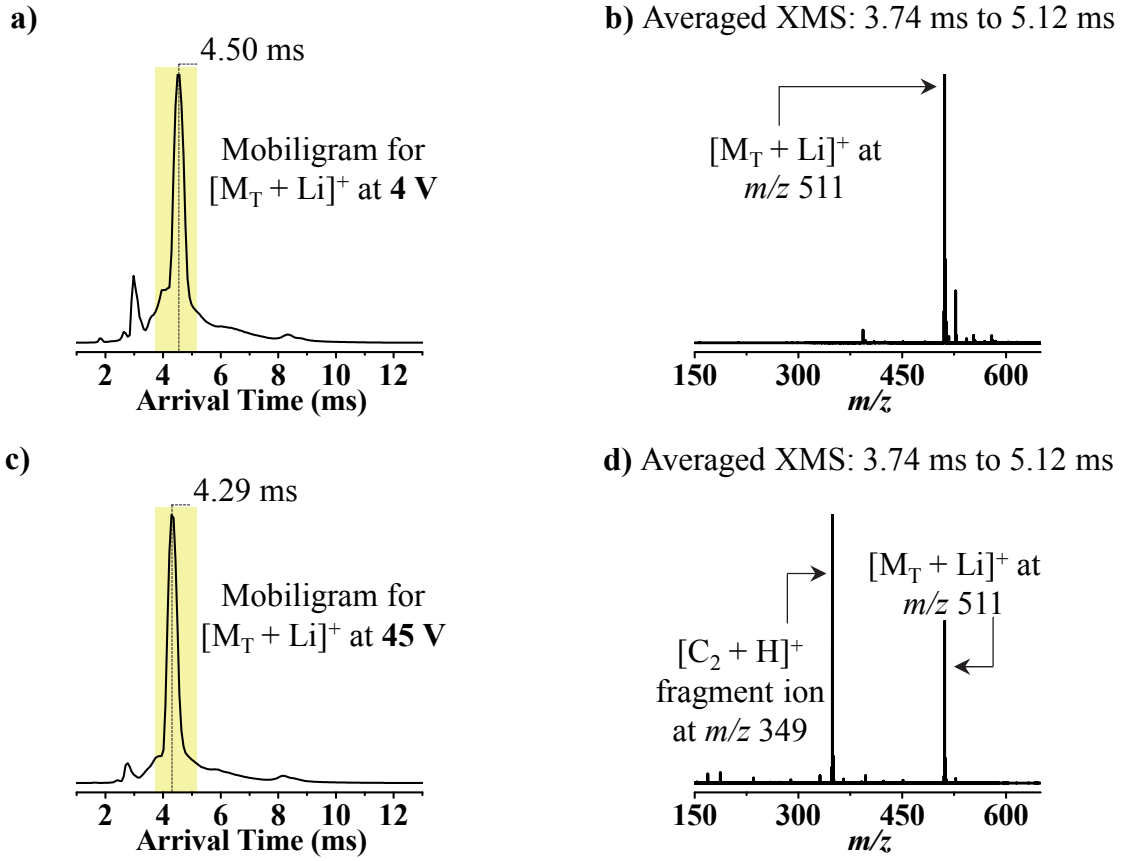

Figure 3.3. Unresolved broadband mobiligram and mass spectra of binary trisaccharide isomer mixture (containing [D-(+)-raffinose + Li]$^+$ and [D-(+)-isomaltotriose + Li]$^+$) using a data acquisition time of 1 minute. (a) Total ion mobiligram from AT 0 ms to 13.8 ms measured using a 4 V collision-energy and (b) a representative mass spectrum generated using MS data corresponding to IM AT region 3.74 ms to 5.12 ms in Fig. 3.3a. (c) Total ion mobiligram from AT of 0 ms to 13.8 ms measured using a 45 V collision-energy and (d) a representative high collision-energy CID mass spectrum generated using MS data corresponding to IM AT region 3.74 ms to 5.12 ms in Fig. 3.3c. Yellow rectangles (a) and (c) denote data-notching windows from IM AT of 3.74 ms to 5.12 ms.

(*viz*., highlighted regions in Figures 3.3a and 3.3c) is expanded in Figures 3.4a (after performing AIMD) and 3.4d (for individually ran pure samples). The deconvoluted IM profiles in Figure 3.4a correspond to [D-(+)-raffinose + Li]$^+$ (blue) and [D-(+)-isomaltotriose + Li]$^+$ (red) and have IM ATs of 4.26 ms and 4.40 ms, respectively. To validate the deconvolution results, isomerically pure IM profiles were individually measured using the same 45 V collision-energy and are displayed in Figure 3.4d as SIM

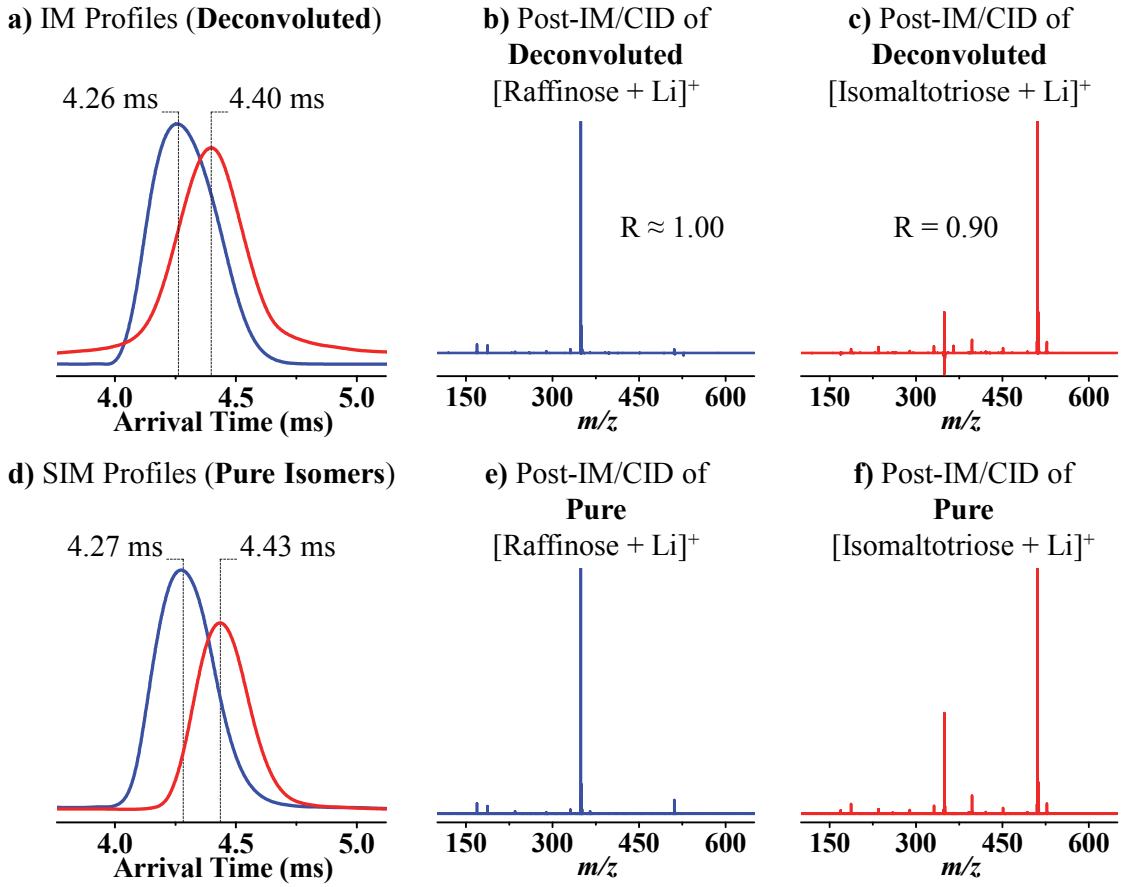

Figure 3.4. Broadband deconvolution of [M$_T$ + Li]$^+$ using a 45 V collision-energy and a data acquisition time of 1 minute. (a) Deconvoluted IM profiles for the two trisaccharide isomers and their corresponding post-IM/CID mass spectra for (b) [D-(+)-raffinose + Li]$^+$ (blue) and (c) [D-(+)-isomaltotriose + Li]$^+$ (red). (d) Pure SIM profiles and pure CID mass spectra for (e) [D-(+)-raffinose + Li]$^+$ and (f) [D-(+)-isomaltotriose + Li]$^+$ were individually measured using a 45 V collision-energy.

profiles. IM deconvolution results for the binary sugar mixture (Figure 3.4a) are in agreement with results from the analysis of their isomerically pure counterparts (Figure 3.4d), and deconvoluted IM peak centroids for both isomers match their pure counterparts' values to within 1 IM bin.

Each pure trisaccharide sample was a ~3.3 μM solution of either isomer and concentrations of each sugar in the binary trisaccharide mixture were ~3.3 μM. The IM peak ratio of $[\text{D-(+)-isomaltotriose} + \text{Li}]^+$ to $[\text{D-(+)-raffinose} + \text{Li}]^+$ was 0.90 ± 0.40 (value reported as 95% confidence interval for n = 3) for the deconvoluted data in Figure 3.4a. When independently measured as pure isomer solutions, the IM peak ratio was 0.78 ± 0.47 (Figure 3.4d). At the 95% confidence level, this observed decrease in sugar isomer peak ratio was statistically insignificant (Student's *t*-test, Case 2 for $n_1 = n_2 = 3$). Deconvoluted post-IM/CID mass spectra in Figures 3.4b and 3.4c matched their isomerically pure counterparts with *R*-values of ~1.00 and 0.90, respectively. Please note that broadband IM-MS deconvolution using AIMD is successful even when unresolved components are not prepared at equimolar concentrations (see Figure B.3).

3.6.2 Broadband IM-MS Deconvolution of a Complex Mixture

Broadband AIMD deconvolution was performed on a simulated complex mixture to evaluate the performance of our broadband approach in the presence of high-intensity background ions. The complex mixture contained the two hexapeptide isomers, the two trisaccharide isomers, PPG 425, and PPG 1000. Although only LiCl was added to the simulated complex mixture (to ensure the formation of Li-trisaccharide adducts), various other alkali metal complexes and charge-states of the peptides, sugars, and PPG species were also observed.

The convoluted IM peaks and mass spectra of the simulated complex mixture are shown in Figure 3.5. The highlighted data-notching windows (Figure 3.5a, central panel) spanning from IM AT of 2.08 ms to 3.18 ms and 3.74 ms to 5.12 ms were utilized for AIMD analysis of $[M_P + 2H]^{2+}$ and $[M_T + Li]^+$ isomers, respectively.

The convoluted high collision-energy mobiligram of the complex mixture is shown in Figure 3.5a. The IM peaks at 2.42 ms and 4.36 ms correspond to isomeric peptide and trisaccharide precursor ions, respectively, and include additional interfering background species. The convoluted XMS shown in Figures 3.5b and 3.5c were generated by summing mass spectra of all peptide, sugar and PPG ions with mobility times between 2.08 ms to 3.18 ms (for Figure 3.5b) and 3.74 ms to 5.12 ms (for Figure 3.5c). Sixty-five of the 100 most abundant MS

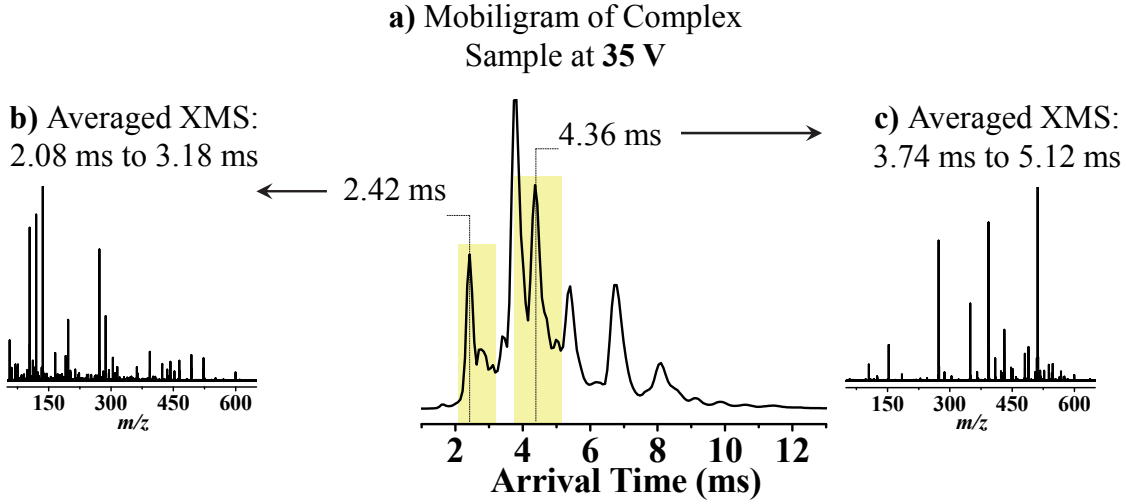

Figure 3.5. Unresolved broadband mobiligram and mass spectra of the simulated complex mixture collected using a 35 V collision-energy and a data acquisition time of 1 minute. (a) Total ion mobiligram from AT of 0 to 13.8 ms. Yellow rectangles in (a) denote data-notching windows from IM ATs of 2.08 ms to 3.18 ms (left) and 3.74 ms to 5.12 ms (right). Representative post-IM/CID mass spectra at 35 V for (b) ions with IM ATs ranging from 2.08 ms to 3.18 ms and (c) ions with IM ATs ranging from 3.74 ms to 5.12 ms).

peaks corresponding to mobility times 2.08 ms to 3.18 ms were not unique to either one of the two isomeric hexapeptides (these assignments were confirmed by both raw IM and MS data and AIMD deconvolution). Likewise, for the IM AT region of 3.74 ms to 5.12 ms, seventy-six of the 100 MS peaks were not unique to either one of the two trisaccharide isomers. In other words, despite the presence of a large number of unrelated MS peaks within each selected window (*i.e.*, Figures 3.5b and 3.5c), AIMD analyses of multiple IM regions corresponding to two sets of co-eluting isomers were successful.

The unresolved peptide data (Figures 3.5a and 3.5b) were deconvoluted from the simulated complex mixture without prior knowledge of the total number of convolved components, and the results are shown in Figure 3.6. The 2.08 ms to 3.18 ms region in Figure 3.5a is expanded in Figures 3.6a (deconvoluted IM for peptide isomers) and 3.6d (IM for pure peptide isomers) to show the correlation between deconvoluted and pure component data. The deconvoluted IM profiles in Figure 3.6a, corresponding to $[MGRYGF + 2H]^{2+}$ (orange solid trace) and $[FRMYGG + 2H]^{2+}$ (purple solid trace), have IM ATs of 2.37 and 2.49 ms, respectively. IM profiles of nine other interfering background species are also shown in Figure 3.6a as gray IM traces. Representative mass spectra for these background species are provided and further discussed in the Supplementary Information (Figure B.4). AIMD does not utilize any curve fitting for generating IM profiles;[131] therefore, the observed Gaussian-like shapes of background IM profiles match the expected physical reality for peak broadening in ion mobility separation[132] and support the validity of broadband deconvolution. Isomerically pure peptide isomers were individually measured using a 35 V collision-energy to validate their deconvolution from the complex mixture, and IM AT values of 2.43 ms and 2.46 ms were observed for pure

$[MGRYGF + 2H]^{2+}$ and pure $[FRMYGG + 2H]^{2+}$, respectively. The deconvoluted IM ATs matched their corresponding single components within a single IM bin (drift time differences of less than 69 μs).

Deconvolution of data collected at a 26 V collision-energy yielded an IM AT of 2.40 ms for $[MGRYGF + 2H]^{2+}$ (orange trace in Figure 3.2a). As expected,[125,134] deconvolution of data collected at a higher collision-energy of 35 V yielded a shorter IM AT of 2.37 ms for $[MGRYGF + 2H]^{2+}$ (orange solid trace in Figure 3.6a) which corresponded to a difference of less than one IM bin. These IM AT shifts may not be assigned accurately if IM data are under-sampled. To better identify peak centroids and extract more accurate IM arrival times from the AIMD generated outputs, we utilized cubic spline interpolation for IM peak fitting.[132] Please note that small IM AT shifts (*i.e.*, < 0.01 ms) might go unnoticed when rounding fitted data (*e.g.*, deconvoluted IM ATs for $[FRMYGG + 2H]^{2+}$ at 26 V *vs* 35 V in Figures 3.2a and 3.6a, respectively).

The deconvoluted post-IM/CID mass spectrum corresponding to $[MGRYGF + 2H]^{2+}$ is shown in Figure 3.6b; comparison between this deconvoluted mass spectrum (Figure 3.6b) and its corresponding pure mass spectrum (Figure 3.6e) yields a mass spectral matching factor of 0.85. Figure 3.6c shows the deconvoluted post-IM/CID mass spectrum of $[FRMYGG + 2H]^{2+}$; the mass spectral matching factor between the deconvoluted (Figure 3.6c) and pure (Figure 3.6f) mass spectra for $[FRMYGG + 2H]^{2+}$ was 0.75. Spectral matching factors of 0.85 and 0.75 indicate successful deconvolution of both peptides at a 35 V collision-energy.

The unresolved IM peaks and mass spectrum of $[M_T + Li]^+$ (Figures 3.5a and 3.5c, respectively) were deconvoluted using AIMD without prior knowledge of the total number

of convolved components, and results are shown in Figure 3.7. The IM regions of 3.74 ms to 5.12 ms for deconvoluted and pure isomers of the two trisaccharides are expanded in Figures 3.7a and 3.7d. Figure 3.7a shows the deconvoluted IM profiles for raffinose (blue solid trace) and isomaltotriose (red solid trace) with IM ATs of 4.31 ms and 4.46 ms, respectively. Although negative values can be present in AIMD deconvoluted mobiligrams,[263] we consider IM deconvolution successful if negative values are less than 15% of the base peak intensity (*e.g.*, ~4.20 ms to ~4.25 ms for [isomaltotriose + Li]$^+$ in Figure 3.7a). IM profiles of ten other interfering background species are also shown in Figure 3.7a as gray IM traces. Representative mass spectra for these background species are provided and further discussed in the Supplementary Information (Figure B.5). Again, the Gaussian-like shapes of background IM profiles support the validity of broadband deconvolution. Moreover, the truncated IM profiles of background species 1, 2, 9, and 10, as generated by AIMD, match the physical reality of these background species not being completely within the notched window and further support the validity of broadband deconvolution.

The deconvoluted ATs (Figure 3.7a) are in agreement with those of pure components (Figure 3.7d). The mass spectral matching factors of raffinose (Figure 3.7b) and isomaltotriose (Figure 3.7c) were 0.83 and 0.88, respectively. According to the criteria for broadband deconvolution outlined in the Data Analysis section, all four components were successfully extracted *via* broadband deconvolution of the complex mixture's IM-MS data.

A 2 second data acquisition time, rather than 1 minute, was also used with a 35 V collision-energy for AIMD analysis of the simulated complex mixture. Table 3.1 provides

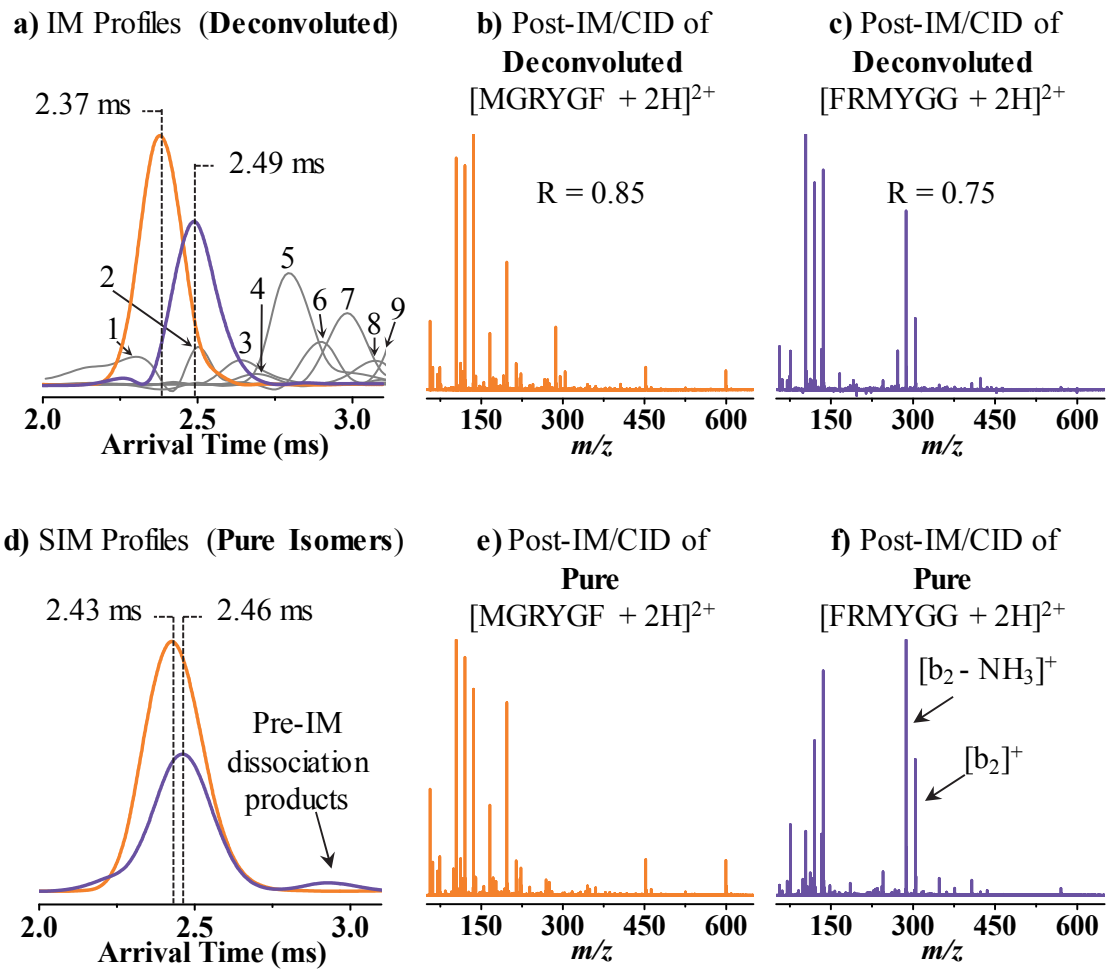

Figure 3.6. Broadband deconvolution of $[M_P + 2H]^{2+}$ from the simulated complex mixture using a 35 V collision-energy and a data acquisition time of 1 minute. (a) Deconvoluted IM profiles for the two peptide isomers and corresponding post-IM/CID mass spectra for (b) $[MGRYGF + 2H]^{2+}$ (orange solid trace) and (c) $[FRMYGG + 2H]^{2+}$ (purple solid trace). (d) Pure SIM profiles and pure CID mass spectra for (e) $[MGRYGF + 2H]^{2+}$ and (f) $[FRMYGG + 2H]^{2+}$ were individually measured using a 35 V collision-energy. In (a), gray IM traces correspond to background species 1 to 9 that were also present in the deconvoluted IM AT region 2.08 ms to 3.18 ms.

deconvoluted IM ATs and *R*-values for each isomer using a 1 minute and 2 second acquisition. All values reported in Table 3.1 are from deconvoluted IM profiles and mass spectra that comply with the three criteria for successful broadband IM-MS deconvolution. Values in Table 3.1 were calculated as 95% confidence intervals with n = 3. The deconvoluted IM ATs for each data acquisition time were compared using Student's *t*-test

(Case 2), and the difference between the two measurements at the 95% confidence level was insignificant. As expected, spectral matching factors decreased at the shorter acquisition time (with exception of raffinose) but remained within the designated limit (of $1 \geq R \geq 0.70$) for successful deconvolution.

3.6.3 Comparison of Broadband and m/z-isolated Approaches

A broadband or DIA deconvolution approach (a) eliminates ion isolation losses and (b) reduces the analysis time *via* multiplexed detection, both of which should enhance sensitivity. The magnitude of such enhancements for both (a) and (b) will depend on the width of the ion isolation window: narrow windows can result in both larger ion losses and require more scans to cover the *m/z* range of interest. In other words, sensitivity enhancement of a broadband deconvolution approach will be greater for complex mixtures that require high resolution ion isolation. As explained below, combined ion transmission and multiplexing improvements in broadband deconvolution can (theoretically) yield three orders of magnitude sensitivity enhancement for a binary mixture.

To demonstrate the sensitivity advantage of DIA deconvolution with broadband acquisition compared to DDA deconvolution with *m/z*-isolated acquisitions, the binary hexapeptide mixture was analyzed at concentrations of ~340 nM, ~34 nM, and ~3.4 nM. Deconvolution using AIMD was ten times more sensitive using broadband IM-MS data acquisition (see Figure B.6). Using AIMD, broadband acquisition allowed IM-MS deconvolution of both hexapeptide isomers from the ~34 nM solution; however, *m/z*-isolated acquisition of $[M_P + 2H]^{2+}$ at *m/z* 365 (using the same ~34 nM solution) did not allow IM-MS deconvolution. It should be noted that this tenfold sensitivity enhancement for DIA deconvolution is due to elimination of ion losses and does not include benefits of

multiplexing. Based on the experimental MS data, compared to *m/z*-isolation, the use of broadband acquisition improved ion transmission of $[M_P + 2H]^{2+}$ at *m/z* 365 by more than 140%; this sensitivity enhancement is analogous to Jacquinot's throughput advantage.[255] Use of *m/z*-isolation in DDA-like experiments limited our data acquisition to a 2 Da

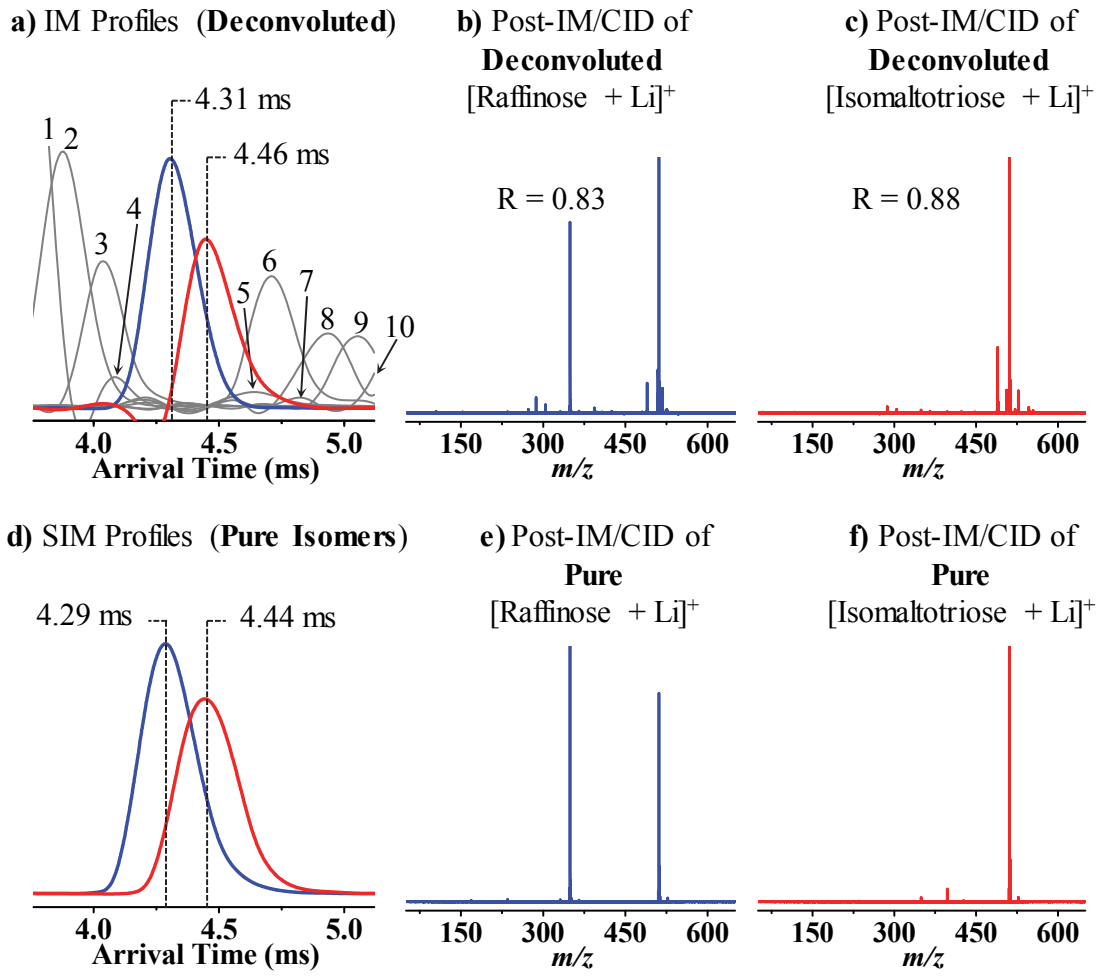

Figure 3.7. Broadband deconvolution of $[M_T + Li]^+$ from the simulated complex mixture using a 35 V collision-energy and a data acquisition time of 1 minute. (a) Deconvoluted IM profiles for the two trisaccharide isomers and corresponding post-IM/CID mass spectra for (b) [D-(+)-raffinose + $Li]^+$ (blue solid trace) and (c) [D-(+)-isomaltotriose + $Li]^+$ (red solid trace). (d) Pure SIM profiles and pure CID mass spectra for (e) [D-(+)-raffinose + $Li]^+$ and (f) [D-(+)-isomaltotriose + $Li]^+$ were individually measured using a 35 V collision-energy. In (a), gray IM traces correspond to background species 1 to 10 that were also present in the deconvoluted IM AT region 3.74 ms to 5.12 ms.

Table 3.1. Ion mobility arrival times (IM ATs) and spectral matching factors (*R*-values) from broadband IM-MS deconvolution of the simulated complex mixture. Data were collected using a 35 V transfer collision-energy and are compared at 1 minute and 2 second data acquisition times. Uncertainty values were calculated as 95% confidence intervals (n = 3). Ion mobility arrival times were compared using Student's *t*-test at the 95% confidence interval ($n_1 = n_2 = 3$) and no statistical differences were observed.

	Ion Mobility Arrival Time (IM AT)		Spectral Matching Factor (*R*-value)	
Isomer	1 minute	2 seconds	1 minute	2 seconds
$[MGRYGF + 2H]^{2+}$	2.374 ± 0.004	2.366 ± 0.004	0.85 ± 0.03	0.80 ± 0.02
$[FRMYGG + 2H]^{2+}$	2.492 ± 0.002	2.477 ± 0.020	0.73 ± 0.04	0.71 ± 0.12
$[D\text{-}(+)\text{-raffinose} + Li]^{+}$	4.306 ± 0.002	4.351 ± 0.077	0.83 ± 0.01	0.83 ± 0.07
$[D\text{-}(+)\text{-isomaltotriose} + Li]^{+}$	4.456 ± 0.009	4.432 ± 0.026	0.88 ± 0.01	0.80 ± 0.05

window which would require 725 *m/z*-isolation events to cover the entire experimental *m/z* range from 50 to 1500 amu (or 725 minutes, based on a 1-minute MS data acquisition time per experiment). However, we used a single 1-minute broadband experiment to measure the entire *m/z* and drift time ranges; this time saving aspect of DIA deconvolution is analogous to Fellgett's multiplex advantage[254] and scales as narrower *m/z*-isolation windows are employed. In this particular example, the combined sensitivity enhancements of DIA deconvolution would exceed three orders of magnitude (*i.e.*, 10 × 725 = 7250) when compared to a comparable DDA experiment of the entire *m/z* range. Because convoluted IM drift time regions are selected *after* data collection, broadband data collection is faster and allows AIMD interrogation of multiple IM regions from the available drift time range using a single IM-MS experiment.

3.6.4 Broadband Deconvolution of UPLC-HDMS^E Proteomics Data

Figure 3.8 shows IM profiles and associated CID mass spectra of IM-MS unresolved peptides from broadband IM-MS deconvolution of UPLC-HDMS^E proteomics data from a rat brain tissue digest. The broadband IM profile in Figure 3.8a represents the IM data that corresponded to the UPLC retention time region of 10.5 minutes to 11.5 minutes (Figure B.7b) from a relatively short 15-minute UPLC-HDMS^E dataset. The highlighted region in Figure 3.8a spans the IM AT region of 2.69 ms to 3.80 ms and corresponds to the IM AT data that was submitted to AIMD for deconvolution of the peptides; the averaged XMS corresponding to this IM drift time region is displayed in Figure 3.8b. The corresponding deconvoluted IM profiles (Figure 3.8c) and deconvoluted post-IM/CID mass spectra (Figures 3.8d and 3.8e) indicate IM-MS deconvolution of the two peptides LIETYFSK and VLSIGDGIAR. The AIMD results in Figures 3.8c-e were validated by PLGS results from a 60-minute UPLC-HDMS^E dataset where these peptides were UPLC resolved.

From the 60-minute UPLC-HDMS^E dataset, the isobaric peptides $[LIETYFSK]^{2+}$ at *m/z* 500.7725 and $[VLSIGDGIAR]^{2+}$ at *m/z* 500.7941 (Figure B.7) were detected and used by PLGS to identify two separate proteins (UniProtKB accession numbers of P60203 and P15999, respectively). Despite being UPLC-IM-MS unresolvable in the 15-minute dataset (Figure 3.8a-b), $[LIETYFSK]^{2+}$ and $[VLSIGDGIAR]^{2+}$ were identified in the 60-minute dataset by PLGS because they had distinct UPLC retention times of 22.38 minutes and 21.98 minutes, respectively (Figure B.7a). In the 15-minute UPLC-HDMS^E dataset, UPLC co-elution prevented PLGS identification of $[VLSIGDGIAR]^{2+}$ (Figure B.7b); in other words, a unique retention time, drift time, or *m/z* value was no longer available for

[VLSIGDGIAR]$^{2+}$as required for successful identification by PLGS. Because [VLSIGDGIAR]$^{2+}$ was not identified from the 15-minute dataset, the sequence coverage of its associated protein (*i.e.*, P15999) fell from 18.6% in the 60-minute dataset to 15.4% in the 15-minute dataset. However, AIMD was used to extract IM (Figure 3.8c, blue trace) and post-IM/CID MS data of [VLSIGDGIAR]$^{2+}$ (Figure 3.8e) from the 15-minute UPLC-HDMS^{E} dataset. The deconvoluted IM ATs of 3.17 ms for [LIETYFSK]$^{2+}$ and 3.24 ms for [VLSIGDGIAR]$^{2+}$ (red and blue traces in Figure 3.8c, respectively) matched the PLGS results from the 60-minute dataset (3.167 ms and 3.241 ms, respectively).

PLGS processing of the 15-minute UPLC-HDMS^{E} dataset yielded 10 total product ion assignments for [LIETYFSK]$^{2+}$; 9 of these 10 product ions were assigned using AIMD deconvolution. Moreover, AIMD allowed 13 additional product ion assignments for [LIETYFSK]$^{2+}$ that were absent from PLGS results. The 22 product ions of [LIETYFSK]$^{2+}$ identified using AIMD had an average mass accuracy error of 9.30 ppm. PLGS did not identify [VLSIGDGIAR]$^{2+}$ in the 15-minute dataset. However, from the 60-minute dataset, PLGS identified 9 product ions for [VLSIGDGIAR]$^{2+}$. In total, broadband deconvolution of 15-minute dataset using AIMD allowed identification of 25 product ions for [VLSIGDGIAR]$^{2+}$ (including all 9 product ions identified by PLGS processing of the 60-minute dataset) with an average mass measurement error of 8.45 ppm.

Agreement between PLGS and AIMD, in terms of equivalent IM peak arrival times and common precursor-product assignments, indicates that AIMD can be used to (i) improve protein identification from PLGS processing of HDMS^{E} proteomics data and (ii) decrease UPLC separation time requirements for high-throughput bottom-up experiments. Based on the reduced number of peptides detected using a shortened UPLC separation, it

is likely that there are many other IM-MS unresolved peptides in the 15-minute dataset that can be deconvoluted.

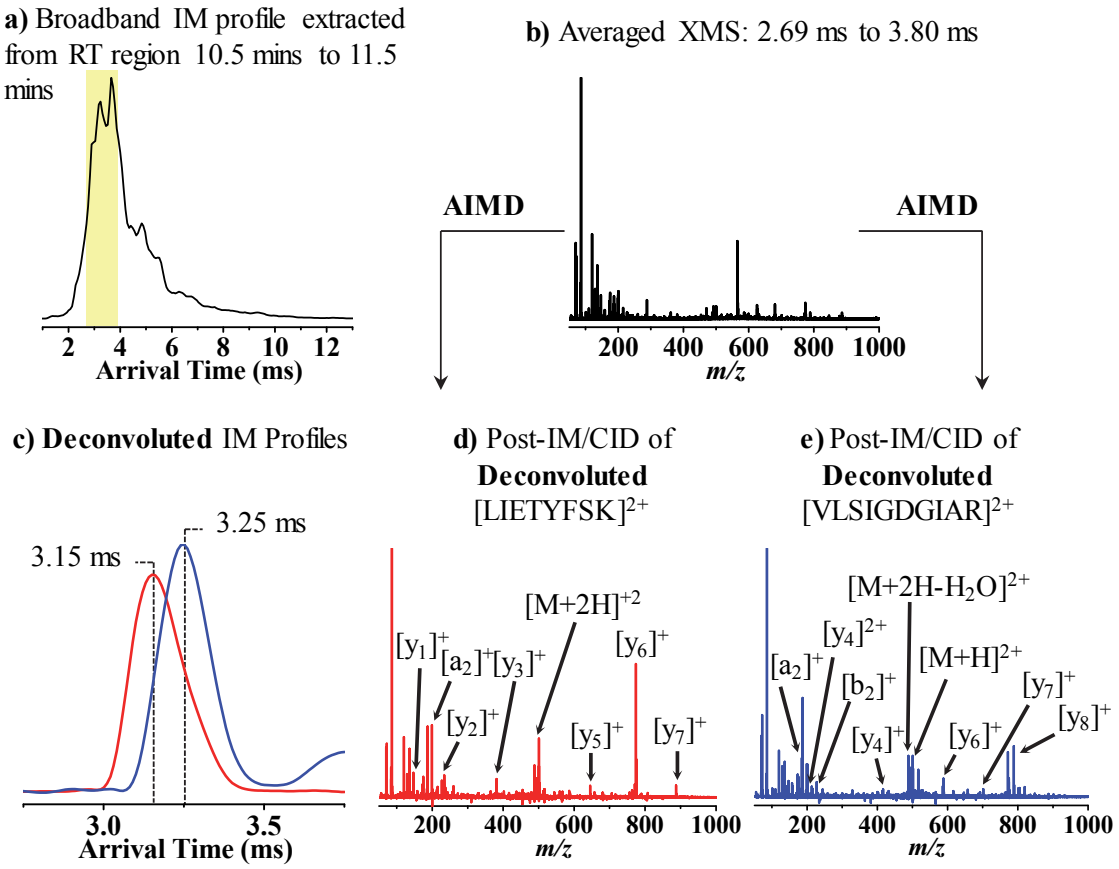

Figure 3.8. Broadband deconvolution of peptides from UPLC-HDMS^E proteomics analysis of a rat brain tissue digest. The broadband mobiligram of the proteolytic digest in (a) was generated by extracting IM data that corresponded to the convolved UPLC retention time region 10.5 min. to 11.5 min. in the 15-minute UPLC-HDMS^E dataset. The yellow rectangle in (a) spans the IM AT region 2.69 ms to 3.80 ms; this IM AT region was deconvoluted using AIMD. The convoluted XMS in (b) was generated by integrating the highlighted IM AT region of interest shown in (a). (c) Deconvoluted IM profiles of the isobaric peptides $[LIETYFSK]^{2+}$ and $[VLSIGDGIAR]^{2+}$ have IM ATs (3.17 ms and 3.24 ms, respectively) that match the results from PLGS analysis (3.167 ms and 3.241 ms, respectively). Deconvoluted post-IM/CID MS data for $[LIETYFSK]^{2+}$ and $[VLSIGDGIAR]^{2+}$ are shown in (d) and (e), respectively.

3.7 Conclusions

Previously, we demonstrated that *m/z*-isolation and subsequent post-IM/CID could be used in combination with AIMD to extract pure IM and MS data from IM unresolved species.[87,131,133,250] However, the use of *m/z*-isolation limited the suitability of AIMD for use with high-throughput MS-based proteomics. One drawback of using *m/z*-isolation with AIMD is that only one IM AT region is interrogated per deconvolution experiment. Using broadband IM-MS deconvolution, AIMD analysis of a single convoluted IM-MS dataset allowed extraction of pure IM peaks and post-IM/CID mass spectra for two unrelated pairs of isomers. Additionally, we demonstrated that broadband IM-MS deconvolution using AIMD was successful despite the presence of unrelated high-intensity background ions such as PPG species. By deconvoluting doubly-charged hexapeptides *and* singly-charged trisaccharides using a single dataset, we further demonstrated that AIMD was successful even when ion fragmentation *via* CID involved fragmenting different chemical bond types with varied bond dissociation energies (*i.e.*, amide bonds *versus* glycosidic bonds[231-233]).

In addition to interrogating multiple IM ATs from a single dataset, broadband data collection also improved AIMD throughput by reducing the data acquisition time for deconvolution. A quadrupole device's ion transmission efficiency decreases when operating as a mass filter (as opposed to operating as an rf-only ion guide). Therefore, the use of *m/z*-isolation in combination with AIMD may require long data acquisition times[87] (*i.e.*, 5 to 45 mins) to achieve successful deconvolution. On the other hand, due to its fundamental throughput and multiplex advantages, broadband data collection effectively reduced the amount of time required to achieve appropriate S/N ratios for all ions in the

deconvoluted mass spectra. For instance, here, 2 second broadband data acquisition was sufficient for AIMD deconvolution of unresolved post-IM/CID data.

We also demonstrated that broadband IM-MS deconvolution can improve results from an IM-assisted DIA proteomics workflow (*i.e.*, HDME^{E}). AIMD is attractive for integration with IM-assisted DIA workflows, such as HDMS^{E}, because it allows for: (i) deconvolution of various IM AT regions (and molecular classes/charge-states) from a broadband post-IM/CID MS dataset, (ii) deconvolution of unresolved IM-MS data collected at UPLC compatible timescales, and (iii) extraction of precursor-product ion assignments from (previously) mischaracterized UPLC-IM-MS regions for improved characterization of real proteomics samples. However, two questions must be addressed before AIMD can be combined with IM-assisted DIA methodologies. The first question is how to identify IM AT regions that contain co-eluting species for subsequent targeted deconvolution. We recently reported on an IM peak fitting methodology that facilitates detection of IM co-elution by identifying *m/z*-values whose IM peak widths are inappropriately wide.[132] Once IM AT regions that are suspected of containing multiple components have been tagged, the number of IM unresolved species can be ascertained using chemical rank determination techniques.[69,87,131,223] The second question is related to characterization of the AIMD method's dynamic range, as it pertains to concentration differences between co-eluting species and will be addressed in future reports. In summary, the results presented in this manuscript demonstrate the advantages of broadband IM-MS deconvolution for potential high-throughput applications such as IM-assisted DIA methodologies.

3.8 Acknowledgments

The authors would like to acknowledge the financial support provided by the National Science Foundation (NSF) (NSF-IDBR Award # 1455668 and CHE-1709526). The authors thank Dr. D. G. Baker (School of Veterinary Medicine, Louisiana State University) for providing rat brain tissue samples.

CHAPTER FOUR

Infrared Laser Ablation Sampling Coupled with Data Independent High Resolution UPLC-IM-MS/MS for Tissue Analysis

This chapter is prepared for publication in *Analytica Chimica Acta* as: Pettit, M. E., Donnarumma, F., Murray, K. K., Solouki, T., Infrared Laser Ablation Sampling Coupled with Data Independent High Resolution UPLC-IM-MS/MS for Tissue Analysis.

4.1 Abstract

Infrared laser ablation microsampling was used with ion mobility enhanced data-independent acquisition ($HDMS^E$) and data-dependent acquisition (DDA) for mass spectrometry based bottom-up proteomics analysis of rat brain tissue. Results from $HDMS^E$ and DDA analyses of the 12 laser ablated rat brain samples showed that $HDMS^E$ consistently identified about 7 times more peptides and 4 times more proteins than DDA. To evaluate the impact of ultra-performance liquid chromatography (UPLC) peak congestions on $HDMS^E$ and DDA approaches, whole tissue digests from rat brain were analyzed at six different UPLC separation times. Analogous to results from laser ablated samples, $HDMS^E$ analyses of whole tissue digests yielded about four times more proteins identified than DDA for all six UPLC separation times.

4.2 Introduction

High-throughput identification and quantification of the constituent biomolecules in tissue is a significant challenge for biological mass spectrometry.[180] Compound identification is particularly difficult in conventional mass spectrometry imaging because tissue sampling and ion introduction to the mass spectrometer are typically performed

concurrently, precluding many advantageous processing and separation steps. Quantification of material directly ionized from tissue is challenging because the desorption and ionization processes are sensitive to sample morphology[264] and to signal suppression from components in the complex mixtures of compounds.[265,266] In the case of MALDI imaging, there is the additional issue of homogeneous matrix addition.[267]

Identification and quantification of compounds in tissue can be improved by sample extraction and subsequent detailed off-line mass spectrometry analyses.[268-272] Extraction of material from tissue for off-line LC-MS and MS/MS analysis can be done with complete sections,[273-275] excised portions of tissue,[268,269,276] or by localized sampling.[274] Tissue sections can be manually dissected, for example, using a thin plastic film to assist in region of interest (ROI) selection for compound extraction.[268,277,278] In this technique, MALDI mass spectrometry is used to identify regions of interest (ROIs); consecutive sections are subsequently deposited on parafilm covered glass microscope slides and ROIs are manually excised. Laser microdissection uses a laser in conjunction with an optical microscope to select portions of a tissue section for removal.[279-281] Laser microdissection systems use either an ultraviolet (UV) laser to cut the tissue or an infrared laser to melt a plastic film to physically capture the tissue. Microdissected regions can be analyzed directly using mass spectrometry[4,282-284] or with liquid chromatography coupled with mass spectrometry.[206,285-288]

We have developed an infrared laser ablation microsampling method that has advantages of speed and efficiency compared to surface sampling, laser microdissection, and ablation at UV laser wavelengths.[289-294] Using an IR laser, tissue is ablated and captured in a solvent therefore this sampling method does not require coated slides or

thermal polymer and does not require cell lysis by sonication or the addition of detergent. Unlike a liquid microjunction, laser ablation removal does not require surface contact which eliminates analyte diffusion and memory effects. We have coupled laser ablation sampling to liquid chromatography and tandem mass spectrometry for proteomic analysis of tissue.[259]

Tandem mass spectrometry has traditionally been performed using DDA, where the most abundant precursor ions are selected in series (*i.e.*, one at a time) for fragmentation.[295] DIA is a more recent approach that applies fragmentation to all ions within a large *m/z* range.[197-205] With DIA, an entire *m/z* range of interest is probed by precursor ion scans (MS1) followed by product ion scans (MS2) in which all detectable ions are fragmented within either sequentially scanned smaller windows (ranging from ~2.5 Da to ~20 Da)[197,198,200-202,205] or the full *m/z* range.[199,203,204] Fragmentation of all ions in a large *m/z* range can lead to higher dynamic range, better sensitivity, and better quantification accuracy.[206] The use of alternating low and high collision-energy in DIA facilitates multiplex detection of precursor and product ions (analogous to Fellgett's advantage[254]) and can result in a near 100% duty cycle.[206] Currently, "all ion fragmentation" strategies are licensed by Thermo Scientific as "DIA", AB Sciex as "sequential window acquisition of all theoretical spectra" (SWATH), Agilent as "All Ions MS/MS", and Waters as "MS^E". During LC-MS^E experiments, the full *m/z* range is probed using continuously alternating MS1 and MS2 scans. Ion mobility (IM)[79,81-83] with LC-MS^E is a recent approach to DIA called $HDMS^E$.[195] Data acquisition for $HDMS^E$ is in three-dimensions: LC retention time, IM drift time, and *m/z*. Specifically, in $HDMS^E$, IM drift time and accurate mass and

retention time (AMRT) correlation are used to facilitate assignment of precursor and product ions from the three-dimensional data.[207-210]

In this work, we report on the use of HDMS^E for analysis of laser ablated tissue samples. Here, we use laser ablation sample transfer (LAST) for biomolecule extraction from rat brain tissue to compare bottom-up protein identification by DDA and HDMS^E acquisition. Using whole tissue digests from rat brain, we also examine the effect of UPLC separation time on the number of peptides and proteins identified by DDA and HDMS^E.

4.3 Materials and Methods

Laser ablation sample transfer and trypsin digestions were performed at Louisiana State University (LSU), and all MS experiments and data processing were carried out at Baylor University (BU).

4.3.1 Chemicals, Supplies, and Solvents

Trimethamine (tris) base was purchased from Bio-Rad (Hercules, CA, USA). DL-dithiothreitol (DTT, 98%), iodoacetamide (IAA, BioUltra, 99%) and ammonium bicarbonate (ABC, BioUltra, 99.5%) were obtained from Sigma-Aldrich (St. Louis, MO, USA). Tris (50 mM) and ABC (10 mM) buffers were adjusted to pH values of 8.5 and 7.4, respectively. Sequencing grade modified trypsin was purchased from Promega (Madison, WI, USA).

Ultrapure water with an overall ionic concentration of <0.1 ppb and resistivity of ~18.2 MΩ·cm at 25 °C was produced in-house, using either a NANOpure ultrapure water system at LSU (Barnstead, Van Nuys, CA, USA) or a Direct-Q 3 UV water purification system at BU (EMD Millipore Corporation, Billerica, MA, USA). Ultracentrifugation

cartridges (10 kDa cutoff) were obtained from Pall (Port Washington, NY, USA). Glass microscope slides (25×75 mm) were obtained from VWR (West Chester, PA, USA). Sodium formate and [Glu^1]-fibrinopeptide B were purchased from Waters Corp. (Milford, MA, USA). Acetic acid, acetonitrile (ACN, ≥99.9%), formic acid (FA), and methanol (≥99.9%) were purchased from Fisher-Scientific (Waltham, MA, USA).

4.3.2 Tissue Samples

Tissue samples were obtained from four-week-old breeding rats at the Louisiana State University School of Veterinary Medicine Division of Laboratory Animal Medicine (DLAM). All protocols for animal care and use were approved by the Institutional Animal Care and Use Committee at LSU, and samples were handled as outlined by the Department of Environmental Health and Safety at BU. The animals were sacrificed by CO_2 (5 psi) exposure. Brain samples were collected, washed in 50 mM ammonium bicarbonate buffer for 30 seconds, and frozen in liquid nitrogen within 30 minutes. Frozen samples were stored at -80 °C. Thin sections were prepared with a Leica CM1850 cryostat (Leica Microsystems, Wetzlar, Germany) directly from the frozen tissue. Optimal cutting temperature (OCT) solution was used to fix one side of the sample to the cryostat support. Coronal rat brain sections were cut at a thickness of 50 μm, thaw-mounted on uncoated microscope slides, and stored at -80 °C.

4.3.3 Laser Ablation Sample Transfer

Tissue sections were dried under vacuum for 30 minutes prior to sampling. Laser ablation and material collection were performed as previously described.[259] Ablation was conducted on 2×2 mm regions at a laser fluence of 27 kJ m^{-2} using an OPO IR laser (IR

Opolette, OPOTEK, Carlsbad, CA, USA) at 2940 nm wavelength. After ablation, the microcentrifuge tubes containing the captured sample (collected in liquid)[259] were vortexed for 30 seconds and stored at -20 °C until filter aided sample processing.

4.3.4 Microscopy Imaging

Microscopy images were acquired with a fluorescence stereomicroscope (SteREO Lumar V12, Zeiss) equipped with a 0.8× Neolumar S objective and a high resolution digital camera (AxioCam HRc, Zeiss). Images were recorded in bright field mode and exported using Zen 2012 software (Zeiss).

4.3.5 Filter Aided Sample Processing

Proteomic sample processing was performed at LSU as previously described.[259] Samples were collected into tubes, and after addition of 500 µL of tris buffer (50 mM, pH 8.5), they were homogenized with a high-power ultrasonic homogenizer (Sonifier S-450, Emerson Electric, St. Louis, MO). Protein disulfide bond reduction was achieved by adding DTT to each tube to a final concentration of 10 mM. Samples were incubated at 80 ºC for 45 minutes, and after cooling at room temperature for 15 minutes, transferred to ultrafiltration cartridges (with a molecular weight cutoff of 10 kDa) and centrifuged at 14,000 g for 20 minutes. Alkylation was performed by adding 100 µL of a 20 mM IAA solution to each unit followed by incubation in the dark for 30 minutes. After incubation, the samples were centrifuged again at 14,000 g for 10 minutes. Buffer exchanges and washing steps were performed by adding 100 µL of ABC buffer to each tube and centrifugation at 14,000 g for 10 minutes. This step was repeated twice, after which filter units were placed in clean tubes. Enzymatic digestion of the protein material was achieved

using 50 µL of ABC buffer and 1 µL of a 50 ng/µL trypsin solution. Samples were incubated at 37 ºC overnight and shaken at 200 rpm. After digestion, the filter units were centrifuged at 14,000 g for 10 minutes, 50 µL of ABC buffer were added, and filter units were centrifuged again. The filter units were removed and the tryptic mixtures were vacuum dried. The centrifuge tubes containing the dried samples were packaged in dry ice and shipped to Baylor where they were stored at -40 ºC before use.

Prior to MS analyses, dried samples were thawed and re-suspended in aqueous solutions containing 5% ACN and 0.1% FA. Based on a previous protocol,[259] sample concentrations were ~80 ng/µL and ~184 ng/µL for the digested LAST and whole tissue samples, respectively. The re-suspended samples were vortexed for 30 seconds using a vortex mixer (VWR International, Radnor, PA) and centrifuged at 1,000 g for 1 minute using a microcentrifuge (Sorvall Legend Micro 21R, Thermo Scientific, Waltham, MA); the vortex/centrifuge step was repeated once.

4.3.6 UPLC-MS/MS

The ultra-performance LC-MS/MS (UPLC-MS/MS) method was adapted from Geromanos *et al.*[206] Separation of tryptic peptides was performed using a UPLC system (nanoAcquity, Waters Corporation, Milford, MA) equipped with a Symmetry C18 pre-column (5 µm, 20 mm × 180 µm) and a BEH130 C18 analytical reversed-phase (RP) column (1.7 µm, 100 mm × 100 µm). Mobile phase solvents A and B were water and ACN, respectively (each with 0.1% FA). For each sample, a 4.0 µL partial loop injection was transferred to the pre-column for desalting and pre-concentration using 99% solvent A at a flow rate of 10 µL min^{-1} for 3 minutes. The pre-concentrated peptides were eluted to the analytical column and separated using a gradient of 5% to 45% solvent B at a flow rate of

600 nL min^{-1}; a 90-minute separation was performed unless otherwise stated. Following separation, the mobile phase was ramped to 99% solvent B for 5 minutes and held at 99% solvent B for an additional 5-minutes. The mobile phase was ramped to 5% solvent B over 5 minutes, and the column was re-equilibrated at 5% solvent B for 15 minutes. Throughout the separation, the UPLC column temperature was held at 40 ºC. The lock mass compound, [Glu^1]-fibrinopeptide B (at a concentration of 300 fmol μL^{-1}), was delivered at 500 nL min^{-1} by the auxiliary pump of the UPLC system to the reference sprayer of the NanoLockSpray source of the mass spectrometer. To minimize disparities, DDA and $HDMS^E$ runs were made in alternating order.

MS was performed in positive-ion electrospray ionization (ESI) mode using a Synapt G2-S HDMS (Waters, Milford, MA) that was set to sensitivity mode (*i.e.*, V mode), with a typical mass resolving power ($M/\Delta M_{50\%}$) of ~10,000. The time-of-flight (TOF) analyzer was externally calibrated with a sodium formate solution from *m/z* 50 to 2 000; all samples were measured in the same *m/z* range of 50 to 2 000. The reference sprayer was sampled every 30 seconds, and all TOF MS data were lock mass corrected (post acquisition) using the doubly-charged monoisotopic ions of [Glu^1]-fibrinopeptide B at *m/z* 785.8426. The IM drift cell was filled with nitrogen gas during $HDMS^E$ experiments at direct measurement readout of ~3.5 mbar N_2.

UPLC data-dependent acquisition (UPLC-DDA) was accomplished using the "Fast DDA" function of MassLynx (Ver. 4.1, Waters: Milford, MA) as follows: MS survey scans were acquired using a 4 V transfer collision-energy for 0.6 seconds, and MS/MS data were obtained for up to three multiply charged ions of 2^+, 3^+ or 4^+ detected in the survey scan. For each precursor ion selected from the survey scan, MS/MS data were collected at a scan

time of 0.3 seconds, using a transfer collision-energy ramp from 15 V to 45 V. A dynamic exclusion window of 0.100 Da was set to 60 seconds to avoid unnecessary repetition of MS/MS for observed common ions within the 60 s window periods. Acquisition automatically switched from MS to MS/MS mode when the base peak intensity exceeded a threshold of 150 counts s^{-1} and returned to MS mode after three MS/MS scans were acquired per selected ion (*i.e.*, 0.9 seconds for one ion or when the TIC in the MS/MS function exceeded 8,000,000 counts s^{-1}). A 0.01 second inter-scan delay was used and thus each MS scan and associated MS/MS scans required a maximum of 3.4 seconds.

UPLC data-independent acquisition (UPLC-HDMS^E) was accomplished using the IM enhanced "MS^E Continuum" function of MassLynx which utilizes IM separation in conjunction with TOF detection, using alternating low and high collision-energies. The acquisition times for the low and high collision-energy scans were 1 second each. The low energy scans were collected using a constant 4 V transfer collision-energy. For the high-energy scans, the transfer collision-energy was ramped from 15 V to 45 V during each 1 second data integration. A 0.015 second inter-scan delay was used and thus a pair of low and high collision-energy scans was collected every 2.030 seconds.

4.3.7 Data Analysis

Peptide detections from raw DDA and HDMS^E datasets were generated by ProteinLynx Global Server (PLGS Ver. 2.5.2; Waters Corporation, Milford, MA) using the default processing parameters specific to "Electrospray DDA" and "Electrospray MS^E" in PLGS data modes, respectively. Peptides identified by PLGS with sequence lengths greater than 5 amino acids were utilized for a customized BLAST search against a UniprotKB/Swiss-Prot database[260] that contained 9676 protein entries (8126 proteins and

1641 isoforms) corresponding to the *Rattus norvegicus* proteome (version 2017_11, accessed December 18, 2017). Database searching BLAST command line tool (PeptideMatchCMD version 1.0) from the Protein Information Resource (PIR).[296] The resulting protein matches were filtered to retain only proteins with at least two matched peptides. Database search results were manually compared using a spreadsheet. All averaged values are reported as 95% confidence intervals with n = 12).

4.4 Results

Rat brain tissue extracts were obtained from 2×2 mm regions of tissue sections *via* LAST for DDA and HDMS^E analysis. Whole tissue digests were obtained from the same rat specimen and used to examine the impact of separation time on DDA and HDMS^E protein identification. The collected material was subjected to enzymatic digestion prior to bottom-up proteomics analysis. Duplicate UPLC-DDA and duplicate UPLC-HDMS^E experiments were performed on laser ablated samples such that each sample obtained *via* LAST was measured a total of four times. Six UPLC-DDA and six UPLC-HDMS^E experiments, corresponding to separation times of 15, 30, 60, 90, 120, and 150 minutes, were performed on aliquots of a whole tissue digest sample. Raw UPLC-DDA and UPLC-HDMS^E data were processed and searched as indicated above.

4.4.1 DDA and HDMS^E of Brain Tissue Extracts Collected via LAST

Figure 4.1 shows an optical microscopy image of a coronal rat brain tissue section (Section 1) after sample collection *via* LAST. Each of the four laser-ablated (2×2 mm) regions correspond to a tissue sampling quadrant and are labeled Q1, Q2, Q3, and Q4. The tissue sections were 50 μm thick, and an estimated ~2 μg of material was removed from

each quadrant.[259] Three consecutive tissue sections from the same animal were used to obtain the MS results from the twelve sampled positions. The samples are identified by quadrant and section; for example, the sample obtained from Quadrant 1, Section 1 is identified as Q1S1, and so on. Microscopy images of S2 and S3 before and after LAST are shown in Supplementary Figure C.1.

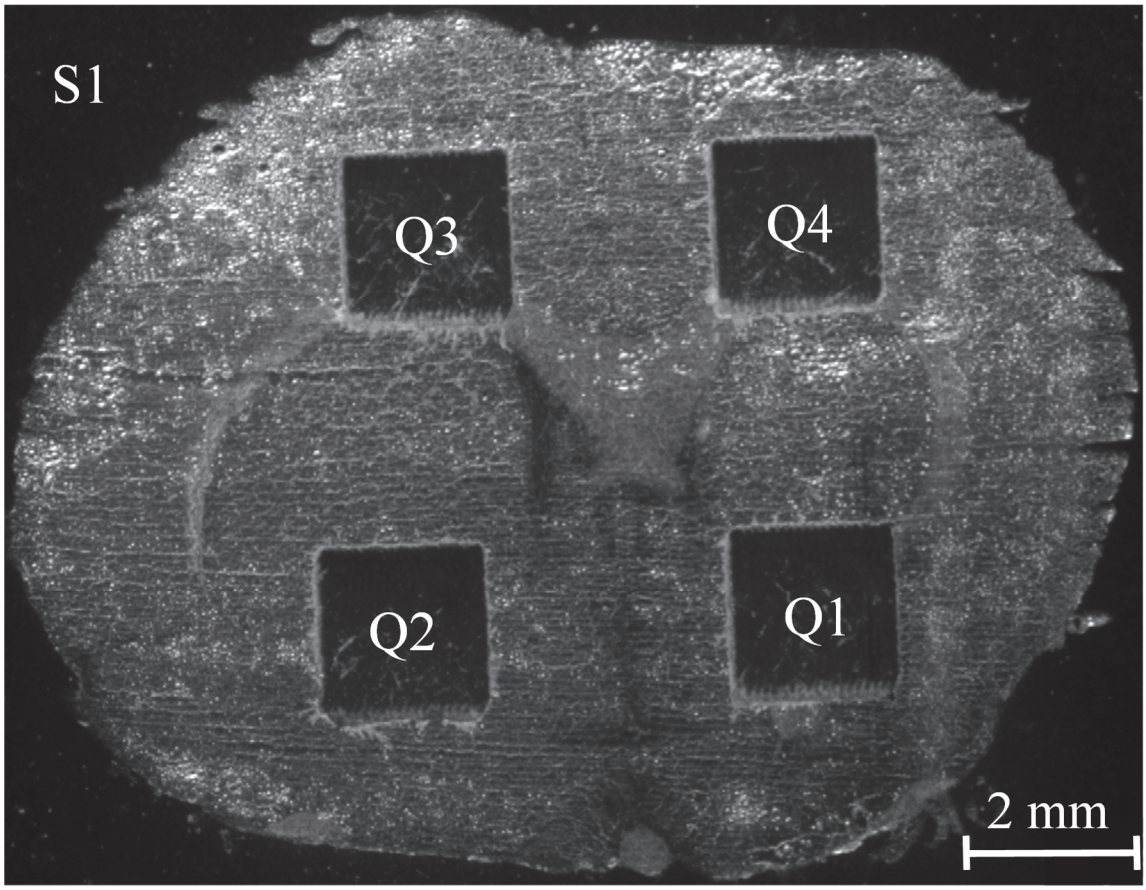

Figure 4.1. Microscopy image of rat brain whole tissue section 1 (S1) after tissue extraction *via* LAST. Rat brain tissue was collected from four spatially localized quadrants of the brain. Sampling quadrants 1 through 4 are indicated by Q1, Q2, Q3, and Q4.

Figure 4.2 shows representative base peak chromatograms (BPCs) and examples of extracted mass spectra (XMS) generated from UPLC-DDA and UPLC-HDMS^E acquisitions of Q1S3. Representative BPCs from DDA (Figure 4.2a) and HDMS^E

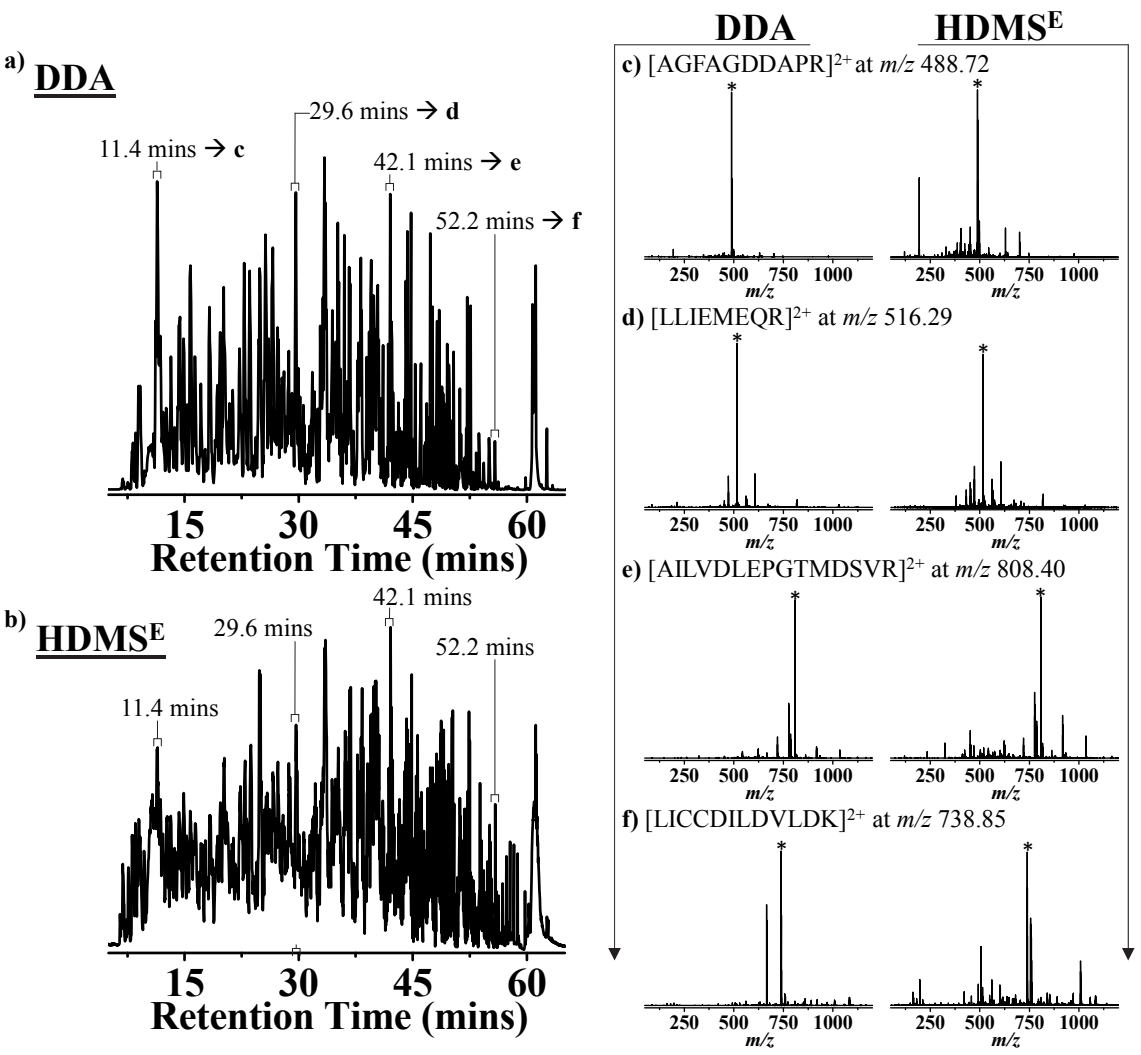

Figure 4.2. Representative UPLC-DDA and UPLC-HDMS^E data from analyses of Q1S3. Base peak chromatograms (BPCs) corresponding to peptide elution from (a) DDA and (b) HDMS^E data acquisition modes. For peaks at 11.4, 29.6, 42.1, and 52.2 minutes, precursor ion mass spectra are in (c)-(f) for DDA (left) and HDMS^E (right). Precursor ion mass spectra of (c) $[AGFAGDDAPR]^{2+}$ at *m/z* 488.72, (d) $[LLIEMEQR]^{2+}$ at *m/z* 516.29, (e) $[AILVDLEPGTMDSVR]^{2+}$ at *m/z* 808.40, and (f) $[LICCDILDVLDK]^{2+}$ at *m/z* 738.85. The base peak in each mass spectra is designated with (*) and corresponds to the named precursor peptide ion.

(Figure 4.2b) correspond to peptide elution. Corresponding precursor ion XMS for the indicated retention times are shown in Figure 4.2c through 4.2f. The precursor ion data was extracted from MS survey scans collected at a collision-energy of 4 V. This energy was selected to minimize unwanted peptide fragmentation for collection of MS survey scans

during both DDA and $HDMS^E$.[297] The chromatography data span the retention time interval from 0 to 65 minutes corresponding to the gradient of 5% to ~34% solvent B. Chromatographic features in representative BPCs from DDA and $HDMS^E$ runs are within ~2.5 seconds of each other. The small LC retention time (t_R) difference for replicate trials is not excessive[205,298] and could be caused by differences in mobile phase pH[299] from solvent evaporation or ingress of CO_2.

Representative precursor ion mass spectra generated from DDA and $HDMS^E$ are shown in Figure 4.2c through 4.2f and correspond to peptides eluting at 11.4, 29.6, 42.1, and 52.2 minutes, respectively. Comparison of mass spectra in Figure 4.2c through 4.2f shows that DDA (left) and $HDMS^E$ (right) generate similar precursor ion mass spectra and confirms the chromatographic alignment between the two data sets. For example, in both DDA and $HDMS^E$, the peptide AGFAGDDAPR eluted at t_R=11.4 minutes (Figure 4.2c). Figure 4.2d shows the mass spectra for LLIEMEQR peptide at t_R=29.6 minutes for UPLC-DDA and UPLC-$HDMS^E$. Similarly, chromatographic peaks at t_R=42.1 minutes for AILVDLEPGTMDSVR (Figure 4.2e) and at t_R=52.2 minutes for LICCDILDVLDK (Figure 4.2f) were observed. The reported *m/z* values (*i.e.*, 488.72, 516.29, 808.40, and 738.85) are from MassLynx output prior to PLGS processing and are within 50 ppm of their respective theoretical masses. The peptide LICCDILDVLDK in Figure 4.2f was detected in its modified form with carbamidomethylation of both cysteines.

The MS peak intensity maxima in the precursor ion scans were generally lower for DDA than MS^E, presumably because of the lower MS signal averaging in DDA.[206] However, in comparison to MS^E (MS^E data not shown), the use of ion mobility in $HDMS^E$ reduced ion transmission by an order of magnitude, which may be due to scattering

collisions between analyte ions and IM drift gas.[300,301] This is reflected in greater intensities in the BPC of DDA compared to HDMS^E (Figure 4.2a and 4.2b).

Results from UPLC-DDA and UPLC-HDMS^E analyses of the brain tissue samples collected *via* LAST are summarized using Table 4.1. For each of the twelve LAST samples (Column 1), the number of proteins identified by DDA (Column 2) or HDMS^E (Column 3), proteins identified by DDA only (Column 4), and the total number of proteins (Column 5), excluding duplicated protein identifications, are reported. For all twelve sampling quadrants HDMS^E identified more proteins than DDA. This enhancement ranged from a factor of about two and a half (Q1S1, Table 4.1) to five and a half (Q3S1), and the averaged enhancement for all twelve quadrants was approximately a factor of four. Although HDMS^E provided more proteins for all twelve laser ablation samples, some proteins were identified by DDA only (*viz.*, Column 4 in Table 4.1). On average, for all sampling quadrants, DDA contributed about 2% (Column 4) of the total proteins identified (Column 5).

In DDA, precursor ions are selected for *m/z*-isolation and subsequent MS/MS based on their MS signal intensities. Precursor-product ion correlation is straightforward because product ions are detected from *m/z*-isolated precursor ions. Although DDA does not explicitly use LC retention times for precursor-product ion correlation, shortening of LC separation times can shift elution profiles of lower abundance peptides to highly congested regions where their selection for MS/MS may be limited by the instrument duty cycle (Supplementary Figure C.2). Precursor-product ion correlation with HDMS^E requires a distinct "three-dimensional address" such as LC retention time, IM drift time, and *m/z* value for each precursor.[209] At shorter LC separation times, there are fewer unique retention times

Table 4.1. Summary of proteins identified by DDA and HDMS^E analyses of the 12 laser ablation sampling positions. For each LAST position (Column 1), the number of proteins identified by DDA (Column 2) and HDMS^E (Column 3) are reported. Column 4 reports the number of proteins that were identified only by DDA. Results from DDA and HDMS^E were combined, and the total number of proteins identified is provided in Column 5 with duplicate identifications removed.

LAST Sample ID	DDA	HDMS^E	DDA Only	Total
Q1S1	341	814	33	847
Q1S2	322	1020	10	1030
Q1S3	393	1674	6	1680
Q2S1	115	297	9	306
Q2S2	208	835	9	844
Q2S3	379	1723	15	1738
Q3S1	133	751	4	755
Q3S2	326	1322	19	1341
Q3S3	319	1139	34	1173
Q4S1	336	1369	19	1388
Q4S2	365	1575	14	1589
Q4S3	386	1204	48	1252

because there are fewer LC data points. Moreover, peak congestion at shorter LC separation times can result in more co-elution. To evaluate the effect of separation speed on protein identification, we acquired UPLC-DDA and UPLC-HDMS^E data at LC separation times of 15, 30, 60, 90, 120, and 150 minutes. For these experiments, a whole brain tissue section was freshly prepared as a ~184 ng/μL tryptic digest.).

Figure 4.3 shows the number of peptides (Figure 4.3a) and proteins (Figure 4.3b) identified by DDA and HDMS^E approaches at six different UPLC separation times ranging from 15 minutes to 150 minutes. As expected, shorter separation times resulted in (i) increased UPLC peak congestion (Supplemental Figure C.3) and (ii) decreased numbers of peptides and proteins identified by both DDA (empty white bars) and HDMS^E (solid black bars) analyses. Switching from the longest (150 minutes) to the shortest (15 minutes) measured UPLC separation times yielded fewer peptides (by 80%) and proteins (by 77%) identified *via* DDA; for HDMS^E, these reductions were 67% for both peptides and proteins identified. Moreover, HDMS^E outperformed DDA at all measured UPLC separation times (Figure 4.3). For example, HDMS^E identified about 2 times more peptides and about 10% more proteins from the 15 minute separation than DDA from the 150 minute separation. Hence, HDMS^E was less sensitive to UPLC congestion than DDA.

4.5 Discussion

Results from high-throughput MS-based proteomics analyses of rat brain tissue samples show that the HDMS^E approach identified more peptides and proteins than DDA. On average for the twelve LAST samples, 94 ± 2% of the proteins identified by DDA were also identified by HDMS^E. Additionally, proteins were identified more confidently with HDMS^E than DDA. Specifically, the average number of peptides detected per protein identified (from the twelve LAST samples) was 10.4 ± 1.4 for HDMS^E and 4.5 ± 0.7 for DDA.

The same precursor ions were present in corresponding DDA and HDMS^E datasets (Figure 4.2); however, 73 ± 4% of the total proteins identified from each sampling position were not found by DDA. In DDA, current duty cycle limitations may not allow precursor

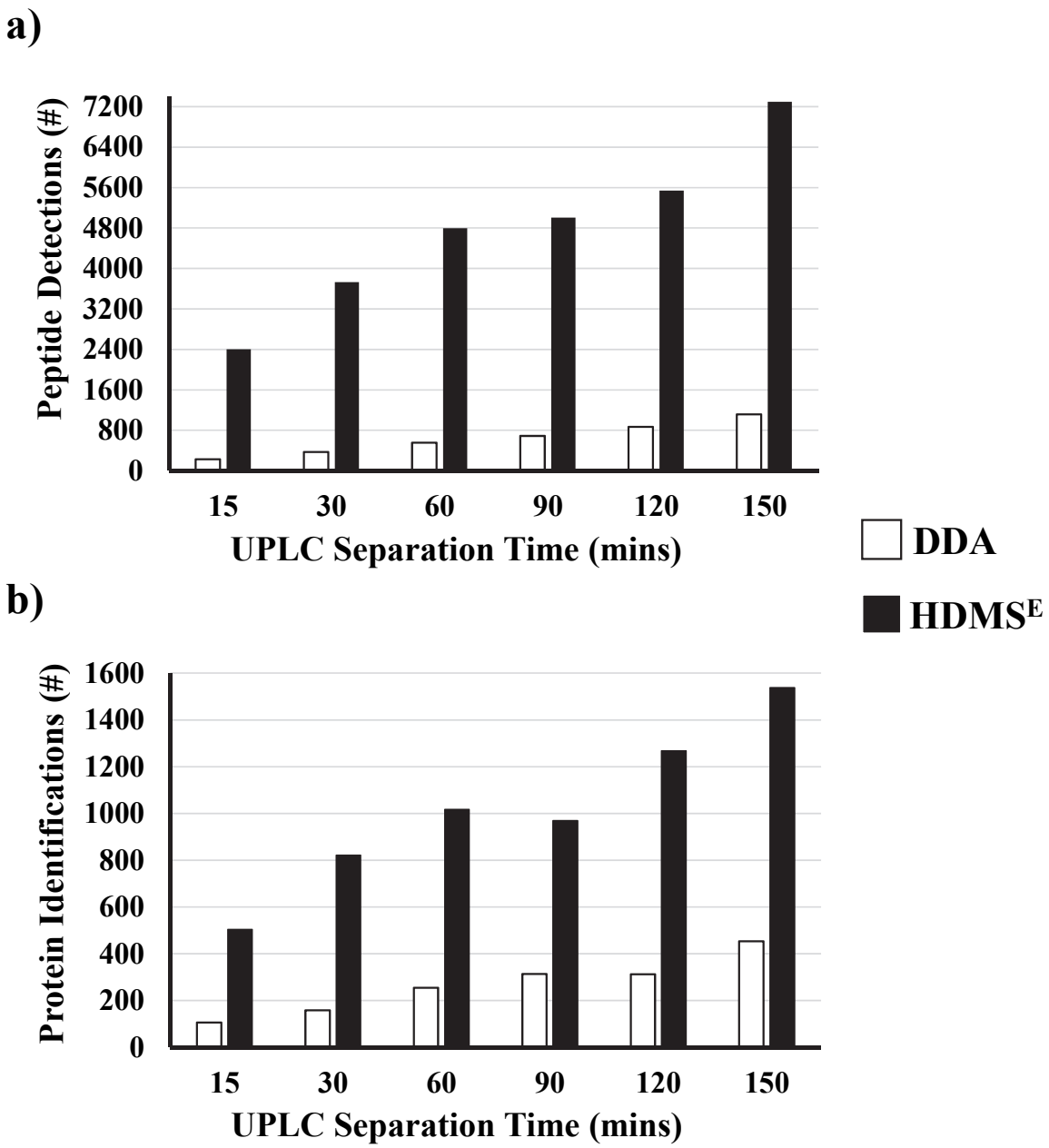

Figure 4.3. Representation of the number of (a) peptides and (b) proteins identified by DDA (empty white bars) and HDMS^E (solid black bars) as a function of separation time. Separation times of 15, 30, 60, 120, and 150 minutes were used.

ion selection for subsequent MS/MS, even if precursor ion signal intensities are above the user-defined threshold for ion selection (*i.e.*, >150 counts s^{-1} in this study). Complementary $HDMS^E$ data can reveal locations of these congested UPLC regions (*i.e.*, regions corresponding to elution of peptides not selected for MS/MS in DDA). For instance, as shown in Supplemental Figure C.2, we were able to use complementary $HDMS^E$ data to identify four low abundance peptides (in DDA data that were not selected for MS/MS) with UPLC retention times between 19.9 and 20.8 minutes

Although UPLC-IM-MS data congestions preclude peptide identification in $HDMS^E$ and adversely impact protein identification, enhancing peak capacity in any of the three dimensions (*i.e.*, UPLC, MS, or IM) could improve our ability to correlate product ions with their corresponding precursor ions. For instance, LC congestion can be addressed by using longer UPLC separations; however, increased time costs and potential sensitivity reductions associated with longer LC runs limit the utility of this approach for high-throughput applications. Moreover, increasing mass resolving power and improving mass measurement accuracy can also enhance identification of LC co-eluting isobaric peptide ions in *m/z* dimension. However, LC co-eluting isomers with the same chemical compositions cannot be differentiated by increasing the peak capacity in the *m/z* dimension. Alternatively, increasing the IM resolving power can expand "data volume" such that LC co-eluting analytes with indistinguishable *m/z* values can be assigned unique three-dimensional addresses. Conventional approaches to increase IM resolving power include hardware modifications, drift gas modifications, and/or post acquisition data processing strategies. The latter is an attractive approach for improving IM resolving power because it requires no instrumental modifications. Also, it can be applied to any post-IM tandem

MS dataset. For instance, results in Table 4.1 for rat brain proteins missed by HDMS^E (identified by DDA only, column 4) suggest that improved IM peak capacity could increase the total number of identified proteins by 1% to 3%. HDMS^E is unable to identify this small percentage of proteins primarily because of three-dimensional data convolution of peptides used for protein identification. Hence, use of IM-MS deconvolution algorithms, such as automated ion mobility deconvolution (AIMD),[131] could enhance IM peak capacity and improve precursor-product ion correlation by allowing extraction of unique IM profiles, MS, and MS/MS spectra of species that are "hidden" in convoluted IM-MS datasets.

4.6 Conclusions

Over four thousand proteins were identified by combined use of DDA and HDMS^E from high-throughput bottom-up proteomics analyses of rat brain tryptic digests from laser ablated and whole tissue samples (full list in supplemental information). Compared to collecting data in series (*e.g.*, as in DDA), collecting ion fragmentation data in parallel as implemented in HDMS^E analysis resulted in identification of about 7 times more peptides and about 4 times more proteins. Although more peptides and proteins are identified using HDMS^E (than using DDA), inherent differences between the serial and parallel data collection strategies render DDA and HDMS^E as complementary strategies. For example, the combined use of both techniques increased the numbers of proteins identified by about 1 to 3% for all measured samples. Analysis of a whole tissue digest sample as a function of UPLC separation time (*i.e.*, comparing results from the 150 minute and 15 minute UPLC separations) demonstrated that chromatographic overlap reduced the number of proteins identified by about 80% for DDA and 67% for HDMS^E. At all measured times for UPLC separation, HDMS^E identified more peptides and proteins than DDA. The ability to

pinpoint UPLC regions that are congested can provide crucial information to judiciously improve UPLC separations in a manner that would enhance MS/MS selection by DDA or decrease three-dimensional data convolutions in HDMS^{E}.

4.7 Acknowledgments

This material is based upon work supported by the National Science Foundation under Grant No. IDBR-1455668 and Grant No. CHE-1709526.

CHAPTER FIVE

Overview of Dissertation and Future Directions

5.1 Dissertation Overview

Chapter One provided a general introduction to mass spectrometry and its use in the field of bottom-up proteomics. The first half of Chapter One included an outline of ionization sources, mass analyzers, and detectors that are most commonly utilized in mass spectrometry. Detailed descriptions and/or figures were provided for all techniques used to collect the data presented in this dissertation. The second half of Chapter One described the use of mass spectrometry in high-throughput bottom-up proteomics investigations and included discussions of MS/MS data collection techniques. Chapter One ended with a justification for the research presented in Chapters Two through Four. Namely, this work is justified by the need to develop improved methods for generating precursor-product ion correlations from data collected *via* data-independent acquisition strategies. When applied to bottom-up proteomics investigations, integrating IM-MS deconvolution with IM-enhanced data-independent acquisition strategies has the potential to improve protein recovery, sequence coverages of identified proteins, overall identification confidence, and throughput.

Chapter Two introduced a novel collision-energy resolved data acquisition strategy for deconvoluting three and four component mixtures that contained IM-MS unresolved isomers. Successful deconvolution using Automated Ion Mobility Deconvolution requires detectable differences in post-IM/CID fragmentation patterns as a function of IM arrival

time. Therefore, deconvolution is more successful when using a collision-energy which yields different fragmentation patterns for all mixture components. Performing post-IM/CID at varying collision-energies is a straightforward means for identifying the collision-energy "sweet-spot" which allows successful deconvolution of all mixture components. A potential drawback of the collision-energy resolved approach is that it utilizes *m/z*-isolation prior to IM separation and CID. IM-MS deconvolution approaches which utilize *m/z*-isolation may require undesirably long data acquisition times due to unintentional ion losses incurred when operating the quadrupole as a band-pass mass filter.

Chapter Three introduced an improved approach for IM-MS deconvolution that utilizes broadband data acquisition. In broadband data acquisition, the quadrupole is operated in RF-only mode such that all detectable ions generated by ESI (in the measured *m/z* range) are transmitted to the IM cell. Broadband acquisition has multiplex and throughput advantages over the collision-energy resolved approach. Using the broadband approach, a two second data acquisition was sufficient for successfully extracting IM and MS data for two separate and unrelated pairs of isomers from a simulated complex mixture. Additionally, it was shown that broadband IM-MS deconvolution is well-suited for integration with HDMS^E methodology. Combined use of broadband IM-MS deconvolution and commercial HDMS^E data processing software improved sequence coverages for proteins identified from rat brain tissue digests.

Chapter Four reported on the use of HDMS^E methodology for improved protein recovery from bottom-up analysis of rat brain tissue samples obtained *via* laser ablation sample transfer. It was shown that use of HDMS^E resulted in more peptides and proteins identified compared to DDA. Moreover, the influence of UPLC separation time on the

numbers of peptides and proteins identified was explored. It was found that HDMS^E was less sensitive to UPLC congestion than DDA. However, some peptides and proteins were only found by DDA; this suggests that improved algorithms for generating precursor-product ion correlations in HDMS^E data are needed. As shown in Chapter Three, integrating broadband IM-MS deconvolution strategies with HDMS^E data processing software allows extraction of IM and MS data from regions of three-dimensional data convolution.

5.2 Future Directions

The United States biotherapeutic monoclonal antibody (mAb) market generates over $50 billion in yearly revenue.[302] Because patent protection for many of the most profitable biotherapeutic mAbs expires by 2019,[302] development of biosimilar alternatives is accelerating. Despite this momentum, the US FDA has approved only five biosimilar alternatives as of June 2017 according to the Purple Book, none of which have been granted interchangeable status (the ability of pharmacists to substitute a biosimilar for an originator without prescriber approval). This is due to the fact that significant gaps remain in our ability to identify and quantitate structural elements responsible for specific biological activities. Specifically, improved analytical fingerprint technologies are needed to reduce potential patient risk prior to clinical testing and encourage rapid, cost-effective product release.[303-305] According to the quality by design (QbD) approach, biotherapeutic product quality attributes (PQAs) must be rigorously characterized prior to advancement.[306] Ideally, quantitative MS-based assays would be used for correlating differences in site-specific PQAs (*e.g.*, glycosylation, oxidation, deamidation, glycation, aggregation "hotspots", *etc*.) to differences in biological activities.[307] Currently, however, biosimilarity

is demonstrated using an array of electrophoretic, chromatographic, and biophysical assays that inform only on global heterogeneity.[308] It is reasonable that the combined use of stable isotope-tagged reference standards (SITRS),[309] IM-MS deconvolution,[87,129,131-134,223,225] and DIA methodology[200] could yield a comprehensive fingerprint technology to answer the question: how similar is "similar"?

The recently developed MS-based multi-attribute method (MAM) allows simultaneous monitoring of a wide variety of PQAs.[310] The MS-based MAM can be generalized as follows: (a) proteins are digested into smaller peptides with an enzyme such as trypsin, (b) digested peptides are separated using one-dimensional liquid chromatography, and (c) separated peptides are ionized and introduced to a mass spectrometer for on-line detection. Despite simultaneously measuring a wide variety of PQAs using a single analytical platform, identifying low-abundance post-translational modifications (PTMs) using the MAM remains challenging.[311] Additionally, reliable quantitation is a persistent analytical challenge due to instrument and method variability.[311] Using the MAM in a quality control (QC) and biosimilar evaluation environment would require increased sensitivity, reduced analysis times, and improved quantitative capability. We hypothesize that integrating IM-MS deconvolution and DIA techniques to the MS-based MAM will improve method sensitivity and throughput, respectively, and concurrent use of a SITRS will increase the MAM's quantitative reproducibility. Integrating IM-MS deconvolution, DIA, and SITRS would yield a novel "all in one" method for pre-clinical MS-based evaluations of biotherapeutic mAbs that utilizes the combined strengths of state-of-the-art separations science, MS/MS data collection, and quantitative MS. Hence, we predict that improvements in aforementioned technologies will enhance our analytical

capabilities for “fingerprinting” complex sample mixtures. Future research should focus on automating both data acquisition and data interpretation aspects of multiprong approaches for handling complex and large data sets. Improvements in these areas should enhance our abilities in various other areas of omics research including identification of biomarkers and panels of makers for early detection of diseases.

APPENDICES

APPENDIX A

Supplementary Information for Chapter Two: Collision-energy Resolved Ion Mobility Characterization of Isomeric Mixtures

Table A.1. Experimental parameters used in this study.

Instrument parameter	Ternary Mixture	Quaternary Mixture
ESI flow rate (μL/min)	0.5	0.5
ESI voltage (kV)	3.5	2.25
Source temperature (C)	100	100
Sampling cone voltage (V)	0	35
Source offset voltage (V)	0	35
Trap DC bias (V)	45.8	30.8
Trap cell pressure (bar)*	1.99×10^{-5}	1.55×10^{-5}
Transfer cell pressure (bar)*	2.25×10^{-5}	$1. \times 10^{-5}$
Helium cell pressure (bar)*	1.36×10^{3}	1.36×10^{3}
IM cell pressure (bar)*	3.79×10^{-3}	3.88×10^{-3}
IM wave velocity (m/s)	652	2000
IM wave height (V)	40	40

Table A.2. Calculated *R* Values for (a) $[M_T + Li]^+$ and (b) $[M_P + 2H]^{2+}$ at each measured collision-energy. *R* values greater than 0.75 qualified as an acceptable match when comparing an isomer's deconvoluted mass spectrum to its pure counterpart.

a)

Collision-energy (V)	*R* Value		
	$[Raff + Li]^+$	$[Iso + Li]^+$	$[Cello + Li]^+$
20	--	--	--
25	--	--	--
30	0.7598	--	--
35	0.9976	--	--
40	0.9601	0.9175	--
45	0.9869	0.8198	0.9136
50	0.9629	0.8831	0.9362
55	0.8925	--	0.955
60	0.7804	--	--
65	--	0.8510	--
70	--	0.9186	--
75	0.7980	--	--
80	0.7578	--	--

b)

Collision-energy (V)	*R* Value			
	$[MGRYGF]^{2+}$	$[MFRYGG]^{2+}$	$[MFGRYG]^{2+}$	$[FRMYGG]^{2+}$
20	--	0.9278	--	--
22	--	0.8938	--	--
24	0.8335	0.9594	--	--
26	0.8260	0.9287	0.7889	0.7983
28	0.8383	--	--	--

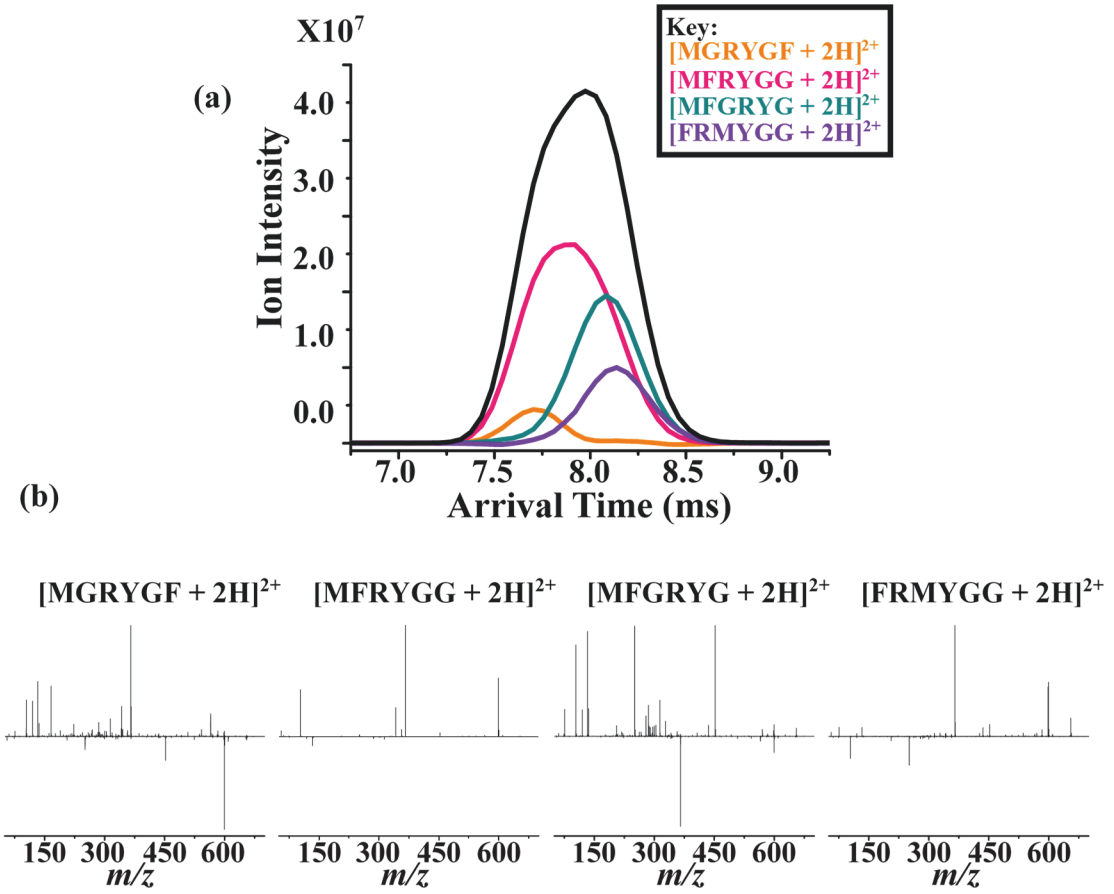

Figure A.1. Suboptimal IM-MS deconvolution at a 20 V collision-energy. (a) IM distribution for the quaternary mixture of hexapeptide isomers shown before (black profile) and after (colored profiles) deconvolution. While deconvoluted arrival times match corresponding pure samples when individually measured under similar conditions, deconvoluted CID mass spectra (b) for $[MGRYGF + 2H]^{2+}$, $[MFGRYG + 2H]^{2+}$, and $[FRMYGG + 2H]^{2+}$ have negative intensity values that are greater than 15% of the respective base peak intensities. According to the criteria described in the experimental section of the main text, deconvolution results for $[MGRYGF + 2H]^{2+}$, $[MFGRYG + 2H]^{2+}$, and $[FRMYGG + 2H]^{2+}$ were classified as unsuccessful.

APPENDIX B

Supplementary Information for Chapter Three: Broadband Ion Mobility Deconvolution for Rapid Analysis of Complex Mixtures

Table B.1. Experimental parameters used in this study. Please note that the gas pressures (*) reported in Table S1 are direct instrument readouts and have not been corrected for geometry or chemical sensitivity factors. Factory-set default settings were used for all parameters related to ion transmission.

Parameter	Value
ESI Flow rate (μL min-1)	0.5
ESI voltage (kV)	3.5
Source Temperature (°C)	150
Sampling cone voltage (V)	30
Source offset voltage (V)	0
Trap cell pressure (bar)*	~1.43×10^{-5}
Transfer cell pressure (bar)*	~1.73×10^{-5}
Helium cell pressure (bar)*	~1.36
IM cell pressure (bar)*	~3.61×10^{-3}

B.1 Differences in Pre-IM/CID between $[MGRYGF + 2H]^{2+}$ and $[FRMYGG + 2H]^{2+}$

Differences in the degree of (a) unintentional pre-IM dissociation of isomers and (b) alkali metal adduct formation can influence the observed relative intensities of IM deconvoluted isomers. In other words, anything that can reduce the relative abundance of intact molecular ions reaching to the IM cell should reduce their corresponding deconvoluted IM peak intensities. For example, if two isomers are mixed at equimolar concentrations, the isomer that forms a higher total number of alkali metal adducts and/or dissociates more easily (*i.e.*, unintentionally dissociates prior to reaching the IM cell) should exhibit a *lower* relative intensity for its intact molecular ion upon IM deconvolution.

Under our experimental conditions (*i.e.*, instrument parameter settings such as the ion acceleration voltage, ion isolation settings, background pressure, *etc.* used to acquire the data in Figure B.1), unintentional pre-IM dissociation of the FRMYGG isomer was greater than the MGRYGF isomer. Furthermore, a higher total number of alkali metal adducts (for both sodium and potassium) were observed for FRMYGG than MGRYGF. Total ion mobiligrams and averaged extracted mass spectra (XMS) are represented in Figure B.1 for pure MGRYGF (Figures B.1a and B.1b) and pure FRMYGG (Figures B.1c and B.1d) sample solutions. The yellow rectangles in Figures B.1a and B.1c are used to highlight the IM AT region from 2.08 ms to 3.18 ms that contained the doubly-charged hexapeptide ions; MS data corresponding to highlighted IM regions in Figures B.1a and B.1c were averaged to generate the XMS displayed in Figures B.1b and B.1d, respectively.

For the pure MGRYGF sample, the most abundant IM peak in the low collision-energy mobiligram (Figure B.1a; orange) had an IM AT of 2.56 ms and corresponded to the doubly-charged peptide ion $[MGRYGF + 2H]^{2+}$ (*i.e.*, $[M + 2H]^{2+}$ in Figure B.1a). IM peaks corresponding to unintentional pre-IM dissociation product ions of MGRYGF were also observed at IM ATs of 4.78 ms for $[a_4]^+$ and $[b_4]^+$ ions and 5.47 ms for $[y_4]^+$, $[b_5]^+$, and $[y_5]^+$ ions. The IM peak at 6.93 ms corresponded to the singly-charged peptide ion $[MGRYGF + H]^+$ at *m/z* 730. As shown in the averaged XMS displayed in Figure B.1b, the doubly-charged MGRYGF peptide ion and its doubly-charged metal-adducts (*i.e.*, Na- and K-adducts) corresponded to the IM AT region 2.08 ms to 3.18 ms in Figure B.1a; a neutral-loss ion (*viz*., $[M - NH_3 + 2H]^{2+}$) and an unassigned doubly-charged ion (*viz.*, at *m/z* 341.66) were also observed in this IM AT region.

Similarly, the base IM peak in the low collision-energy mobiligram of the pure FRMYGG sample (Figure B.1c, purple) had an IM AT of 2.56 ms and corresponded to the doubly-charged peptide ion $[FRMYGG + 2H]^{2+}$ (*i.e.*, $[M + 2H]^{2+}$ in Figure B.1c). IM peaks corresponding to unintentional pre-IM dissociation product ions of FRMYGG were also observed at IM ATs of 3.05 ms for $[b_2]^+$, $[b_2 - NH_3]^+$, and $[y_3]^+$ ions, 4.43 ms for $[b_3]^+$ ions, 5.54 ms for $[y_5]^+$ and $[b_4]^+$ ions, 6.23 ms for $[a_4]^+$ and $[b_5]^+$ ions, and 6.79 ms for singly-charged $[FRMYGG + H]^+$. As shown in the averaged XMS displayed in Figure B.1d, the doubly-charged FRMYGG and its doubly-charged metal-adducts (*i.e.*, Na- and K-adducts) corresponded to the IM AT region 2.08 ms to 3.18 ms in Figure B.1c; three singly-charged product ions of FRMYGGG (*viz*., $[y_3]^+$, $[b_2]^+$, and $[b_2 – NH_3]^+$ (not labeled in Figure B.1d)), three doubly-charged product ions of FRMYGG (*viz*., $[a_4]^{2+}$, $[a_5]^{2+}$, $[b_5]^{2+}$), and three unassigned singly-charged ions (*viz*., at *m/z* 256.97, 396.62, and 403.61) were also observed in this IM AT region.

Comparison of low collision-energy broadband mobiligrams (Figures B.1a and B.1c) and averaged XMS (Figures B.1b and B.1d) of the two pure hexapeptide sample solutions confirmed that the FRMYGG peptide ion exhibited a higher degree of unintentional pre-IM/CID and metal-adduct formation than its MGRYGF counterpart peptide ion. Our deconvolution results (Figures 3.2a and 3.6a) and observed pure SIM profiles (Figures 3.2d and 3.6d) are consistent with the concept of metal-adduct formation and pre-IM dissociation (as discussed above with Figure B.1) influencing the observed relative abundance of deconvoluted IM peaks (*i.e.*, intensity of the deconvoluted $[FRMYGG + 2H]^{2+}$ IM peak is 0.75 ± 0.46 times that of $[MGRYGF + 2H]^{2+}$ counterpart in Figure 3.2a).

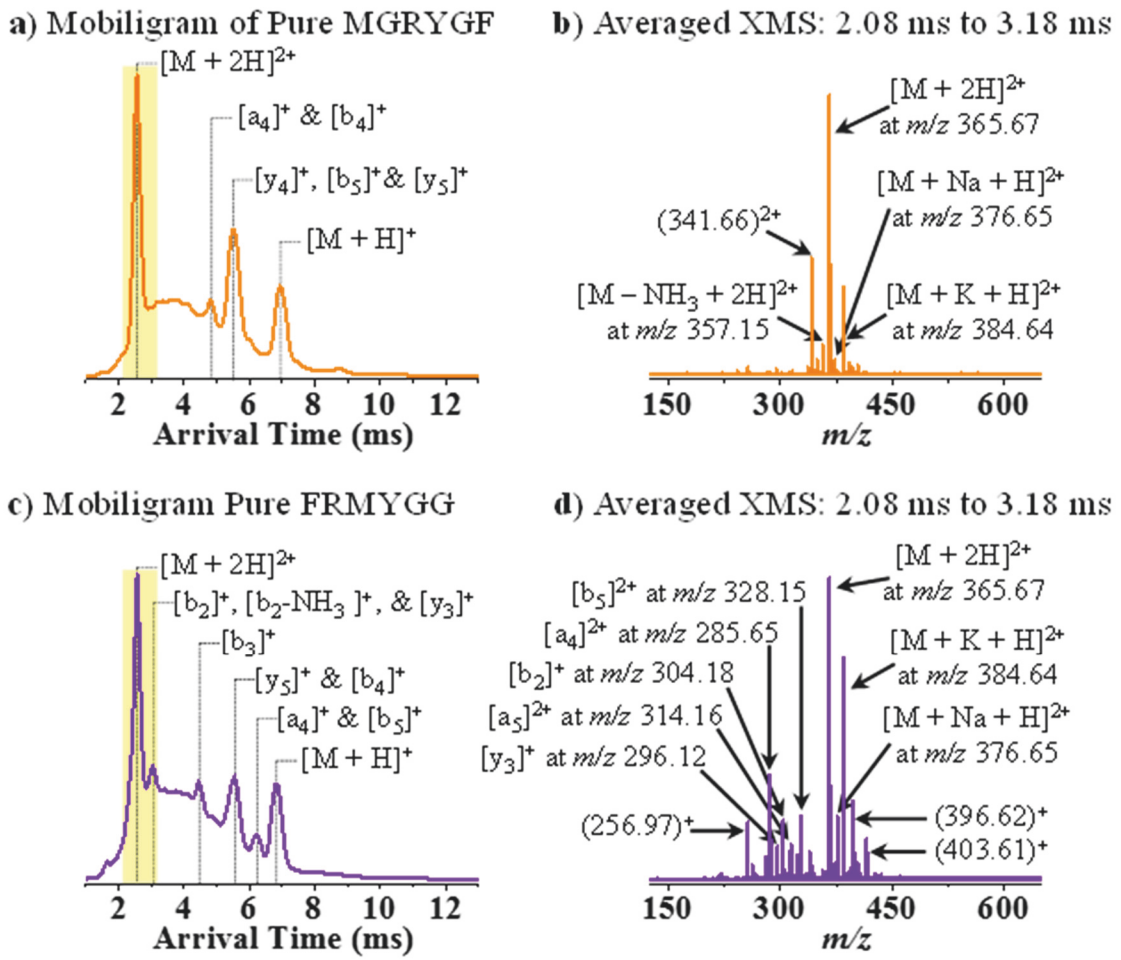

Figure B.1. Representative low collision-energy IM profiles and mass spectra for pure solutions of either MGRYGF peptide (top, data represented in orange) or FRMYGG peptide (bottom, data represented in purple). The yellow rectangles in (a) and (c) are used to highlight the IM AT region from 2.08 ms to 3.18 ms that contains the doubly-charged precursor ion (*i.e.*, $[M + 2H]^{2+}$). The MS data corresponding to highlighted IM regions in (a) and (c) were averaged to generate the extracted mass spectra (XMS) displayed in (b) and (d), respectively. Labels are provided in (a-d) to indicate identities of peptide-related fragment ions. Parentheses are used in (b) and (d) to include *m/z*-values of unidentified ions.

The pure SIM profile of FRMYGG (purple trace in Figure 3.2d) had an observable base IM peak at ~2.45 ms and a second, less intense IM peak at ~2.91 ms; this smaller IM peak corresponds to pre-IM dissociation products of the FRMYGG peptide ion. In this study, all high collision-energy broadband SIM profiles were generated by summing the

IM data corresponding to the top 10 most abundant post-IM/CID ions in the corresponding pure isomer's CID mass spectrum. Two of the top 10 most abundant post-IM/CID product ions (*i.e.*, $[b_2 - NH_3]^+$ and $[b_2]^+$) that were used to generate the pure SIM profile of FRMYGG were also unintentionally generated prior to entering the IM cell. Therefore, the pure SIM profile of FRMYGG in Figure 3.2d includes IM peaks at ~2.45 ms and ~2.91 ms because the IM data corresponding to the $[b_2 - NH_3]^+$ and $[b_2]^+$ fragment ions of FRMYGG included ion populations from both intentional post-IM/CID (IM ATs of ~2.45 ms) and unintentional pre-IM dissociation (IM ATS of ~2.91 ms). Similarly, the smaller IM peak in Figure 3.6d was characterized as belonging to unintentional pre-IM dissociation of FRMYGG ions.

B.2 Preparation of Biological Samples

Biological sample preparation was performed at Louisiana State University and all MS experiments and data processing were carried out at Baylor University. Trimethamine (tris) base was purchased from Bio-Rad (Hercules, CA, USA). DL-dithiothreitol (DTT, 98%), iodoacetamide (IAA, BioUltra, 99%) and ammonium bicarbonate (ABC, BioUltra, 99.5%) were obtained from Sigma-Aldrich (St. Louis, MO, USA). Sequencing grade modified trypsin was purchased from Promega (Madison, WI, USA). Ultrapure water with an overall ionic concentration of <0.1 ppb and a resistivity of ~18.2 MΩ·cm at 25 °C was produced in-house using a Direct-Q 3 UV water purification system (EMD Millipore Corporation, Billerica, MA, USA). Optima grade methanol and acetic acid were purchased from Fisher-Scientific (Waltham, MA, USA). Ultracentrifugation cartridges (10 kDa cut-off) were obtained from PALL (Port Washington, NY, USA). Glass microscope slides

(25×75 mm) were obtained from VWR (West Chester, PA, USA). Tris (50 mM) and ABC (10 mM) buffers were adjusted to pH values of 8.5 and 7.4, respectively.

Tissue samples were obtained from four-week-old breeding rats at the Louisiana State University School of Veterinary Medicine Division of Laboratory Animal Medicine (DLAM). All protocols for animal care and use were approved by the Institutional Animal Care and Use Committee at LSU and samples were handled as outlined by the Department of Environmental Health and Safety at BU. The animals were sacrificed by CO_2 (5 psi) exposure. Brain samples were collected, washed in 50 mM ammonium bicarbonate buffer for 30 seconds, and frozen in liquid nitrogen within 30 minutes. Frozen samples were stored at -80 °C. Thin sections were prepared with a Leica CM1850 cryostat (Leica Microsystems, Wetzlar, Germany) directly from the frozen tissue. Optimal cutting temperature (OCT) solution was used to fix one side of the sample to the cryostat support. Horizontal (transverse) rat brain sections were cut at a thickness of 50 µm, thaw-mounted on uncoated microscope slides, and stored at -80 °C.

Proteomic sample processing was performed at LSU as previously described.[259] Samples were collected into tubes and after addition of 500 µL of tris buffer (50 mM, pH 8.5), they were homogenized with a high-power ultrasonic homogenizer (Sonifier S-450, Emerson Electric, St. Louis, MO). Protein disulfide bond reduction was achieved by adding DTT to each tube to a final concentration of 10 mM. Samples were incubated at 80 ºC for 45 minutes and, after cooling at room temperature for 15 minutes, transferred to ultrafiltration cartridges (with a molecular weight cutoff of 10 kDa) and centrifuged at 14,000 g for 20 minutes. Alkylation was performed by adding 100 µL of a 20 mM IAA solution to each unit followed by incubation in the dark for 30 minutes. After incubation,

the samples were centrifuged again at 14,000 g for 10 minutes. Buffer exchanges and washing steps were performed by adding 100 µL of ABC buffer to each tube and centrifugation at 14,000 g for 10 minutes. This step was repeated twice, after which filter units were placed in clean tubes. Enzymatic digestion of the protein material was achieved using 50 µL of ABC buffer and 1 µL of a 50 ng/µL trypsin solution. Samples were incubated at 37 ºC overnight and shaken at 200 rpm. After digestion, the filter units were centrifuged at 14,000 g for 10 min, 50 µL of ABC buffer added, and centrifuged again. The filter units were removed and the tryptic mixtures were vacuum dried. The centrifuge tubes containing the dried samples were packaged in dry ice and shipped to Baylor where they were stored at -40 ºC before use.

Prior to MS analyses, dried samples were thawed and re-suspended in aqueous solutions containing 5% ACN and 0.1% FA. Based on a previous protocol,[259] sample concentration was estimated to be ~184 ng/µL. The re-suspended samples were vortexed for 30 seconds using a vortex mixer (VWR International, Radnor, PA) and centrifuged at 1,000 g for 1 minute using a microcentrifuge (Sorvall Legend Micro 21R, Thermo Scientific, Waltham, MA); the vortex/centrifuge step was repeated once.

B.3 HDMS^E Data Acquisition

The ultra-performance LC-MS/MS (UPLC-MS/MS) method was adapted from Geromanos *et al.*[206] Separation of tryptic peptides was performed using a UPLC system (nanoAcquity, Waters Corporation, Milford, MA) equipped with a Symmetry C18 pre-column (5 µm, 20 mm × 180 µm) and a BEH130 C18 analytical reversed-phase (RP) column (1.7 µm, 100 mm × 100 µm). Mobile phase solvents A and B were water and ACN, respectively (each with 0.1% formic acid (FA)). For each sample, a 4.0 µL partial loop

injection was transferred to the pre-column to desalt and pre-concentrate using 99% solvent A at a flow rate of 10 μL min^{-1} for 3 minutes. The pre-concentrated peptides were eluted to the analytical column and separated using a gradient of 5% to 45% solvent B at a flow rate of 600 nL min^{-1}; a 60-minute and 15-minute separation were performed. Following separation, the mobile phase was ramped to 99% solvent B for 5 minutes and held at 99% solvent B for an additional 5-minutes. The mobile phase was ramped to 5% solvent B over 5 minutes, and the column was re-equilibrated at 5% solvent B for 15 minutes. Throughout the separation, the UPLC column temperature was held at 40 ºC. The lock mass compound, [Glu^1]-fibrinopeptide B (at a concentration of 300 fmol μL^{-1}), was delivered at 500 nL min^{-1} by the auxiliary pump of the UPLC system to the reference sprayer of the NanoLockSpray source of the mass spectrometer.

MS was performed in positive-ion mode ESI using a Synapt G2-S HDMS that was set to sensitivity mode (*i.e.*, V mode with a typical resolution of >10,000 FWHM). The TOF analyzer was externally calibrated using a sodium formate solution that yielded ions within the measured *m/z* window of 50 to 2000; all samples were measured in the same *m/z* range. The reference sprayer (containing [Glu^1]-fibrinopeptide B at 300 fmol μl^{-1}) was sampled every 30 seconds, and all TOF MS data were lock mass corrected (post acquisition) using the doubly-charged monoisotopic ions of [Glu^1]-fibrinopeptide B at *m/z* 785.8426.

B.4 HDMS^E Data Processing

Raw HDMS^E data were analyzed using ProteinLynx Global Server (PLGS Ver. 2.5.2; Waters Corporation) using the default processing parameters specific to HDMS^E (*i.e.*, "Electrospray MS^E" in PLGS). The processed data were searched against a

UniprotKB/Swiss-Prot database[260] corresponding to the *rattus norvegicus* proteome (organism:"Rattus norvegicus (Rat) [10116]" AND proteome:up000002494, July 2016, 7,963 entries) appended with a one-time randomized version of the database using the following query parameters: precursor tryptic peptide tolerance of 5 ppm, fragment ion tolerance of 5 ppm, minimum fragment ion matches per peptide set to 3, minimum fragment ion matches per protein set to 7, minimum peptide matches per protein set 1, maximum protein mass set to 200,000,000 Da, trypsin was set as the primary digest reagent (no secondary digest reagent was used), 2 missed cleavages were allowed, fixed and variable modifications were set as carbamidomethyl C and oxidation M, respectively, and the false positive rate was set to 5.

B.5 Improper Application of AIMD to Single Component IM Peaks

Applying AIMD to single component IM peaks (mostly) yields erroneous IM profiles and mass spectra (Figure B.2). Using the Malinowski factor indicator function[261] (previously integrated with AIMD[131]), it was determined that potentially six chemical "components" were present in a post-IM/CID MS dataset that corresponded to a single component solution of isomaltotriose (LiCl was added to solution for generated of Li-adducts). As expected, AIMD successfully deconvoluted the IM profile (Figure B.2a, red trace with IM AT = 4.40 ms) and corresponding post-IM/CID mass spectrum (Figure B.2b, R = 0.91) for [isomaltotriose + Li]$^+$. Also as expected, AIMD separated "non-real" (*i.e.*, noise) components (Figure B.2a, black traces) from the real IM data of [isomaltotriose + Li]$^+$. IM traces of "non-real" components generated by AIMD have (i) non-Gaussian shapes, (ii) >15% negative values, and/or (iii) >15% negative values in their corresponding MS data. As an example of "non-real" MS data generated by improper application of

AIMD to single component IM peaks, the MS data corresponding to the highest intensity noise component (black IM trace in Figure B.2a labeled as "c") is shown in Figure B.2c.

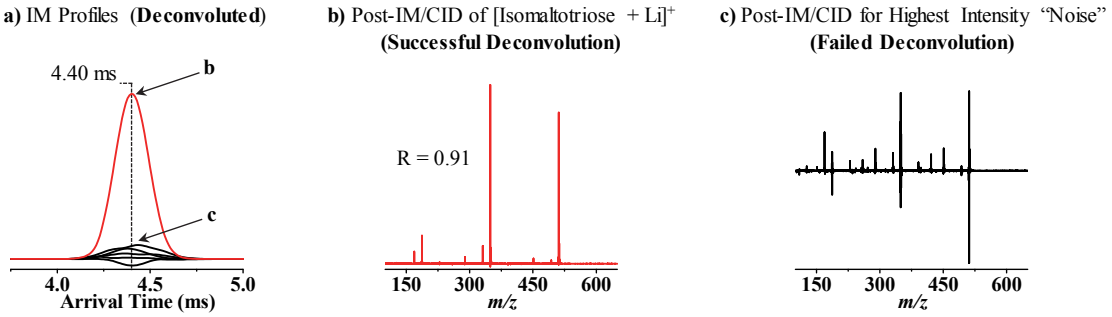

Figure B.2. Six IM profiles generated by improper application of AIMD to a single component solution of isomaltotriose (a). As expected, AIMD successfully generated IM (red trace in (a)) and post-IM/CID (b) data for [isomaltotriose + Li]$^+$. The remaining five black IM traces in (a) correspond to "non-real" (*i.e.*, noise) components. The non-real mass spectrum shown in (c) corresponds to the highest intensity noise component (arrow labeled with "c" in (a)).

B.6 Successful IM-MS Deconvolution of Components that have a 10x Concentration Difference

Broadband IM-MS deconvolution was successfully performed on IM-MS data of a solution containing 10 µM [raffinose + Li]$^+$ and 1 µM [isomaltotriose + Li]$^+$ using a 45 V collision-energy and a data acquisition time of 1 minute (Figure B.3). The deconvoluted IM ATs for [raffinose + Li]$^+$ (blue trace in Figure B.3a with an IM AT = 4.26 ms) and [isomaltotriose + Li]$^+$ (red trace in Figure B.3a with an IM AT = 4.40 ms) were within 1 IM bin of their corresponding single component validation sets, and the *R*-values were >0.70 for both isomers. When individually ran as single component solutions, the IM peak ratio of [isomaltotriose + Li]$^+$ to [raffinose + Li]$^+$ was about 10%. The deconvoluted IM peak ratio of [isomaltotriose + Li]$^+$ to [raffinose + Li]$^+$ was about 30%.

The success of AIMD depends on the presence of detectable differences in post-IM/CID mass spectra as a function of IM bin number; many fragment ions generated *via* post-IM/CID of [raffinose + Li]$^+$ and [isomaltotriose + Li]$^+$ at the 45 V collision-energy have equivalent exact masses and comparable relative intensities. In cases where IM unresolved ions generate similar post-IM/CID fragment ions (*e.g.*, as for raffinose and isomaltotriose), it is more difficult for AIMD to detect differences in post-IM/CID mass spectra when the IM unresolved ions are present at significantly different concentrations (*i.e.*, one order of magnitude or greater). Nevertheless, broadband IM-MS deconvolution *via* AIMD was successful for a solution of 10 μM [raffinose + Li]$^+$ and 1 μM [isomaltotriose + Li]$^+$.

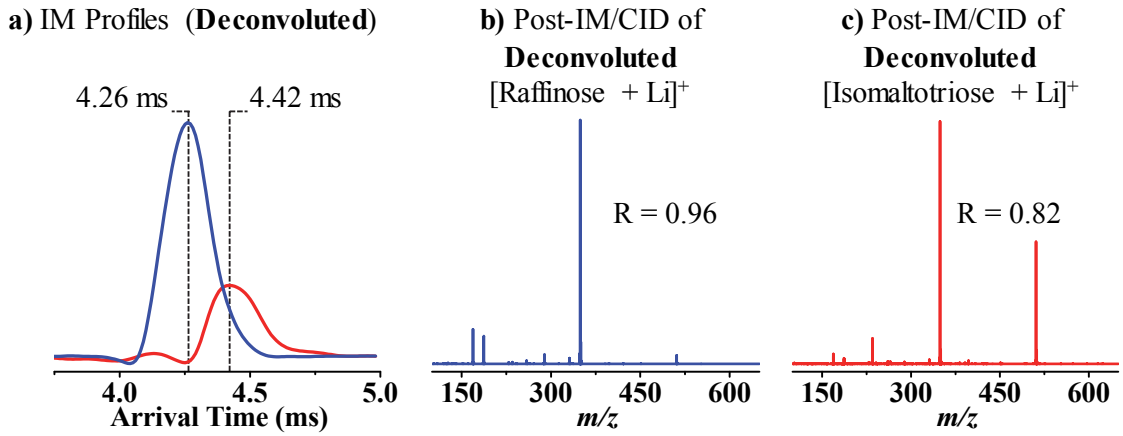

Figure B.3. Broadband deconvolution was performed on IM-MS data of a solution containing 10 μM [raffinose + Li]$^+$ and 1 μM [isomaltotriose + Li]$^+$. (a) Deconvoluted IM profiles for the two isomers and corresponding post-IM/CID mass spectra for (b) [raffinose + Li]$^+$ (blue) and (c) [isomaltotriose + Li]$^+$ (red).

B.7 Background Species from Broadband Deconvolution of the Simulated Complex Mixture

For the simulated complex mixture, broadband AIMD analysis of the IM AT region 2.08 ms to 3.18 ms allowed for deconvolution of the two hexapeptide isomers ([MGRYGF

+ 2H]$^{2+}$ and [FRMYGG + 2H]$^{2+}$ with orange and purple solid traces in Figure 3.6a, respectively) and nine additional background species (gray IM traces for background species 1 to 9 in Figure 3.6a). Representative mass spectra from AIMD output for selected background species are displayed in Figures B.4a-c (*viz.*, background species 5 (Figure B.4a), 7 (Figure B.4b), and 9 (Figure B.4c)). The IM ATs for background species 5, 7, and 9 from AIMD output were 2.770 ms, 2.978 ms, and 3.185 ms, respectively. For comparison, counterpart mass spectra corresponding to these same three IM ATs were extracted from the data for simulated complex mixture (*i.e.*, each XMS corresponds to a single IM AT data point from the raw data) and are displayed in Figures B.4d-f. Because mass spectra in Figure B.4 were acquired at a 35 V collision-energy, observed ions include pseudo-molecular and fragment ions. Differences between AIMD output and extracted mass spectra are expected (and observed) because XMS from single data points (Figures B.4d-f) are sums of all ions exiting the drift cell at a specified IM AT, whereas mass spectra from AIMD output correspond only to those ions that AIMD assigns to specific IM peaks (*i.e.*, specific background species).

Similarly, broadband AIMD analysis of the IM AT region 3.74 ms to 5.12 ms for the simulated complex mixture was utilized to deconvolute the two trisaccharide isomers ([raffinose + Li]$^{+}$ and [isomaltotriose + Li]$^{+}$ blue and red solid traces in Figure 3.7a, respectively) and ten additional background species (gray IM traces for background species 1 to 10 in Figure 3.7a). Representative mass spectra from AIMD output for selected background species are displayed in Figures B.5a-c (*viz*., background species 2 (Figure B.5a), 3 (Figure B.5b), and 9 (Figure B.5c)). The deconvoluted IM ATs for background species 2, 3, and 9 were 3.878 ms, 4.016 ms, and 5.055 ms, respectively. Counterpart mass

spectra corresponding to these same three IM ATs were extracted from the data for the simulated complex mixture (*i.e.*, each XMS corresponds to a single IM AT data point from raw data) and are displayed in Figure B.5d-f. As explained in the previous paragraph, the observed differences between mass spectra from AIMD output (Figures B.5a-c) and XMS from the raw data (Figures B.5d-f) were expected. In addition, observed common ions in AIMD output and XMS counterparts support the validity of the broadband IM deconvolution. Moreover, because AIMD does not use any curve fitting functions, Gaussian-like shapes of deconvoluted IM peaks further strengthen our confidence in broadband AIMD analysis as IM peak shapes conform to physical reality (Figure 3.7a).

B.8 Comparison of Broadband and m/z-isolated Approaches

The binary hexapeptide isomer mixture was freshly prepared, and serial dilutions were prepared at ~340 nM, ~34 nM, and ~3.4 nM concentrations to compare the sensitivities of the *m/z* isolation[28] and broadband approaches. Broadband analysis of $[M_P + 2H]^{2+}$ was re-performed on diluted samples according to the procedure described in the "Experimental" section. The settings for *m/z*-isolation of $[M_P + 2H]^{2+}$ at *m/z* 365 were identical to those used in a previous publication.[87] Except for the experimental settings used for ion isolation, identical experimental settings were utilized for broadband and *m/z*-isolated data acquisitions. Figures B.6a and B.6d represent convoluted IM and MS data collected *via m/z*-isolated and broadband data acquisitions, respectively. The base IM peaks at 2.42 ms in S6a and S6d correspond to the isomeric hexapeptide ions, and the inset post-IM/CID mass spectra in S6a and S6d are from corresponding *m/z*-isolated and broadband acquisitions, respectively. Deconvolution results for *m/z*- isolated

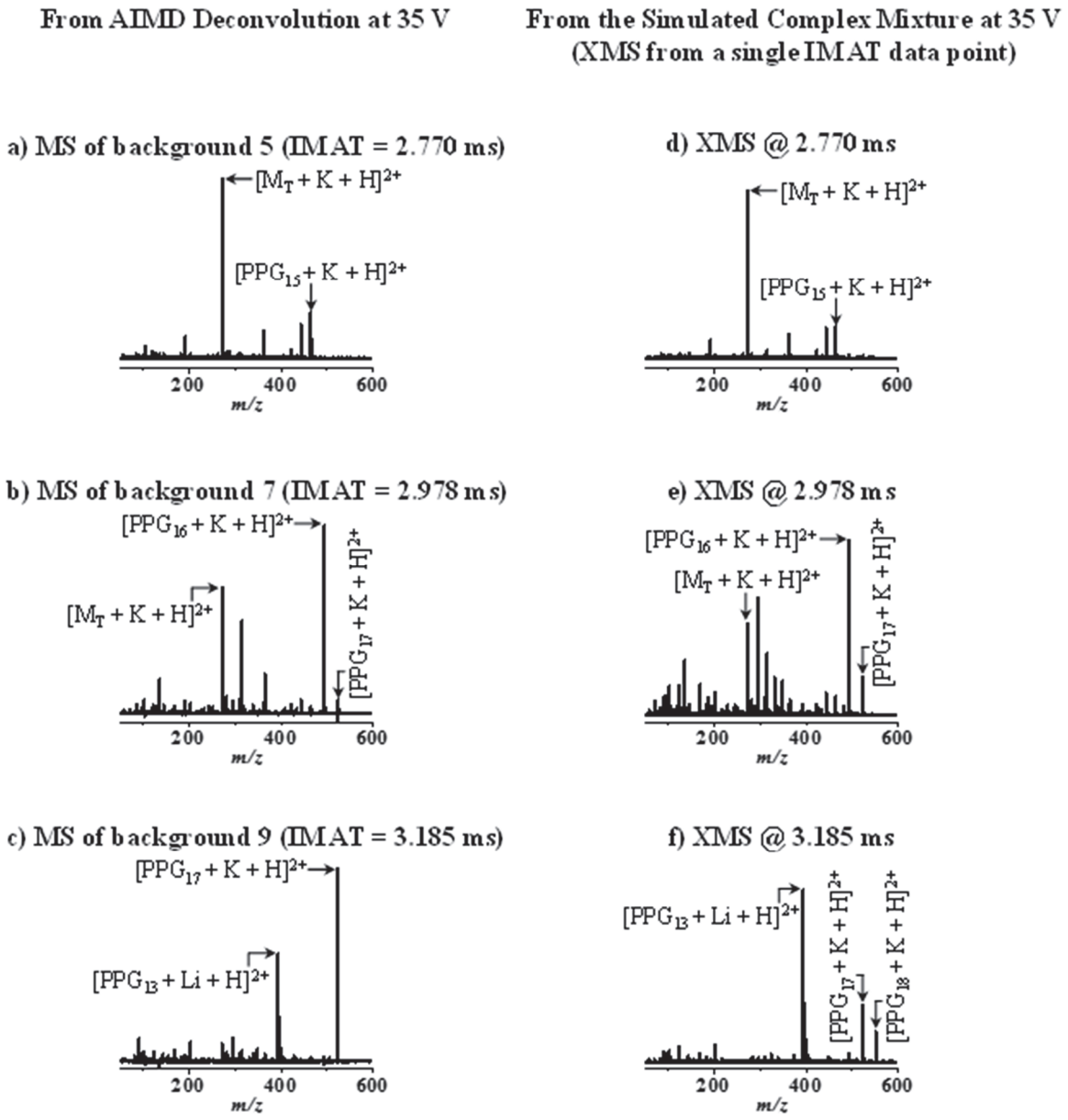

Figure B.4. Representative mass spectra of background species present in the IM AT region 2.08 ms to 3.18 ms for the simulated complex mixture. Deconvoluted mass spectra of background species (a) 5, (b) 7, and (c) 9. Raw XMS corresponding to single IM AT data points of (d) 2.770 ms, (e) 2.978 ms, and (f) 3.185 ms. Data displayed in Figure B.4 were collected using a 35 V collision-energy. Please refer to Figure 3.6a (main text) for deconvoluted IM profiles of background species 1 to 9.

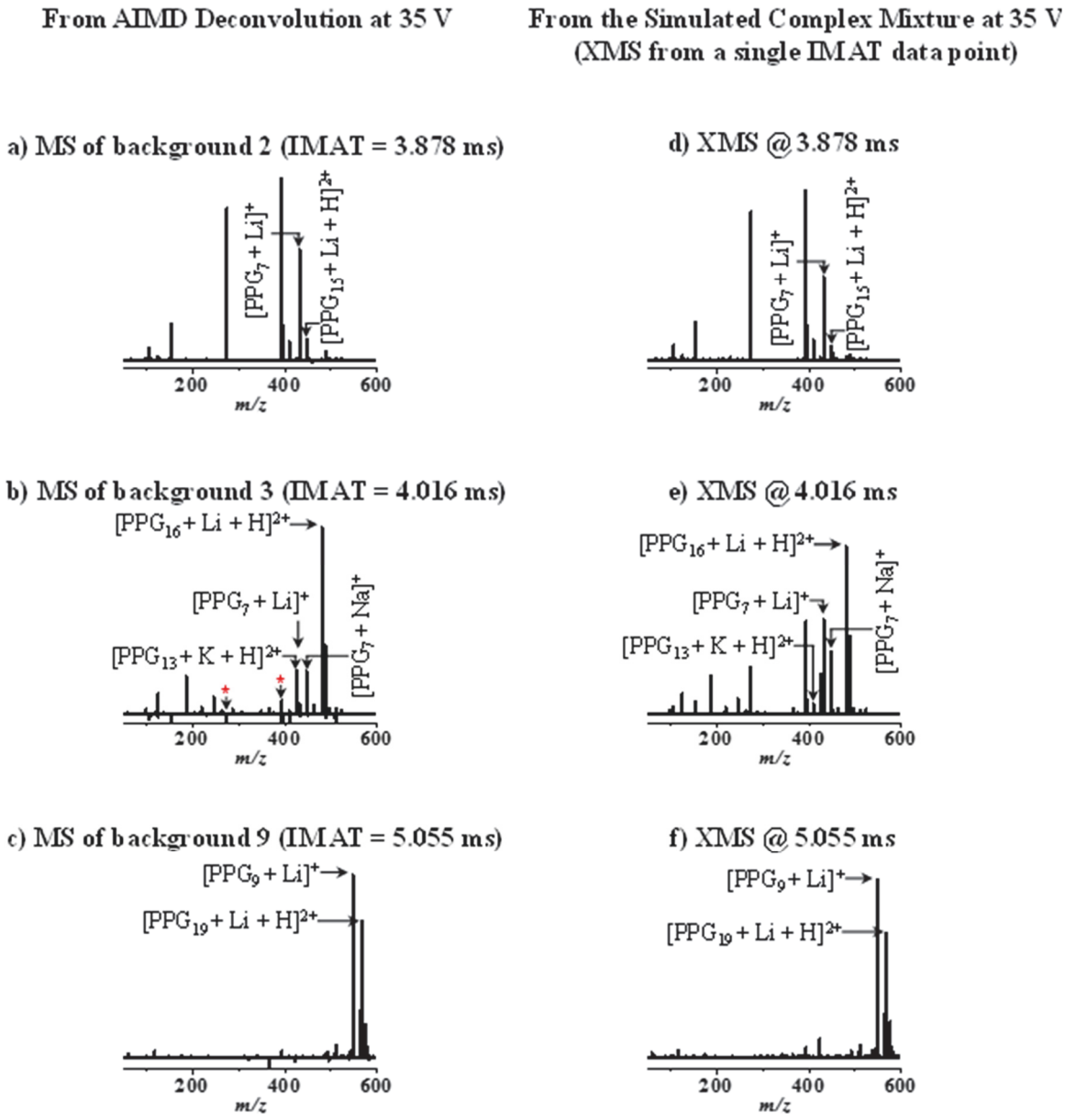

Figure B.3. Representative mass spectra of background species present in the IM AT region 3.74 ms to 5.12 ms for the simulated complex mixture. Deconvoluted mass spectra of background species (a) 2, (b) 3, and (c) 9. Raw XMS corresponding to single IM AT data points of (d) 3.878 ms, (e) 4.016 ms, and (f) 5.055 ms. Data displayed in Figure B.5 were collected using a 35 V collision-energy. The red asterisks at *m/z* 273 and 393 in (b) signify negative relative intensity values that were > 15% of the base peak intensity. Please refer to Figure 3.7a (main text) for deconvoluted IM profiles of background species 1 to 10.

(Figures B.6b-c) and broadband (Figures B.6e-f) approaches are shown for the 340 nM (column 2) and 34 nM (column 3) solutions.

As discussed in the main text (section on "Comparison of Broadband and *m/z*-isolated Approaches"), including both throughput and multiplex advantages, broadband data acquisition provides a sensitivity enhancement of more than three orders of magnitude. For example, considering only the throughput advantage,[255] deconvolution using AIMD was 10 times more sensitive for broadband acquisition than for the *m/z*-isolated approach (see Figure B.6). Both approaches allowed IM-MS deconvolution of the ~340 nM solution. The *m/z*-isolated datasets had minimal IM and MS interference from unrelated ions, however, the *m/z*-isolation approach did not allow IM-MS deconvolution of the ~34 nM or ~3.4 nM (data not shown) hexapeptide isomer solutions. As the hexapeptide isomer concentration decreased, extracting accurate MS data from IM-MS data collected *via m/z*-isolation was unsuccessful because of insufficient product ion signal. Using *m/z*-isolation and a concentration of 34 nM (Figure B.6c), the reconstructed MS data had abnormalities inconsistent with acceptable mass spectra (indicated by black "X" symbols in Figure B.6c). Additionally, the relative intensity of the deconvoluted IM peaks in Figure B.6c (*i.e.*, purple trace > orange trace) and the shape of the orange trace are inconsistent with the presented successful deconvolution of $[M_P + 2H]^{2+}$. However, AIMD assigned two groups of *m/z* values to two IM peaks with arrival times of 2.39 ms and 2.50 ms (orange and purple traces in Figure B.6c, respectively).

Broadband analysis of the ~34 nM isomer solution allowed successful IM-MS deconvolution of $[MGRYGF + 2H]^{2+}$ and $[FRMYGG + 2H]^{2+}$. However, broadband analysis of the ~3.4 nM solution was unsuccessful because AIMD did not output acceptable

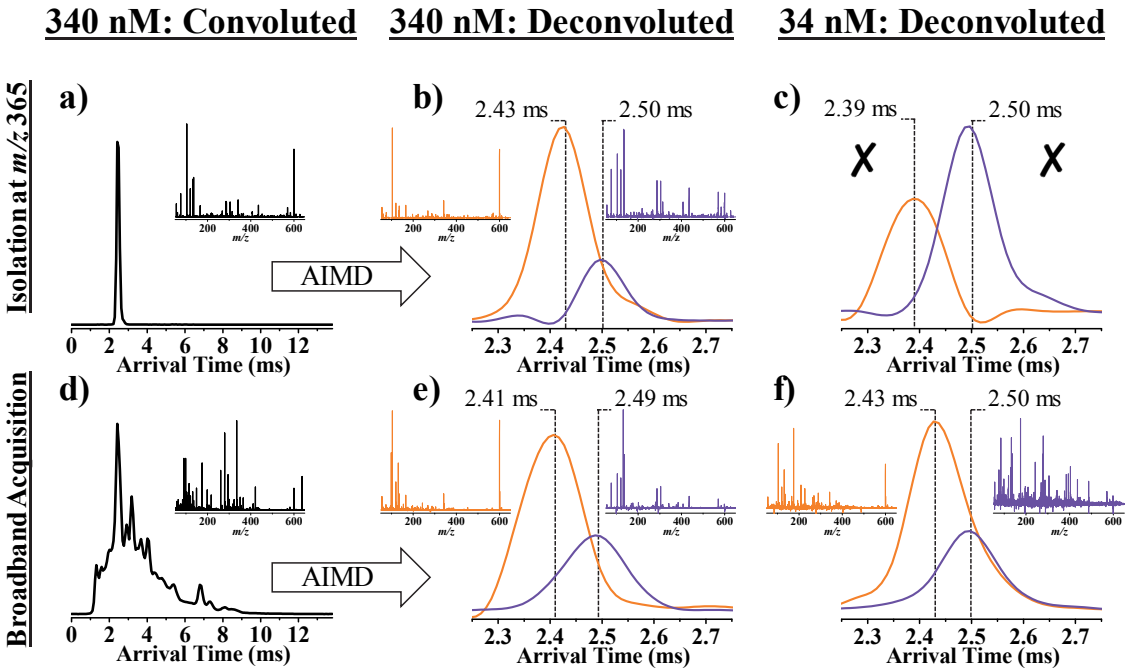

Figure B.6. Sensitivity comparison of AIMD results obtained *via* *m/z*-isolated and broadband data acquisition. A 340 nM solution of MGRYGF and FRMYGG isomers was used to collect convoluted IM-MS data *via* (a) *m/z*-isolation of $[M_P + 2H]^{2+}$ at *m/z* 365 and (d) broadband data acquisition; the black IM profiles and inset mass spectra in (a) and (d) represent convoluted IM-MS data prior to deconvolution using AIMD. Results from deconvolution of (a) and (d) from the 340 nM solution *via* AIMD are represented in (b) and (e) respectively. The 340 nM solution was diluted to 34 nM (column 3), and AIMD results from this solution are shown in (c) and (f) for *m/z*-isolated and broadband data acquisitions, respectively. A black "X" is used to indicate "unacceptable results" in (c).

post-IM/CID mass spectra (please see "Data Analysis" section in main text for details on these requirements). Despite not yielding acceptable post-IM/CID mass spectra, broadband analysis of the ~3.4 nM solution allowed AIMD assignment of two groups of *m/z* values to two IM peaks with drift times of ~2.40 ms and ~2.50 ms (not shown).

B.9 Comparison of UPLC Retention Times using 60 min. and 15 min. Separation

We hypothesized that when analyzing the same sample using longer and shorter UPLC separations, the presence of IM-MS unresolved precursor ions could be determined by comparing peptide assignments from analyses of the longer and shorter UPLC

separations; all peptide assignments in Figure B.7 were made using ProteinLynx Global Server (PLGS) software. To examine the validity of our hypothesis, we utilized PLGS to process LC-IM-MS data from 60-minute and 15-minute UPLC separations using identical solvent ramps of 5% to ~45% Solvent B for both runs. To identify potential IM-MS unresolved peptide ions, we tagged peptides that were assigned in the 60-min run but unassigned in the 15-min run. For example, PLGS processing of the 60-min UPLC run allowed successful characterization of VLSIGDGIAR (Figure B.7a); however, this peptide was not assigned by PLGS in the 15-min UPLC run (Figure B.7b). Figure B.7 contains portions of selected ion chromatograms from $HDMS^E$ analysis of a rat brain whole tissue digest that correspond to elution of VLSIGDGIAR and LIETYFSK peptides (blue and red traces in B.7a, respectively). Using a 60-min UPLC separation, retention times of $t_R = 21.98$ mins for LIETYFSK and $t_R = 22.38$ for VLSIGDGIAR were sufficiently different for their successful identification by PLGS. Upon careful examination of the IM and MS data for these peptides, it was confirmed that ions corresponding to these two peptides (*viz*., $[VLSIGDGIAR]^{2+}$ and $[LIETYFSK]^{2+}$), were IM-MS unresolved. For example, the closeness of experimentally measured ion mobility arrival times (*viz.*, 3.243 ms and 3.174 ms) and *m/z* values (500.7941 and 500.7725) for $[VLSIGDGIAR]^{2+}$ and $[LIETYFSK]^{2+}$ prevented successful PLGS assignment of VLSIGDGIAR using the dataset from the 15-min UPLC separation. The use of AIMD allowed successful deconvolution of IM profiles and post-IM/CID mass spectra of $[VLSIGDGIAR]^{2+}$ and $[LIETYFSK]^{2+}$ from the $HDMS^E$ dataset of the 15-min UPLC separation (for additional details, please refer to "Broadband Deconvolution of UPLC-$HDMS^E$ Proteomics Data" section within the main text).

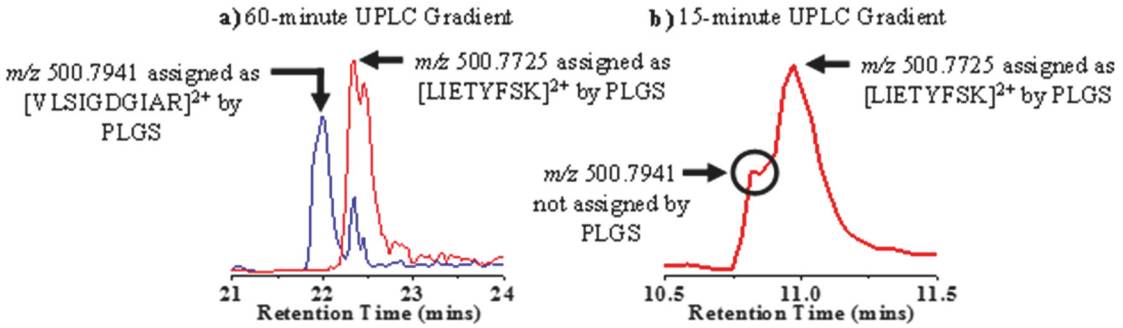

Figure B.7. Representative UPLC chromatograms corresponding to small chromatographic windows from HDMS^E analysis of a rat brain whole tissue digest using a (a) 60 minute and (b) 15 minute UPLC separation time. The peptides $[VLSIGDGIAR]^{2+}$ (blue) and $[LIETYFSK]^{2+}$ (red) are identified by PLGS using a 60 minute separation. Using a 15-minute separation, $[VLSIGDGIAR]^{2+}$ is UPLC unresolved and not identified by PLGS. The black circle in (b) indicates the unresolved elution of peptide VLSIGDGIAR.

APPENDIX C

Supplementary Information for Chapter Four: Infrared Laser Ablation Sampling Coupled with Data Independent High Resolution UPLC-IM-MS/MS for Tissue Analysis

C.1 Microscopy Images of Rat Brain Tissue Sections Before and After LAST

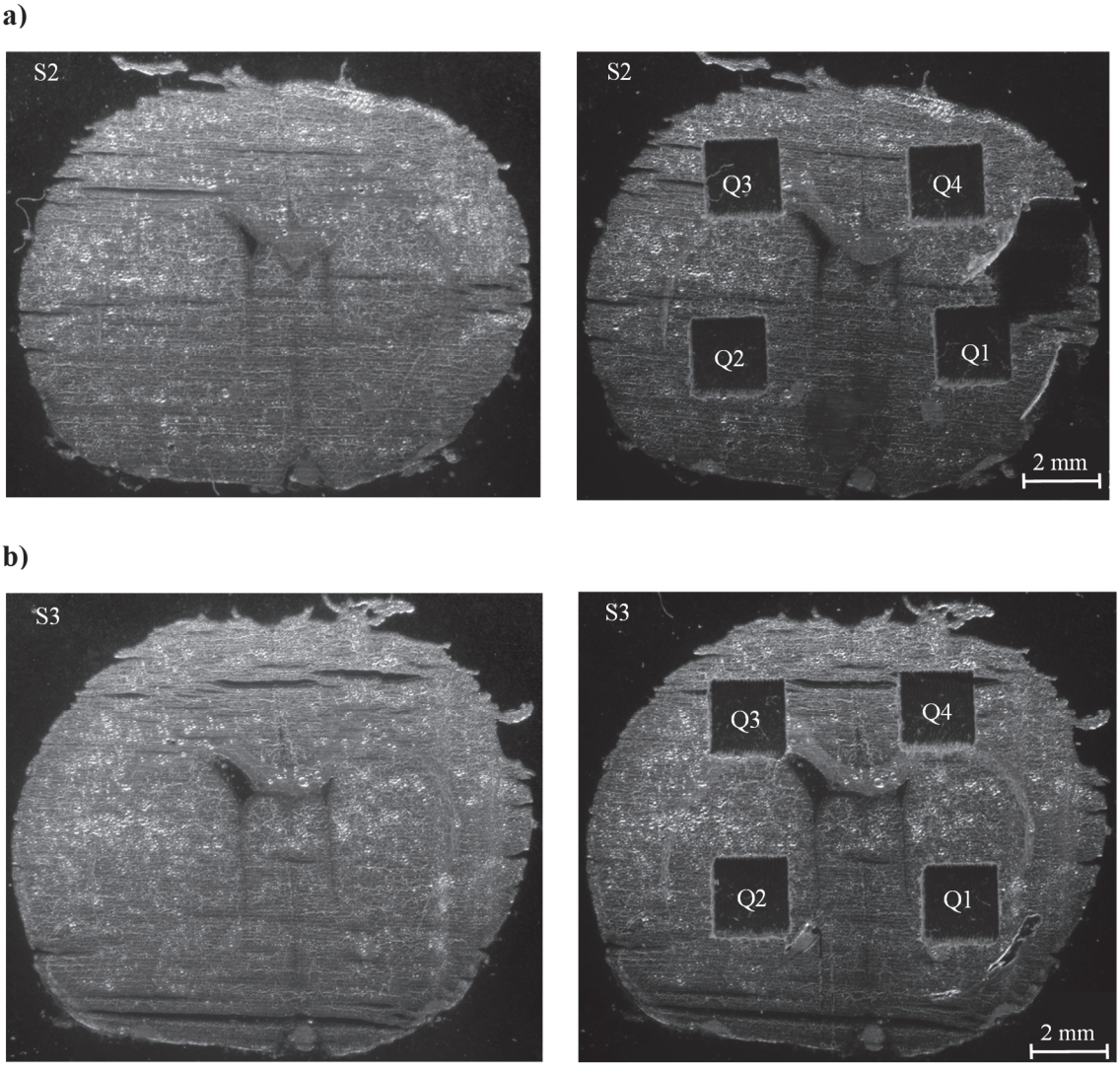

Figure C.1. Microscopy images of (a) section 2 and (b) section 3 of rat brain tissue taken before (left) and after performing LAST (right). Sections 2 and 3 are abbreviated as S2 and S3, respectively, and the four laser ablation sampling quadrants are labeled as Q1, Q2, Q3, and Q4. Sections 1 (main text), 2, and 3 were consecutive tissue sections from the same specimen.

C.2 Example of Duty Cycle Limitations in DDA Separation

Inadequate interrogation of all LC eluting compounds can be a potential limitation of DDA when the instrumental duty cycle is insufficient for *m/z* selection and fragmentation of all suitable ions. In other words, there may not be sufficient time for DDA selection of peptides that closely elute from the LC column. Figure C.2 is an averaged mass spectrum from DDA analysis of Q2 corresponding to the LC time window of 19.9 minutes to 20.8 minutes. Although this mass spectrum contained approximately 4,350 peaks that were suitable for MS/MS selection (*i.e.*, ions with counts >150 per s^{-1}, as required for DDA selection), the limited instrumental duty cycle precluded the selection of many suitable ions. For example, although ions with *m/z* values of 362.20, 622.36, 678.33, and 682.83 had counts >150 per s^{-1} in the raw DDA, they were not selected for MS/MS analysis. These four ions were detected as peptide ions by $HDMS^E$ and subsequently utilized for protein identification. Therefore, in this case, LC peak congestion was less restrictive for $HDMS^E$ than for DDA.

C.3 Correlation between UPLC Separation and UPLC Congestion

Figure C.3 shows base peak chromatograms from $HDMS^E$ analysis at different UPLC separation periods of 150 minutes (Figure C.3a), 120 minutes (Figure C.3b), 90 minutes (Figure C.3c), 60 minutes (Figure C.3d), 30 minutes (Figure C.3e), and 15 minutes (Figure C.3f). These UPLC runs correspond to the $HDMS^E$ results plotted in Figure 4.3 (*i.e.*, number of peptides and proteins identified at varying UPLC separation periods). As expected, Figure C.3 shows that reducing the UPLC separation time (while maintaining a solvent gradient of 5% to 45% acetonitrile for all runs) increases the observed UPLC peak congestion.

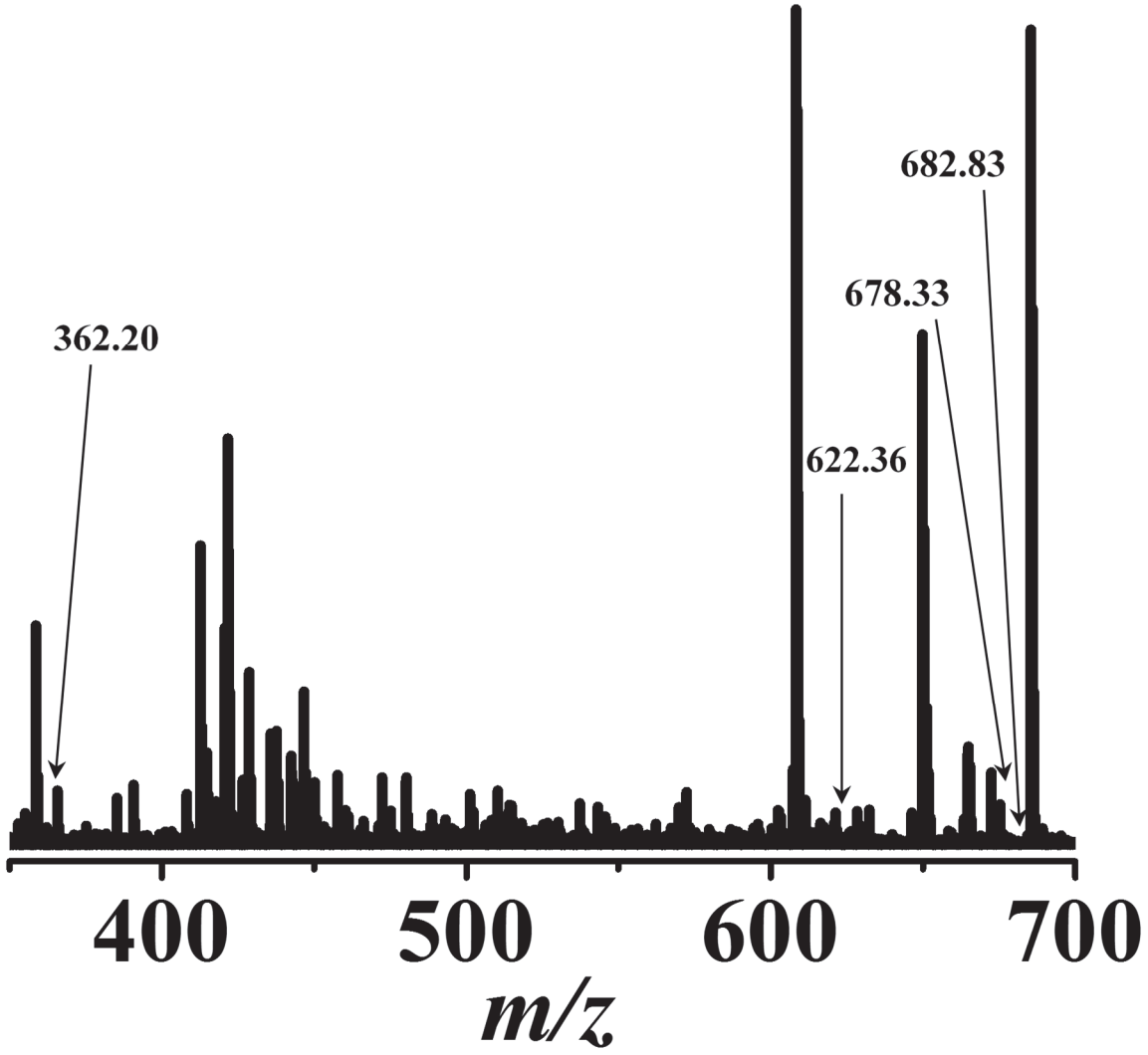

Figure C.2. Representative mass spectrum from *m/z* 350 to 700 corresponding to ions with UPLC retention times between 19.9 and 20.8 minutes from DDA analysis of Q2. Labeled arrows pointing to *m/z* values at 362.20, 622.36, 678.33, and 682.83 indicate that these peptide precursor ions were present in the DDA dataset but not selected for MS/MS because of duty cycle limitations.

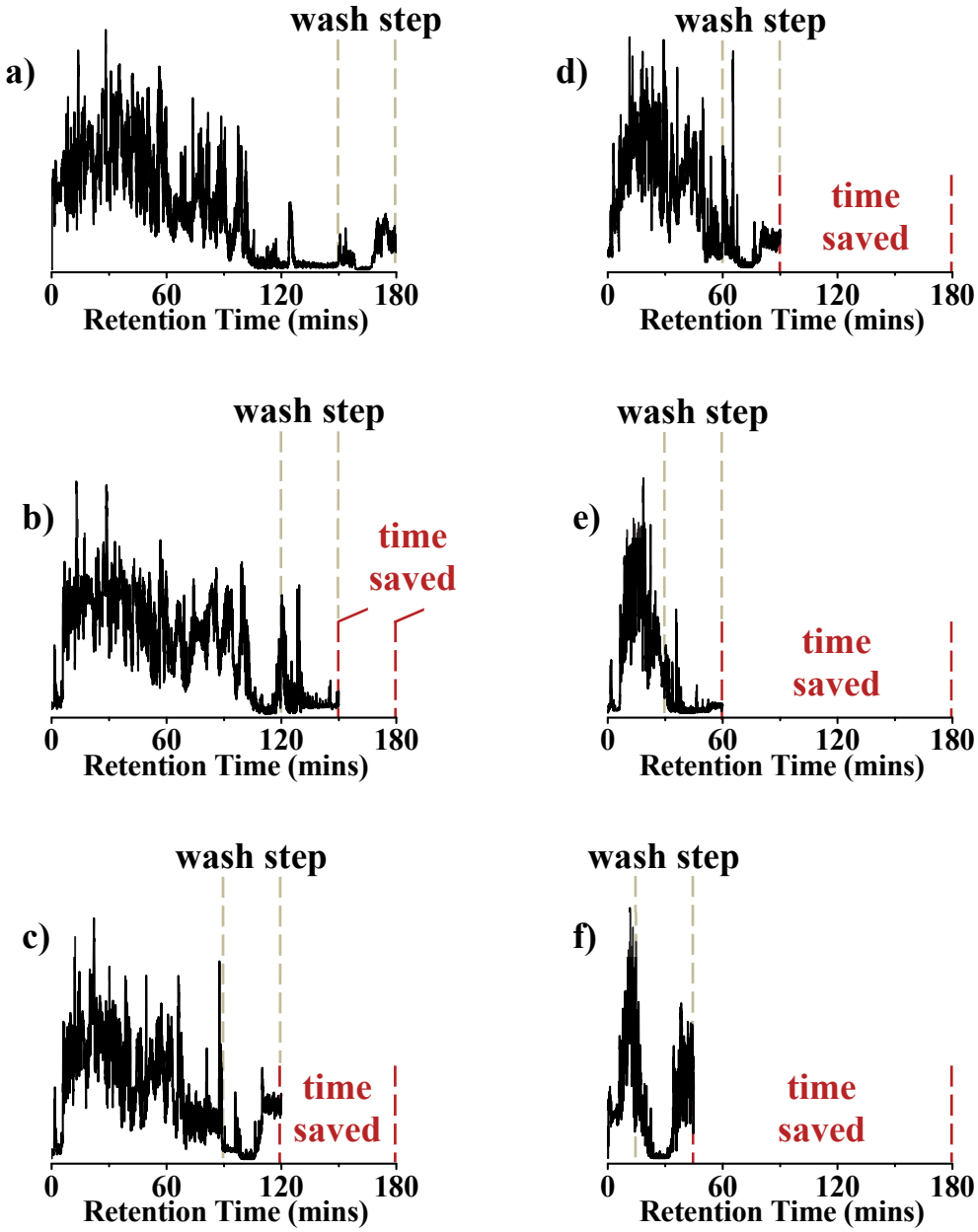

Figure C.3. Representative base peak chromatograms from HDMS^E analysis of a whole rat brain tissue digest sample using UPLC separation times of (a) 150 (b) 120 (c) 90 (d) 60 (e) 30 (f) 15 minutes. Solvent gradient compositions from the start to end of all six measured separation times were kept identical at 5% to 45% acetonitrile. The gray dashed lines in (a-f) represent the 30 minute intervals used for washing the UPLC column. The red dashed lines in (b-f) represent the time saved by using shortened separation times (as compared to (a)).

C.4 Complete List of Proteins Identified in this Study

Table C.1. Proteins identified by combined use of DDA and HDMS^E from rat brain tissues. Proteins are listed in alphabetical order

Listing #	UniprotKB #	Listing #	UniprotKB #	Listing #	UniprotKB #
1	A0A096MJY4	1403	P43322-2	2805	Q63035
2	A0A0G2JXN2	1404	P43322-3	2806	Q63041
3	A0A0G2K344	1405	P43322-4	2807	Q63046
4	A0A0G2KBC9	1406	P43425	2808	Q63060
5	A0A0G2KBC9-2	1407	P43428	2809	Q63065
6	A0JPJ7	1408	P43527	2810	Q63072
7	A0JPM9	1409	P43884	2811	Q63081
8	A0JPN3	1410	P43884-2	2812	Q63083
9	A0JPP7	1411	P45479	2813	Q63085
10	A0JPQ1	1412	P45592	2814	Q63092
11	A0JPQ4	1413	P45953	2815	Q63099
12	A0MZ67	1414	P46418	2816	Q63117
13	A0MZ67-2	1415	P46462	2817	Q63120
14	A1A5P5	1416	P46844	2818	Q63132
15	A1A5P9	1417	P46892	2819	Q63132-2
16	A1A5Q0	1418	P46953	2820	Q63135
17	A1A5Q4	1419	P47196	2821	Q63135-2
18	A1A5Q6	1420	P47245	2822	Q63147
19	A1A5Q7	1421	P47245-2	2823	Q63148
20	A1A5R8	1422	P47727	2824	Q63150
21	A1A5S1	1423	P47728	2825	Q63155
22	A1EC95	1424	P47819	2826	Q63159
23	A1IGU3	1425	P47819-2	2827	Q63164
24	A1L108	1426	P47858	2828	Q63164-2
25	A1L108-2	1427	P47860	2829	Q63170
26	A1L1J9	1428	P47861	2830	Q63180
27	A1L1K1	1429	P47942	2831	Q63184
28	A1L1K3	1430	P48037	2832	Q63186
29	A1L1K7	1431	P48056	2833	Q63190
30	A2RRU1	1432	P48500	2834	Q63198
31	A2RRU4	1433	P48675	2835	Q63210
32	A2RUV9	1434	P48679	2836	Q63226
33	A2RUW0	1435	P48721	2837	Q63259
34	A2VCW9	1436	P48763	2838	Q63269

Table C.1. Proteins identified by combined use of DDA and HDMS^E from rat brain tissues. Proteins are listed in alphabetical order—Continued

Listing #	UniprotKB #	Listing #	UniprotKB #	Listing #	UniprotKB #
35	A2VD13	1437	P48763-2	2839	Q63270
36	A4GG66	1438	P48768	2840	Q63272
37	A4L9P5	1439	P48965	2841	Q63273
38	A4L9P5-2	1440	P49000	2842	Q63279
39	A4L9P7	1441	P49002	2843	Q63302
40	A4L9P8	1442	P49185	2844	Q63312
41	A6N6J5	1443	P49186	2845	Q63313
42	A6YP92	1444	P49186-2	2846	Q63342
43	A7E3N2	1445	P49187	2847	Q63344
44	A7VJC2	1446	P49303	2848	Q63345
45	A7VJC2-2	1447	P49303-2	2849	Q63347
46	A7VJC2-3	1448	P49432	2850	Q63355
47	A7VJC2-4	1449	P49744	2851	Q63356
48	A8WCF8	1450	P49793	2852	Q63357
49	A9UMV8	1451	P49793-2	2853	Q63358
50	A9ZSY0	1452	P49797	2854	Q63369
51	B0BMX9	1453	P49803	2855	Q63372
52	B0BN85	1454	P49804	2856	Q63372-1
53	B0BN93	1455	P49805	2857	Q63372-10
54	B0BNA5	1456	P49805-2	2858	Q63372-11
55	B0BND0	1457	P49806	2859	Q63372-12
56	B0BNF1	1458	P49816	2860	Q63372-13
57	B0BNG0	1459	P49816-2	2861	Q63372-3
58	B0BNK7	1460	P49816-3	2862	Q63372-4
59	B0BNK8	1461	P49816-4	2863	Q63372-5
60	B0BNK9	1462	P49911	2864	Q63372-6
61	B0BNN3	1463	P50123	2865	Q63372-7
62	B0K019	1464	P50123-2	2866	Q63372-8
63	B0K020	1465	P50137	2867	Q63372-9
64	B0LPN4	1466	P50232	2868	Q63373
65	B0LPN4-2	1467	P50233	2869	Q63373-2
66	B1H222	1468	P50279	2870	Q63374
67	B1H224	1469	P50279-2	2871	Q63374-10
68	B1H228	1470	P50279-3	2872	Q63374-2
69	B1H234	1471	P50282	2873	Q63374-3
70	B1H268	1472	P50298	2874	Q63374-4
71	B1H285	1473	P50398	2875	Q63374-5

Table C.1. Proteins identified by combined use of DDA and HDMS^E from rat brain tissues. Proteins are listed in alphabetical order—Continued

Listing #	UniprotKB #	Listing #	UniprotKB #	Listing #	UniprotKB #
72	B1WBT0	1474	P50399	2876	Q63374-6
73	B1WBU5	1475	P50408	2877	Q63374-7
74	B1WBU8	1476	P50411	2878	Q63374-8
75	B1WC10	1477	P50503	2879	Q63374-9
76	B1WC58	1478	P50545	2880	Q63376
77	B2DD29	1479	P50545-2	2881	Q63376-2
78	B2GUV7	1480	P50554	2882	Q63376-3
79	B2GUY0	1481	P50745	2883	Q63376-4
80	B2GUY1	1482	P50745-2	2884	Q63376-5
81	B2GUY2	1483	P50745-3	2885	Q63376-6
82	B2GUZ1	1484	P50745-4	2886	Q63376-7
83	B2GUZ5	1485	P50753	2887	Q63376-8
84	B2GV05	1486	P50753-2	2888	Q63377
85	B2GV06	1487	P50878	2889	Q63406
86	B2GV24	1488	P50904	2890	Q63413
87	B2GV50	1489	P51111	2891	Q63416
88	B2GV54	1490	P51146	2892	Q63418
89	B2GV87	1491	P51156	2893	Q63421
90	B2GV87-2	1492	P51179	2894	Q63425
91	B2GV87-3	1493	P51538	2895	Q63429
92	B2RYD2	1494	P51556	2896	Q63433
93	B2RYD2-2	1495	P51574	2897	Q63448
94	B2RYF7	1496	P51590	2898	Q63450
95	B2RYG6	1497	P51635	2899	Q63454
96	B2RYJ4	1498	P51639	2900	Q63468
97	B2RYJ8	1499	P51647	2901	Q63470
98	B2RYM0	1500	P51650	2902	Q63470-2
99	B2RYM5	1501	P51650-2	2903	Q63472
100	B2RYR0	1502	P51673	2904	Q63481
101	B2RYW9	1503	P51792	2905	Q63484
102	B2RZ55	1504	P51792-2	2906	Q63486
103	B2RZ86	1505	P51799	2907	Q63487
104	B3DMA2	1506	P51840	2908	Q63487-2
105	B3EY83	1507	P51842	2909	Q63503
106	B3GNI6	1508	P51868	2910	Q63504
107	B3GNI6-2	1509	P51869	2911	Q63505
108	B3GNI6-3	1510	P51870	2912	Q63514

Table C.1. Proteins identified by combined use of DDA and HDMS^E from rat brain tissues. Proteins are listed in alphabetical order—Continued

Listing #	UniprotKB #	Listing #	UniprotKB #	Listing #	UniprotKB #
109	B3STU3	1511	P51871	2913	Q63518
110	B4F766	1512	P51882	2914	Q63520
111	B4F785	1513	P51907	2915	Q63525
112	B4F7A7	1514	P51952	2916	Q63530
113	B4F7E8	1515	P52191	2917	Q63531
114	B4F7E9	1516	P52287	2918	Q63537
115	B5DEL3	1517	P52296	2919	Q63537-2
116	B5DF21	1518	P52303	2920	Q63538
117	B5DF27	1519	P52303-2	2921	Q63540
118	B5DF89	1520	P52481	2922	Q63544
119	B5DF91	1521	P52590	2923	Q63553
120	B5DF93	1522	P52631	2924	Q63556
121	B5DFA1	1523	P52632	2925	Q63560
122	B5DFC8	1524	P52873	2926	Q63560-2
123	B5DFC9	1525	P52909	2927	Q63562
124	B5DFH9	1526	P53534	2928	Q63563
125	B5DFM7	1527	P53565	2929	Q63563-2
126	B5DFN2	1528	P53669	2930	Q63569
127	C0HJX2	1529	P53670	2931	Q63570
128	C0HJX3	1530	P53670-2	2932	Q63584
129	C0HL12	1531	P53670-3	2933	Q63598
130	D2XV59	1532	P53767	2934	Q63603
131	D3Z8E6	1533	P53809	2935	Q63610
132	D3Z8K2	1534	P53812-2	2936	Q63610-2
133	D3Z8N4	1535	P54258	2937	Q63610-3
134	D3Z8X7	1536	P54275	2938	Q63615
135	D3Z8X7-2	1537	P54282	2939	Q63616
136	D3Z987	1538	P54282-2	2940	Q63617
137	D3Z9Z9	1539	P54287	2941	Q63618
138	D3ZA12	1540	P54311	2942	Q63618-3
139	D3ZA50	1541	P54313	2943	Q63618-4
140	D3ZA76	1542	P54645	2944	Q63622
141	D3ZA76-2	1543	P54690	2945	Q63622-2
142	D3ZAF6	1544	P54708	2946	Q63622-3
143	D3ZAL8	1545	P54708-2	2947	Q63622-4
144	D3ZAQ5	1546	P54748	2948	Q63622-5
145	D3ZAR1	1547	P54748-2	2949	Q63622-6

Table C.1. Proteins identified by combined use of DDA and HDMS^E from rat brain tissues. Proteins are listed in alphabetical order—Continued

Listing #	UniprotKB #	Listing #	UniprotKB #	Listing #	UniprotKB #
146	D3ZAW2	1548	P54748-3	2950	Q63622-7
147	D3ZBM7	1549	P54748-4	2951	Q63623
148	D3ZBN0	1550	P54748-5	2952	Q63624
149	D3ZBP4	1551	P54748-6	2953	Q63625
150	D3ZBP4-2	1552	P54758	2954	Q63625-2
151	D3ZCM9	1553	P54759	2955	Q63627
152	D3ZD32	1554	P54759-2	2956	Q63632
153	D3ZE55	1555	P54777	2957	Q63633
154	D3ZE55-2	1556	P54921	2958	Q63633-2
155	D3ZEF4	1557	P55016	2959	Q63635
156	D3ZEN0	1558	P55051	2960	Q63638
157	D3ZF42	1559	P55053	2961	Q63639
158	D3ZF92	1560	P55062	2962	Q63644
159	D3ZG52	1561	P55063	2963	Q63648
160	D3ZGB1	1562	P55067	2964	Q63651
161	D3ZGS3	1563	P55068	2965	Q63661
162	D3ZGX1	1564	P55068-2	2966	Q63663
163	D3ZH22	1565	P55094	2967	Q63665
164	D3ZHA0	1566	P55146	2968	Q63665-2
165	D3ZHH1	1567	P55161	2969	Q63665-3
166	D3ZHP7	1568	P55266	2970	Q63666
167	D3ZHS6	1569	P55280	2971	Q63666-2
168	D3ZHV2	1570	P55281	2972	Q63666-3
169	D3ZJ96	1571	P55926	2973	Q63666-4
170	D3ZJ96-2	1572	P55926-2	2974	Q63688
171	D3ZJP6	1573	P55926-3	2975	Q63689
172	D3ZK93	1574	P56163	2976	Q63692
173	D3ZKB9	1575	P56163-4	2977	Q63699
174	D3ZKD3	1576	P56223	2978	Q63704
175	D3ZKX9	1577	P56522	2979	Q63707
176	D3ZLH5	1578	P56536	2980	Q63713
177	D3ZML2	1579	P56558	2981	Q63716
178	D3ZML2-2	1580	P56574	2982	Q63734
179	D3ZN43	1581	P56603	2983	Q63754
180	D3ZND0	1582	P56719	2984	Q63755
181	D3ZPX4	1583	P56720	2985	Q63767
182	D3ZQF9	1584	P56720-1	2986	Q63767-2

Table C.1. Proteins identified by combined use of DDA and HDMS^E from rat brain tissues. Proteins are listed in alphabetical order—Continued

Listing #	UniprotKB #	Listing #	UniprotKB #	Listing #	UniprotKB #
183	D3ZQG6	1585	P56741	2987	Q63788
184	D3ZSC8	1586	P56932	2988	Q63789
185	D3ZSZ3	1587	P57093	2989	Q63796
186	D3ZTL1	1588	P57097	2990	Q63797
187	D3ZTQ1	1589	P57113	2991	Q63802
188	D3ZTV3	1590	P57760	2992	Q63803
189	D3ZU57	1591	P58365	2993	Q63862
190	D3ZU96	1592	P58366	2994	Q63862-2
191	D3ZUA0	1593	P58751	2995	Q63862-3
192	D3ZUC4	1594	P58751-2	2996	Q63941
193	D3ZUC6	1595	P58751-3	2997	Q63942
194	D3ZUQ0	1596	P58775	2998	Q63965
195	D3ZVB0	1597	P58775-2	2999	Q63ZV7
196	D3ZVM4	1598	P59215	3000	Q63ZY7
197	D3ZWK4	1599	P59215-2	3001	Q64057
198	D3ZX08	1600	P59241	3002	Q64119
199	D3ZXK7	1601	P59622	3003	Q64122
200	D3ZXS4	1602	P59895	3004	Q641W4
201	D3ZXW3	1603	P59924	3005	Q641W9
202	D3ZYB7	1604	P59926	3006	Q641X2
203	D3ZYR1	1605	P60123	3007	Q641X7
204	D3ZZ80	1606	P60192	3008	Q641Y5
205	D3ZZL9	1607	P60203	3009	Q641Y6
206	D3ZZW6	1608	P60570	3010	Q641Y8
207	D4A055	1609	P60571	3011	Q641Z1
208	D4A055-1	1610	P60669	3012	Q641Z2
209	D4A1F2	1611	P60711	3013	Q641Z4
210	D4A1F2-2	1612	P60756	3014	Q641Z6
211	D4A208	1613	P60825	3015	Q64230
212	D4A2K4	1614	P60881	3016	Q64270
213	D4A3K5	1615	P60881-2	3017	Q64289
214	D4A4D7	1616	P60892	3018	Q642A7
215	D4A523	1617	P60901	3019	Q642B3
216	D4A5U3	1618	P60924	3020	Q642B6
217	D4A612	1619	P61023	3021	Q642C0
218	D4A615	1620	P61078	3022	Q64303
219	D4A631	1621	P61107	3023	Q64319

Table C.1. Proteins identified by combined use of DDA and HDMS^E from rat brain tissues. Proteins are listed in alphabetical order—Continued

Listing #	UniprotKB #	Listing #	UniprotKB #	Listing #	UniprotKB #
220	D4A666	1622	P61203	3024	Q64359
221	D4A6D8	1623	P61203-2	3025	Q64380
222	D4A6L0	1624	P61206	3026	Q64428
223	D4A702	1625	P61212	3027	Q64535
224	D4A7N1	1626	P61227	3028	Q64535-2
225	D4A7P2	1627	P61265	3029	Q64535-3
226	D4A7T3	1628	P61312	3030	Q64541
227	D4A7V9	1629	P61589	3031	Q64542
228	D4A8G9	1630	P61751	3032	Q64542-2
229	D4A929	1631	P61765	3033	Q64542-3
230	D4A9R4	1632	P61765-2	3034	Q64542-4
231	D4AB34	1633	P61810	3035	Q64548
232	D4AB66	1634	P61943	3036	Q64548-2
233	D4AB98	1635	P61954	3037	Q64550
234	D4ABB8	1636	P61959	3038	Q64559
235	D4ABL6	1637	P61980	3039	Q64559-1
236	D4ABL6-2	1638	P61983	3040	Q64560
237	D4ABW7	1639	P62024	3041	Q64565
238	D4ABX8	1640	P62138	3042	Q64566
239	D4ABY2	1641	P62142	3043	Q64566-2
240	D4AC13	1642	P62166	3044	Q64568
241	D4ACE5	1643	P62166-2	3045	Q64568-10
242	D4ACX8	1644	P62168	3046	Q64568-11
243	D4AD02	1645	P62193	3047	Q64568-12
244	D4AD53	1646	P62198	3048	Q64568-2
245	D4AE41	1647	P62250	3049	Q64568-3
246	D4AEC2	1648	P62260	3050	Q64568-4
247	E9PT23	1649	P62332	3051	Q64568-5
248	E9PT87	1650	P62425	3052	Q64568-6
249	E9PTA2	1651	P62494	3053	Q64568-7
250	E9PU17	1652	P62501	3054	Q64568-8
251	F1LM93	1653	P62510	3055	Q64568-9
252	F1LMY4	1654	P62510-2	3056	Q64573
253	F1LMZ8	1655	P62603	3057	Q64578
254	F1LN46	1656	P62628	3058	Q64581
255	F1LNJ2	1657	P62630	3059	Q64595
256	F1LP64	1658	P62632	3060	Q64598

Table C.1. Proteins identified by combined use of DDA and HDMS^E from rat brain tissues. Proteins are listed in alphabetical order—Continued

Listing #	UniprotKB #	Listing #	UniprotKB #	Listing #	UniprotKB #
257	F1LP64-2	1659	P62697	3061	Q64604
258	F1LP90	1660	P62716	3062	Q64605
259	F1LPQ2	1661	P62738	3063	Q64605-2
260	F1LQ70	1662	P62747	3064	Q64610
261	F1LRS8	1663	P62749	3065	Q64610-2
262	F1LSG8	1664	P62762	3066	Q64611
263	F1LU71	1665	P62804	3067	Q64612
264	F1LV46	1666	P62804-2	3068	Q64627
265	F1LYQ8	1667	P62815	3069	Q64632
266	F1LZ52	1668	P62824	3070	Q64633
267	F1LZF0	1669	P62828	3071	Q64634
268	F1M0Z1	1670	P62832	3072	Q64637
269	F1M386	1671	P62836	3073	Q64638
270	F1M3G7	1672	P62839	3074	Q64640
271	F1M3L7	1673	P62853	3075	Q64649
272	F1M5F3	1674	P62859	3076	Q64680
273	F1M5M3	1675	P62890	3077	Q64709
274	F1M5N7	1676	P62898	3078	Q64709-4
275	F1M649	1677	P62914	3079	Q64716
276	F1M7Y5	1678	P62944	3080	Q64LC9
277	F1MA98	1679	P62944-2	3081	Q65Z14
278	F8WLE0	1680	P62959	3082	Q66H07
279	G3V645	1681	P62963	3083	Q66H15
280	G3V735	1682	P62982	3084	Q66H16
281	G3V7L5	1683	P62986	3085	Q66H19
282	G3V7P1	1684	P63004	3086	Q66H20
283	G3V7Q0	1685	P63012	3087	Q66H20-2
284	G3V7X8	1686	P63018	3088	Q66H23
285	G3V893	1687	P63025	3089	Q66H35
286	G3V8H4	1688	P63029	3090	Q66H39
287	G3V8T1	1689	P63035	3091	Q66H43
288	G3V9A7	1690	P63036	3092	Q66H45
289	G3V9D0	1691	P63039	3093	Q66H50
290	G3V9H8	1692	P63041	3094	Q66H52
291	G3V9H8-2	1693	P63043	3095	Q66H54
292	G3V9Q9	1694	P63043-2	3096	Q66H60
293	G3V9R8	1695	P63043-3	3097	Q66H61

Table C.1. Proteins identified by combined use of DDA and HDMS^E from rat brain tissues. Proteins are listed in alphabetical order—Continued

Listing #	UniprotKB #	Listing #	UniprotKB #	Listing #	UniprotKB #
294	H1UBN0	1696	P63045	3098	Q66H65
295	M0R8U1	1697	P63057	3099	Q66H68
296	M0RC99	1698	P63057-2	3100	Q66H80
297	O08557	1699	P63077	3101	Q66H85
298	O08560	1700	P63086	3102	Q66HA1
299	O08562	1701	P63088	3103	Q66HA2
300	O08590	1702	P63088-2	3104	Q66HA4
301	O08593	1703	P63095	3105	Q66HA4-2
302	O08618	1704	P63095-2	3106	Q66HA5
303	O08619	1705	P63095-3	3107	Q66HA5-2
304	O08625	1706	P63100	3108	Q66HA6
305	O08629	1707	P63100-2	3109	Q66HA8
306	O08651	1708	P63102	3110	Q66HB3
307	O08653	1709	P63155	3111	Q66HB5
308	O08654	1710	P63161	3112	Q66HB6
309	O08658	1711	P63245	3113	Q66HC9
310	O08662	1712	P63259	3114	Q66HD0
311	O08700	1713	P63269	3115	Q66HD0-2
312	O08701	1714	P63319	3116	Q66HD2
313	O08722	1715	P63322	3117	Q66HD3
314	O08725	1716	P63324	3118	Q66HD5
315	O08730	1717	P63329	3119	Q66HF1
316	O08764	1718	P63329-2	3120	Q66HF8
317	O08770	1719	P63331	3121	Q66HG8
318	O08773	1720	P67779	3122	Q66HR2
319	O08774	1721	P67999	3123	Q66HR5
320	O08775	1722	P67999-2	3124	Q66HR9
321	O08815	1723	P68035	3125	Q66HR9-2
322	O08816	1724	P68136	3126	Q66MI6
323	O08837	1725	P68182	3127	Q66MI6-2
324	O08838	1726	P68255	3128	Q672K1
325	O08839	1727	P68370	3129	Q673L6
326	O08839-2	1728	P68403	3130	Q673L6-2
327	O08839-3	1729	P68403-2	3131	Q675A5
328	O08839-4	1730	P68511	3132	Q67ES5
329	O08839-5	1731	P68907	3133	Q67ET3
330	O08839-6	1732	P69060	3134	Q68A21

Table C.1. Proteins identified by combined use of DDA and HDMS^E from rat brain tissues. Proteins are listed in alphabetical order—Continued

Listing #	UniprotKB #	Listing #	UniprotKB #	Listing #	UniprotKB #
331	O08873	1733	P69526	3135	Q68EJ0
332	O08875	1734	P69527	3136	Q68EJ0-2
333	O08876	1735	P69682	3137	Q68FN9
334	O08961	1736	P69735	3138	Q68FP1
335	O08962	1737	P69736	3139	Q68FP1-2
336	O09018	1738	P69897	3140	Q68FP2
337	O09139	1739	P69897-2	3141	Q68FP9
338	O09175	1740	P70478	3142	Q68FQ0
339	O09178	1741	P70486	3143	Q68FQ7
340	O35049	1742	P70496	3144	Q68FR3
341	O35094	1743	P70496-2	3145	Q68FR6
342	O35095	1744	P70498	3146	Q68FR7
343	O35119	1745	P70499	3147	Q68FR8
344	O35119-2	1746	P70501	3148	Q68FR9
345	O35142	1747	P70503	3149	Q68FR9-2
346	O35158	1748	P70505	3150	Q68FS1
347	O35158-2	1749	P70507	3151	Q68FS2
348	O35162	1750	P70507-2	3152	Q68FS6
349	O35179	1751	P70541	3153	Q68FT3
350	O35180	1752	P70549	3154	Q68FT6
351	O35244	1753	P70550	3155	Q68FT9
352	O35263	1754	P70555	3156	Q68FU3
353	O35264	1755	P70566	3157	Q68FU4
354	O35274	1756	P70567	3158	Q68FU7
355	O35276	1757	P70569	3159	Q68FV2
356	O35303	1758	P70579	3160	Q68FW7
357	O35303-2	1759	P70582	3161	Q68FX0
358	O35303-3	1760	P70584	3162	Q68FX7
359	O35303-4	1761	P70587	3163	Q68FY0
360	O35303-5	1762	P70587-2	3164	Q68G30
361	O35303-6	1763	P70587-3	3165	Q68LP1
362	O35314	1764	P70587-4	3166	Q68SB1
363	O35331	1765	P70587-5	3167	Q68SB1-2
364	O35346	1766	P70604	3168	Q68SB1-3
365	O35353	1767	P70605	3169	Q68SB1-4
366	O35412	1768	P70606	3170	Q69CM7
367	O35413	1769	P70610	3171	Q69CM7-2

Table C.1. Proteins identified by combined use of DDA and HDMS^E from rat brain tissues. Proteins are listed in alphabetical order—Continued

Listing #	UniprotKB #	Listing #	UniprotKB #	Listing #	UniprotKB #
368	O35430	1770	P70615	3172	Q69FB3
369	O35430-2	1771	P70618	3173	Q6AXM9
370	O35431	1772	P70618-2	3174	Q6AXN9
371	O35433	1773	P70623	3175	Q6AXP1
372	O35433-2	1774	P70628	3176	Q6AXP3
373	O35433-3	1775	P70705	3177	Q6AXP6
374	O35462	1776	P70708	3178	Q6AXQ7
375	O35509	1777	P70711	3179	Q6AXQ7-2
376	O35550	1778	P70712	3180	Q6AXQ8
377	O35552-4	1779	P80203	3181	Q6AXR8
378	O35552-5	1780	P80254	3182	Q6AXT0
379	O35552-6	1781	P81128	3183	Q6AXT4
380	O35552-8	1782	P81155	3184	Q6AXT5
381	O35567	1783	P81556	3185	Q6AXT7
382	O35569	1784	P82252	3186	Q6AXU0
383	O35569-2	1785	P82458	3187	Q6AXU1
384	O35569-3	1786	P82471	3188	Q6AXV2
385	O35569-4	1787	P82995	3189	Q6AXV4
386	O35569-7	1788	P83732	3190	Q6AXX6
387	O35757	1789	P83829	3191	Q6AXY2
388	O35763	1790	P83868	3192	Q6AXY7
389	O35774	1791	P83900	3193	Q6AXZ4
390	O35787	1792	P83953	3194	Q6AXZ6
391	O35795	1793	P84025	3195	Q6AY05
392	O35795-2	1794	P84060	3196	Q6AY09
393	O35796	1795	P84076	3197	Q6AY13
394	O35814	1796	P84079	3198	Q6AY14
395	O35817	1797	P84082	3199	Q6AY17
396	O35821	1798	P84083	3200	Q6AY19
397	O35827	1799	P84087	3201	Q6AY22
398	O35831	1800	P84092	3202	Q6AY30
399	O35832	1801	P84245	3203	Q6AY41
400	O35867	1802	P84551	3204	Q6AY43
401	O35870	1803	P84586	3205	Q6AY43-2
402	O35889	1804	P84817	3206	Q6AY47
403	O35889-2	1805	P85108	3207	Q6AY56
404	O35920	1806	P85125	3208	Q6AY57

Table C.1. Proteins identified by combined use of DDA and HDMS^E from rat brain tissues. Proteins are listed in alphabetical order—Continued

Listing #	UniprotKB #	Listing #	UniprotKB #	Listing #	UniprotKB #
405	O35921	1807	P85515	3209	Q6AY61
406	O35923	1808	P85834	3210	Q6AY62
407	O35964	1809	P85845	3211	Q6AY84
408	O35987	1810	P85967	3212	Q6AY88
409	O54697	1811	P85969	3213	Q6AY92
410	O54701	1812	P85971	3214	Q6AY97
411	O54701-2	1813	P85972	3215	Q6AYA1
412	O54715	1814	P85973	3216	Q6AYA5
413	O54728	1815	P86252	3217	Q6AYB3
414	O54735	1816	P86410	3218	Q6AYB4
415	O54747	1817	P97523	3219	Q6AYC8
416	O54753	1818	P97524	3220	Q6AYD2
417	O54772	1819	P97526	3221	Q6AYD6
418	O54783	1820	P97527	3222	Q6AYE2
419	O54800	1821	P97528	3223	Q6AYE4
420	O54835	1822	P97531	3224	Q6AYE4-2
421	O54852	1823	P97536	3225	Q6AYE8
422	O54853	1824	P97544	3226	Q6AYF7
423	O54861	1825	P97546	3227	Q6AYG0
424	O54874	1826	P97546-1	3228	Q6AYG3
425	O54880	1827	P97546-3	3229	Q6AYH5
426	O54888	1828	P97557	3230	Q6AYH9
427	O54889	1829	P97571	3231	Q6AYI4
428	O54898	1830	P97573	3232	Q6AYI5
429	O54922	1831	P97577	3233	Q6AYJ5
430	O54923	1832	P97587	3234	Q6AYK6
431	O54952	1833	P97592	3235	Q6AYK9-2
432	O54960	1834	P97603	3236	Q6AYL2
433	O54968	1835	P97607	3237	Q6AYL2-2
434	O54968-2	1836	P97608	3238	Q6AYL6
435	O54975	1837	P97616	3239	Q6AYL6-2
436	O55007	1838	P97629	3240	Q6AYL8
437	O55007-3	1839	P97636	3241	Q6AYM0
438	O55012	1840	P97636-2	3242	Q6AYN9
439	O55012-2	1841	P97679	3243	Q6AYP0
440	O55081	1842	P97680	3244	Q6AYP2
441	O55099	1843	P97685	3245	Q6AYP4

Table C.1. Proteins identified by combined use of DDA and HDMS^E from rat brain tissues. Proteins are listed in alphabetical order—Continued

Listing #	UniprotKB #	Listing #	UniprotKB #	Listing #	UniprotKB #
442	O55156	1844	P97685-2	3246	Q6AYP7
443	O55159	1845	P97685-3	3247	Q6AYQ0
444	O55164	1846	P97686	3248	Q6AYQ2
445	O55165	1847	P97686-2	3249	Q6AYQ6
446	O55166	1848	P97686-3	3250	Q6AYR2
447	O55173	1849	P97689	3251	Q6AYR5
448	O55207	1850	P97689-2	3252	Q6AYR6
449	O55207-2	1851	P97690	3253	Q6AYT0
450	O55207-3	1852	P97691	3254	Q6AYT2
451	O55528	1853	P97691-2	3255	Q6AYT3
452	O70127	1854	P97691-3	3256	Q6AYT9
453	O70142	1855	P97694	3257	Q6AYU4
454	O70150	1856	P97696	3258	Q6AYX5
455	O70150-2	1857	P97697	3259	Q6AYX5-2
456	O70156	1858	P97700	3260	Q6AYX5-3
457	O70173	1859	P97710	3261	Q6AYX5-4
458	O70196	1860	P97711	3262	Q6AYX5-5
459	O70215	1861	P97756	3263	Q6AYY8
460	O70239	1862	P97779	3264	Q6AYZ1
461	O70276	1863	P97829	3265	Q6AZ28
462	O70351	1864	P97829-2	3266	Q6AZ61
463	O70418	1865	P97830	3267	Q6DG50
464	O70441	1866	P97834	3268	Q6DGG0
465	O70467	1867	P97836	3269	Q6DKG0
466	O70511	1868	P97836-4	3270	Q6DTM3
467	O70511-2	1869	P97836-5	3271	Q6E0V2
468	O70511-3	1870	P97836-6	3272	Q6ED65
469	O70511-4	1871	P97836-7	3273	Q6ED65-2
470	O70511-5	1872	P97836-8	3274	Q6ED65-3
471	O70511-6	1873	P97837	3275	Q6ED65-4
472	O70511-7	1874	P97838	3276	Q6EV76
473	O70513	1875	P97838-2	3277	Q6F6B3
474	O70535	1876	P97839	3278	Q6GMN2
475	O70593	1877	P97849	3279	Q6GMN2-2
476	O70595	1878	P97852	3280	Q6GQP4
477	O70597	1879	P97874	3281	Q6GX83
478	O70608	1880	P97879	3282	Q6HA10

Table C.1. Proteins identified by combined use of DDA and HDMS^E from rat brain tissues. Proteins are listed in alphabetical order—Continued

Listing #	UniprotKB #	Listing #	UniprotKB #	Listing #	UniprotKB #
479	O88201	1881	P97879-2	3283	Q6IE24
480	O88202	1882	P97887	3284	Q6IE52
481	O88269	1883	P97888	3285	Q6IE70
482	O88275	1884	P97924	3286	Q6IE75
483	O88275-2	1885	P97924-2	3287	Q6IFT6
484	O88277	1886	P97924-3	3288	Q6IFU7
485	O88278	1887	P97924-4	3289	Q6IFU8
486	O88279	1888	P97924-5	3290	Q6IFV1
487	O88279-2	1889	P97924-6	3291	Q6IFV3
488	O88279-3	1890	P97924-7	3292	Q6IFV4
489	O88279-4	1891	P97924-8	3293	Q6IFW2
490	O88280	1892	P98158	3294	Q6IFW3
491	O88302	1893	P98166	3295	Q6IFW5
492	O88339	1894	Q00195	3296	Q6IFW6
493	O88382	1895	Q00495	3297	Q6IFW8
494	O88382-2	1896	Q00566	3298	Q6IFX0
495	O88382-3	1897	Q00566-2	3299	Q6IFX1
496	O88387	1898	Q00657	3300	Q6IG00
497	O88419	1899	Q00715	3301	Q6IG01
498	O88420	1900	Q00728	3302	Q6IG02
499	O88420-2	1901	Q00729	3303	Q6IG03
500	O88422	1902	Q00900	3304	Q6IG04
501	O88453	1903	Q00911	3305	Q6IG05
502	O88457	1904	Q00939	3306	Q6IG12
503	O88480	1905	Q00960	3307	Q6IMA3
504	O88483	1906	Q00981	3308	Q6IMF1
505	O88484	1907	Q01062	3309	Q6IMF3
506	O88488	1908	Q01066	3310	Q6IMG5
507	O88496	1909	Q01205	3311	Q6IMX7
508	O88506	1910	Q01460	3312	Q6IMY8
509	O88563	1911	Q01579	3313	Q6IMZ0
510	O88588	1912	Q01621	3314	Q6IRE4
511	O88588-2	1913	Q01728	3315	Q6IRI9
512	O88600	1914	Q01728-2	3316	Q6IRK9
513	O88658	1915	Q01728-3	3317	Q6IV68
514	O88658-2	1916	Q01728-4	3318	Q6J2U6
515	O88658-3	1917	Q01728-5	3319	Q6J4I0

Table C.1. Proteins identified by combined use of DDA and HDMS^E from rat brain tissues. Proteins are listed in alphabetical order—Continued

Listing #	UniprotKB #	Listing #	UniprotKB #	Listing #	UniprotKB #
516	O88664	1918	Q01728-6	3320	Q6JAM9
517	O88677	1919	Q01728-7	3321	Q6JHU9
518	O88751	1920	Q01754	3322	Q6JP77
519	O88751-2	1921	Q01812	3323	Q6JP77-2
520	O88751-3	1922	Q01986	3324	Q6LED0
521	O88758	1923	Q02253	3325	Q6MG08
522	O88761	1924	Q02294	3326	Q6MG11
523	O88764	1925	Q02356	3327	Q6MG12
524	O88764-2	1926	Q02435	3328	Q6MG48
525	O88767	1927	Q02485	3329	Q6MG49
526	O88778	1928	Q02485-2	3330	Q6MG49-2
527	O88807	1929	Q02527	3331	Q6MG60
528	O88831	1930	Q02563	3332	Q6MG61
529	O88831-2	1931	Q02759	3333	Q6MG62
530	O88850	1932	Q02769	3334	Q6MG64
531	O88871	1933	Q02874	3335	Q6MG81
532	O88900	1934	Q02874-2	3336	Q6MG84
533	O88902	1935	Q02955	3337	Q6MG84-2
534	O88923	1936	Q03114	3338	Q6NYB7
535	O88923-1	1937	Q03248	3339	Q6P0K8
536	O88923-2	1938	Q03336	3340	Q6P3V7
537	O88923-3	1939	Q03343	3341	Q6P3V7-2
538	O88923-4	1940	Q03344	3342	Q6P4Z6
539	O88923-5	1941	Q03346	3343	Q6P4Z9
540	O88923-6	1942	Q03386	3344	Q6P502
541	O88943	1943	Q03410	3345	Q6P6Q2
542	O88943-2	1944	Q03555	3346	Q6P6R2
543	O88943-3	1945	Q03555-2	3347	Q6P6S3
544	O88943-4	1946	Q03555-3	3348	Q6P6S4
545	O88943-5	1947	Q03555-4	3349	Q6P6T1
546	O88943-6	1948	Q03555-5	3350	Q6P6U0
547	O88943-7	1949	Q03555-6	3351	Q6P6V0
548	O88943-8	1950	Q03626	3352	Q6P6V1
549	O88943-9	1951	Q03626-2	3353	Q6P6V7
550	O88954	1952	Q04400	3354	Q6P6W3
551	O88989	1953	Q04462	3355	Q6P730
552	O88994	1954	Q04589	3356	Q6P747

Table C.1. Proteins identified by combined use of DDA and HDMS^E from rat brain tissues. Proteins are listed in alphabetical order—Continued

Listing #	UniprotKB #	Listing #	UniprotKB #	Listing #	UniprotKB #
553	O89000	1955	Q04667	3357	Q6P799
554	O89040	1956	Q04940	3358	Q6P7A9
555	O89042	1957	Q04970	3359	Q6P7B0
556	O89043	1958	Q05030	3360	Q6P7B4
557	O89047	1959	Q05096	3361	Q6P7C4
558	P00173	1960	Q05096-2	3362	Q6P7D4
559	P00173-2	1961	Q05096-3	3363	Q6P7Q0
560	P00176	1962	Q05140	3364	Q6P7Q4
561	P00388	1963	Q05140-2	3365	Q6P7R8
562	P00406	1964	Q05175	3366	Q6P9T8
563	P00502	1965	Q05546	3367	Q6P9U4
564	P00507	1966	Q05546-2	3368	Q6P9V9
565	P00564	1967	Q05695	3369	Q6P9Z6
566	P00697	1968	Q05695-2	3370	Q6P9Z8
567	P00762	1969	Q05764	3371	Q6PCT3
568	P00763	1970	Q05764-2	3372	Q6PCU2
569	P00884	1971	Q05820	3373	Q6PCU8
570	P01026	1972	Q05941	3374	Q6PDU7
571	P01114	1973	Q05962	3375	Q6PEC4
572	P01186	1974	Q05982	3376	Q6PNM1
573	P01244	1975	Q06145	3377	Q6PNM1-2
574	P01346	1976	Q06226	3378	Q6PTT0
575	P01830	1977	Q06437	3379	Q6Q0N0
576	P01946	1978	Q06496	3380	Q6Q0N1
577	P02091	1979	Q06518	3381	Q6Q629
578	P02262	1980	Q06647	3382	Q6Q760
579	P02401	1981	Q06996	3383	Q6Q7Y5
580	P02466	1982	Q06BI3	3384	Q6QA27
581	P02563	1983	Q07014	3385	Q6QD51
582	P02564	1984	Q07014-2	3386	Q6QI44
583	P02600	1985	Q07071	3387	Q6QLM7
584	P02600-2	1986	Q07266	3388	Q6QZQ4
585	P02650	1987	Q07266-2	3389	Q6R556
586	P02651	1988	Q07310	3390	Q6R6I6
587	P02665	1989	Q07310-10	3391	Q6REY9
588	P02688	1990	Q07310-11	3392	Q6REY9-2
589	P02688-2	1991	Q07310-12	3393	Q6RI86

Table C.1. Proteins identified by combined use of DDA and HDMS^E from rat brain tissues. Proteins are listed in alphabetical order—Continued

Listing #	UniprotKB #	Listing #	UniprotKB #	Listing #	UniprotKB #
590	P02688-3	1992	Q07310-13	3394	Q6RI88
591	P02688-4	1993	Q07310-14	3395	Q6RJR6
592	P02688-5	1994	Q07310-15	3396	Q6RJR6-2
593	P02770	1995	Q07310-16	3397	Q6RUG5
594	P02773	1996	Q07310-17	3398	Q6RUV5
595	P02773-2	1997	Q07310-18	3399	Q6RVG2
596	P03133	1998	Q07310-19	3400	Q6RVG2-2
597	P03305	1999	Q07310-2	3401	Q6RVG2-3
598	P03305-2	2000	Q07310-3	3402	Q6T3U3
599	P03306	2001	Q07310-4	3403	Q6TLK4
600	P03306-2	2002	Q07310-5	3404	Q6TMG5
601	P03307	2003	Q07310-6	3405	Q6TRW4
602	P03307-2	2004	Q07310-7	3406	Q6TRW4-2
603	P03308	2005	Q07310-8	3407	Q6TRW4-3
604	P03308-2	2006	Q07310-9	3408	Q6UPR8
605	P03309	2007	Q07647	3409	Q6URK4
606	P03309-2	2008	Q07652	3410	Q6URK4-2
607	P03310	2009	Q07803	3411	Q6UVM4
608	P03310-2	2010	Q07977	3412	Q6VEU1
609	P03311	2011	Q08163	3413	Q6W3B0
610	P03311-2	2012	Q08201	3414	Q6W3E9
611	P03889	2013	Q08415	3415	Q6X936
612	P04073	2014	Q08415-2	3416	Q6XQN1
613	P04157	2015	Q08420	3417	Q6XVN8
614	P04157-2	2016	Q08603	3418	Q6Y306
615	P04157-3	2017	Q08834	3419	Q6Y306-2
616	P04157-4	2018	Q08851	3420	Q700K0
617	P04157-5	2019	Q08851-2	3421	Q703I1
618	P04166	2020	Q08877	3422	Q704E8
619	P04167	2021	Q08877-10	3423	Q710E6
620	P04167-2	2022	Q08877-11	3424	Q71F54
621	P04176	2023	Q08877-12	3425	Q71HP2
622	P04177	2024	Q08877-13	3426	Q71LX6
623	P04182	2025	Q08877-2	3427	Q71QF9
624	P04218	2026	Q08877-3	3428	Q75N33
625	P04256	2027	Q08877-4	3429	Q75Q39
626	P04462	2028	Q08877-5	3430	Q75Q41

Table C.1. Proteins identified by combined use of DDA and HDMS^E from rat brain tissues. Proteins are listed in alphabetical order—Continued

Listing #	UniprotKB #	Listing #	UniprotKB #	Listing #	UniprotKB #
627	P04631	2029	Q08877-6	3431	Q75WE7
628	P04636	2030	Q08877-7	3432	Q765A7
629	P04639	2031	Q08877-8	3433	Q765I2
630	P04642	2032	Q08877-9	3434	Q769K2
631	P04692	2033	Q09073	3435	Q76EI6
632	P04692-2	2034	Q09137	3436	Q76HP2
633	P04692-3	2035	Q09426	3437	Q76LD0
634	P04692-4	2036	Q09429	3438	Q76M68
635	P04692-5	2037	Q09429-2	3439	Q78E65
636	P04692-6	2038	Q09429-3	3440	Q78EH2
637	P04692-7	2039	Q0HA29	3441	Q78EH2-2
638	P04692-8	2040	Q0KL00	3442	Q78EH2-3
639	P04764	2041	Q0PMD2	3443	Q78EH2-4
640	P04774	2042	Q0V8T3	3444	Q78EH2-5
641	P04775	2043	Q0V8T4	3445	Q78PB6
642	P04785	2044	Q0V8T5	3446	Q78PB6-2
643	P04797	2045	Q0V8T6	3447	Q792H5
644	P04800	2046	Q0VGK2	3448	Q792H5-2
645	P04897	2047	Q0ZHH6	3449	Q792H5-3
646	P04903	2048	Q0ZHH6-2	3450	Q792H5-4
647	P04904	2049	Q10728	3451	Q792I0
648	P04905	2050	Q10728-2	3452	Q794E4
649	P04906	2051	Q10728-3	3453	Q794F9
650	P04916	2052	Q10746	3454	Q7M0E3
651	P04937	2053	Q10746-2	3455	Q7M6Z5
652	P04937-2	2054	Q10758	3456	Q7M733
653	P04937-3	2055	Q10836	3457	Q7M734
654	P04937-4	2056	Q157S1	3458	Q7TMA5
655	P05065	2057	Q1EHB3	3459	Q7TMB7
656	P05178	2058	Q1EHB3-2	3460	Q7TMD5
657	P05179	2059	Q1HG60	3461	Q7TMD5-2
658	P05182	2060	Q1JU68	3462	Q7TNJ2
659	P05183	2061	Q1LZ50	3463	Q7TNJ7
660	P05197	2062	Q1M168	3464	Q7TNJ7-4
661	P05370	2063	Q1WIM2	3465	Q7TNZ5
662	P05503	2064	Q1WIM2-2	3466	Q7TP36
663	P05539	2065	Q29RW1	3467	Q7TP54

Table C.1. Proteins identified by combined use of DDA and HDMS^E from rat brain tissues. Proteins are listed in alphabetical order—Continued

Listing #	UniprotKB #	Listing #	UniprotKB #	Listing #	UniprotKB #
664	P05541	2066	Q2A865	3468	Q7TP65
665	P05544	2067	Q2HWF0	3469	Q7TP65-2
666	P05696	2068	Q2HWF0-2	3470	Q7TP98
667	P05708	2069	Q2HWF0-3	3471	Q7TPB1
668	P05710	2070	Q2IBC5	3472	Q7TPK6
669	P05712	2071	Q2IBD0	3473	Q7TQ20
670	P05714	2072	Q2IBD0-2	3474	Q7TQ20-2
671	P05942	2073	Q2IBD4	3475	Q7TQ94
672	P06214	2074	Q2IBD4-2	3476	Q7TQ94-2
673	P06238	2075	Q2KJ09	3477	Q7TQP6
674	P06300	2076	Q2KJ09-2	3478	Q7TSF2
675	P06302	2077	Q2KN99	3479	Q7TSP2
676	P06349	2078	Q2L4T2	3480	Q7TST9
677	P06447	2079	Q2LC84	3481	Q7TSU1
678	P06494	2080	Q2LC84-2	3482	Q7TT47
679	P06536	2081	Q2M2R8	3483	Q7TT47-2
680	P06536-2	2082	Q2PQA9	3484	Q7TT49
681	P06685	2083	Q2Q0I9	3485	Q80T22
682	P06686	2084	Q2QDE7	3486	Q80VJ4
683	P06687	2085	Q2TA68	3487	Q80W87
684	P06761	2086	Q2TA68-2	3488	Q80W98
685	P06765	2087	Q2TA68-3	3489	Q80WA4
686	P06829	2088	Q2TGJ1	3490	Q80X08
687	P06882	2089	Q2TL32	3491	Q80YE2
688	P06883	2090	Q2VUH7	3492	Q80YN4
689	P07092	2091	Q2VWP9	3493	Q80Z30
690	P07153	2092	Q2WEA5	3494	Q80Z36
691	P07171	2093	Q2WEA5-2	3495	Q80ZA5
692	P07308	2094	Q2YDU6	3496	Q80ZA5-2
693	P07314	2095	Q2YDU8	3497	Q80ZA5-3
694	P07323	2096	Q32PZ3	3498	Q80ZA5-4
695	P07335	2097	Q32Q06	3499	Q80ZA5-5
696	P07340	2098	Q32Q86	3500	Q80ZA5-6
697	P07632	2099	Q32WR5	3501	Q80ZA5-7
698	P07687	2100	Q3B7D0	3502	Q80ZF0
699	P07722	2101	Q3B7D3	3503	Q80ZG0
700	P07722-2	2102	Q3B7D5	3504	Q80ZG2

Table C.1. Proteins identified by combined use of DDA and HDMS^E from rat brain tissues. Proteins are listed in alphabetical order—Continued

Listing #	UniprotKB #	Listing #	UniprotKB #	Listing #	UniprotKB #
701	P07756	2103	Q3B7L1	3505	Q810H6
702	P07825	2104	Q3B7T8	3506	Q810H6-2
703	P07861	2105	Q3B7U4	3507	Q810I1
704	P07867	2106	Q3B8Q0	3508	Q810T5
705	P07882	2107	Q3B8Q1	3509	Q810T5-2
706	P07895	2108	Q3B8Q2	3510	Q810U0
707	P07897	2109	Q3C2P8	3511	Q810W7
708	P07897-2	2110	Q3KR56	3512	Q810W7-2
709	P07936	2111	Q3KR73	3513	Q810W9
710	P07943	2112	Q3KR86	3514	Q811A3
711	P07953	2113	Q3KR92	3515	Q811A3-2
712	P07953-2	2114	Q3KR97	3516	Q811M5
713	P08009	2115	Q3KR97-2	3517	Q811Q0
714	P08010	2116	Q3KR99	3518	Q811Q1
715	P08081	2117	Q3KRC5	3519	Q811S9
716	P08081-2	2118	Q3KRC6	3520	Q811U3
717	P08082	2119	Q3KRD0	3521	Q811X5
718	P08082-2	2120	Q3KRD5	3522	Q811X6
719	P08104	2121	Q3KRE0	3523	Q812E9
720	P08289	2122	Q3KRE8	3524	Q812E9-2
721	P08290	2123	Q3KRF3	3525	Q86517
722	P08413	2124	Q3LRZ1	3526	Q8CF82
723	P08430	2125	Q3LUD3	3527	Q8CF82-2
724	P08461	2126	Q3MHT4	3528	Q8CF97
725	P08482	2127	Q3MHU3	3529	Q8CFC1
726	P08503	2128	Q3MHU3-2	3530	Q8CFC9
727	P08523	2129	Q3MIB4	3531	Q8CFD1
728	P08592	2130	Q3MID2	3532	Q8CFG5
729	P08592-2	2131	Q3MIE4	3533	Q8CFG6
730	P08644	2132	Q3MIF2	3534	Q8CFM6
731	P08644-2	2133	Q3MIF4	3535	Q8CFN2
732	P08649	2134	Q3MJK5	3536	Q8CFN2-2
733	P08661	2135	Q3MJK5-2	3537	Q8CG07
734	P08723	2136	Q3SWS9	3538	Q8CG09
735	P08753	2137	Q3SWT0	3539	Q8CG09-2
736	P09006	2138	Q3SWT4	3540	Q8CG45
737	P09117	2139	Q3SWT5	3541	Q8CGS4

Table C.1. Proteins identified by combined use of DDA and HDMS^E from rat brain tissues. Proteins are listed in alphabetical order—Continued

Listing #	UniprotKB #	Listing #	UniprotKB #	Listing #	UniprotKB #
738	P09215	2140	Q3SWU3	3542	Q8CGS5
739	P09216	2141	Q3T1H2	3543	Q8CGU4
740	P09217	2142	Q3T1I3	3544	Q8CGU6
741	P09330	2143	Q3T1I4	3545	Q8CGU9
742	P09414	2144	Q3T1I5	3546	Q8CGV7
743	P09483	2145	Q3T1I9	3547	Q8CGX0
744	P09483-2	2146	Q3T1J8	3548	Q8CHI9
745	P09495	2147	Q3T1K5	3549	Q8CHI9-2
746	P09527	2148	Q3ZAV0	3550	Q8CHN8
747	P09605	2149	Q3ZAV8	3551	Q8CHN8-2
748	P09606	2150	Q3ZB98	3552	Q8CHN8-3
749	P09626	2151	Q3ZB98-2	3553	Q8CIN7
750	P09759	2152	Q3ZB98-3	3554	Q8CIN9
751	P09760	2153	Q3ZB98-4	3555	Q8CIN9-2
752	P09810	2154	Q3ZB98-5	3556	Q8CIS9
753	P09811	2155	Q3ZB98-6	3557	Q8CIY2
754	P09812	2156	Q3ZU82	3558	Q8CIZ5
755	P09951	2157	Q45GW3	3559	Q8CIZ5-4
756	P09951-2	2158	Q460M5	3560	Q8CJ11
757	P0C089	2159	Q496Z9	3561	Q8CJ11-2
758	P0C0R5	2160	Q497B3	3562	Q8CJ11-3
759	P0C0S7	2161	Q498C7	3563	Q8CJ42
760	P0C0T2	2162	Q498D1	3564	Q8CJ52
761	P0C152	2163	Q498D6	3565	Q8CJ99
762	P0C169	2164	Q498R1	3566	Q8CJ99-2
763	P0C170	2165	Q498R1-2	3567	Q8CJB9
764	P0C1T0	2166	Q498R3	3568	Q8CJH6
765	P0C1T0-3	2167	Q498T9	3569	Q8JZQ0
766	P0C1T0-4	2168	Q498U3	3570	Q8K1P7
767	P0C1X8	2169	Q499M5	3571	Q8K1Q0
768	P0C219	2170	Q499M7	3572	Q8K1Q3
769	P0C546	2171	Q499N6	3573	Q8K1Q4
770	P0C588	2172	Q499R0	3574	Q8K3F3
771	P0C5E3	2173	Q499T7	3575	Q8K3K1
772	P0C5H6	2174	Q499U2	3576	Q8K3K4
773	P0C5I0	2175	Q499U4	3577	Q8K3M6
774	P0C5X8	2176	Q499V8	3578	Q8K3M6-2

Table C.1. Proteins identified by combined use of DDA and HDMS^E from rat brain tissues. Proteins are listed in alphabetical order—Continued

Listing #	UniprotKB #	Listing #	UniprotKB #	Listing #	UniprotKB #
775	P0C5Y8	2177	Q4AE70	3579	Q8K3P4
776	P0C606	2178	Q4AE70-2	3580	Q8K3Y6
777	P0C644	2179	Q4AE70-3	3581	Q8K415
778	P0C6B1	2180	Q4AE70-4	3582	Q8K4B7
779	P0C6B8	2181	Q4AEF8	3583	Q8K4D6
780	P0C6C0	2182	Q4FZT0	3584	Q8K4D8
781	P0C6P5	2183	Q4FZT6	3585	Q8K4F7
782	P0C6P7	2184	Q4FZT9	3586	Q8K4F8
783	P0C6S7	2185	Q4FZU2	3587	Q8K4G9
784	P0C6Y7	2186	Q4FZU3	3588	Q8K4G9-2
785	P0C7N0	2187	Q4FZU6	3589	Q8K4H4
786	P0C865	2188	Q4FZU8	3590	Q8K4K5
787	P0C8N6	2189	Q4FZV0	3591	Q8K4M9
788	P0C927	2190	Q4FZV0-2	3592	Q8K4S7
789	P0CAX5	2191	Q4FZV3	3593	Q8K4T4
790	P0CB49	2192	Q4FZX7	3594	Q8K4T4-2
791	P0CC09	2193	Q4FZY0	3595	Q8K4V2
792	P0CE43	2194	Q4G005	3596	Q8K4V4
793	P0CG51	2195	Q4G008	3597	Q8K4V4-2
794	P0DMW0	2196	Q4G017	3598	Q8K4Y5
795	P0DMW1	2197	Q4G033	3599	Q8K581
796	P0DP29	2198	Q4G050	3600	Q8K586
797	P0DP30	2199	Q4G059	3601	Q8K589
798	P0DP31	2200	Q4G061	3602	Q8K593
799	P10111	2201	Q4G064	3603	Q8QZV1
800	P10158	2202	Q4G073	3604	Q8R1R5
801	P10354	2203	Q4KLF8	3605	Q8R2H5
802	P10362	2204	Q4KLG2	3606	Q8R2H7
803	P10499	2205	Q4KLG9	3607	Q8R2H7-2
804	P10536	2206	Q4KLH6	3608	Q8R424
805	P10610	2207	Q4KLH6-2	3609	Q8R491
806	P10633	2208	Q4KLI1	3610	Q8R4A1
807	P10634	2209	Q4KLI2	3611	Q8R4A1-2
808	P10686	2210	Q4KLL4	3612	Q8R4C0
809	P10687	2211	Q4KLL5	3613	Q8R4C1
810	P10715	2212	Q4KLL9	3614	Q8R4G1
811	P10719	2213	Q4KLN4	3615	Q8R4T5

Table C.1. Proteins identified by combined use of DDA and HDMS^E from rat brain tissues. Proteins are listed in alphabetical order—Continued

Listing #	UniprotKB #	Listing #	UniprotKB #	Listing #	UniprotKB #
812	P10760	2214	Q4KLN8	3616	Q8R4U9
813	P10824	2215	Q4KLP0	3617	Q8R4V0
814	P10860	2216	Q4KLY0	3618	Q8R4Z1
815	P10888	2217	Q4KLY2	3619	Q8R4Z9
816	P10960	2218	Q4KLY3	3620	Q8R500
817	P11030	2219	Q4KLY6	3621	Q8R508
818	P11232	2220	Q4KLY8	3622	Q8R512
819	P11240	2221	Q4KLZ1	3623	Q8R515
820	P11275	2222	Q4KLZ6	3624	Q8R5I7
821	P11348	2223	Q4KM32	3625	Q8VBU2
822	P11442	2224	Q4KM34	3626	Q8VBU2-2
823	P11466	2225	Q4KM35	3627	Q8VD50
824	P11475	2226	Q4KM47	3628	Q8VDA1
825	P11497	2227	Q4KM49	3629	Q8VDA5
826	P11497-2	2228	Q4KM51	3630	Q8VDA6
827	P11505	2229	Q4KM52	3631	Q8VGC3
828	P11505-2	2230	Q4KM62	3632	Q8VGC3-2
829	P11505-3	2231	Q4KM73	3633	Q8VGC3-3
830	P11505-4	2232	Q4KM86	3634	Q8VGC3-4
831	P11505-5	2233	Q4KM95	3635	Q8VGC3-5
832	P11505-6	2234	Q4KMA0	3636	Q8VH46
833	P11506	2235	Q4KMA2	3637	Q8VHE9
834	P11506-1	2236	Q4KMC4	3638	Q8VHF5
835	P11506-10	2237	Q4KSH7	3639	Q8VHJ4-2
836	P11506-11	2238	Q4L1J4	3640	Q8VHK2
837	P11506-12	2239	Q4L1J4-2	3641	Q8VHN2
838	P11506-14	2240	Q4L208	3642	Q8VHQ7
839	P11506-2	2241	Q4QQS0	3643	Q8VHQ7-2
840	P11506-3	2242	Q4QQS1	3644	Q8VHT6
841	P11506-4	2243	Q4QQS8	3645	Q8VHT8
842	P11506-5	2244	Q4QQT0	3646	Q8VHU4
843	P11506-6	2245	Q4QQT3	3647	Q8VHV7
844	P11506-7	2246	Q4QQT4	3648	Q8VHV7-2
845	P11506-8	2247	Q4QQT5	3649	Q8VHV7-3
846	P11506-9	2248	Q4QQV8	3650	Q8VHW5
847	P11507	2249	Q4QQW4	3651	Q8VHW7
848	P11507-2	2250	Q4QR75	3652	Q8VHX0

Table C.1. Proteins identified by combined use of DDA and HDMS^E from rat brain tissues. Proteins are listed in alphabetical order—Continued

Listing #	UniprotKB #	Listing #	UniprotKB #	Listing #	UniprotKB #
849	P11510	2251	Q4QR99	3653	Q8VHZ8
850	P11517	2252	Q4QR99-2	3654	Q8VI02
851	P11530	2253	Q4QRB4	3655	Q8VI04
852	P11598	2254	Q4R180	3656	Q8VID6
853	P11711	2255	Q4V793	3657	Q8VID6-2
854	P11730	2256	Q4V7B0	3658	Q8VID6-3
855	P11730-2	2257	Q4V7B1	3659	Q8VIG2
856	P11730-3	2258	Q4V7B5	3660	Q8VII6
857	P11883	2259	Q4V7C1	3661	Q8VII6-2
858	P11884	2260	Q4V7C6	3662	Q8VIL3
859	P11915	2261	Q4V7C7	3663	Q8VIP2
860	P11915-2	2262	Q4V7C8	3664	Q91V33
861	P11951	2263	Q4V7D2	3665	Q91XJ1
862	P11960	2264	Q4V7D3	3666	Q91XS8
863	P11980	2265	Q4V7D6	3667	Q91XT5
864	P11980-2	2266	Q4V7E0	3668	Q91XT9
865	P12001	2267	Q4V7E5	3669	Q91XU1
866	P12007	2268	Q4V7G1	3670	Q91XU7
867	P12075	2269	Q4V885	3671	Q91XU8
868	P12336	2270	Q4V886	3672	Q91Y53
869	P12346	2271	Q4V888	3673	Q91Y78
870	P12346-2	2272	Q4V890	3674	Q91Y80
871	P12368	2273	Q4V896	3675	Q91Y81
872	P12369	2274	Q4V897	3676	Q91Z63
873	P12389	2275	Q4V898	3677	Q91Z79
874	P12390	2276	Q4V8A1	3678	Q91Z80
875	P12391	2277	Q4V8A2	3679	Q91ZN1
876	P12711	2278	Q4V8A3	3680	Q91ZN7
877	P12785	2279	Q4V8A9	3681	Q91ZT1
878	P12839	2280	Q4V8B0	3682	Q91ZT1-2
879	P12843	2281	Q4V8B0-2	3683	Q91ZW6
880	P12847	2282	Q4V8B0-3	3684	Q91ZW6-2
881	P12928	2283	Q4V8B5	3685	Q91ZY6
882	P12928-2	2284	Q4V8B8	3686	Q920F3
883	P12938	2285	Q4V8C2	3687	Q920F5
884	P12939	2286	Q4V8C3	3688	Q920F5-2
885	P12969	2287	Q4V8C3-2	3689	Q920G0

Table C.1. Proteins identified by combined use of DDA and HDMS^E from rat brain tissues. Proteins are listed in alphabetical order—Continued

Listing #	UniprotKB #	Listing #	UniprotKB #	Listing #	UniprotKB #
886	P13084	2288	Q4V8C7	3690	Q920H8
887	P13084-2	2289	Q4V8C8	3691	Q920J3
888	P13086	2290	Q4V8C9	3692	Q920L2
889	P13107	2291	Q4V8D9	3693	Q920L6
890	P13221	2292	Q4V8F3	3694	Q920P0
891	P13233	2293	Q4V8F4	3695	Q920P6
892	P13234	2294	Q4V8F5	3696	Q920Q0
893	P13264	2295	Q4V8F7	3697	Q920R3
894	P13264-2	2296	Q4V8G2	3698	Q923I8
895	P13265	2297	Q4V8G5	3699	Q923J6
896	P13286	2298	Q4V8G7	3700	Q923K1
897	P13383	2299	Q4V8G8	3701	Q923V4
898	P13437	2300	Q4V8J2	3702	Q924A5
899	P13596	2301	Q4V8J4	3703	Q924C3
900	P13599	2302	Q4V8K2	3704	Q924C3-2
901	P13601	2303	Q4V9H5	3705	Q924I2
902	P13638	2304	Q4V9H5-2	3706	Q924K2
903	P13668	2305	Q501L3	3707	Q924N5
904	P13676	2306	Q501R9	3708	Q924S4
905	P13697	2307	Q505J6	3709	Q924S5
906	P13803	2308	Q505J9	3710	Q924U0
907	P13832	2309	Q52RG8	3711	Q924U5
908	P13838	2310	Q535K8	3712	Q925B3
909	P14046	2311	Q535K8-2	3713	Q925B3-2
910	P14056	2312	Q53B90	3714	Q925B4
911	P14095	2313	Q53UA7	3715	Q925B5
912	P14270	2314	Q561S0	3716	Q925C0
913	P14270-1	2315	Q562A2	3717	Q925F0
914	P14270-2	2316	Q562B5	3718	Q925G1
915	P14270-3	2317	Q562C7	3719	Q925G1-2
916	P14270-4	2318	Q562C9	3720	Q925N3
917	P14270-6	2319	Q566R0	3721	Q925N6
918	P14270-7	2320	Q566R3	3722	Q925Q9
919	P14270-8	2321	Q566R4	3723	Q925Q9-2
920	P14270-9	2322	Q566R4-2	3724	Q925Q9-3
921	P14272	2323	Q568Z7	3725	Q925Q9-6
922	P14408	2324	Q569B5	3726	Q925Q9-7

Table C.1. Proteins identified by combined use of DDA and HDMS^E from rat brain tissues. Proteins are listed in alphabetical order—Continued

Listing #	UniprotKB #	Listing #	UniprotKB #	Listing #	UniprotKB #
923	P14408-2	2325	Q569C1	3727	Q925S8
924	P14480	2326	Q569C4	3728	Q925T0
925	P14480-2	2327	Q56A18	3729	Q925T8
926	P14604	2328	Q56A18-2	3730	Q99376
927	P14644	2329	Q56A18-3	3731	Q99J86
928	P14646	2330	Q56A18-4	3732	Q99J86-2
929	P14646-1	2331	Q56A27	3733	Q99JD2
930	P14646-2	2332	Q56R16	3734	Q99JD4
931	P14646-4	2333	Q5BJ92	3735	Q99JE6
932	P14646-5	2334	Q5BJL5	3736	Q99M76
933	P14650	2335	Q5BJN8	3737	Q99MA2
934	P14659	2336	Q5BJN8-2	3738	Q99MB4
935	P14668	2337	Q5BJP2	3739	Q99MG9
936	P14669	2338	Q5BJP3	3740	Q99MG9-2
937	P14841	2339	Q5BJP6	3741	Q99MI7
938	P14881	2340	Q5BJQ0	3742	Q99ML5
939	P14881-2	2341	Q5BJR4	3743	Q99MS0
940	P14882	2342	Q5BJS0	3744	Q99MU5
941	P15072	2343	Q5BJS7	3745	Q99MZ4
942	P15072-2	2344	Q5BJT0	3746	Q99MZ8
943	P15087	2345	Q5BJT1	3747	Q99N27
944	P15127	2346	Q5BJT7	3748	Q99N37
945	P15127-2	2347	Q5BJU3	3749	Q99N37-2
946	P15129	2348	Q5BJU7	3750	Q99N37-3
947	P15146	2349	Q5BJX5	3751	Q99N37-4
948	P15146-2	2350	Q5BJY9	3752	Q99NA5
949	P15146-3	2351	Q5BJZ6	3753	Q99NH3
950	P15146-4	2352	Q5BK13	3754	Q99NI4
951	P15149	2353	Q5BK26	3755	Q99P39
952	P15205	2354	Q5BK32	3756	Q99P63
953	P15207	2355	Q5BK43	3757	Q99P74
954	P15337	2356	Q5BK48	3758	Q99P75
955	P15337-2	2357	Q5BK63	3759	Q99P84
956	P15385	2358	Q5BK65	3760	Q99P99
957	P15387	2359	Q5BK68	3761	Q99PD4
958	P15389	2360	Q5BKC6	3762	Q99PE7
959	P15389-2	2361	Q5BKC9	3763	Q99PF5

Table C.1. Proteins identified by combined use of DDA and HDMS^E from rat brain tissues. Proteins are listed in alphabetical order—Continued

Listing #	UniprotKB #	Listing #	UniprotKB #	Listing #	UniprotKB #
960	P15390	2362	Q5BKD0	3764	Q99PK0
961	P15393	2363	Q5CD77	3765	Q99PP0
962	P15429	2364	Q5CZZ9	3766	Q99PR0
963	P15651	2365	Q5D006	3767	Q99PT0
964	P15791	2366	Q5DRK1	3768	Q9BW11
965	P15791-2	2367	Q5DWV1	3769	Q9BW11-2
966	P15791-3	2368	Q5DWV2	3770	Q9DUD8
967	P15791-4	2369	Q5EAJ6-2	3771	Q9EPA0
968	P15791-5	2370	Q5EAN7	3772	Q9EPB1
969	P15791-6	2371	Q5EB59	3773	Q9EPC6
970	P15791-7	2372	Q5EB62	3774	Q9EPH8
971	P15800	2373	Q5EB77	3775	Q9EPI0
972	P15865	2374	Q5EB92	3776	Q9EPI8
973	P15950	2375	Q5EB94	3777	Q9EPI9
974	P15999	2376	Q5EB96	3778	Q9EPJ3
975	P16036	2377	Q5EBA1	3779	Q9EPU2
976	P16067	2378	Q5EBA3	3780	Q9EPV5
977	P16086	2379	Q5EBA8	3781	Q9EPY0
978	P16232	2380	Q5EGZ1	3782	Q9EQ60
979	P16232-2	2381	Q5EIC4	3783	Q9EQG6
980	P16290	2382	Q5EXX3	3784	Q9EQG6-2
981	P16296	2383	Q5FB95	3785	Q9EQH1
982	P16310	2384	Q5FVC2	3786	Q9EQH5
983	P16573	2385	Q5FVC7	3787	Q9EQH5-2
984	P16573-2	2386	Q5FVF4	3788	Q9EQN5
985	P16617	2387	Q5FVI3	3789	Q9EQR2
986	P16638	2388	Q5FVI4	3790	Q9EQS0
987	P16638-2	2389	Q5FVI6	3791	Q9EQX9
988	P16884	2390	Q5FVJ0	3792	Q9ER24
989	P17078	2391	Q5FVJ0-2	3793	Q9ER30
990	P17209	2392	Q5FVK6	3794	Q9ER34
991	P17425	2393	Q5FVL0	3795	Q9ERB4
992	P17625	2394	Q5FVL3	3796	Q9ERB4-3
993	P17712	2395	Q5FVL7	3797	Q9ERC1
994	P17712-2	2396	Q5FVM4	3798	Q9ERC1-2
995	P17712-3	2397	Q5FVM5	3799	Q9ERC5
996	P17764	2398	Q5FVM7	3800	Q9ERE6

Table C.1. Proteins identified by combined use of DDA and HDMS^E from rat brain tissues. Proteins are listed in alphabetical order—Continued

Listing #	UniprotKB #	Listing #	UniprotKB #	Listing #	UniprotKB #
997	P17982	2399	Q5FVN0	3801	Q9ERE6-2
998	P18088	2400	Q5FVN6	3802	Q9ERH3
999	P18113	2401	Q5FVP8	3803	Q9ERH3-2
1000	P18113-2	2402	Q5FVQ8	3804	Q9ERQ6
1001	P18125	2403	Q5FVR2	3805	Q9ERQ6-2
1002	P18163	2404	Q5FVR4	3806	Q9ERR2
1003	P18265	2405	Q5FVR8	3807	Q9ES45
1004	P18266	2406	Q5FWS6	3808	Q9ES45-2
1005	P18292	2407	Q5FWT5	3809	Q9ES53
1006	P18331	2408	Q5FWT9	3810	Q9ES54
1007	P18418	2409	Q5FWU3	3811	Q9ES66
1008	P18420	2410	Q5FWU5	3812	Q9ES67
1009	P18421	2411	Q5FWY5	3813	Q9ES71
1010	P18484	2412	Q5GFD9	3814	Q9ESI7
1011	P18588	2413	Q5HZB6	3815	Q9ESM0
1012	P18589	2414	Q5HZE8	3816	Q9ESN0
1013	P18590	2415	Q5HZV9	3817	Q9ESQ5
1014	P18596	2416	Q5HZY2	3818	Q9ESQ5-2
1015	P18596-2	2417	Q5I034	3819	Q9ESQ7
1016	P18614	2418	Q5I0D1	3820	Q9ESR9
1017	P18645	2419	Q5I0D6	3821	Q9ESS6
1018	P18666	2420	Q5I0D7	3822	Q9EST6
1019	P18910	2421	Q5I0E9	3823	Q9EST9
1020	P19024	2422	Q5I0H3	3824	Q9ESV1
1021	P19132	2423	Q5I0H5	3825	Q9ESV6
1022	P19139	2424	Q5I0H5-2	3826	Q9ESW0
1023	P19222	2425	Q5I0H9	3827	Q9ET61
1024	P19234	2426	Q5I0I4	3828	Q9ET62
1025	P19332	2427	Q5I0J5	3829	Q9ET64
1026	P19332-2	2428	Q5I0K8	3830	Q9IKD0
1027	P19332-3	2429	Q5I0L6	3831	Q9JHL3
1028	P19332-4	2430	Q5JCS6	3832	Q9JHL4
1029	P19332-5	2431	Q5M7A7	3833	Q9JHL4-2
1030	P19332-6	2432	Q5M7U5	3834	Q9JHL4-3
1031	P19332-7	2433	Q5M7U6	3835	Q9JHL4-4
1032	P19332-8	2434	Q5M7W5	3836	Q9JHU0
1033	P19491	2435	Q5M7W5-2	3837	Q9JHU5

Table C.1. Proteins identified by combined use of DDA and HDMS^E from rat brain tissues. Proteins are listed in alphabetical order—Continued

Listing #	UniprotKB #	Listing #	UniprotKB #	Listing #	UniprotKB #
1034	P19491-2	2436	Q5M7W7	3838	Q9JHU6
1035	P19491-3	2437	Q5M821	3839	Q9JHW1
1036	P19493	2438	Q5M864	3840	Q9JHW1-2
1037	P19493-2	2439	Q5M882	3841	Q9JHW5
1038	P19493-3	2440	Q5M887	3842	Q9JHX0
1039	P19511	2441	Q5M936	3843	Q9JHX4
1040	P19527	2442	Q5M939	3844	Q9JHY2
1041	P19627	2443	Q5M947	3845	Q9JHY8
1042	P19629	2444	Q5M9F1	3846	Q9JHZ4
1043	P19643	2445	Q5M9F5	3847	Q9JHZ4-2
1044	P19686	2446	Q5M9F8	3848	Q9JI12
1045	P19804	2447	Q5M9G5	3849	Q9JI66
1046	P19945	2448	Q5M9G7	3850	Q9JI66-2
1047	P19969	2449	Q5M9G9	3851	Q9JI66-3
1048	P20068	2450	Q5M9H0	3852	Q9JI85
1049	P20069	2451	Q5M9I5	3853	Q9JID2
1050	P20156	2452	Q5MJ12	3854	Q9JIH7
1051	P20171	2453	Q5MPA9	3855	Q9JIH7-2
1052	P20236	2454	Q5MPA9-2	3856	Q9JIH7-3
1053	P20266	2455	Q5MPA9-3	3857	Q9JIK1
1054	P20266-2	2456	Q5MYT7	3858	Q9JIK1-2
1055	P20395	2457	Q5MYT9	3859	Q9JIL3
1056	P20420	2458	Q5MYU0	3860	Q9JIL3-2
1057	P20595	2459	Q5NDF0	3861	Q9JIL8
1058	P20611	2460	Q5PPF5	3862	Q9JIL9
1059	P20646	2461	Q5PPG6	3863	Q9JIM0
1060	P20646-2	2462	Q5PPJ9	3864	Q9JIR0
1061	P20651	2463	Q5PPN4	3865	Q9JIR0-2
1062	P20689	2464	Q5PPN7	3866	Q9JIR4
1063	P20720	2465	Q5PQJ5	3867	Q9JIR4-2
1064	P20781	2466	Q5PQJ5-2	3868	Q9JIS1
1065	P20786	2467	Q5PQJ6	3869	Q9JIS1-2
1066	P20788	2468	Q5PQJ7	3870	Q9JIS1-3
1067	P20793	2469	Q5PQJ9	3871	Q9JIS1-4
1068	P20793-2	2470	Q5PQK1	3872	Q9JIS1-5
1069	P20814	2471	Q5PQK4	3873	Q9JIS1-6
1070	P20816	2472	Q5PQM2	3874	Q9JIS1-7

Table C.1. Proteins identified by combined use of DDA and HDMS^E from rat brain tissues. Proteins are listed in alphabetical order—Continued

Listing #	UniprotKB #	Listing #	UniprotKB #	Listing #	UniprotKB #
1071	P20817	2473	Q5PQN0	3875	Q9JIS1-8
1072	P20974	2474	Q5PQN1	3876	Q9JIS1-9
1073	P21139	2475	Q5PQN2	3877	Q9JIT3
1074	P21263	2476	Q5PQN4	3878	Q9JIX5
1075	P21263-2	2477	Q5PQN5	3879	Q9JIX5-2
1076	P21396	2478	Q5PQN9	3880	Q9JJ09
1077	P21531	2479	Q5PQP5	3881	Q9JJ19
1078	P21571	2480	Q5PQP9	3882	Q9JJ22
1079	P21575	2481	Q5PQQ1	3883	Q9JJ22-2
1080	P21575-2	2482	Q5PQQ2	3884	Q9JJ25
1081	P21575-3	2483	Q5PQQ4	3885	Q9JJ31
1082	P21575-4	2484	Q5PQQ5	3886	Q9JJ40
1083	P21575-5	2485	Q5PQQ5-2	3887	Q9JJ54
1084	P21575-6	2486	Q5PQQ6	3888	Q9JJ54-2
1085	P21575-7	2487	Q5PQQ9	3889	Q9JJ54-3
1086	P21575-8	2488	Q5PQR4	3890	Q9JJ54-4
1087	P21588	2489	Q5PQR6	3891	Q9JJ79
1088	P21670	2490	Q5PQS3	3892	Q9JJK1
1089	P21704	2491	Q5PQS7	3893	Q9JJL4
1090	P21707	2492	Q5PQT2	3894	Q9JJM7
1091	P21708	2493	Q5PT56	3895	Q9JJM9
1092	P21708-2	2494	Q5PXE9	3896	Q9JJM9-2
1093	P21807	2495	Q5QD51	3897	Q9JJM9-3
1094	P21818	2496	Q5QD51-2	3898	Q9JJP6
1095	P21913	2497	Q5QD51-3	3899	Q9JJP6-2
1096	P21932	2498	Q5QE78	3900	Q9JJP6-3
1097	P21994	2499	Q5QE79	3901	Q9JJP6-4
1098	P22002	2500	Q5QE80	3902	Q9JJP6-7
1099	P22002-2	2501	Q5QJC9	3903	Q9JJP6-8
1100	P22002-3	2502	Q5QJV7	3904	Q9JJP9
1101	P22002-4	2503	Q5RJP0	3905	Q9JJS5
1102	P22002-5	2504	Q5RJP9	3906	Q9JJV7
1103	P22057	2505	Q5RJQ4	3907	Q9JJZ1
1104	P22063	2506	Q5RJR2	3908	Q9JK11
1105	P22071	2507	Q5RJT2	3909	Q9JK11-2
1106	P22086	2508	Q5RJZ1	3910	Q9JK11-3
1107	P22199	2509	Q5RJZ1-2	3911	Q9JK11-4

Table C.1. Proteins identified by combined use of DDA and HDMS^E from rat brain tissues. Proteins are listed in alphabetical order—Continued

Listing #	UniprotKB #	Listing #	UniprotKB #	Listing #	UniprotKB #
1108	P22199-2	2510	Q5RK00	3912	Q9JK25
1109	P22199-3	2511	Q5RK19	3913	Q9JK66
1110	P22717	2512	Q5RK27	3914	Q9JK66-2
1111	P22756	2513	Q5RK30	3915	Q9JK66-4
1112	P22756-2	2514	Q5RKG1	3916	Q9JK66-5
1113	P22756-3	2515	Q5RKG3	3917	Q9JK71
1114	P22756-4	2516	Q5RKH6	3918	Q9JKA8
1115	P22829	2517	Q5RKI0	3919	Q9JKA9
1116	P22985	2518	Q5RKI1	3920	Q9JKB8
1117	P23266	2519	Q5RKI3	3921	Q9JKC9
1118	P23267	2520	Q5RKI7	3922	Q9JKC9-2
1119	P23347	2521	Q5RKI8	3923	Q9JKC9-3
1120	P23358	2522	Q5RKL5	3924	Q9JKC9-4
1121	P23377	2523	Q5SGD7	3925	Q9JKL8
1122	P23385	2524	Q5SGE0	3926	Q9JKS6
1123	P23514	2525	Q5TKR9	3927	Q9JKS6-2
1124	P23562	2526	Q5U1X7	3928	Q9JKS6-3
1125	P23562-2	2527	Q5U1Y1	3929	Q9JKT8
1126	P23565	2528	Q5U1Y4	3930	Q9JKU3
1127	P23571	2529	Q5U1Z0	3931	Q9JKU6
1128	P23640	2530	Q5U206	3932	Q9JKY3
1129	P23739	2531	Q5U211	3933	Q9JLA3
1130	P23897	2532	Q5U216	3934	Q9JLH6
1131	P23965	2533	Q5U2M8	3935	Q9JLJ3
1132	P23977	2534	Q5U2N4	3936	Q9JLP1
1133	P24062	2535	Q5U2P0	3937	Q9JLS3
1134	P24135	2536	Q5U2P1	3938	Q9JLS3-2
1135	P24155	2537	Q5U2Q7	3939	Q9JLT0
1136	P24268	2538	Q5U2R1	3940	Q9JLU4
1137	P24329	2539	Q5U2R2	3941	Q9JLU4-2
1138	P24368	2540	Q5U2S6	3942	Q9JLU4-3
1139	P24470	2541	Q5U2V4	3943	Q9JLZ1
1140	P24587	2542	Q5U2W5	3944	Q9JLZ1-2
1141	P24898	2543	Q5U2X0	3945	Q9JM01
1142	P24942	2544	Q5U2X2	3946	Q9JM01-2
1143	P24942-2	2545	Q5U2X4	3947	Q9JM01-3
1144	P25030	2546	Q5U2X7	3948	Q9JM04

Table C.1. Proteins identified by combined use of DDA and HDMS^E from rat brain tissues. Proteins are listed in alphabetical order—Continued

Listing #	UniprotKB #	Listing #	UniprotKB #	Listing #	UniprotKB #
1145	P25094	2547	Q5U2Y1	3949	Q9JMD2
1146	P25110	2548	Q5U2Y1-2	3950	Q9JMI1
1147	P25113	2549	Q5U2Y3	3951	Q9JMI9
1148	P25114	2550	Q5U2Y6	3952	Q9JMJ4
1149	P25122	2551	Q5U2Y9	3953	Q9JMK8
1150	P25235	2552	Q5U2Z2	3954	Q9QUH3
1151	P25286	2553	Q5U2Z5	3955	Q9QUH6
1152	P25286-2	2554	Q5U300	3956	Q9QUH6-2
1153	P25304	2555	Q5U301	3957	Q9QUH6-3
1154	P25304-2	2556	Q5U303	3958	Q9QUH6-4
1155	P25304-3	2557	Q5U303-2	3959	Q9QUH6-5
1156	P25304-4	2558	Q5U309	3960	Q9QUL6
1157	P25304-5	2559	Q5U310	3961	Q9QUR2
1158	P25304-6	2560	Q5U312	3962	Q9QUR2-2
1159	P25409	2561	Q5U312-2	3963	Q9QUZ8
1160	P25809	2562	Q5U315	3964	Q9QVC8
1161	P25977	2563	Q5U316	3965	Q9QW07
1162	P25977-2	2564	Q5U318	3966	Q9QW07-2
1163	P26255	2565	Q5U367	3967	Q9QW07-3
1164	P26284	2566	Q5U3Z0	3968	Q9QWG5
1165	P26431	2567	Q5U3Z6	3969	Q9QWG5-2
1166	P26434	2568	Q5U4E6	3970	Q9QWM1
1167	P26453	2569	Q5UEM7	3971	Q9QWM1-2
1168	P26453-2	2570	Q5UEM7-2	3972	Q9QWN8
1169	P26769	2571	Q5XHX6	3973	Q9QWS8
1170	P26770	2572	Q5XHX6-2	3974	Q9QX01
1171	P26772	2573	Q5XHY5	3975	Q9QX05
1172	P26794	2574	Q5XHY7	3976	Q9QX74
1173	P26817	2575	Q5XHZ0	3977	Q9QX74-2
1174	P26896	2576	Q5XHZ6	3978	Q9QX74-3
1175	P27008	2577	Q5XHZ9	3979	Q9QX74-4
1176	P27049	2578	Q5XI00	3980	Q9QX74-5
1177	P27139	2579	Q5XI02	3981	Q9QX74-6
1178	P27314	2580	Q5XI05	3982	Q9QX74-7
1179	P27364	2581	Q5XI06	3983	Q9QXL7
1180	P27590	2582	Q5XI32	3984	Q9QXQ0
1181	P27605	2583	Q5XI42	3985	Q9QXQ5

Table C.1. Proteins identified by combined use of DDA and HDMS^E from rat brain tissues. Proteins are listed in alphabetical order—Continued

Listing #	UniprotKB #	Listing #	UniprotKB #	Listing #	UniprotKB #
1182	P27653	2584	Q5XI43	3986	Q9QXU9
1183	P27704	2585	Q5XI46	3987	Q9QXY2
1184	P27732	2586	Q5XI52	3988	Q9QXY2-2
1185	P27732-10	2587	Q5XI53	3989	Q9QXY4
1186	P27732-12	2588	Q5XI55	3990	Q9QY17
1187	P27732-2	2589	Q5XI55-2	3991	Q9QY17-2
1188	P27732-3	2590	Q5XI56	3992	Q9QY17-3
1189	P27732-4	2591	Q5XI57	3993	Q9QY17-4
1190	P27732-5	2592	Q5XI57-2	3994	Q9QY78
1191	P27732-6	2593	Q5XI58	3995	Q9QYF3
1192	P27732-7	2594	Q5XI59	3996	Q9QYH1
1193	P27732-8	2595	Q5XI63	3997	Q9QYJ6
1194	P27732-9	2596	Q5XI65	3998	Q9QYJ6-2
1195	P27768	2597	Q5XI69	3999	Q9QYJ6-3
1196	P27791	2598	Q5XI73	4000	Q9QYJ6-4
1197	P27791-2	2599	Q5XI74	4001	Q9QYJ6-5
1198	P27881	2600	Q5XI78	4002	Q9QYJ6-6
1199	P27926	2601	Q5XI81	4003	Q9QYK2
1200	P27952	2602	Q5XI95	4004	Q9QYM2
1201	P28023	2603	Q5XIA0	4005	Q9QYP0
1202	P28037	2604	Q5XIA1	4006	Q9QYP1
1203	P28470	2605	Q5XIA2	4007	Q9QYP2
1204	P28480	2606	Q5XIA3	4008	Q9QYU3
1205	P28492	2607	Q5XIB3	4009	Q9QYU4
1206	P28492-2	2608	Q5XIB4	4010	Q9QYV8
1207	P28494	2609	Q5XIC0	4011	Q9QYW0
1208	P28570	2610	Q5XIC3	4012	Q9QZ81
1209	P28646	2611	Q5XIE3	4013	Q9QZA2
1210	P28818	2612	Q5XIE6	4014	Q9QZE3
1211	P29101	2613	Q5XIE6-2	4015	Q9QZE9
1212	P29266	2614	Q5XIF4	4016	Q9QZL2
1213	P29314	2615	Q5XIF6	4017	Q9QZM5
1214	P29315	2616	Q5XIF9	4018	Q9QZR6
1215	P29321	2617	Q5XIG6	4019	Q9QZR6-2
1216	P29348	2618	Q5XIH6	4020	Q9QZR6-3
1217	P29410	2619	Q5XIH7	4021	Q9QZR6-4
1218	P29410-2	2620	Q5XIH9	4022	Q9QZR8

Table C.1. Proteins identified by combined use of DDA and HDMS^E from rat brain tissues. Proteins are listed in alphabetical order—Continued

Listing #	UniprotKB #	Listing #	UniprotKB #	Listing #	UniprotKB #
1219	P29419	2621	Q5XIJ4	4023	Q9QZU7
1220	P29457	2622	Q5XIJ9	4024	Q9QZX8
1221	P29476	2623	Q5XIK1	4025	Q9QZX8-1
1222	P29476-2	2624	Q5XIK6	4026	Q9QZX8-3
1223	P29476-3	2625	Q5XIK7	4027	Q9R011
1224	P29534	2626	Q5XIK8	4028	Q9R012
1225	P29596	2627	Q5XIL5	4029	Q9R037
1226	P29994	2628	Q5XIL8	4030	Q9R044
1227	P29994-2	2629	Q5XIM4	4031	Q9R044-2
1228	P29994-3	2630	Q5XIM9	4032	Q9R044-3
1229	P29994-4	2631	Q5XIN3	4033	Q9R063
1230	P29994-5	2632	Q5XIN6	4034	Q9R063-2
1231	P29994-6	2633	Q5XIN9	4035	Q9R064
1232	P29994-7	2634	Q5XIP6	4036	Q9R066
1233	P29994-8	2635	Q5XIQ3	4037	Q9R066-2
1234	P29995	2636	Q5XIQ5	4038	Q9R080
1235	P30009	2637	Q5XIR6	4039	Q9R080-2
1236	P30083	2638	Q5XIR6-2	4040	Q9R080-3
1237	P30086	2639	Q5XIR8	4041	Q9R080-4
1238	P30099	2640	Q5XIS2	4042	Q9R085
1239	P30100	2641	Q5XIS9	4043	Q9R095
1240	P30348	2642	Q5XIT0	4044	Q9R095-2
1241	P30349	2643	Q5XIT1	4045	Q9R095-3
1242	P30427	2644	Q5XIV2	4046	Q9R0A8
1243	P30427-2	2645	Q5XIW8	4047	Q9R0L4
1244	P30427-3	2646	Q5XIX0	4048	Q9R0L4-2
1245	P30427-4	2647	Q5XXR3	4049	Q9R0L4-3
1246	P30713	2648	Q5Y4N8	4050	Q9R0T3
1247	P30823	2649	Q60587	4051	Q9R0T4
1248	P30835	2650	Q60GF7	4052	Q9R141
1249	P30839	2651	Q62600	4053	Q9R154
1250	P30904	2652	Q62625	4054	Q9R172
1251	P30994	2653	Q62625-2	4055	Q9R189
1252	P31000	2654	Q62634	4056	Q9R193
1253	P31016	2655	Q62634-2	4057	Q9R193-2
1254	P31044	2656	Q62635	4058	Q9R1A0
1255	P31325	2657	Q62636	4059	Q9R1J8

Table C.1. Proteins identified by combined use of DDA and HDMS^E from rat brain tissues. Proteins are listed in alphabetical order—Continued

Listing #	UniprotKB #	Listing #	UniprotKB #	Listing #	UniprotKB #
1256	P31399	2658	Q62638	4060	Q9R1K2
1257	P31421	2659	Q62639	4061	Q9R1K2-2
1258	P31422	2660	Q62640	4062	Q9R1K2-3
1259	P31423	2661	Q62645	4063	Q9R1K2-4
1260	P31424	2662	Q62645-2	4064	Q9R1N3
1261	P31424-2	2663	Q62655	4065	Q9R1N3-2
1262	P31503	2664	Q62655-2	4066	Q9R1N3-3
1263	P31596	2665	Q62656	4067	Q9R1N3-4
1264	P31596-2	2666	Q62656-2	4068	Q9R1N3-5
1265	P31643	2667	Q62656-3	4069	Q9R1N3-6
1266	P31646	2668	Q62658	4070	Q9R1Q2
1267	P31647	2669	Q62668	4071	Q9R1T9
1268	P31652	2670	Q62668-2	4072	Q9R1U5
1269	P31977	2671	Q62668-3	4073	Q9R1U7
1270	P32198	2672	Q62668-4	4074	Q9R1Z0
1271	P32232	2673	Q62671	4075	Q9R1Z0-2
1272	P32232-2	2674	Q62673	4076	Q9R237
1273	P32232-3	2675	Q62674	4077	Q9R237-2
1274	P32551	2676	Q62682	4078	Q9R237-3
1275	P32736	2677	Q62687	4079	Q9R283
1276	P32736-2	2678	Q62688	4080	Q9R283-2
1277	P32738	2679	Q62689	4081	Q9WTN5
1278	P32755	2680	Q62696	4082	Q9WTP0
1279	P32851	2681	Q62703	4083	Q9WTP0-2
1280	P33124	2682	Q62711	4084	Q9WTQ0
1281	P33124-2	2683	Q62711-2	4085	Q9WTQ1
1282	P33273	2684	Q62711-3	4086	Q9WTR8
1283	P33274	2685	Q62711-4	4087	Q9WTR8-2
1284	P33578	2686	Q62713	4088	Q9WTT2
1285	P33579	2687	Q62717	4089	Q9WTT6
1286	P34058	2688	Q62718	4090	Q9WTV1
1287	P34080	2689	Q62722	4091	Q9WTW1
1288	P34158	2690	Q62726	4092	Q9WTW1-2
1289	P34926	2691	Q62728	4093	Q9WTW1-3
1290	P34980	2692	Q62728-2	4094	Q9WTW1-4
1291	P34980-2	2693	Q62735	4095	Q9WTW8
1292	P34980-3	2694	Q62736	4096	Q9WTY2

Table C.1. Proteins identified by combined use of DDA and HDMS^E from rat brain tissues. Proteins are listed in alphabetical order—Continued

Listing #	UniprotKB #	Listing #	UniprotKB #	Listing #	UniprotKB #
1293	P34997	2695	Q62739	4097	Q9WTY9
1294	P35053	2696	Q62745	4098	Q9WTZ3
1295	P35171	2697	Q62746	4099	Q9WU34
1296	P35213	2698	Q62746-2	4100	Q9WU34-2
1297	P35213-2	2699	Q62747	4101	Q9WU34-3
1298	P35233	2700	Q62747-2	4102	Q9WU70
1299	P35233-3	2701	Q62747-3	4103	Q9WU70-2
1300	P35234	2702	Q62747-4	4104	Q9WU70-3
1301	P35280	2703	Q62747-5	4105	Q9WU82
1302	P35281	2704	Q62747-6	4106	Q9WUB5
1303	P35284	2705	Q62747-7	4107	Q9WUD9
1304	P35286	2706	Q62753	4108	Q9WUD9-2
1305	P35289	2707	Q62768	4109	Q9WUI9
1306	P35332	2708	Q62768-2	4110	Q9WUJ3
1307	P35349	2709	Q62768-3	4111	Q9WUK5
1308	P35400	2710	Q62769	4112	Q9WUQ1
1309	P35407	2711	Q62769-2	4113	Q9WV48
1310	P35426	2712	Q62770	4114	Q9WV48-2
1311	P35433	2713	Q62771	4115	Q9WV48-3
1312	P35434	2714	Q62771-2	4116	Q9WV48-4
1313	P35435	2715	Q62773	4117	Q9WV48-5
1314	P35439	2716	Q62774	4118	Q9WV50
1315	P35439-2	2717	Q62780	4119	Q9WV57
1316	P35439-3	2718	Q62784	4120	Q9WV78
1317	P35439-4	2719	Q62784-2	4121	Q9WV87
1318	P35439-5	2720	Q62789	4122	Q9WVB1
1319	P35439-6	2721	Q62795	4123	Q9WVB9
1320	P35439-7	2722	Q62796	4124	Q9WVC0
1321	P35444	2723	Q62798	4125	Q9WVC7
1322	P35446	2724	Q62803	4126	Q9WVE9
1323	P35465	2725	Q62807	4127	Q9WVE9-2
1324	P35524	2726	Q62812	4128	Q9WVK7
1325	P35525	2727	Q62813	4129	Q9WVR3
1326	P35559	2728	Q62813-2	4130	Q9WVR3-2
1327	P35560	2729	Q62818	4131	Q9WVR7
1328	P35560-2	2730	Q62824	4132	Q9WVS9
1329	P35560-3	2731	Q62825	4133	Q9WVS9-2

Table C.1. Proteins identified by combined use of DDA and HDMS^E from rat brain tissues. Proteins are listed in alphabetical order—Continued

Listing #	UniprotKB #	Listing #	UniprotKB #	Listing #	UniprotKB #
1330	P35571	2732	Q62826	4134	Q9WVT0
1331	P35704	2733	Q62826-2	4135	Q9Z0J5
1332	P35739	2734	Q62829	4136	Q9Z0J8
1333	P35739-2	2735	Q62833	4137	Q9Z0U4
1334	P35815	2736	Q62835	4138	Q9Z0U4-2
1335	P35815-2	2737	Q62839	4139	Q9Z0U4-3
1336	P35942	2738	Q62844	4140	Q9Z0U4-4
1337	P36365	2739	Q62847	4141	Q9Z0U5
1338	P36372	2740	Q62847-2	4142	Q9Z0V5
1339	P36373	2741	Q62862	4143	Q9Z0V6
1340	P36375	2742	Q62862-2	4144	Q9Z0W5
1341	P36376	2743	Q62862-3	4145	Q9Z0Y8
1342	P36506	2744	Q62865	4146	Q9Z0Y8-2
1343	P36510	2745	Q62868	4147	Q9Z122
1344	P36633	2746	Q62876	4148	Q9Z136
1345	P36860	2747	Q62878	4149	Q9Z143
1346	P36876	2748	Q62889	4150	Q9Z1A5
1347	P36877	2749	Q62889-2	4151	Q9Z1A6
1348	P36877-2	2750	Q62889-3	4152	Q9Z1B2
1349	P37199	2751	Q62889-4	4153	Q9Z1C8
1350	P37285	2752	Q62901	4154	Q9Z1C8-2
1351	P37285-2	2753	Q62909	4155	Q9Z1F1
1352	P37285-3	2754	Q62910	4156	Q9Z1K9
1353	P37377	2755	Q62910-2	4157	Q9Z1L0
1354	P37377-2	2756	Q62910-3	4158	Q9Z1M9
1355	P37377-3	2757	Q62910-4	4159	Q9Z1N3
1356	P37805	2758	Q62910-5	4160	Q9Z1N4
1357	P37996	2759	Q62910-6	4161	Q9Z1P2
1358	P38406	2760	Q62915	4162	Q9Z1X1
1359	P38438	2761	Q62918	4163	Q9Z1Y0
1360	P38650	2762	Q62924	4164	Q9Z1Y3
1361	P38656	2763	Q62925	4165	Q9Z1Z1
1362	P38659	2764	Q62931	4166	Q9Z1Z9
1363	P39020	2765	Q62935	4167	Q9Z214
1364	P39052	2766	Q62936	4168	Q9Z214-2
1365	P39052-2	2767	Q62936-2	4169	Q9Z220
1366	P39052-3	2768	Q62947	4170	Q9Z221

Table C.1. Proteins identified by combined use of DDA and HDMS^E from rat brain tissues. Proteins are listed in alphabetical order—Continued

Listing #	UniprotKB #	Listing #	UniprotKB #	Listing #	UniprotKB #
1367	P39052-4	2769	Q62947-2	4171	Q9Z244
1368	P39069	2770	Q62950	4172	Q9Z250
1369	P39949	2771	Q62951	4173	Q9Z258
1370	P39951	2772	Q62952	4174	Q9Z258-2
1371	P40112	2773	Q62952-2	4175	Q9Z270
1372	P40146	2774	Q62956	4176	Q9Z272
1373	P40307	2775	Q62956-2	4177	Q9Z286
1374	P40329	2776	Q62959	4178	Q9Z2A6
1375	P40748	2777	Q62959-2	4179	Q9Z2I7
1376	P41135	2778	Q62959-3	4180	Q9Z2J4
1377	P41135-2	2779	Q62959-4	4181	Q9Z2J4-2
1378	P41138	2780	Q62959-5	4182	Q9Z2K0
1379	P41156	2781	Q62962-2	4183	Q9Z2K3
1380	P41224	2782	Q62968	4184	Q9Z2L0
1381	P41499	2783	Q62968-2	4185	Q9Z2P5
1382	P41499-2	2784	Q62969	4186	Q9Z2Q1
1383	P41516	2785	Q62976	4187	Q9Z2Q1-2
1384	P41542	2786	Q62976-10	4188	Q9Z2Q4
1385	P41562	2787	Q62976-11	4189	Q9Z2Z8
1386	P41565	2788	Q62976-2	4190	Q9Z301
1387	P41777	2789	Q62976-3	4191	Q9Z311
1388	P42123	2790	Q62976-8	4192	Q9Z311-2
1389	P42260	2791	Q62976-9	4193	Q9Z327
1390	P42264	2792	Q62985	4194	Q9Z327-2
1391	P42264-2	2793	Q62985-2	4195	Q9Z327-3
1392	P42335	2794	Q62986	4196	Q9Z330
1393	P42346	2795	Q62986-2	4197	Q9Z330-2
1394	P42533	2796	Q62986-3	4198	Q9Z330-3
1395	P42676	2797	Q62986-4	4199	Q9Z330-4
1396	P42893	2798	Q62986-5	4200	Q9Z330-5
1397	P42893-2	2799	Q63003	4201	Q9Z330-6
1398	P42893-3	2800	Q63009	4202	Q9Z330-7
1399	P42893-4	2801	Q63010	4203	Q9Z330-8
1400	P43165	2802	Q63014	4204	Q9Z330-9
1401	P43244	2803	Q63028	4205	Q9Z335
1402	P43245	2804	Q63028-2	4206	Q9Z340
				4207	Q9Z340-2

BIBLIOGRAPHY

1. Giorgi, G. Mass Spectrometry and High Resolution Mass Spectrometry: An Overview. In *Molecular Technologies for Detection of Chemical and Biological Agents*; Banoud, J. H., Caprioli, R. M.; Springer: Netherlands, 2017; Vol. 1, pp 89-101.

2. Bantscheff, M.; Lemeer, S.; Savitski, M. M.; Kuster, B., Quantitative mass spectrometry in proteomics: critical review update from 2007 to the present. *Anal. Bioanal. Chem.* **2012,** 404, (4), 939-965.

3. Bantscheff, M.; Schirle, M.; Sweetman, G.; Rick, J.; Kuster, B., Quantitative mass spectrometry in proteomics: a critical review. *Anal. Bioanal. Chem.* **2007,** 389, (4), 1017-1031.

4. Becker, J. S.; Zoriy, M.; Matusch, A.; Wu, B.; Salber, D.; Palm, C.; Becker, J. S., Bioimaging of metals by laser ablation inductively coupled plasma mass spectrometry (LA-ICP-MS). *Mass Spectrom. Rev.* **2010,** 29, (1), 156-175.

5. Jackson, S.; Fryer, B.; Gosse, W.; Healey, D.; Longerich, H.; Strong, D., Determination of the precious metals in geological materials by inductively coupled plasma-mass spectrometry (ICP-MS) with nickel sulphide fire-assay collection and tellurium coprecipitation. *Chem. Geol.* **1990,** 83, (1-2), 119-132.

6. Yin, J.; Jiang, Z.; Chang, G.; Hu, B., Simultaneous on-line preconcentration and determination of trace metals in environmental samples by flow injection combined with inductively coupled plasma mass spectrometry using a nanometer-sized alumina packed micro-column. *Anal. Chim. Acta.* **2005,** 540, (2), 333-339.

7. Han, X. *Lipidomics: Comprehensive Mass Spectrometry of Lipids*; John Wiley & Sons: Hoboken, NJ, 2016.

8. Harkewicz, R.; Dennis, E. A., Applications of mass spectrometry to lipids and membranes. *Annu. Rev. Biochem.* **2011,** 80, 301-325.

9. Han, L.; Costello, C. E., Mass spectrometry of glycans. *Biochemistry-Moscow+* **2013,** 78, (7), 710-720.

10. Leymarie, N.; Zaia, J., Effective Use of mass spectrometry for glycan and glycopeptide structural analysis. *Anal. Chem.* **2012,** *84*, 3040-3048.

11. Hillenkamp, F.; Karas, M.; Beavis, R. C.; Chait, B. T., Matrix-assisted laser desorption/ionization mass spectrometry of biopolymers. *Anal. Chem.* **1991,** 63, (24), 1193A-1203A.

12. Tanaka, K.; Waki, H.; Ido, Y.; Akita, S.; Yoshida, Y.; Yoshida, T.; Matsuo, T., Protein and polymer analyses up to m/z 100 000 by laser ionization time-of-flight mass spectrometry. *Rapid Commun. Mass Spectrom.* **1988,** 2, (8), 151-153.

13. Whitehouse, C. M.; Dreyer, R.; Yamashita, M.; Fenn, J., Electrospray ionization for mass-spectrometry of large biomolecules. *Science* **1989,** 246, (4926), 64-71.

14. Cuyckens, F.; Claeys, M., Mass spectrometry in the structural analysis of flavonoids. *J. Mass. Spectrom.* **2004,** 39, (1), 1-15.

15. Sharp, J. S.; Becker, J. M.; Hettich, R. L., Protein surface mapping by chemical oxidation: structural analysis by mass spectrometry. *Anal. Biochem.* **2003,** 313, (2), 216-225.

16. Qian, K.; Robbins, W. K.; Hughey, C. A.; Cooper, H. J.; Rodgers, R. P.; Marshall, A. G., Resolution and identification of elemental compositions for more than 3000 crude acids in heavy petroleum by negative-ion microelectrospray high-field Fourier transform ion cyclotron resonance mass spectrometry. *Energ. Fuel.* **2001,** 15, (6), 1505-1511.

17. van Hove, E. R. A.; Smith, D. F.; Heeren, R. M., A concise review of mass spectrometry imaging. *J. Chromatogr. A.* **2010,** 1217, (25), 3946-3954.

18. Al-Tarawneh, S. K.; Border, M. B.; Dibble, C. F.; Bencharit, S., Defining salivary biomarkers using mass spectrometry-based proteomics: a systematic review. *Omics.* **2011,** 15, (6), 353-361.

19. Korfmacher, W. A., Foundation review: principles and applications of LC-MS in new drug discovery. *Drug Discov. Today* **2005,** 10, (20), 1357-1367.

20. Lee, M. S.; Kerns, E. H., LC/MS applications in drug development. *Mass Spectrom. Rev.* **1999,** 18, (3-4), 187-279.

21. Murray, K. K.; Boyd, R. K.; Eberlin, M. N.; Langley, G. J.; Li, L.; Naito, Y., Definitions of terms relating to mass spectrometry (IUPAC Recommendations 2013). *Pure Appl. Chem.* **2013,** 85, (7), 1515-1609.

22. Bleakney, W., A new method of positive ray analysis and its application to the measurement of ionization potentials in mercury vapor. *Phys. Rev.* **1929,** 34, (1), 157.

23. Karas, M.; Hillenkamp, F., Laser desorption ionization of proteins with molecular masses exceeding 10,000 daltons. *Anal. Chem.* **1988,** 60, (20), 2299-2301.

24. Vetter, W. Biol. Mass Spectrom.. In *Interpretation of mass spectra*; McLafferty, F. W., Turecek, F.; University science books: Mill Valley, CA, Vol. 23, pp 379.

25. Vékey, K., Internal energy effects in mass spectrometry. *J. Mass. Spectrom.* **1996,** 31, (5), 445-463.

26. Munson, M. S.; Field, F.-H., Chemical ionization mass spectrometry. I. General introduction. *J. Am. Chem. Soc.* **1966,** 88, (12), 2621-2630.

27. Dole, M.; Mack, L.; Hines, R.; Mobley, R.; Ferguson, L.; Alice, M. d., Molecular beams of macroions. *J. Chem. Phys.* **1968,** 49, (5), 2240-2249.

28. Fenn, J. B.; Mann, M.; Meng, C. K.; Wong, S. F.; Whitehouse, C. M., Electrospray ionization–principles and practice. *Mass Spectrom. Rev.* **1990,** 9, (1), 37-70.

29. Ido, Y.; Tanaka, K.; Akita, S.; Yoshida, Y.; Yoshida, T., Development of Laser Ionization Time of Flight Mass Spectrometer III–Sensitive Ion Detection in High Mass Range. *35-kai Shitsuryo Bunseki Rengo Toronkai, Yoshishu* **1987**, 20-21.

30. Karas, M.; Bachmann, D.; Bahr, U. e.; Hillenkamp, F., Matrix-assisted ultraviolet laser desorption of non-volatile compounds. *Int. J. Mass Spectrom.* **1987,** 78, 53-68.

31. Games, D. E., Soft ionization mass spectral methods for lipid analysis. *Chem. Phys. Lipids* **1978,** 21, (4), 389-402.

32. Iavarone, A. T.; Williams, E. R., Mechanism of charging and supercharging molecules in electrospray ionization. *J. Am. Chem. Soc.* **2003,** 125, (8), 2319-2327.

33. Berkenkamp, S.; Kirpekar, F.; Hillenkamp, F., Infrared MALDI mass spectrometry of large nucleic acids. *Science* **1998,** 281, (5374), 260-262.

34. Knochenmuss, R., Ion formation mechanisms in UV-MALDI. *Analyst* **2006,** 131, (9), 966-986.

35. Kebarle, P.; Verkerk, U. H., Electrospray: from ions in solution to ions in the gas phase, what we know now. *Mass Spectrom. Rev.* **2009,** 28, (6), 898-917.

36. Heck, A. J.; van den Heuvel, R. H., Investigation of intact protein complexes by mass spectrometry. *Mass Spectrom. Rev.* **2004,** 23, (5), 368-389.

37. Nilsson, T.; Mann, M.; Aebersold, R.; Yates III, J. R.; Bairoch, A.; Bergeron, J. J., Mass spectrometry in high-throughput proteomics: ready for the big time. *Nat. Methods* **2010,** 7, (9), 681-685.

38. Fernández de La Mora, J., The fluid dynamics of Taylor cones. *Annu. Rev. Fluid Mech.* **2007,** 39, 217-243.

39. Taylor, G.; McEwan, A., The stability of a horizontal fluid interface in a vertical electric field. *J. Fluid Mechanics* **1965,** 22, (1), 1-15.

40. Rayleigh, L., XX. On the equilibrium of liquid conducting masses charged with electricity. *The London, Edinburgh, and Dublin Philosophical Magazine and Journal of Science* **1882,** 14, (87), 184-186.

41. Iribarne, J.; Thomson, B., On the evaporation of small ions from charged droplets. *J. Chem. Phys.* **1976,** 64, (6), 2287-2294.

42. Konermann, L.; Ahadi, E.; Rodriguez, A. D.; Vahidi, S., Unraveling the mechanism of electrospray ionization. *Anal. Chem.* **2013,** *85*, 2-9.

43. Douglas, D. J.; Frank, A. J.; Mao, D., Linear ion traps in mass spectrometry. *Mass Spectrom. Rev.* **2005,** 24, (1), 1-29.

44. Guilhaus, M., Principles and Instrumentation in Time-of-ight Mass Spectrometry. *J. Mass. Spectrom.* **1995,** 30, (1519), 1532.

45. Cody, R. B.; Tamura, J.; Musselman, B. D., Electrospray ionization/magnetic sector mass spectrometry: calibration, resolution, and accurate mass measurements. *Anal. Chem.* **1992,** 64, (14), 1561-1570.

46. Nier, A.; Schlutter, D., High-performance double-focusing mass spectrometer. *Rev. Sci. Inst.* **1985,** 56, (2), 214-219.

47. Comisarow, M. B.; Marshall, A. G., Fourier transform ion cyclotron resonance spectroscopy. *Chem. Phys. Lett.* **1974,** 25, (2), 282-283.

48. Marshall, A. G.; Hendrickson, C. L.; Jackson, G. S., Fourier transform ion cyclotron resonance mass spectrometry: a primer. *Mass Spectrom. Rev.* **1998,** 17, (1), 1-35.

49. Makarov, A., Electrostatic axially harmonic orbital trapping: a high-performance technique of mass analysis. *Anal. Chem.* **2000,** 72, (6), 1156-1162.

50. El-Aneed, A.; Cohen, A.; Banoub, J., Mass spectrometry, review of the basics: electrospray, MALDI, and commonly used mass analyzers. *Appl. Spectrosc. Rev.* **2009,** 44, (3), 210-230.

51. Agarwal, P.; Goyal, A., A Review On Analyzers For Mass Spectrometry. *Int. J. Pharma. Bio. Sci.* **2017,** 8, (4), 139-151.

52. LC/GC's CHROMacademy: Optimizing LC-MS and LC-MS/MS. https://www.chromacademy.com/Optimizing-LC-MS_and_LC-MS-MS.html?tpm=1_1 (accessed Mar. 21, 2018).

53. Lebedev, A.; Zaikin, V., *J. Anal. Chem.*+, **2008,** 63, 1128. Lebedev, A.; Zaikin, V., *J. Anal. Chem.*+, **2008**, 63, 1128.

54. Solouki, T.; Marto, J. A.; White, F. M.; Guan, S.; Marshall, A. G., *Anal. Chem.,* **1995,** 67, 4139-4144.

55. Fiehn Lab Home Page: Accurate Mass. http://fiehnlab.ucdavis.edu/projects/seven-golden-rules/accurate-mass (accessed Mar. 21, 2018).

56. Rose, R. J.; Damoc, E.; Denisov, E.; Makarov, A.; Heck, A. J., *Nat. Methods*, **2012,** 9, 1084-1086.

57. Planet Orbitrap: Exactive Plus EMR Orbitrap LC-MS System. http://planetorbitrap.com/exactive-plus-emr#tab:specifications (accessed Mar. 21, 2018).

58. Chernushevich, I. V.; Loboda, A. V.; Thomson, B. A., An introduction to quadrupole–time-of-flight mass spectrometry. *J. Mass. Spectrom.* **2001,** 36, (8), 849-865.

59. Dawson, P. H. Principles of Operation. In *Quadrupole Mass Spectrometry and Its Applications*; Dawson, P. H.; Elsevier/North-Holland Inc.: New York, NY, 1976; Vol. 1, pp 9-63.

60. Miller, P. E.; Denton, M. B., The quadrupole mass filter: basic operating concepts. *J. Chem. Educ.* **1986,** 63, (7), 617.

61. Skoog, D. A.; Holler, F. J.; Crouch, S. R. *Principles of Instrumental Analysis*; Cengage Learning: Boston, MA, 2017.

62. Watson, J. T.; Sparkman, O. D. *Introduction to Mass Spectrometry: Instrumentation, Applications, and Strategies for Data Interpretation*; John Wiley & Sons: Hoboken, NJ, 2007.

63. Stephens, W. E., A pulsed mass spectrometer with time dispersion. *Phys. Rev.* **1946,** *69*, 674-674.

64. Wolff, M. M.; Stephens, W. E., A pulsed mass spectrometer with time dispersion. *Rev. Sci. Inst.* **1953,** 24, (8), 616-617.

65. Wiley, W.; McLaren, I. H., Time-of-flight mass spectrometer with improved resolution. *Rev. Sci. Inst.* **1955,** 26, (12), 1150-1157.

66. Brown, R. S.; Lennon, J. J., Mass resolution improvement by incorporation of pulsed ion extraction in a matrix-assisted laser desorption/ionization linear time-of-flight mass spectrometer. *Anal. Chem.* **1995,** 67, (13), 1998-2003.

67. Mamyrin, B.; Karataev, V.; Shmikk, D.; Zagulin, V., The massreflect ron, a new non-magnetic time-of-flight mass spectrometer with high resolution. *Zh. Eksp. Teor. Fiz* **1973,** 64, 82-89.

68. Gys, T., Micro-channel plates and vacuum detectors. *Nuc. Instrum. Meth. A* **2015,** 787, 254-260.

69. Miladi, M.; Zekavat, B.; Munisamy, S. M.; Solouki, T., A systematic study on the effect of histidine position and fragment ion size on the formation of b n ions. *Int. J. Mass. Spectrom.* **2012,** 316, 164-173.

70. Green, M. K.; Lebrilla, C. B., Ion-molecule reactions as probes of gas-phase structures of peptides and proteins. *Mass Spectrom. Rev.* **1997,** 16, (2), 53-71.

71. Rose, B., Gas chromatography and its analytical applications. A review. *Analyst* **1959,** 84, (1003), 574b-595.

72. McNair, H. M.; Miller, J. M. *Basic Gas Chromatography*; John Wiley & Sons, Hoboken, NJ, 2011.

73. James, A. T.; Martin, A. J, P, Gas-liquid partition chromatography: the separation and micro-estimation of volatile fatty acids from formic acid to dodecanoic acid. *Biochem. J.* **1952,** 50, (5), 679.

74. Locke, D. C., Gas-Solid Partition Chromatography with Real Carrier Gases. *The J. Phys. Chem.* **1965,** 69, (11), 3768-3773.

75. Ito, Y.; Bowman, R. L., Countercurrent chromatography: liquid-liquid partition chromatography without solid support. *J. Chromatogr. Sci.* **1970,** 8, (6), 315-323.

76. Snyder, L.; Saunders, D., Optimized solvent programming for separations of complex samples by liquid-solid adsorption chromatography in columns. *J. Chromatogr. Sci.* **1969,** 7, (4), 195-208.

77. Walton, H. F., Ion-exchange chromatography. *Anal. Chem.* **1968,** 40, (5), 51-62.

78. Barth, H. G.; Boyes, B. E.; Jackson, C., Size exclusion chromatography. *Anal. Chem.* **1996,** 68, (12), 445-466.

79. Clemmer, D. E.; Hudgins, R. R.; Jarrold, M. F., Naked Protein Conformations: Cytochrome c in the Gas Phase. *J. Am. Chem. Soc.* **1995,** 117, (40), 10141-10142.

80. Clemmer, D. E.; Jarrold, M. F., Ion mobility measurements and their applications to clusters and biomolecules. *J. Mass. Spectrom.* **1997,** 32, (6), 577-592.

81. Giles, K.; Pringle, S. D.; Worthington, K. R.; Little, D.; Wildgoose, J. L.; Bateman, R. H., Applications of a travelling wave-based radio-frequency-only stacked ring ion guide. *Rapid Commun. Mass Spectrom.* **2004,** 18, (20), 2401-2414.

82. Pringle, S. D.; Giles, K.; Wildgoose, J. L.; Williams, J. P.; Slade, S. E.; Thalassinos, K.; Bateman, R. H.; Bowers, M. T.; Scrivens, J. H., An investigation of the mobility separation of some peptide and protein ions using a new hybrid quadrupole/travelling wave IMS/oa-ToF instrument. *Int. J. Mass. Spectrom.* **2007,** 261, (1), 1-12.

83. Wyttenbach, T.; von Helden, G.; Bowers, M. T., Gas-phase conformation of biological molecules: Bradykinin. *J. Am. Chem. Soc.* **1996,** 118, (35), 8355-8364.

84. Cumeras, R.; Figueras, E.; Davis, C.; Baumbach, J. I.; Gracia, I., Review on ion mobility spectrometry. Part 1: current instrumentation. *Analyst* **2015,** 140, (5), 1376-1390.

85. Asbury, G. R.; Hill, H. H., Evaluation of ultrahigh resolution ion mobility spectrometry as an analytical separation device in chromatographic terms. *J. Microcolumn Sep.* **2000,** 12, (3), 172-178.

86. Holland, J. F.; Enke, C. G.; Allison, J.; Stults, J. T.; Pinkston, J. D.; Newcome, B.; Watson, J. T., Mass spectrometry on the chromatographic time scale: realistic expectations. *Anal. Chem.* **1983,** 55, (9), 997A-1012A.

87. Pettit, M. E.; Harper, B.; Brantley, M. R.; Solouki, T., Collision-energy resolved ion mobility characterization of isomeric mixtures. *Analyst* **2015,** 140, (20), 6886-6896.

88. Bush, M. F.; Hall, Z.; Giles, K.; Hoyes, J.; Robinson, C. V.; Ruotolo, B. T., Collision cross sections of proteins and their complexes: a calibration framework and database for gas-phase structural biology. *Anal. Chem.* **2010,** 82, (22), 9557-9565.

89. Ewing, R. G.; Atkinson, D. A.; Eiceman, G.; Ewing, G., A critical review of ion mobility spectrometry for the detection of explosives and explosive related compounds. *Talanta* **2001,** 54, (3), 515-529.

90. Vinopal, R.; Jadamec, J.; Demars, A.; Jakubielski, S.; Green, C.; Anderson, C.; Dugas, J.; DeBono, R., Fingerprinting bacterial strains using ion mobility spectrometry. *Anal. Chim. Acta.* **2002,** 457, (1), 83-95.

91. Cohen, M. J.; Karasek, F., Plasma chromatography™—a new dimension for gas chromatography and mass spectrometry. *J. Chromatogr. Sci.* **1970,** 8, (6), 330-337.

92. Shvartsburg, A. A., *Differential ion mobility spectrometry: nonlinear ion transport and fundamentals of FAIMS*; CRC Press: Boca Raton, FL, 2008.

93. Agbonkonkon, N., *Counter-flow ion mobility analysis: Design, instrumentation, and characterization*; Brigham Young University: 2007.

94. Loboda, A., Novel ion mobility setup combined with collision cell and time-of-flight mass spectrometer. *J. Am. Soc. Mass Spectr.* **2006,** 17, (5), 691-699.

95. Gerlich, D., Inhomogeneous rf fields: a versatile tool for the study of processes with slow ions. In *State-selected and state-to-state ion-molecule reaction dynamics: Part I;* Ng, C. Y., Baer, M.; John Wiley & Sons: Hoboken, NJ, 1992; pp 1-176.

96. Guan, S.; Marshall, A. G., Stacked-ring electrostatic ion guide. *J. Am. Soc. Mass Spectr.* **1996,** 7, (1), 101-106.

97. Luca, A.; Schlemmer, S.; Čermák, I.; Gerlich, D., On the combination of a linear field free trap with a time-of-flight mass spectrometer. *Rev. Sci. Inst.* **2001,** 72, (7), 2900-2908.

98. Giles, K.; Williams, J. P.; Campuzano, I., Enhancements in travelling wave ion mobility resolution. *Rapid Commun. Mass Spectrom.* **2011,** 25, (11), 1559-1566.

99. Shvartsburg, A. A.; Smith, R. D., Fundamentals of Traveling Wave Ion Mobility Spectrometry. *Anal. Chem.* **2008,** 80, (24), 9689-9699.

100. May, J. C.; McLean, J. A., Ion mobility-mass spectrometry: time-dispersive instrumentation. *Anal. Chem.* **2015,** 87, (3), 1422-1436.

101. Hoaglund-Hyzer, C. S.; Counterman, A. E.; Clemmer, D. E., Anhydrous protein ions. *Chem. Rev.* **1999,** 99, (10), 3037-3080.

102. Ruotolo, B. T.; Benesch, J. L.; Sandercock, A. M.; Hyung, S. J.; Robinson, C. V., Ion mobility–mass spectrometry analysis of large protein complexes. *Nat. Protocols* **2008,** 3, (7), 1139-1152.

103. Ridenour, W. B.; Kliman, M.; McLean, J. A.; Caprioli, R. M., Structural characterization of phospholipids and peptides directly from tissue sections by MALDI traveling-wave ion mobility-mass spectrometry. *Anal. Chem.* **2010,** 82, (5), 1881-1889.

104. Ruotolo, B. T.; Giles, K.; Campuzano, I.; Sandercock, A. M.; Bateman, R. H.; Robinson, C. V., Evidence for macromolecular protein rings in the absence of bulk water. *Science* **2005,** 310, (5754), 1658-1661.

105. Smith, D. P.; Knapman, T. W.; Campuzano, I.; Malham, R. W.; Berryman, J. T.; Radford, S. E.; Ashcroft, A. E., Deciphering drift time measurements from travelling wave ion mobility spectrometry-mass spectrometry studies. *Eur. J. Mass Spectrom.* **2008,** 15, (2), 113-130.

106. Williams, J. P.; Bugarcic, T.; Habtemariam, A.; Giles, K.; Campuzano, I.; Rodger, P. M.; Sadler, P. J., Isomer separation and gas-phase configurations of organoruthenium anticancer complexes: ion mobility mass spectrometry and modeling. *J. Am. Soc. Mass Spectr.* **2009,** 20, (6), 1119-1122.

107. Tabrizchi, M.; Khayamian, T.; Taj, N., Design and optimization of a corona discharge ionization source for ion mobility spectrometry. *Rev. Sci. Inst.* **2000,** 71, (6), 2321-2328.

108. Taylor, S. J.; Turner, R. B.; Arnold, P. D., Corona discharge ionization source. U.S. Patent 5,684,300, March, 29, 1997.

109. Merenbloom, S. I.; Flick, T. G.; Williams, E. R., How hot are your ions in TWAVE ion mobility spectrometry? *J. Am. Soc. Mass Spectr.* **2012,** 23, (3), 553-562.

110. Morsa, D.; Gabelica, V.; De Pauw, E., Effective temperature of ions in traveling wave ion mobility spectrometry. *Anal. Chem.* **2011,** 83, (14), 5775-5782.

111. Eschweiler, J. D.; Rabuck-Gibbons, J. N.; Tian, Y.; Ruotolo, B. T., CIUSuite: a quantitative analysis package for collision induced unfolding measurements of gas-phase protein ions. *Anal. Chem.* **2015,** 87, (22), 11516-11522.

112. Hopper, J. T.; Oldham, N. J., Collision induced unfolding of protein ions in the gas phase studied by ion mobility-mass spectrometry: the effect of ligand binding on conformational stability. *J. Am. Soc. Mass Spectr.* **2009,** 20, (10), 1851-1858.

113. Tian, Y.; Han, L.; Buckner, A. C.; Ruotolo, B. T., Collision induced unfolding of intact antibodies: rapid characterization of disulfide bonding patterns, glycosylation, and structures. *Anal. Chem.* **2015,** 87, (22), 11509-11515.

114. Giles, K.; Wildgoose, J. L.; Langridge, D. J.; Campuzano, I., A method for direct measurement of ion mobilities using a travelling wave ion guide. *Int. J. Mass. Spectrom.* **2010,** 298, (1), 10-16.

115. Badman, E. R.; Hoaglund-Hyzer, C. S.; Clemmer, D. E., Dissociation of different conformations of ubiquitin ions. *J. Am. Soc. Mass Spectr.* **2002,** 13, (6), 719-723.

116. Liu, Y.; Clemmer, D. E., Characterizing Oligosaccharides Using Injected-Ion Mobility/Mass Spectrometry. *Anal. Chem.* **1997,** 69, (13), 2504-2509.

117. Shvartsburg, A. A.; Smith, R. D., Accelerated High-Resolution Differential Ion Mobility Separations Using Hydrogen. *Anal. Chem.* **2011,** 83, (23), 9159-9166.

118. Zucker, S. M.; Lee, S.; Webber, N.; Valentine, S. J.; Reilly, J. P.; Clemmer, D. E., An ion mobility/ion trap/photodissociation instrument for characterization of ion structure. *J. Am. Soc. Mass Spectr.* **2011,** 22, (9), 1477.

119. Grob, R. L.; Barry, E. F., *Modern practice of gas chromatography*; John Wiley & Sons: Hoboken, NJ, 2004.

120. Snyder, L. R., HPLC: Past and Present. *Anal. Chem.* **2000,** 72, (11), 412 A-420 A.

121. Snyder, L. R.; Kirkland, J. J.; Dolan, J. W., *Introduction to modern liquid chromatography*; John Wiley & Sons: Hoboken, NJ, 2011.

122. Rokushika, S.; Hatano, H.; Baim, M. A.; Hill, H. H., Resolution measurement for ion mobility spectrometry. *Anal. Chem.* **1985,** 57, (9), 1902-1907.

123. Siems, W. F.; Wu, C.; Tarver, E. E.; Hill, H. H. J.; Larsen, P. R.; McMinn, D. G., Measuring the resolving power of ion mobility spectrometers. *Anal. Chem.* **1994,** 66, (23), 4195-4201.

124. Creese, A. J.; Cooper, H. J., Separation and Identification of Isomeric Glycopeptides by High Field Asymmetric Waveform Ion Mobility Spectrometry. *Anal. Chem.* **2012,** 84, (5), 2597-2601.

125. Garmón-Lobato, S.; Abad-García, B.; Sánchez-Ilárduya, M.; Romera-Fernández, M.; Berrueta, L.; Gallo, B.; Vicente, F., Improvement using chemometrics in ion mobility coupled to mass spectrometry as a tool for mass spectrometry fragmentation studies: Flavonoid aglycone cases. *Anal. Chim. Acta.* **2013,** 771, 56-64.

126. Hoffmann, W.; Hofmann, J.; Pagel, K., Energy-resolved ion mobility-mass spectrometry—a concept to improve the separation of isomeric carbohydrates. *J. Am. Soc. Mass Spectr.* **2014,** 25, (3), 471-479.

127. Lee, S.; Li, Z.; Valentine, S. J.; Zucker, S. M.; Webber, N.; Reilly, J. P.; Clemmer, D. E., Extracted fragment ion mobility distributions: a new method for complex mixture analysis. *Int. J. Mass. Spectrom.* **2012,** 309, 154-160.

128. Xuan, Y.; Creese, A. J.; Horner, J. A.; Cooper, H. J., High-field asymmetric waveform ion mobility spectrometry (FAIMS) coupled with high-resolution electron transfer dissociation mass spectrometry for the analysis of isobaric phosphopeptides. *Rapid Commun. Mass Spectrom.* **2009,** 23, (13), 1963-1969.

129. Zekavat, B.; Solouki, T., Chemometric data analysis for deconvolution of overlapped ion mobility profiles. *J. Am. Soc. Mass Spectr.* **2012,** 23, (11), 1873-1884.

130. Windig, W.; Guilment, J., Interactive self-modeling mixture analysis. *Anal. Chem.* **1991,** 63, (14), 1425-1432.

131. Brantley, M.; Zekavat, B.; Harper, B.; Mason, R.; Solouki, T., Automated deconvolution of overlapped ion mobility profiles. *J. Am. Soc. Mass Spectr.* **2014,** 25, (10), 1810-1819.

132. Brantley, M. R.; Pettit, M. E.; Harper, B.; Brown, B.; Solouki, T., Automated peak width measurements for targeted analysis of ion mobility unresolved species. *Anal. Chim. Acta.* **2016,** 941, 49-60.

133. Harper, B.; Miladi, M.; Solouki, T., Loss of internal backbone carbonyls: additional evidence for sequence-scrambling in collision-induced dissociation of y-type ions. *J. Am. Soc. Mass Spectr.* **2014,** 25, (10), 1716-1729.

134. Harper, B.; Neumann, E. K.; Stow, S. M.; May, J. C.; McLean, J. A.; Solouki, T., Determination of ion mobility collision cross sections for unresolved isomeric mixtures using tandem mass spectrometry and chemometric deconvolution. *Anal. Chim. Acta.* **2016,** 939, 64-72.

135. Kliman, M.; May, J. C.; McLean, J. A., Lipid analysis and lipidomics by structurally selective ion mobility-mass spectrometry. *BBA-Mol. Cel. Biol. L.* **2011,** 1811, (11), 935-945.

136. Zaia, J., Mass spectrometry and the emerging field of glycomics. *Chem. Biol.* **2008,** 15, (9), 881-892.

137. Coon, J. J.; Syka, J.; Shabanowitz, J.; Hunt, D. F., Tandem mass spectrometry for peptide and protein sequence analysis. *Biotechniques* **2005,** 38, (4), 519, 521, 523-519, 521, 523.

138. Zhang, Y.; Fonslow, B. R.; Shan, B.; Baek, M.-C.; Yates III, J. R., Protein analysis by shotgun/bottom-up proteomics. *Chem. Rev.* **2013,** 113, (4), 2343-2394.

139. Jennings, K. R., Collision-induced decompositions of aromatic molecular ions. *Int. J. Mass. Spectrom. Ion Phys.* **1968,** 1, (3), 227-235.

140. McLafferty, F.; Bente, P.; Kornfeld, R.; Tsai, S.-C.; Howe, I., Metastable ion characteristics. XXII. Collisional activation spectra of organic ions. *J. Am. Chem. Soc.* **1973,** 95, (7), 2120-2129.

141. Wells, J. M.; McLuckey, S. A., Collision-induced dissociation (CID) of peptides and proteins. *Method. Enzymol.* **2005,** 402, 148-185.

142. Gauthier, J.; Trautman, T.; Jacobson, D., Sustained off-resonance irradiation for collision-activated dissociation involving Fourier transform mass spectrometry. Collision-activated dissociation technique that emulates infrared multiphoton dissociation. *Anal. Chim. Acta.* **1991,** 246, (1), 211-225.

143. Little, D. P.; Speir, J. P.; Senko, M. W.; O'Connor, P. B.; McLafferty, F. W., Infrared multiphoton dissociation of large multiply charged ions for biomolecule sequencing. *Anal. Chem.* **1994,** 66, (18), 2809-2815.

144. Wysocki, V. H.; Kenttämaa, H. I.; Cooks, R. G., Internal energy distributions of isolated ions after activation by various methods. *Int. J. Mass Spectrom.* **1987,** 75, (2), 181-208.

145. De Hoffmann, E.; Stroobant, V., *Mass spectrometry: principles and applications*. John Wiley & Sons: Hoboken, NJ, 2007.

146. Mabud, M. A.; Dekrey, M. J.; Cooks, R. G., Surface-induced dissociation of molecular ions. *Int. J. Mass Spectrom.* **1985,** 67, (3), 285-294.

147. Wysocki, V. H.; Joyce, K. E.; Jones, C. M.; Beardsley, R. L., Surface-induced dissociation of small molecules, peptides, and non-covalent protein complexes. *J. Am. Soc. Mass Spectr.* **2008,** 19, (2), 190-208.

148. Zubarev, R. A.; Kelleher, N. L.; McLafferty, F. W., Electron capture dissociation of multiply charged protein cations. A nonergodic process. *J. Am. Chem. Soc.* **1998,** 120, (13), 3265-3266.

149. Coon, J. J.; Shabanowitz, J.; Hunt, D. F.; Syka, J. E., Electron transfer dissociation of peptide anions. *J. Am. Soc. Mass Spectr.* **2005,** 16, (6), 880-882.

150. Syka, J. E.; Coon, J. J.; Schroeder, M. J.; Shabanowitz, J.; Hunt, D. F., Peptide and protein sequence analysis by electron transfer dissociation mass spectrometry. *P. Natl. A. Sci. USA* **2004,** 101, (26), 9528-9533.

151. Zubarev, R., *Electron capture dissociation and other ion-electron fragmentation reactions*. John Wiley and Sons: Hoboken, NJ, 2006.

152. Roepstorff, P.; Fohlman, J., Letter to the editors. *Biol. Mass Spectrom.* **1984,** 11, (11), 601-601.

153. Domon, B.; Costello, C. E., A systematic nomenclature for carbohydrate fragmentations in FAB-MS/MS spectra of glycoconjugates. *Glycoconjugate J.* **1988,** 5, (4), 397-409.

154. Tissot, J. D.; Canellini, G.; Rubin, O.; Angelillo-Scherrer, A.; Delobel, J.; Prudent, M.; Lion, N., Blood microvesicles: from proteomics to physiology. *Translational Proteomics* **2013,** 1, (1), 38-52.

155. Csermely, P.; Korcsmáros, T.; Kiss, H. J.; London, G.; Nussinov, R., Structure and dynamics of molecular networks: a novel paradigm of drug discovery: a comprehensive review. *Pharmacol. Therapeut.* **2013,** 138, (3), 333-408.

156. Srinivas, P. R.; Verma, M.; Zhao, Y.; Srivastava, S., Proteomics for cancer biomarker discovery. *Clin. Chem.* **2002,** 48, (8), 1160-1169.

157. Ho, L.; Sharma, N.; Blackman, L.; Festa, E.; Reddy, G.; Pasinetti, G. M., From proteomics to biomarker discovery in Alzheimer's disease. *Brain research reviews* **2005,** 48, (2), 360-369.

158. Rabilloud, T.; Lelong, C., Two-dimensional gel electrophoresis in proteomics: a tutorial. *J. Proteomics* **2011,** 74, (10), 1829-1841.

159. Stoevesandt, O.; Taussig, M. J., Affinity proteomics: the role of specific binding reagents in human proteome analysis. *Expert Rev. Proteomic.* **2012,** 9, (4), 401-414.

160. Kherlopian, A. R.; Song, T.; Duan, Q.; Neimark, M. A.; Po, M. J.; Gohagan, J. K.; Laine, A. F., A review of imaging techniques for systems biology. *BMC Syst. Biol.* **2008,** 2, (1), 74.

161. Righetti, P. G.; Campostrini, N.; Pascali, J.; Hamdan, M.; Astner, H., Quantitative proteomics: a review of different methodologies. *Eur. J. Mass Spectrom.* **2004,** 10, (3), 335-348.

162. Yarmush, M. L.; Jayaraman, A., Advances in proteomic technologies. *Annu. Rev. Biomed. Eng.* **2002,** 4, (1), 349-373.

163. Armirotti, A.; Damonte, G., Achievements and perspectives of top-down proteomics. *Proteomics* **2010,** 10, (20), 3566-3576.

164. Brunner, A. M.; Lössl, P.; Liu, F.; Huguet, R.; Mullen, C.; Yamashita, M.; Zabrouskov, V.; Makarov, A.; Altelaar, A. M.; Heck, A. J., Benchmarking multiple fragmentation methods on an orbitrap fusion for top-down phospho-proteoform characterization. *Anal. Chem.* **2015,** 87, (8), 4152-4158.

165. Dang, X.; Young, N. L., Ultraviolet photodissociation enhances top-down mass spectrometry as demonstrated on green fluorescent protein variants. *Proteomics* **2014,** 14, (10), 1128-1129.

166. Edwards, R. L.; Griffiths, P.; Bunch, J.; Cooper, H. J., Compound heterozygotes and beta-thalassemia: Top-down mass spectrometry for detection of hemoglobinopathies. *Proteomics* **2014,** 14, (10), 1232-1238.

167. Graça, D. C.; Hartmer, R.; Jabs, W.; Beris, P.; Clerici, L.; Stoermer, C.; Samii, K.; Hochstrasser, D.; Tsybin, Y. O.; Scherl, A., Identification of hemoglobin variants by top-down mass spectrometry using selected diagnostic product ions. *Anal. Bioanal. Chem.* **2015,** 407, (10), 2837-2845.

168. Hummel, M.; Wigger, T.; Brockmeyer, J., Characterization of mustard 2S albumin allergens by bottom-up, middle-down, and top-down proteomics: a consensus set of isoforms of Sin a 1. *J. Proteome Res.* **2015,** 14, (3), 1547-1556.

169. Iavarone, F.; Melis, M.; Platania, G.; Cabras, T.; Manconi, B.; Petruzzelli, R.; Cordaro, M.; Siracusano, A.; Faa, G.; Messana, I., Characterization of salivary proteins of schizophrenic and bipolar disorder patients by top-down proteomics. *J. Proteomics* **2014,** 103, 15-22.

170. Li, Y.; Compton, P. D.; Tran, J. C.; Ntai, I.; Kelleher, N. L., Optimizing capillary electrophoresis for top-down proteomics of 30–80 kDa proteins. *Proteomics* **2014,** 14, (10), 1158-1164.

171. Mao, P.; Wang, D., Top-down proteomics of a drop of blood for diabetes monitoring. *J. Proteome Res.* **2014,** 13, (3), 1560-1569.

172. Valeja, S. G.; Xiu, L.; Gregorich, Z. R.; Guner, H.; Jin, S.; Ge, Y., Three dimensional liquid chromatography coupling ion exchange chromatography/hydrophobic interaction chromatography/reverse phase chromatography for effective protein separation in top-down proteomics. *Anal. Chem.* **2015,** 87, (10), 5363-5371.

173. Wu, S.; Brown, J. N.; Tolić, N.; Meng, D.; Liu, X.; Zhang, H.; Zhao, R.; Moore, R. J.; Pevzner, P.; Smith, R. D., Quantitative analysis of human salivary gland-derived intact proteome using top-down mass spectrometry. *Proteomics* **2014,** 14, (10), 1211-1222.

174. Xiu, L.; Valeja, S. G.; Alpert, A. J.; Jin, S.; Ge, Y., Effective protein separation by coupling hydrophobic interaction and reverse phase chromatography for top-down proteomics. *Anal. Chem.* **2014,** 86, (15), 7899-7906.

175. Ye, H.; Mandal, R.; Catherman, A.; Thomas, P. M.; Kelleher, N. L.; Ikonomidou, C.; Li, L., Top-down proteomics with mass spectrometry imaging: a pilot study towards discovery of biomarkers for neurodevelopmental disorders. *PloS one* **2014,** 9, (4), e92831.

176. Zhao, Y.; Riley, N. M.; Sun, L.; Hebert, A. S.; Yan, X.; Westphall, M. S.; Rush, M. J.; Zhu, G.; Champion, M. M.; Medie, F. M., Coupling capillary zone electrophoresis with electron transfer dissociation and activated ion electron transfer dissociation for top-down proteomics. *Anal. Chem.* **2015,** 87, (10), 5422-5429.

177. Zheng, Y.; Fornelli, L.; Compton, P. D.; Sharma, S.; Canterbury, J.; Mullen, C.; Zabrouskov, V.; Fellers, R. T.; Thomas, P. M.; Licht, J. D., Unabridged Analysis of Human Histone H3 by Differential Top-Down Mass Spectrometry Reveals Hypermethylated Proteoforms from MMSET/NSD2 Overexpression. *Mol. Cell. Proteomics* **2016,** 15, (3), 776-790.

178. Zhou, H.; Ning, Z.; E. Starr, A.; Abu-Farha, M.; Figeys, D., Advancements in top-down proteomics. *Anal. Chem.* **2011,** 84, (2), 720-734.

179. Bogdanov, B.; Smith, R. D., Proteomics by FTICR mass spectrometry: top down and bottom up. *Mass Spectrom. Rev.* **2005,** 24, (2), 168-200.

180. Gillet, L. C.; Leitner, A.; Aebersold, R., Mass Spectrometry Applied to Bottom-Up Proteomics: Entering the High-Throughput Era for Hypothesis Testing. *Annu. Rev. Anal. Chem.* **2016**, 9, (1), 449-472.

181. Han, X.; Aslanian, A.; Yates, J. R., Mass spectrometry for proteomics. *Curr. Opin. Chem. Biol.* **2008,** 12, (5), 483-490.

182. Mayne, J.; Ning, Z.; Zhang, X.; Starr, A. E.; Chen, R.; Deeke, S.; Chiang, C.-K.; Xu, B.; Wen, M.; Cheng, K., Bottom-Up Proteomics (2013–2015): Keeping up in the Era of Systems Biology. *Anal. Chem.* **2015,** 88, (1), 95-121.

183. Nesvizhskii, A. I.; Aebersold, R., Interpretation of shotgun proteomic data the protein inference problem. *Mol. Cell. Proteomics* **2005,** 4, (10), 1419-1440.

184. Sun, L.; Zhu, G.; Yan, X.; Zhang, Z.; Wojcik, R.; Champion, M. M.; Dovichi, N. J., Capillary zone electrophoresis for bottom-up analysis of complex proteomes. *Proteomics* **2016,** 16, (2), 188-196.

185. Yates, J. R.; Ruse, C. I.; Nakorchevsky, A., Proteomics by mass spectrometry: approaches, advances, and applications. *Annu. Rev. Biomed. Eng.* **2009,** 11, 49-79.

186. Chait, B. T., Mass spectrometry: bottom-up or top-down? *Science* **2006,** 314, (5796), 65-66.

187. Sleno, L.; Volmer, D. A., Ion activation methods for tandem mass spectrometry. *J. Mass. Spectrom.* **2004,** 39, (10), 1091-1112.

188. UniProt Consortium, UniProt: the universal protein knowledgebase. *Nucleic Acids Res.* **2016,** 45, (D1), D158-D169.

189. Cottrell, J. S.; London, U., Probability-based protein identification by searching sequence databases using mass spectrometry data. *Electrophoresis* **1999,** 20, (18), 3551-3567.

190. Eng, J. K.; McCormack, A. L.; Yates, J. R., An approach to correlate tandem mass spectral data of peptides with amino acid sequences in a protein database. *J. Am. Soc. Mass Spectr.* **1994,** 5, (11), 976-989.

191. Eng, J. K.; Searle, B. C.; Clauser, K. R.; Tabb, D. L., A face in the crowd: recognizing peptides through database search. *Mol. Cell. Proteomics* **2011,** 10, (11), R111. 009522.

192. Goh, W. W. B.; Wong, L., Computational proteomics: designing a comprehensive analytical strategy. *Drug Discov. Today* **2014,** 19, (3), 266-274.

193. Skilling, J.; Denny, R.; Richardson, K.; Young, P.; McKenna, T.; Campuzano, I.; Ritchie, M., ProbSeq—a fragmentation model for interpretation of electrospray tandem mass spectrometry data. *Compar. Funct. Genom.* **2004,** 5, (1), 61-68.

194. Silva, J. C.; Denny, R.; Dorschel, C. A.; Gorenstein, M.; Kass, I. J.; Li, G.-Z.; McKenna, T.; Nold, M. J.; Richardson, K.; Young, P., Quantitative proteomic analysis by accurate mass retention time pairs. *Anal. Chem.* **2005,** 77, (7), 2187-2200.

195. Silva, J. C.; Gorenstein, M. V.; Li, G.-Z.; Vissers, J. P.; Geromanos, S. J., Absolute quantification of proteins by LCMSE a virtue of parallel MS acquisition. *Mol. Cell. Proteomics* **2006,** 5, (1), 144-156.

196. Wrona, M.; Mauriala, T.; Bateman, K. P.; Mortishire-Smith, R. J.; O'Connor, D., 'All-in-One'analysis for metabolite identification using liquid chromatography/hybrid quadrupole time-of-flight mass spectrometry with collision energy switching. *Rapid Commun. Mass Spectrom.* **2005,** 19, (18), 2597-2602.

197. Bern, M.; Finney, G.; Hoopmann, M. R.; Merrihew, G.; Toth, M. J.; MacCoss, M. J., Deconvolution of mixture spectra from ion-trap data-independent-acquisition tandem mass spectrometry. *Anal. Chem.* **2009,** 82, (3), 833-841.

198. Carvalho, P. C.; Han, X.; Xu, T.; Cociorva, D.; Carvalho, M. d. G.; Barbosa, V. C.; Yates III, J. R., XDIA: improving on the label-free data-independent analysis. *Bioinformatics* **2010,** 26, (6), 847-848.

199. Geiger, T.; Cox, J.; Mann, M., Proteomics on an Orbitrap benchtop mass spectrometer using all-ion fragmentation. *Mol. Cell. Proteomics* **2010,** 9, (10), 2252-2261.

200. Gillet, L. C.; Navarro, P.; Tate, S.; Rost, H.; Selevsek, N.; Reiter, L.; Bonner, R.; Aebersold, R., Targeted Data Extraction of the MS/MS Spectra Generated by Data-independent Acquisition: A New Concept for Consistent and Accurate Proteome Analysis. *Mol. Cell. Proteomics* **2012,** 11, (6), O111.016717.

201. Panchaud, A.; Jung, S.; Shaffer, S. A.; Aitchison, J. D.; Goodlett, D. R., Faster, quantitative, and accurate precursor acquisition independent from ion count. *Anal. Chem.* **2011,** 83, (6), 2250-2257.

202. Panchaud, A.; Scherl, A.; Shaffer, S. A.; Von Haller, P. D.; Kulasekara, H. D.; Miller, S. I.; Goodlett, D. R., Precursor acquisition independent from ion count: how to dive deeper into the proteomics ocean. *Anal. Chem.* **2009,** 81, (15), 6481-6488.

203. Plumb, R. S.; Johnson, K. A.; Rainville, P.; Smith, B. W.; Wilson, I. D.; Castro-Perez, J. M.; Nicholson, J. K., UPLC/MSE; a new approach for generating molecular fragment information for biomarker structure elucidation. *Rapid Commun. Mass Spectrom.* **2006,** 20, (13), 1989-1994.

204. Purvine, S.; Yi, E. C.; Goodlett, D. R., Shotgun collision-induced dissociation of peptides using a time of flight mass analyzer. *Proteomics* **2003,** 3, (6), 847-850.

205. Venable, J. D.; Dong, M.-Q.; Wohlschlegel, J.; Dillin, A.; Yates, J. R., Automated approach for quantitative analysis of complex peptide mixtures from tandem mass spectra. *Nat. Methods* **2004,** 1, (1), 39-45.

206. Geromanos, S. J.; Vissers, J. P.; Silva, J. C.; Dorschel, C. A.; Li, G. Z.; Gorenstein, M. V.; Bateman, R. H.; Langridge, J. I., The detection, correlation, and comparison of peptide precursor and product ions from data independent LC-MS with data dependant LC-MS/MS. *Proteomics* **2009,** 9, (6), 1683-1695.

207. Bond, N. J.; Shliaha, P. V.; Lilley, K. S.; Gatto, L., Improving qualitative and quantitative performance for MS^E-based label-free proteomics. *J. Proteome Res.* **2013,** 12, (6), 2340-2353.

208. Distler, U.; Kuharev, J.; Navarro, P.; Levin, Y.; Schild, H.; Tenzer, S., Drift time-specific collision energies enable deep-coverage data-independent acquisition proteomics. *Nat. Methods* **2014,** 11, (2), 167-170.

209. Geromanos, S. J.; Hughes, C.; Ciavarini, S.; Vissers, J. P.; Langridge, J. I., Using ion purity scores for enhancing quantitative accuracy and precision in complex proteomics samples. *Anal. Bioanal. Chem.* **2012,** 404, (4), 1127-1139.

210. Shliaha, P. V.; Bond, N. J.; Gatto, L.; Lilley, K. S., Effects of traveling wave ion mobility separation on data independent acquisition in proteomics studies. *J. Proteome Res.* **2013,** 12, (6), 2323-2339.

211. Zinnel, N. F.; Pai, P. J.; Russell, D. H., Ion mobility-mass spectrometry (IM-MS) for top-down proteomics: increased dynamic range affords increased sequence coverage. *Anal. Chem.* **2012,** 84, (7), 3390-3397.

212. Both, P.; Green, A.; Gray, C.; Šardzík, R.; Voglmeir, J.; Fontana, C.; Austeri, M.; Rejzek, M.; Richardson, D.; Field, R., Discrimination of epimeric glycans and glycopeptides using IM-MS and its potential for carbohydrate sequencing. *Nat. Chem.* **2014,** 6, (1), 65-74.

213. Fasciotti, M.; Lalli, P. M.; Klitzke, C. c. F.; Corilo, Y. E.; Pudenzi, M. A.; Pereira, R. C.; Bastos, W.; Daroda, R. J.; Eberlin, M. N., Petroleomics by Traveling Wave Ion Mobility–Mass Spectrometry Using CO2 as a Drift Gas. *Energ. Fuel.* **2013,** 27, (12), 7277-7286.

214. Paglia, G.; Angel, P. M.; Williams, J. P.; Richardson, K.; Olivos, H. J.; Thompson, J. W.; Menikarachchi, L. C.; Lai, S.; Walsh, C.; Moseley, M. A., Ion-Mobility-Derived Collision Cross Section as an Additional Measure for Lipid Fingerprinting and Identification. *Anal. Chem.* **2014**.

215. Clowers, B.; Dwivedi, P.; Steiner, W.; Hill, H.; Bendiak, B., Separation of sodiated isobaric disaccharides and trisaccharides using electrospray ionization-atmospheric pressure ion mobility-time of flight mass spectrometry. *J. Am. Soc. Mass Spectr.* **2005,** 16, (5), 660-669.

216. Ibrahim, Y. M.; Shvartsburg, A. A.; Smith, R. D.; Belov, M. E., Ultrasensitive Identification of Localization Variants of Modified Peptides Using Ion Mobility Spectrometry. *Anal. Chem.* **2011,** 83, (14), 5617-5623.

217. Hernandez, D. R.; DeBord, J. D.; Ridgeway, M. E.; Kaplan, D. A.; Park, M. A.; Fernandez-Lima, F., Ion dynamics in a trapped ion mobility spectrometer. *Analyst* **2014,** 139, (8), 1913-1921.

218. Giles, K.; Wildgoose, J. L.; Pringle, S.; Langridge, D.; Nixon, P.; Garside, J.; Carney, P. In *Characterising a T-Wave Enabled Multi-Pass Cyclic Ion Mobility Separator*, Proceedings of the 63rd ASMS Conference on Mass Spectrometry and Allied Topics, St. Louis, MO, 2015.

219. Dwivedi, P.; Wu, C.; Matz, L. M.; Clowers, B. H.; Siems, W. F.; Hill, H. H., Gas-Phase Chiral Separations by Ion Mobility Spectrometry. *Anal. Chem.* **2006,** 78, (24), 8200-8206.

220. Fasciotti, M.; Sanvido, G. B.; Santos, V. G.; Lalli, P. M.; McCullagh, M.; de Sá, G. F.; Daroda, R. J.; Peter, M. G.; Eberlin, M. N., Separation of isomeric disaccharides by traveling wave ion mobility mass spectrometry using CO2 as drift gas. *J. Mass. Spectrom.* **2012,** 47, (12), 1643-1647.

221. Liang, X.; Wang, X.; Wang, W.; Zhou, Q.; Chen, C.; Peng, L.; Wen, M.; Qu, T.; Wang, Z.; Zhao, K.; Li, J.; Li, H., Sensitive detection of black powder by stand-alone ion mobility spectrometer with chlorinated hydrocarbon modifiers in drift gas. *Talanta* **2014,** 121, (0), 215-219.

222. Purves, R.; Ozog, A. R.; Ambrose, S.; Prasad, S.; Belford, M.; Dunyach, J.-J., Using Gas Modifiers to Significantly Improve Sensitivity and Selectivity in a Cylindrical FAIMS Device. *J. Am. Soc. Mass Spectr.* **2014,** 25, (7), 1274-1284.

223. Zekavat, B.; Miladi, M.; Becker, C.; Munisamy, S.; Solouki, T., Combined Use of Post-Ion Mobility/Collision-Induced Dissociation and Chemometrics for b Fragment Ion Analysis. *J. Am. Soc. Mass Spectr.* **2013,** 24, (9), 1355-1365.

224. Zekavat, B.; Miladi, M.; Al-Fdeilat, A.; Somogyi, A.; Solouki, T., Evidence for Sequence Scrambling and Divergent H/D Exchange Reactions of Doubly-Charged Isobaric b-Type Fragment Ions. *J. Am. Soc. Mass Spectr.* **2014,** 25, (2), 226-236.

225. Harper, B.; Zekavata, B.; Brantley, M. R.; Pettit, M. E.; Solouki, T. In *Energy Resolved Ion Mobility Deconvolution of Isobaric Compounds*, Proceedings of the 62nd ASMS Conference on Mass Spectrometry and Allied Topics, Baltimore, MD, June 18th, 2014., Baltimore, MD 2014.

226. Hanozin, E.; Morsa, D.; De Pauw, E., Energetics and structural characterization of isomers using ion mobility and gas-phase h/d exchange: learning from lasso peptides. *Proteomics* **2015,** 15, (16), 2823-2834

227. Knappe, T. A.; Linne, U.; Robbel, L.; Marahiel, M. A., Insights into the Biosynthesis and Stability of the Lasso Peptide Capistruin. *Chem. Biol.* **2009,** 16, (12), 1290-1298.

228. Solouki, T.; Szulejko, J., Bimolecular and unimolecular contributions to the disparate self-chemical ionizations of α-Pinene and camphene isomers. *J. Am. Soc. Mass Spectr.* **2007,** 18, (11), 2026-2039.

229. Bartmess, J. E.; Georgiadis, R. M., Empirical methods for determination of ionization gauge relative sensitivities for different gases. *Vacuum* **1983,** 33, (3), 149-153.

230. Spengler, B.; Kirsch, D.; Kaufmann, R.; Cotter, R. J., Metastable decay of peptides and proteins in matrix-assisted laser-desorption mass spectrometry. *Rapid Commun. Mass Spectrom.* **1991,** 5, (4), 198-202.

231. Pauling, L., The Nature of The Chemical Bond. Application of Results Obtained from the Quantum Mechanics and from a Theory of Paramagnetic Susceptibility to the Structure of Molecules. *J. Am. Chem. Soc.* **1931,** 53, (4), 1367-1400.

232. Polce, M. J.; Ren, D.; Wesdemiotis, C., Dissociation of the peptide bond in protonated peptides. *J. Mass. Spectrom.* **2000,** 35, (12), 1391-1398.

233. Fukui, K.; Kameyama, A.; Mukai, Y.; Takahashi, K.; Ikeda, N.; Akiyama, Y.; Narimatsu, H., A computational study of structure–reactivity relationships in Na-adduct oligosaccharides in collision-induced dissociation reactions. *Carbohyd. Res.* **2006,** 341, (5), 624-633.

234. Tang, K.; Page, J. S.; Smith, R. D., Charge competition and the linear dynamic range of detection in electrospray ionization mass spectrometry. *J. Am. Soc. Mass Spectr.* **2004,** 15, (10), 1416-1423.

235. Strobel, F.; Solouki, T.; White, M.; Russell, D., Detection of femtomole and sub-femtomole levels of peptides by tandem magnetic sector/reflectron time-of-flight mass spectrometry and matrix-assisted laser desorption ionization. *J. Am. Soc. Mass Spectr.* **1991,** 2, (1), 91-94.

236. Wang, M.; Han, X. Mass Spectrometry in Metabolomics: Methods and Protocols. In *Methods in Molecular Biology*; Weckweth, W.; Humana Press Inc.: Totowa, NJ, 2014; Vol. 358 pp 203-220.

237. Marshall, A. G.; Rodgers, R. P., Petroleomics: Chemistry of the underworld. *P. Natl. Acad. Sci. USA* **2008,** 105, (47), 18090-18095.

238. Bensimon, A.; Heck, A. J.; Aebersold, R., Mass spectrometry-based proteomics and network biology. *Annu. Rev. Biochem.* **2012,** 81, 379-405.

239. Mishur, R. J.; Rea, S. L., Applications of mass spectrometry to metabolomics and metabonomics: Detection of biomarkers of aging and of age-related diseases. *Mass Spectrom. Rev.* **2012,** 31, (1), 70-95.

240. Aoki, K.; Perlman, M.; Lim, J.-M.; Cantu, R.; Wells, L.; Tiemeyer, M., Dynamic developmental elaboration of N-linked glycan complexity in the Drosophila melanogaster embryo. *J. Biol. Chem.* **2007,** 282, (12), 9127-9142.

241. Xian, F.; Hendrickson, C. L.; Marshall, A. G., High resolution mass spectrometry. *Anal. Chem.* **2012,** 84, (2), 708-719.

242. Crawford, C. L.; Graf, S.; Gonin, M.; Fuhrer, K.; Zhang, X.; Hill Jr, H. H., The novel use of gas chromatography-ion mobility-time of flight mass spectrometry with secondary electrospray ionization for complex mixture analysis. *Int. J. Ion Mobil. Spectrom.* **2011,** 14, (1), 23-30.

243. Liu, X.; Plasencia, M.; Ragg, S.; Valentine, S. J.; Clemmer, D. E., Development of high throughput dispersive LC—ion mobility—TOFMS techniques for analysing the human plasma proteome. *Brief. Funct. Genomic. Proteomic.* **2004,** 3, (2), 177-186.

244. Hilderbrand, A. E.; Myung, S.; Barnes, C. A. S.; Clemmer, D. E., Development of LC-IMS-CID-TOFMS techniques: analysis of a 256 component tetrapeptide combinatorial library. *J. Am. Soc. Mass Spectr.* **2003,** 14, (12), 1424-1436.

245. Lin, S. N.; Griffin, G.; Horning, E.; Wentworth, W., Dependence of polyatomic ion mobilities on ionic size. *J. Chem. Phys.* **1974,** 60, (12), 4994-4999.

246. Fernandez-Lima, F. A.; Becker, C.; McKenna, A. M.; Rodgers, R. P.; Marshall, A. G.; Russell, D. H., Petroleum crude oil characterization by IMS-MS and FTICR MS. *Anal. Chem.* **2009,** 81, (24), 9941-9947.

247. Plasencia, M. D.; Isailovic, D.; Merenbloom, S. I.; Mechref, Y.; Clemmer, D. E., Resolving and assigning N-linked glycan structural isomers from ovalbumin by IMS-MS. *J. Am. Soc. Mass Spectr.* **2008,** 19, (11), 1706-1715.

248. Smith, R. D.; Anderson, G. A.; Lipton, M. S.; Masselon, C.; Paša-Tolic, L.; Shen, Y.; Udseth, H. R., Review: The Use of Accurate Mass Tags for High-Throughput Microbial Proteomics. *Omics.* **2002,** 6, (1), 61-90.

249. Valentine, S. J.; Plasencia, M. D.; Liu, X.; Krishnan, M.; Naylor, S.; Udseth, H. R.; Smith, R. D.; Clemmer, D. E., Toward plasma proteome profiling with ion mobility-mass spectrometry. *J. Proteome Res.* **2006,** 5, (11), 2977-2984.

250. Miladi, M.; Olaitan, A. D.; Zekavat, B.; Solouki, T., Competing Noncovalent Host-guest Interactions and H/D Exchange: Reactions of Benzyloxycarbonyl-Proline Glycine Dipeptide Variants with ND3. *J. Am. Soc. Mass Spectr.* **2015,** 26, (11), 1938-1949.

251. Tuckerman, M. E., Ab initio molecular dynamics: Basic concepts, current trends and novel applications. *J. Phys. Condens. Mat.* **2002,** 14, (50), R1297.

252. Stahl, D. C.; Swiderek, K. M.; Davis, M. T.; Lee, T. D., Data-controlled automation of liquid chromatography/tandem mass spectrometry analysis of peptide mixtures. *J. Am. Soc. Mass Spectr.* **1996,** 7, (6), 532-540.

253. Li, G. Z.; Vissers, J. P.; Silva, J. C.; Golick, D.; Gorenstein, M. V.; Geromanos, S. J., Database searching and accounting of multiplexed precursor and product ion spectra from the data independent analysis of simple and complex peptide mixtures. *Proteomics* **2009,** 9, (6), 1696-1719.

254. Fellgett, P., On the ultimate sensitivity and practical performance of radiation detectors. *JOSA* **1949,** 39, (11), 970-976.

255. Jacquinot, P., The luminosity of spectrometers with prisms, gratings, or Fabry-Perot etalons. *JOSA* **1954,** 44, (10), 761-765.

256. Bateman, R.; Carruthers, R.; Hoyes, J.; Jones, C.; Langridge, J.; Millar, A.; Vissers, J., A novel precursor ion discovery method on a hybrid quadrupole orthogonal acceleration time-of-flight (Q-TOF) mass spectrometer for studying protein phosphorylation. *J. Am. Soc. Mass Spectr.* **2002,** 13, (7), 792-803.

257. Helm, D.; Vissers, J. P.; Hughes, C. J.; Hahne, H.; Ruprecht, B.; Pachl, F.; Grzyb, A.; Richardson, K.; Wildgoose, J.; Maier, S. K., *Mol. Cell. Proteomics*, **2014,** 13, 3709-3715.

258. Wong, S.; Meng, C.; Fenn, J., Multiple charging in electrospray ionization of poly (ethylene glycols). *The J. Phys. Chem.* **1988,** 92, (2), 546-550.

259. Donnarumma, F.; Murray, K. K., Laser ablation sample transfer for localized LC-MS/MS proteomic analysis of tissue. *J. Mass. Spectrom.* **2016,** 51, (4), 261-268.

260. Uniprot Consortium, UniProt: a hub for protein information. *Nucleic Acids Res.* **2014,** gku989.

261. Malinowski, E. R., *Anal. Chem.*, **1977,** 49, (4), 612-617.

262. Bro, R.; De Jong, S., *J. Chemom.*, **1997,** 11, 393-401.

263. Zekavat, B; Harper, B.; Brantley, M. R.; Pettit, M. E.; Solouki, T. In *Use of Multivariate Curve Resolution and Ion Mobility-Mass Spectrometry for Isomer Differentiation*, Proceedings of 62nd ASMS Conference on Mass Spectrometry and Allied Topics, Baltimore, MD, June 18th, 2014.

264. Ong, S. E.; Mann, M., Mass spectrometry–based proteomics turns quantitative. *Nat. Chem. Biol.* **2005,** 1, (5), 252-262.

265. Norris, J. L.; Caprioli, R. M., Analysis of Tissue Specimens by Matrix-Assisted Laser Desorption/Ionization Imaging Mass Spectrometry in Biological and Clinical Research. *Chem. Rev.* **2013,** 113, (4), 2309-2342.

266. Gessel, M. M.; Norris, J. L.; Caprioli, R. M., MALDI imaging mass spectrometry: Spatial molecular analysis to enable a new age of discovery. *J. Proteomics* **2014**, 1-12.

267. Lietz, C. B.; Gemperline, E.; Li, L., Qualitative and quantitative mass spectrometry imaging of drugs and metabolites. *Adv. Drug Deliv. Rev.* **2013,** 65, (8), 1074-1085.

268. Franck, J.; Quanico, J.; Wisztorski, M.; Day, R.; Salzet, M.; Fournier, I., Quantification-Based Mass Spectrometry Imaging of Proteins by Parafilm Assisted Microdissection. *Anal. Chem.* **2013,** 85, (17), 8127-8134.

269. Loziuk, P.; Meier, F.; Johnson, C.; Ghashghaei, H. T.; Muddiman, D. C., TransOmic analysis of forebrain sections in Sp2 conditional knockout embryonic mice using IR-MALDESI imaging of lipids and LC-MS/MS label-free proteomics. *Anal. Bioanal. Chem.* **2016,** 408, (13), 3453-3474.

270. Maier, S. K.; Hahne, H.; Gholami, A. M.; Balluff, B.; Meding, S.; Schoene, C.; Walch, A. K.; Kuster, B., Comprehensive identification of proteins from MALDI imaging. *Mol. Cell. Proteomics* **2013,** 12, (10), 2901-2910.

271. Quanico, J.; Franck, J.; Dauly, C.; Strupat, K.; Dupuy, J.; Day, R.; Salzet, M.; Fournier, I.; Wisztorski, M., Development of liquid microjunction extraction strategy for improving protein identification from tissue sections. *J. Proteomics* **2013,** 79, 200-218.

272. Sarsby, J.; Martin, N. J.; Lalor, P. F.; Bunch, J.; Cooper, H. J., Top-down and bottom-up identification of proteins by liquid extraction surface analysis mass spectrometry of healthy and diseased human liver tissue. *J. Am. Soc. Mass Spectr.* **2014,** 25, (11), 1953-1961.

273. Assadi, M.; Lamerz, J.; Jarutat, T.; Farfsing, A.; Paul, H.; Gierke, B.; Breitinger, E.; Templin, M. F.; Essioux, L.; Arbogast, S., Multiple protein analysis of formalin-fixed and paraffin-embedded tissue samples with reverse phase protein arrays. *Mol. Cell. Proteomics* **2013,** 12, (9), 2615-2622.

274. Scicchitano, M. S.; Dalmas, D. A.; Boyce, R. W.; Thomas, H. C.; Frazier, K. S., Protein extraction of formalin-fixed, paraffin-embedded tissue enables robust proteomic profiles by mass spectrometry. *J. Histochem. Cytochem.* **2009,** 57, (9), 849-860.

275. Zhang, W.; Sakashita, S.; Taylor, P.; Tsao, M. S.; Moran, M. F., Comprehensive proteome analysis of fresh frozen and optimal cutting temperature (OCT) embedded primary non-small cell lung carcinoma by LC–MS/MS. *Methods* **2015,** 81, 50-55.

276. Spraggins, J. M.; Rizzo, D. G.; Moore, J. L.; Rose, K. L.; Hammer, N. D.; Skaar, E. P.; Caprioli, R. M., MALDI FTICR IMS of intact proteins: using mass accuracy to link protein images with proteomics data. *J. Am. Soc. Mass Spectr.* **2015,** 26, (6), 974-985.

277. Quanico, J.; Franck, J.; Gimeno, J. P.; Sabbagh, R.; Salzet, M.; Day, R.; Fournier, I., Parafilm-assisted microdissection: a sampling method for mass spectrometry-based identification of differentially expressed prostate cancer protein biomarkers. *Chem. Com.* **2015,** 51, (22), 4564-4567.

278. Quanico, J.; Franck, J.; Wisztorski, M.; Salzet, M.; Fournier, I., Integrated mass spectrometry imaging and omics workflows on the same tissue section using grid-aided, parafilm-assisted microdissection. *BBA-Gen. Subjects* **2017**.

279. Simone, N.; Bonner, R.; Gillespie, J.; Emmert-Buck, M.; Liotta, L., Laser-capture microdissection: opening the microscopic frontier to molecular analysis. *Trends. Genet.* **1998,** 14, (7), 272-276.

280. Cheng, L.; Zhang, S.; Davidson, D.; Kuhar, M.; Wang, M.; Williamson, S.; Zhang, D.; MacLennan, G., Laser Capture Microdissection in Molecular Diagnostics. In *Molecular Genetic Pathology*, Cheng, L.; Zhang, D. Y.; Eble, J. N., Eds. Springer New York: 2012; pp 465-482.

281. Legres, L. G.; Janin, A.; Masselon, C.; Bertheau, P., Beyond laser microdissection technology: follow the yellow brick road for cancer research. *Am. J. Canc. Res.* **2014,** 4, (1), 1-28.

282. Palmer-Toy, D. E.; Sarracino, D. A.; Sgroi, D.; LeVangie, R.; Leopold, P. E., Direct Acquisition of Matrix-assisted Laser Desorption/Ionization Time-of-Flight Mass Spectra from Laser Capture Microdissected Tissues. *Clin. Chem.* **2000,** 46, (9), 1513-1516.

283. Bhattacharya, S. H.; Gal, A.; Murray, K. K., Laser Capture Microdissection MALDI for Direct Analysis of Archival Tissue. *J. Proteome Res.* **2003,** 2, (1), 95-98.

284. Xu, B.; Caprioli, R. M.; Sanders, M.; Jensen, R., Direct analysis of laser capture microdissected cells by MALDI mass spectrometry. *J. Am. Soc. Mass Spectr.* **2002,** 13, (11), 1292-1297.

285. He, J.; Zhu, J.; Liu, Y.; Wu, J.; Nie, S.; Heth, J. A.; Muraszko, K. M.; Fan, X.; Lubman, D. M., Immunohistochemical staining, laser capture microdissection, and filter-aided sample preparation-assisted proteomic analysis of target cell populations within tissue samples. *Electrophoresis* **2013,** 34, (11), 1627-1636.

286. Zhu, J.; Nie, S.; Wu, J.; Lubman, D. M., Target Proteomic Profiling of Frozen Pancreatic CD24+ Adenocarcinoma Tissues by Immuno-Laser Capture Microdissection and Nano-LC–MS/MS. *J. Proteomics Res.* **2013,** 12, (6), 2791-2804.

287. Hebbar, S.; Schulz, W. D.; Sauer, U.; Schwudke, D., Laser Capture Microdissection Coupled with On-Column Extraction LC-MS nEnables Lipidomics of Fluorescently Labeled DrosophilaNeurons. *Anal. Chem.* **2014,** 86, (11), 5345-5352.

288. Sethi, S.; Vrana, J. A.; Theis, J. D.; Leung, N.; Sethi, A.; Nasr, S. H.; Fervenza, F. C.; Cornell, L. D.; Fidler, M. E.; Dogan, A., Laser microdissection and mass spectrometry-based proteomics aids the diagnosis and typing of renal amyloidosis. *Kidney Int.* **2012,** 82, (2), 226-234.

289. Huang, M. Z.; Jhang, S. S.; Cheng, C. N.; Cheng, S. C.; Shiea, J., Effects of matrix, electrospray solution, and laser light on the desorption and ionization mechanisms in electrospray-assisted laser desorption ionization mass spectrometry. *Analyst* **2010,** 135, (4), 759-766.

290. Lorenz, M.; Ovchinnikova, O. S.; Van Berkel, G. J., Fully automated laser ablation liquid capture surface analysis using nanoelectrospray ionization mass spectrometry. *Rapid Commun. Mass Spectrom.* **2014,** 28, (11), 1312-1320.

291. Ovchinnikova, O. S.; Kertesz, V.; Van Berkel, G. J., Combining Laser Ablation/Liquid Phase Collection Surface Sampling and High-Performance Liquid Chromatography−Electrospray Ionization-Mass Spectrometry. *Anal. Chem.* **2011,** 83, (6), 1874-1878.

292. Park, S. G.; Murray, K. K., Infrared laser ablation sample transfer for MALDI and electrospray. *J. Am. Soc. Mass Spectr.* **2011,** 22, (8), 1352-1362.

293. Park, S. G.; Murray, K. K., Infrared laser ablation sample transfer for on-line liquid chromatography electrospray ionization mass spectrometry. *J. Mass Spectrom.* **2012,** 47, (10), 1322-1326.

294. Park, S. G.; Murray, K. K., Ambient laser ablation sampling for capillary electrophoresis mass spectrometry. *Rapid Commun. Mass Spectrom.* **2013,** 27, 1673-1680.

295. Domon, B.; Aebersold, R., Mass spectrometry and protein analysis. *Science* **2006,** 312, 5771, 212-217.

296. Chen, C.; Li, Z.; Huang, H.; Suzek, B. E.; Wu, C. H.; UniProt Consortium, A fast peptide match service for UniProt knowledgebase. *Bioinformatics* **2013,** 29, (21), 2808-2809.

297. Paizs, B.; Suhai, S., Fragmentation pathways of protonated peptides. *Mass Spectrom. Rev.* **2005,** 24, (4), 508-548.

298. Vandenbogaert, M.; Li-Thiao-Té, S.; Kaltenbach, H. M.; Zhang, R.; Aittokallio, T.; Schwikowski, B., Alignment of LC-MS images, with applications to biomarker discovery and protein identification. *Proteomics* **2008,** 8, (4), 650-672.

299. Neue, U. D.; Phoebe, C. H.; Tran, K.; Cheng, Y.-F.; Lu, Z., Dependence of reversed-phase retention of ionizable analytes on pH, concentration of organic solvent and silanol activity. *J. Chromatogr. A.* **2001,** 925, (1), 49-67.

300. Wyttenbach, T.; Kemper, P. R.; Bowers, M. T., Design of a new electrospray ion mobility mass spectrometer. *Int. J. Mass. Spectrom.* **2001,** 212, (1), 13-23.

301. Mason, E. A.; McDaniel, E. W., Transport properties of ions in gases. *NASA STI/Recon Technical Report A* **1988,** 89.

302. Walsh, G., Biopharmaceutical benchmarks 2014. *Nat. Biotechnol.* **2014,** 32, (10), 992.

303. Chen, W.; Doneanu, C. E.; Lauber, M.; Koza, S.; Prakash, K.; Stapels, M.; Fountain, K. J., Improved Identification and Quantification of Host Cell Proteins (HCPs) in Biotherapeutics Using Liquid Chromatography-Mass Spectrometry. In *State-of-the-Art and Emerging Technologies for Therapeutic Monoclonal Antibody Characterization Volume 3. Defining the Next Generation of Analytical and Biophysical Techniques*; Schiel, J. E., Davis, D. L., Borisov, O. V.; ACS Publications: Washington, DC, 2015; Vol. 3, pp 357-393.

304. Pisupati, K.; Tian, Y.; Okbazghi, S.; Benet, A.; Ackermann, R.; Ford, M.; Saveliev, S.; Hosfield, C. M.; Urh, M.; Carlson, E., A multidimensional analytical comparison of Remicade and the biosimilar Remsima. *Anal. Chem.* **2017,** 89, (9), 4838-4846.

305. Rosenberg, A. S.; Verthelyi, D.; Cherney, B. W., Managing uncertainty: a perspective on risk pertaining to product quality attributes as they bear on immunogenicity of therapeutic proteins. *J. Pharm. Sci.* **2012,** 101, (10), 3560-3567.

306. Flynn, G. C.; Nyberg, G. B., Using quality by design principles in setting a control strategy for product quality attributes. In *State-of-the-Art and Emerging Technologies for Therapeutic Monoclonal Antibody Characterization Volume 1. Monoclonal Antibody Therapeutics: Structure, Function, and Regulatory Space*; Schiel, J. E., Davis, D. L., Borisov, O. V.; ACS Publications: Washington, DC, 2014; Vol. 1, pp 117-150.

307. Li, W.; Kerwin, J. L.; Schiel, J.; Formolo, T.; Davis, D.; Mahan, A.; Benchaar, S. A., Structural elucidation of post-translational modifications in monoclonal antibodies. In *State-of-the-Art and Emerging Technologies for Therapeutic Monoclonal Antibody Characterization Volume 2. Biopharmaceutical Characterization: The NISTmAb Case Study*; Schiel, J. E., Davis, D. L., Borisov, O. V.; ACS Publications: Washington, DC, 2014; Vol. 2, pp 119-183.

308. Alsenaidy, M. A.; Jain, N. K.; Kim, J. H.; Middaugh, C. R.; Volkin, D. B., Protein comparability assessments and potential applicability of high throughput biophysical methods and data visualization tools to compare physical stability profiles. *Front. Pharmacol.* **2014,** 5, 39.

309. Manuilov, A. V.; Radziejewski, C. H.; Lee, D. H., Comparability analysis of protein therapeutics by bottom-up LC-MS with stable isotope-tagged reference standards. *MAbs* **2011,** 3, (4), 387-395.

310. Rogers, R. S.; Nightlinger, N. S.; Livingston, B.; Campbell, P.; Bailey, R.; Balland, A., Development of a quantitative mass spectrometry multi-attribute method for characterization, quality control testing and disposition of biologics. *MAbs* **2015,** 7, (5), 881-890.

311. Zhang, Y.; Guo, J., Characterization and QC of biopharmaceuticals by MS-based 'multi-attribute method': advantages and challenges. *Bioanalysis* **2017,** 9, (6), 499-502.